# Synthesis of Diblock Copolymer Nanoparticles for Agrochemical Applications

## Derek H. H. Chan

A thesis submitted in partial fulfilment of the requirements
for the degree of Doctor of Philosophy

The University of Sheffield
Faculty of Science
Department of Chemistry

December 2021

# Declaration

The work described in this Thesis was carried out at the University of Sheffield under the supervision of Professor Steven P. Armes between October 2017 and December 2021. It has not been submitted, either wholly or in part, for this or any other degree. All the work is the original work of the author, except where acknowledged by references.

Signature: ______________________________

Derek H. H. Chan December 2021

## Acknowledgements

I am very lucky to have had the support of many people over the last four years. Firstly, I would like to say thank you to my supervisor Professor Steve Armes. Thank you for the opportunity to carry out my PhD in your group. Your knowledge and attention to detail is incredible and I have certainly learnt a lot from you. Thank you for all the advice, encouragement, and hours of proof reading.

Thank you to my industrial sponsor Syngenta for funding and supporting my PhD. In particular, a big thank you to my industrial supervisors Dr. Chris Lindsay, Dr. Phil Taylor and Dr. Emily Kynaston. I appreciated their guidance throughout and making me feel welcome when visiting Jealott's Hill.

I would like to thank all the staff in the Chemistry Department who have been immensely helpful during my PhD. Thank you to all the people who helped on the many analytical techniques: Dr. Sandra van Meurs for her advice on NMR experiments; Dr. Tom Neal for his help with the SAXS work; Dr. Chris Hill and Dr. Svet Tzokov for their support at the TEM facilities. Also thank you to Dr. Ian Ross and the team at the Sorby Centre for their help with SEM.

A massive thank you to the past and present Armes Group members. I have really enjoyed being part of such a wonderful group who are always supportive. Going beyond work, the pints, pub lunches, conferences, ArmesFest, BBQ, Christmas meals, football summer tournaments are just a few highlights that I will always remember.

I would also like to thank my old housemate Joe for welcoming me to Sheffield. Our TV series binge sessions and visits to the ice hockey were always a welcome distraction.

A huge thank you to my entire family for their support with everything over the years. My brother Gary who is always up for doing something fun. I am grateful to you and Vivian for our regular meetups in Yorkshire. Of course, thank you to my Mum and Dad. I know you are maybe still a bit unsure on what I actually do, but I appreciate all your unconditional love and support with everything. I am very lucky to have you both.

Finally, a special thank you to Xue. I have always been able to rely on your support and I am extremely grateful for everything you do. Thank you for all the adventures over the last few years and I look forward to many more.

# Publications

Chan, D. H. H.; Cockram, A. A.; Gibson, R. R.; Kynaston, E. L.; Lindsay, C.; Taylor, P.; Armes, S. P. RAFT Aqueous Emulsion Polymerization of Methyl Methacrylate: Observation of Unexpected Constraints When Employing a Non-Ionic Steric Stabilizer Block. *Polym. Chem.* **2021**, *12*, 5760–5769.

Chan, D. H. H.; Kynaston, E. L.; Lindsay, C.; Taylor, P.; Armes, S. P. Block Copolymer Nanoparticles Are Effective Dispersants for Micrometer-Sized Organic Crystalline Particles. *ACS Appl. Mater. Interfaces* **2021**, *13*, 30235–30243.

Chan, D. H. H.; Millet, A.; Fisher, C. R.; Price, M. C.; Burchell, M. J.; Armes, S. P. Synthesis and Characterization of Polypyrrole-Coated Anthracene Microparticles: A New Synthetic Mimic for Polyaromatic Hydrocarbon-Based Cosmic Dust. *ACS Appl. Mater. Interfaces* **2021**, *13*, 3175–3185.

Chan, D. H. H.; Deane, O. J.; Kynaston, E. L.; Lindsay, C.; Taylor, P.; Armes, S. P. Sterically-Stabilized Diblock Copolymer Nanoparticles Enable Facile Preparation of Suspension Concentrates Comprising Various Agrochemical Actives. *Langmuir* **2022**, *38*, 2885-2894.

# Abstract

In this Thesis, reversible addition-fragmentation chain transfer (RAFT) polymerization has been used to prepare various types of sterically-stabilized diblock copolymer nanoparticles *via* polymerization-induced self-assembly (PISA). These nanoparticles are then evaluated as putative dispersants for a specific agrochemical formulation known as a suspension concentrate (SC).

Firstly, RAFT aqueous emulsion polymerization of methyl methacrylate (MMA) was conducted at 70 °C using poly(glycerol monomethacrylate) (PGMA) as a water-soluble precursor block. Targeting a mean degree of polymerization (DP) of 20 to 100 for the PMMA block led to colloidal dispersions of kinetically-trapped spheres with *z*-average diameters ranging from 17 nm to 31 nm. However, targeting DPs above 100 only produced aggregates comprising flocculated spheres. This unexpected constraint appears to be related to the relatively high glass transition temperature ($T_g$) of the PMMA block. In contrast, colloidally stable dispersions could be obtained when targeting similar (or higher) PMMA DPs simply by switching from a non-ionic PGMA stabilizer to either an anionic poly(methacrylic acid) stabilizer or a cationic poly(2-(methacryloyloxy)ethyl trimethylammonium chloride) stabilizer. RAFT end-groups from $PGMA_{50}$-$PMMA_{80}$ nanoparticles were cleaved by visible light irradiation using a blue LED source ($\lambda$ = 405 nm). UV GPC studies indicated that 87% dithiobenzoate end-groups were removed within 12 h at 80 °C. This approach proved to be more effective than using excess $H_2O_2$ under the same conditions, presumably because such water-soluble reagents suffer from restricted access to the hydrophobic PMMA cores.

$PGMA_{50}$-$PMMA_{80}$ nanoparticles were evaluated as a dispersant for the preparation of organic crystalline microparticles of a widely-used fungicide, azoxystrobin, *via* ball milling. Stable SCs were readily obtained at 20% w/w solids after milling for 10 min. Laser diffraction and optical microscopy studies indicate the formation of ~2 μm azoxystrobin microparticles, which is comparable to that obtained using commercial water-soluble dispersants such as Morwet D-425. Nanoparticle adsorption onto the surface of the azoxystrobin microparticles was confirmed by electron microscopy studies. An adsorbed amount of approximately 5.5 mg $m^{-2}$ was estimated using a supernatant assay based on solution densitometry. Moreover, further evidence for nanoparticle adsorption was provided by aqueous electrophoresis and X-ray photoelectron spectroscopy (XPS) studies. Similar data were obtained when changing the nature of the core-forming block from PMMA to poly(2,2,2-trifluoroethyl methacrylate) (PTFEMA). Fractional nanoparticle surface coverages were 0.24 to 0.28 by XPS.

Follow-up studies examined the effect of varying the nature of the steric stabilizer block, the mean nanoparticle diameter and the $T_g$ of the core-forming block on the particle size and colloidal stability of the nanoparticle-coated azoxystrobin microparticles. Diblock copolymer nanoparticles prepared using a non-ionic steric stabilizer – rather than a cationic or an anionic steric stabilizer – were demonstrated to be more effective dispersants. Furthermore, nanoparticles of up to 51 nm diameter enabled efficient milling and produced stable SCs, whereas larger nanoparticles proved to be less effective. Moreover, crosslinking the nanoparticle cores and lowering the $T_g$ of the core-forming block had little effect on the formation of azoxystrobin microparticles. This versatile approach was also shown to be applicable to five other organic crystalline agrochemicals, suggesting generic behaviour.

Finally, ball milling was used to produce anthracene microparticles of 2 to 4 μm diameter in the presence of an anionic commercial polymeric dispersant (Morwet D-425) using two different ball milling techniques. These anthracene microparticles were then coated with a thin overlayer of polypyrrole (PPy), which is an air-stable organic conducting polymer. The uncoated and PPy-coated anthracene microparticles were characterized using optical microscopy, scanning electron microscopy, laser diffraction, aqueous electrophoresis, FT-IR spectroscopy, Raman microscopy, and XPS. Moreover, our collaborations with space scientists at U. Kent confirmed that both types of microparticles can be accelerated up to hypervelocities (~ 6 km $s^{-1}$) using a light gas gun. Thus, these PPy-coated anthracene microparticles are expected to serve as the first useful synthetic mimic for understanding the behaviour of polyaromatic hydrocarbon-based cosmic dust.

# List of Abbreviations

| | |
|---|---|
| ACVA | 4,4′-azobis(4-cyanopentanoic acid) |
| AI | active ingredient |
| AM | acrylamide |
| AN | acrylonitrile |
| ATRP | atom transfer radical polymerization |
| CCZ | cyproconazole |
| CDA | cosmic dust analyzer |
| CMC | critical micelle concentration |
| CPDB | 2-cyanopropyl dithiobenzoate |
| CRP | controlled radical polymerization |
| CTA | chain transfer agent |
| DAAM | diacetone acrylamide |
| DDMAT | 2-(dodecylthiocarbonothioylthio)-2-methylpropionic acid |
| DEAAm | *N,N′*-diethylacrylamide |
| DEGMA | di(ethylene glycol) methyl ether methacrylate |
| DFZ | difenoconazole |
| DLS | dynamic light scattering |
| DMF | dimethylformamide |
| DNA | deoxyribonucleic acid |
| DP | degree of polymerization |
| EDL | electrical double layer |
| EGDMA | ethylene glycol dimethylacrylate |
| FRP | free radical polymerization |
| GlyMA | glycidyl methacrylate |
| GPC | gel permeation chromatography |
| HBA | 4-hydroxybutyl acrylate |
| HBMA | 2-hydroxybutyl methacylate |
| HEAA | N-hydroxyethyl acrylamide |
| HPMA | 2-hydroxypropyl methacrylate |
| IPGMA | isopropylideneglycerol methacrylate |
| IZM | isopyrazam |
| LAM | less-activated monomer |
| LAP | living anionic polymerization |
| LRP | living radical polymerization |
| MAM | more-activated monomer |
| MEA | 2-methoxyethyl acrylate |
| MMA | methyl methacrylate |
| $M_n$ | number-average molecular weight |
| MOEMA | 2-methoxyethyl methacrylate |
| $M_w$ | weight-average molecular weight |
| MWD | molecular weight distribution |
| nBA | *n*-butyl acrylate |

| | |
|---|---|
| NIPAM | N-isopropylacrylamide |
| NMP | nitroxide-mediated polymerization |
| NVP | N-vinylpyrrolidone |
| ODT | order-disorder transition |
| OOT | order-order transition |
| PAA | poly(acrylic acid) |
| PAH | polyaromatic hydrocarbon |
| PBzMA | poly(benzyl methacrylate) |
| PCS | photon correlation spectroscopy |
| PDI | polydispersity index |
| PDMA | poly(2-(dimethylamino)ethyl methacrylate |
| PDMAC | poly(N,N'-dimethylacrylamide) |
| PEG | poly(ethylene glycol) |
| PEGA | poly(ethylene glycol) methyl ether acrylate |
| PEO | poly(ethylene oxide) |
| PEOMA | poly(ethylene oxide) methyl ether methacrylate |
| PETTC | 4-cyano-4-(2-phenylethanesulfanylthiocarbonyl)sulfanylpentanoic acid |
| PGMA | poly(glycerol monomethacrylate) |
| PISA | polymerization-induced self-assembly |
| PLMA | poly(lauryl methacrylate) |
| PMAA | poly(methacrylic acid) |
| PMETAC | poly(2-(methacryloyloxy)ethyl trimethylammonium chloride) |
| PMPC | poly(2-(methacryloyloxy)ethyl phosphorylcholine |
| PNAEP | poly(2-(*N*-acryloyloxy)ethyl pyrrolidone) |
| PNMEP | poly(*N*-(2-methacryloyloxy)ethyl pyrrolidone) |
| PNVP | poly(N-vinylpyrrolidone) |
| PPO | poly(propylene oxide) |
| PPy | polypyrrole |
| PRE | persistent radical effect |
| PS | polystyrene |
| PVA | poly(vinyl alcohol) |
| PXD | pinoxaden |
| QCM-D | quartz crystal microbalance with dissipation |
| RAFT | reversible addition-fragmentation chain transfer |
| RDRP | reversible deactivation radical polymerization |
| S | styrene |
| SC | suspension concentrate |
| SDS | sodium dodecyl sulfate |
| SEM | scanning electron microscopy |
| TEB | tebuconazole |
| TEM | transmission electron microscopy |
| TFEMA | 2,2,2-trifluoroethyl methacrylate |
| $T_g$ | glass transition temperature |
| THF | tetrahydrofuran |

| | |
|---|---|
| VAc | vinyl acetate |
| XPS | X-ray photoelectron spectroscopy |

# Table of Contents

# Chapter 1

# Introduction

## 1.1 Polymer Science

Polymers are high molecular weight molecules made up of many individual repeat units known as monomers.[1] Their long-chain structure was originally proposed by Staudinger in 1920.[2] Polymers are essential to everyday life and have been developed for a remarkably wide range of applications since the mid-20th century. Examples include textiles, paints and coatings, lightweight transportation, biomaterials, home and personal care products and packaging.[3] Certain polymers are also found in nature, e.g. deoxyribonucleic acid (DNA), all proteins and various carbohydrates such as cellulose.

In 1929, Carothers distinguished between addition and condensation polymers depending on the chemical structure of the initial monomer and final polymer. In the case of addition polymers, individual monomer units add to growing polymer chains, whereas for condensation polymers a small molecule (condensate) is released during the formation of each repeat unit, which may involve the reaction of monomer, dimer, oligomers or polymeric species.[4] However, these definitions became inadequate as further types of polymers were developed (e.g. polyurethanes). Instead, Flory proposed a new classification system based on polymerization mechanism that distinguished between step and chain polymerization. Step polymerization is an appropriate description for all condensation polymers but also includes polyurethanes, for which no small molecule is generated during polymerization. In contrast, chain polymerization proceeds by addition of multiple monomer units *via* reactive centres located at the end of the growing chains.[5]

The mean number of repeat units per chain is termed the number-average degree of polymerization (DP). Synthetic polymers do not exhibit a unique molecular weight: instead, they comprise a mixture of chains of differing lengths (and hence masses). Thus, such polymers exhibit a molecular weight distribution (MWD). The two most common moments used to describe the MWD are the number-average molecular weight ($M_n$) and the weight-average molecular weight ($M_w$), see **Figure 1.1** and **Equations 1.1 and 1.2**.

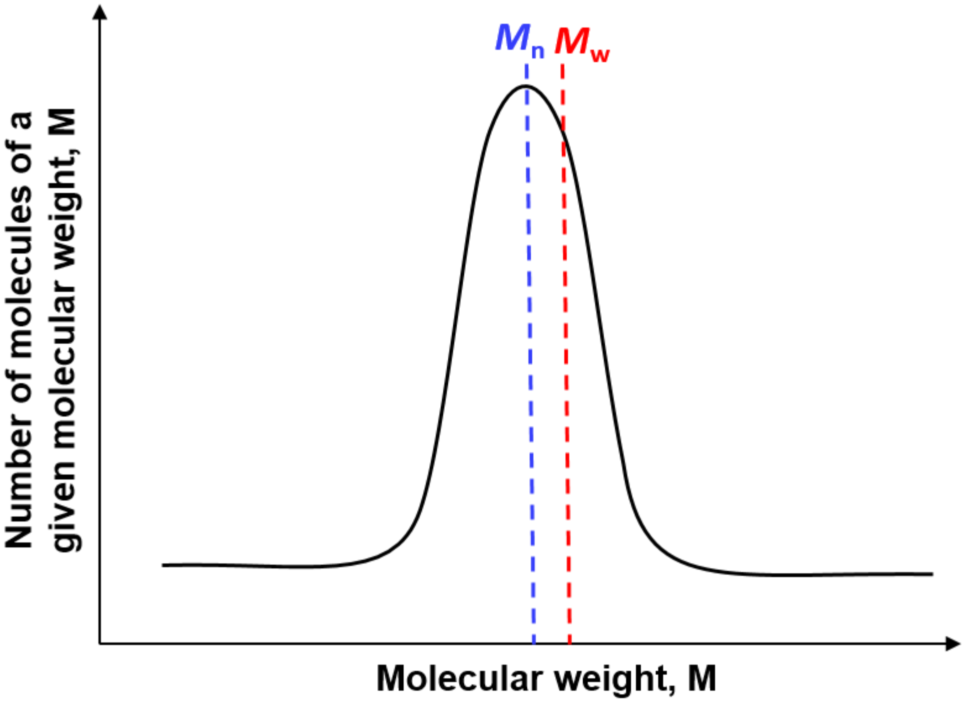

**Figure 1.1.** Schematic representation of a molecular weight distribution curve for a typical synthetic polymer, which indicates the number-average ($M_n$) and weight-average ($M_w$) molecular weight.[1,6]

$$M_n = \frac{\sum n_i M_i}{\sum n_i} \tag{1.1}$$

$$M_w = \frac{\sum n_i M_i^2}{\sum n_i M_i} \tag{1.2}$$

Here $n_i$ relates to the number of chains comprising $i$ monomer units and $M_i$ is the molecular weight of each chain. $M_n$ is biased towards shorter chains, while $M_w$ is biased towards longer chains. The polydispersity index (PDI), also known as the dispersity, is equal to $M_w/M_n$ and gives an indication of the width of the MWD. $M_w/M_n$ will always be equal or greater than unity (since $M_w \geq M_n$). If $M_w = M_n$, then the polymer is said to be perfectly monodisperse and all chains have identical mass, which is a characteristic not yet achieved for synthetic polymers.[6] A polymer with an $M_w/M_n$ below 1.5 is considered to have a relatively narrow MWD, while an $M_w/M_n$ above 1.5 indicates a relatively broad MWD.[7]

## 1.2 Polymerization Techniques

### 1.2.1 Free Radical Polymerization

Free radical polymerization (FRP) is a commonly used type of chain polymerization. It is widely utilized in industry since it is applicable to many functional vinyl monomers and is tolerant of both protic and aprotic solvents.[8] Furthermore, FRP can be employed under various different physical conditions, including bulk, solution, dispersion, suspension or emulsion polymerization.[1,9] The FRP mechanism comprises four main steps: initiation, propagation, termination and transfer (see **Figure 1.2**).

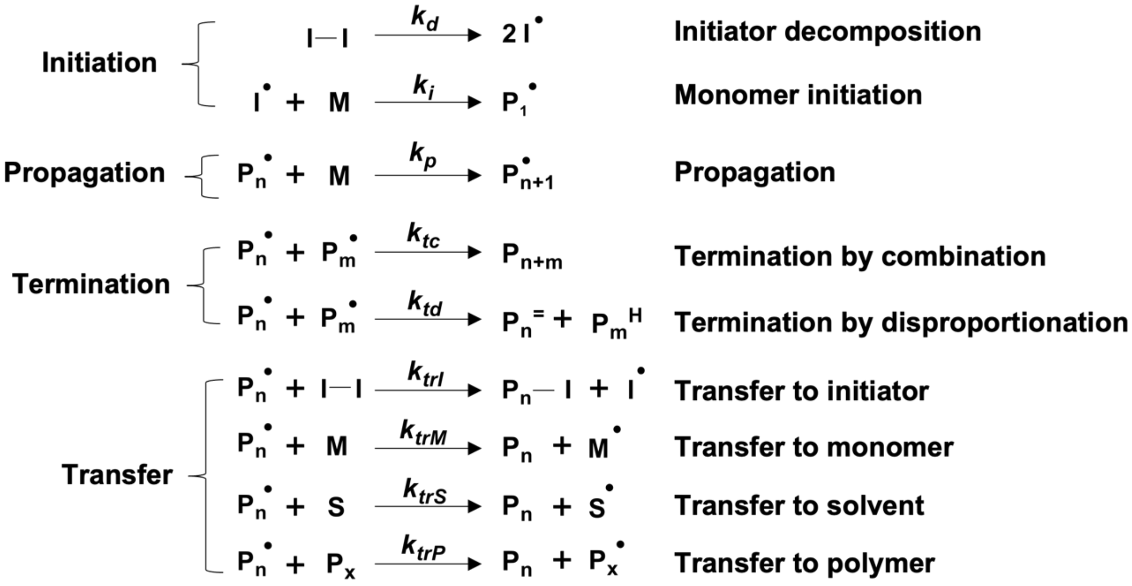

**Figure 1.2.** Reaction mechanism for free radical polymerization, which consists of the following four steps: initiation, propagation, termination and transfer.[8]

Firstly, decomposition of the initiator *via* homolytic fission generates two free radical species (I•). This can occur through thermal decomposition, photolysis or redox chemistry.[10] The next step is initiation, which involves reaction of such free radicals with a single monomer molecule to form a new active radical adduct, $P_1$•. The rate of decomposition, $k_d$, is relatively slow compared to the rate of initiation, $k_i$, and hence is usually the rate-limiting step.[11] As a result, the rate of initiation ($R_i$) is simply given by **Equation 1.3**.

$$R_i = -\frac{\mathrm{d}[P_1^{\bullet}]}{dt} = 2fk_d[\mathrm{I}_2] \quad \mathbf{(1.3)}$$

Here the initiator efficiency (*f*) describes the probability that any given free radical reacts with monomer, rather than undergoing an unwanted side reaction. A numerical factor of two is required in **Equation 1.3** because each initiator molecule forms two radicals *via* homolytic fission. Propagation then proceeds *via* rapid addition of many monomer units to each radical centre ($P_1$•), to afford polymer radicals ($P_n$•, $P_{n+1}$•). The rate of propagation ($R_p$) is given by **Equation 1.4**.

$$R_p = -\frac{\mathrm{d}[\mathrm{M}]}{dt} = k_p[P_n^{\bullet}][\mathrm{M}] \quad \mathbf{(1.4)}$$

Termination can occur *via* either combination or disproportionation when two polymer radicals (e.g. $P_n$• and $P_m$•) react together. The mechanism for combination involves two propagating polymer radicals reacting to yield a single non-propagating polymer chain whose mass is the sum of that of the two reactants. In contrast, termination by disproportionation occurs when a hydrogen atom is abstracted from one polymer radical by another. This reaction produces two non-propagating polymer chains comprising a saturated ($P_m^H$) and unsaturated chain-end ($P_n^=$), respectively. The rate of termination ($R_t$; **Equation 1.5**) involves a composite rate constant, $k_t$, which combines the rate constant for termination by combination with that for termination by disproportionation ($k_t = k_{tc} + k_{td}$).

$$R_t = -\frac{\mathrm{d}[P^{\bullet}]}{dt} = 2k_t[P^{\bullet}]^2 \quad \mathbf{(1.5)}$$

Chain transfer can also occur in FRP (**Figure 1.2**). Thus, polymer radicals can react with solvent, initiator, monomer, or dormant chains to give a non-propagating polymer chain and a new radical species. Such side reactions cause chain branching, which affects the final molecular weight and dispersity. The overall polymerization kinetics remain unchanged since chain transfer is relatively fast and there is no net loss of radicals. Hence the relative rates of initiation, propagation and termination dictate the overall rate of polymerization ($R_{poly}$), see **Equation 1.6**.

$$R_{poly} = k_p[\mathrm{M}]\sqrt{\frac{fk_d[I]}{k_t}} \qquad \textbf{(1.6)}$$

This equation can be derived by applying the steady-state approximation, which assumes that the rate of initiation is equal to the rate of termination. It is also assumed that the number of monomer molecules consumed during initiation is negligible compared to that consumed during propagation.[5] According to **Equation 1.6,** increasing either the monomer concentration [$M$] or the initiator concentration [$I$] leads to a faster rate of polymerization.

The kinetic chain length ($D_k$) is the average number of monomer units consumed per radical active species and is given by $D_k = R_p/R_t$. Invoking the steady-state approximation ($R_i = R_t$), the polymer radical concentration, [$P$•], can be calculated from **Equation 1.7** while $D_\mathrm{k}$ can be calculated using **Equation 1.8**.

$$[P^{\bullet}] = \sqrt{\frac{fk_p[\mathrm{I}]}{k_t}} \qquad \textbf{(1.7)}$$

$$D_k = \frac{R_p}{R_t} = \frac{k_p[\mathrm{M}][P_n^{\bullet}]}{2k_t[P_n^{\bullet}]^2} = \frac{k_p[\mathrm{M}]}{2\sqrt{fk_dk_t[I_2]}} \qquad \textbf{(1.8)}$$

**Equation 1.8** states that the $D_k$, and therefore the molecular weight, is proportional to [$M$] and $[I]^{-1/2}$. As a result, higher molecular weight polymers can be obtained if the monomer concentration is increased or if the initiator concentration is reduced.[10] The $D_k$ can be used to calculate the mean DP and depends on the nature of the termination mechanism. For example, DP = $2D_\mathrm{k}$ corresponds to termination purely by combination whereas DP = $D_k$ describes termination solely by disproportionation.[1] The latter termination mechanism predominates for the methacrylic polymers prepared in this Thesis.

FRP is important for producing many vinyl polymers on an industrial scale.[12] However, one disadvantage is the lack of control over the target DP and hence polymer molecular weight. It is also not possible to prepare well-defined diblock copolymers owing to the relatively short lifetimes of the propagating radicals. Alternative synthesis techniques that address these shortcomings are discussed further.

### 1.2.2 Living Anionic Polymerization

Living anionic polymerization (LAP) is a type of chain polymerization where the reactive chain-end is an anion. The first well-controlled LAP was reported by Szwarc *et al.*, who described the polymerization of styrene in tetrahydrofuran (THF) using a sodium-naphthalene complex as a bifunctional initiator.[13,14] The 'living' nature of the polymerization was established using viscosity measurements to confirm that successful chain extension occurred on addition of further monomer, indicating no intrinsic termination step. This is because the mutually repulsive anionic chain-ends cannot react with each other. In LAP, the rate of initiation is much faster than the rate of propagation ($k_i >> k_p$). Thus, rapid initiation of all chains occurs prior to any propagation, which ensures equal probability for chain growth. Consequently, a linear increase in molecular weight with conversion is observed and relatively low final dispersities ($M_w/M_n < 1.10$) can be achieved. This is in striking contrast to FRP which produces high molecular weights (and dispersities) even at relatively low conversion (**Figure 1.3**).

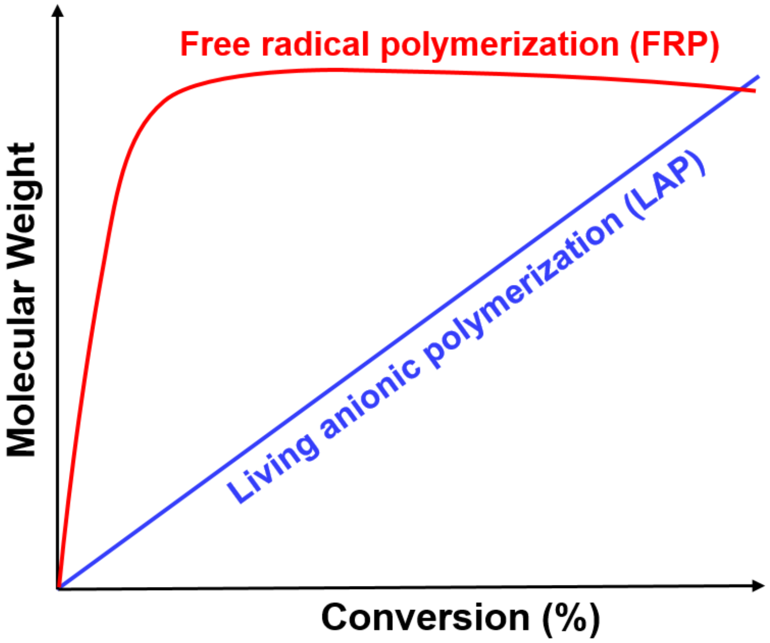

**Figure 1.3.** Variation of molecular weight with monomer conversion for free radical polymerization (FRP, red data) and living anionic polymerization (LAP, blue data).

In LAP, propagation is the rate-limiting step so the rate of polymerization is equal to the rate of propagation. The rate of polymerization, $R_p$, is given by **Equation 1.9,** where $[P_n^-]$ is the concentration of propagating anionic polymer chains and $[M]$ is the monomer concentration. The integrated rate equation is described in **Equation 1.10,** where $[M]_0$ is the initial monomer concentration.

$$R_p = k_p[P_n^-][M] \tag{1.9}$$

$$[M] = [M]_0 e^{(-k_p[P_n^-]t)} \tag{1.10}$$

The $D_k$ can be calculated at any given time using **Equation 1.11**. Assuming there is no termination, the DP can be calculated using **Equation 1.12**. Therefore, final polymers with a pre-determined DP can be achieved by simply adjusting the monomer to initiator molar ratio.

$$D_k = \frac{[M]_0 - [M]}{[I]} \tag{1.11}$$

$$DP = \frac{[M]_0}{[I]} \tag{1.12}$$

LAP is only feasible for a rather small subset of vinyl monomers with electron-withdrawing substituents (e.g. styrene, isoprene, butadiene, 2-vinylpyridine etc.), which severely restricts the scope of this particular technique. Another disadvantage of LAP is its high sensitivity to impurities and protic solvents, such as water or alcohol. As a result, premature termination of the polymerization occurs if the monomer, solvent and glassware are not purified adequately.[9]

### 1.2.3 Reversible Deactivation Radical Polymerization

Reversible deactivation radical polymerizations (RDRP) exhibit so-called ‘pseudo-living’ character. Until recently, RDRP was described as controlled radical polymerization (CRP) or living radical polymerization (LRP). However, since termination is only suppressed rather than eliminated, RDRP has become the IUPAC-approved term.[15] RDRP combines some of the advantages associated with LAP and FRP, while eliminating some of the disadvantages. As with FRP, RDRP can be used to polymerize many vinyl monomers in various solvents, including protic solvents such as water or lower alcohols. Unlike FRP, RDRP enables the convenient synthesis of polymers with pre-determined molecular weights and narrow MWD. RDRP is also used to prepare well-defined diblock copolymers and complex copolymer architectures *via* sequential monomer addition. Some examples of these architectures are illustrated in **Figure 1.4**.[16,17]

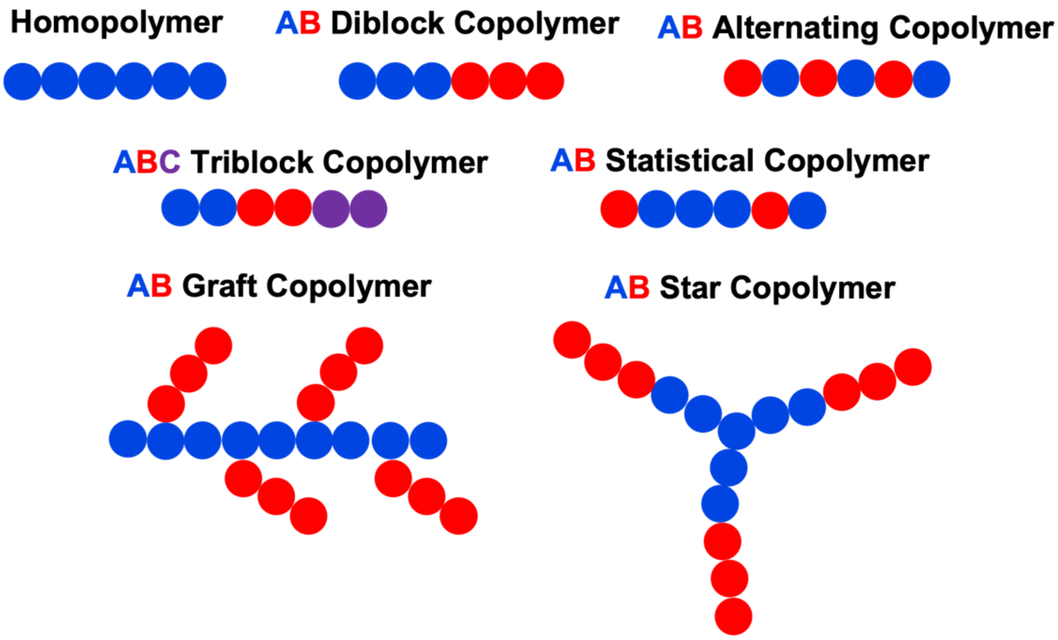

**Figure 1.4.** Schematic representation of various types of copolymer architectures.[16,17]

All examples of RDRP involve a dynamic equilibrium between active propagating radicals and dormant species. This equilibrium can be achieved either by reversible deactivation/activation (**Figure 1.5**) or by rapid reversible chain transfer (**Figure 1.6**).[12,18,19]

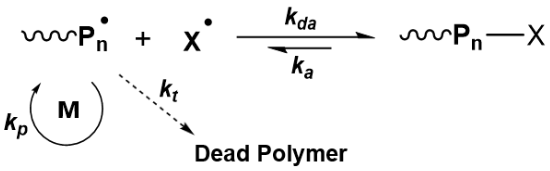

**Figure 1.5.** Reversible deactivation/activation mechanism of propagating polymer radicals with species X•.

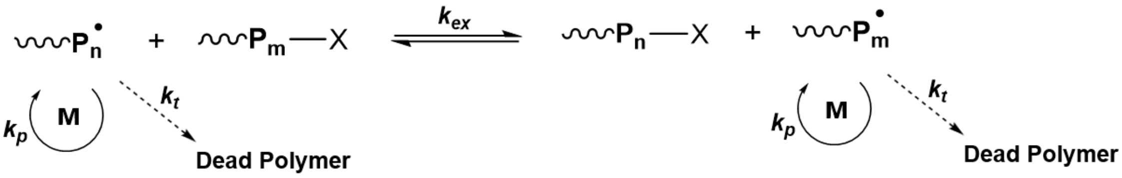

**Figure 1.6.** Rapid reversible transfer mechanism for propagating polymer radicals.

The three most common examples of RDRP are atom transfer radical polymerization (ATRP),[20,21] nitroxide-mediated polymerization (NMP),[22] and reversible addition-fragmentation chain transfer (RAFT) polymerization.[23] The reversible deactivation/activation mechanism is the basis for both ATRP and NMP and is reliant on the persistent radical effect (PRE).[24] More specifically, the propagating polymer radical ($P_n$•) is reversibly deactivated by reacting with a capping species (X•) to form a dormant $P_n$-X species, which can be subsequently reactivated to generate a propagating radical. These species can either undergo further propagation ($k_p$) or succumb to irreversible termination ($k_t$). X• radicals can react with propagating radicals but not with themselves. The rate of deactivation is greater than the rate of activation ($k_{da} > k_a$), which causes the dormant species to be favoured. This reduces both the concentration of propagating radicals and the rate of termination. Alternatively, RAFT polymerization involves rapid reversible transfer (**Figure 1.6**), which does not rely on the PRE.[8] Instead, this mechanism employs essentially the same initiation and termination steps as those observed in FRP. An organosulfur-based chain transfer agent (CTA) enables fast exchange between the propagating and dormant species.[25] Since this technique is the main focus of this Thesis, it is discussed in more detail below.

## 1.3 Reversible Addition-Fragmentation Chain Transfer Polymerization

Reversible addition-fragmentation chain transfer (RAFT) polymerization was first reported by Chiefari *et al.*[26] in 1998 and has been the focus of thousands of publications over the last two decades.[27,28] It is arguably a more convenient and versatile RDRP technique than either NMP or ATRP.[29] Compared to NMP, RAFT is applicable to a significantly wider range of monomers (particularly methacrylates) and it can be conducted at relatively low reaction temperatures.[30] The main disadvantage of ATRP is that the resulting polymers are typically contaminated by the transition metal catalyst, which has to be removed (and preferably recycled).[31]

The RAFT polymerization mechanism involves initiation, propagation, reversible chain transfer and termination (see **Figure 1.7**).[32–34] Like conventional FRP, initiation occurs *via* homolytic cleavage of initiator molecules to form radicals, which then react with monomer to form polymer radicals ($P_n$•). These species then react with the RAFT CTA **(1)** to generate the intermediate radical adduct **(2)**. Fragmentation *via* β-scission generates a thiocarbonylthio-capped polymer chain **(3)** and a new radical species (R•). The correct choice of CTA for a given monomer class is important because the Z group activates the C=S double bond and must be able to stabilize the intermediate radical adduct **(2)**, which influences the rate of addition and fragmentation.[26] Similarly, the R group must be a better leaving group than $P_n$• to ensure efficient fragmentation. Furthermore, the R• must be capable of reinitiating the polymerization by reacting with further monomer to form new polymer radicals ($P_m$•). As a result, there is a rapid, reversible equilibrium between the propagating polymer radicals ($P_n$• and $P_m$•) and the dormant polymer chains **(4)**. This ensures equal probability for each chain to grow and leads to polymers with relatively narrow MWDs. The final step is termination, which generates 'dead' polymer chains. Termination in RAFT polymerization is suppressed rather than eliminated, with the probability of termination increasing under monomer-starved conditions (e.g. towards the end of the polymerization).

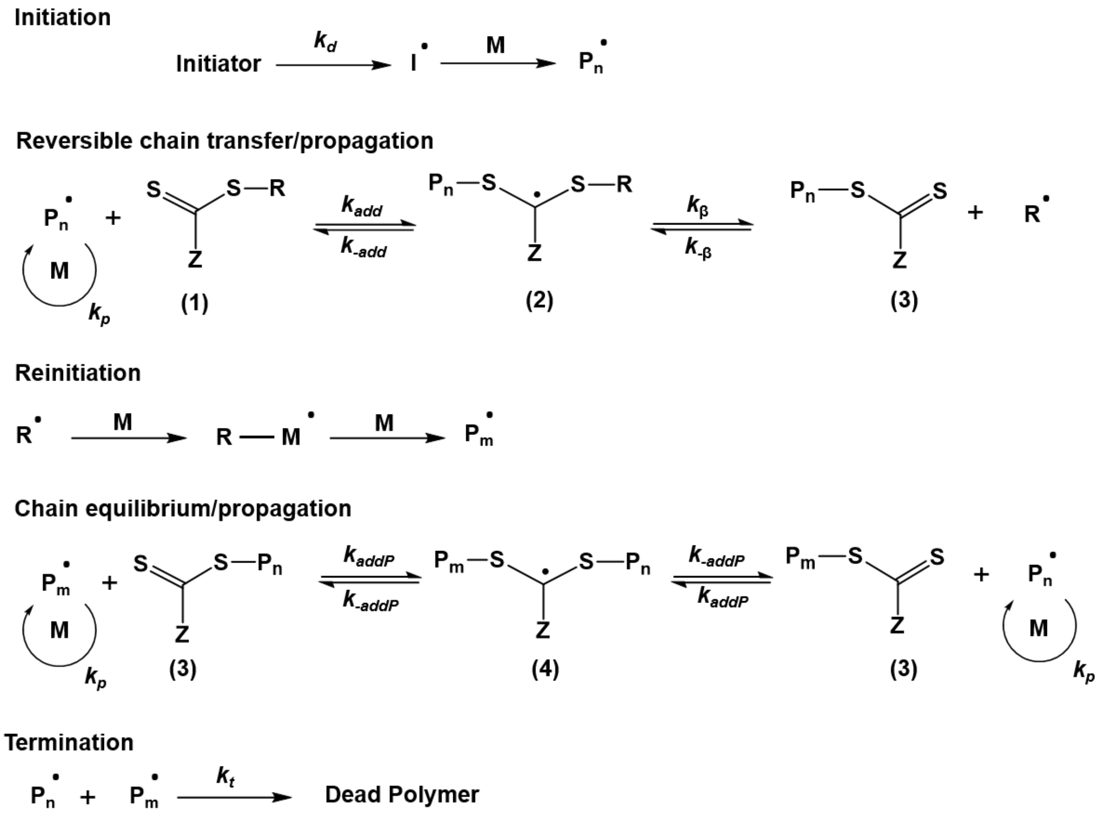

**Figure 1.7.** RAFT polymerization mechanism as proposed by Rizzardo *et al.*[32–34]

In RAFT polymerization, the sum of the RAFT CTA concentration and the concentration of initiator-derived radicals dictate the number of polymer chains that are formed. Therefore, the target DP at full conversion can be determined using **Equation 1.13**. However, the CTA concentration is significantly higher than the initiator concentration. Therefore, the number of polymer chains formed that contain initiator-derived end-groups is negligible compared to chains containing the CTA (i.e. $[CTA]_0 >> 2f[\mathrm{I}]_o$). Under such conditions, the DP of the final polymer can be calculated using **Equation 1.14**.

$$DP = \frac{[M]_0}{([CTA]_0 + 2f[I]_0)} \qquad \textbf{(1.13)}$$

$$DP = \frac{[M]_0}{[CTA]_0} \qquad \textbf{(1.14)}$$

As previously stated, the level of control exerted during RAFT polymerization strongly depends on the addition of a suitable CTA. The generic chemical structure of a RAFT CTA is shown **Figure 1.8**. Suitable classes of RAFT CTAs include trithiocarbonates, dithiocarbamates, dithiobenzoates and xanthates.[12] The appropriate choice of R and Z groups depends on the monomer type. The selection of R and Z groups are significant in the overall mechanism.

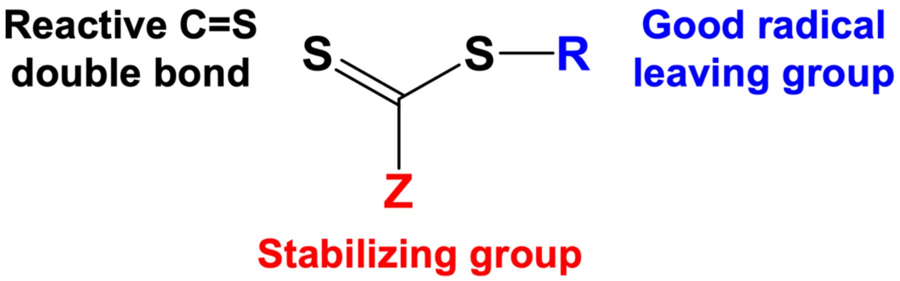

**Figure 1.8.** Generic chemical structure of a thiocarbonylthio RAFT chain transfer agent (CTA), where the R and Z groups are chosen to suit a particular monomer class (e.g. styrene, acrylates, methacrylates, vinyl acetate etc.).[26]

Moad *et al.* provided a useful set of guidelines to indicate the compatibility of specific R and Z groups for various monomer classes (**Figure 1.9**).[32] Vinyl monomers can be sub-divided into more-activated monomers (MAMs) and less-activated monomers (LAMs). MAMs are characterized by a carbon-carbon double bond conjugated to a carbonyl group, aromatic ring or a nitrile group. LAMs are characterized by a carbon-carbon double bond adjacent to an unsaturated carbon atom or a heteroatom. The solid lines illustrate that good control over the polymerization can be achieved, whereas the dashed lines indicate only partial control. Therefore, dithioesters (Z = aryl or alkyl) or trithiocarbonates (Z = alkylthio) provide more controlled polymerizations for MAMs [e.g. methyl methacrylate (MMA), styrene (S), acrylamide (AM) and acrylonitrile (AN)], whereas xanthates and dithiocarbamates confer only poor control. Conversely, well-controlled polymerizations of LAMs [e.g. vinyl acetate (VAc) and N-vinylpyrrolidone (NVP)] can be achieved when using xanthates or dithiocarbamates, but not with dithioesters or trithiocarbonates.

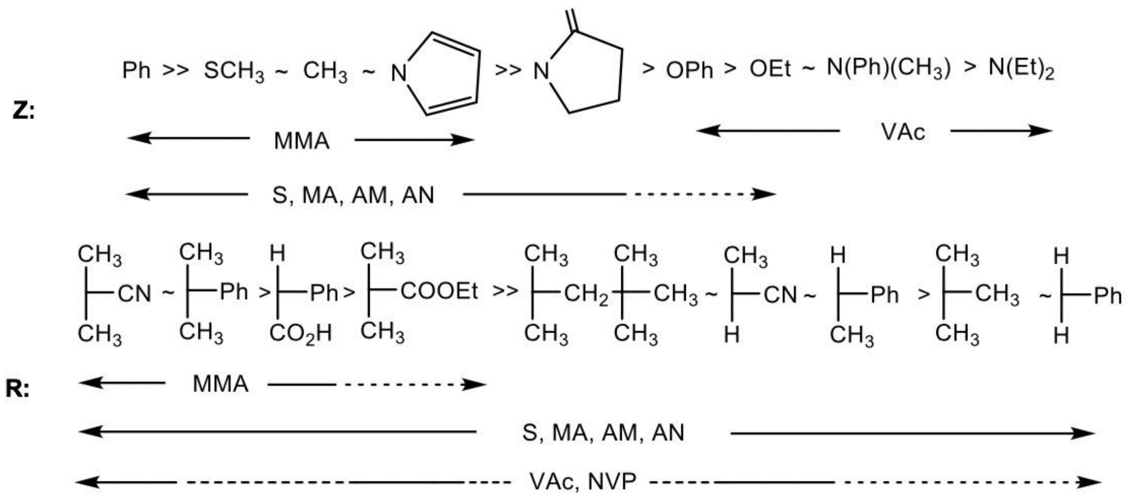

**Figure 1.9.** Summary of suitable Z and R groups for various polymerizations by Moad *et al*.[32]

This Thesis will mainly mostly focus on the polymerizations of MAMs, but it is still important to choose the appropriate RAFT CTA. For example, 2-cyanopropyl dithiobenzoate (CPDB) or 4-cyano-4-(2-phenylethanesulfanylthiocarbonyl)sulfanylpentanoic acid (PETTC) are well-suited for the polymerization of methacrylates,[35,36] whereas 2-(dodecylthiocarbonothioylthio)-2-methylpropionic acid (DDMAT) is preferred for the polymerization of styrenes, acrylates and acrylamides.[37,38] The chemical structures for these three RAFT CTAs are shown in **Figure 1.10**.

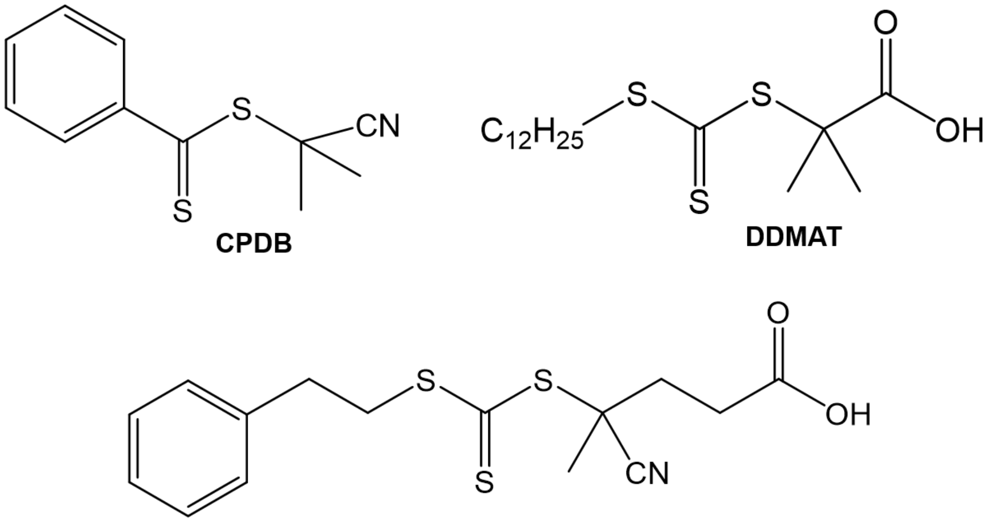

**CPDB**

**DDMAT**

**PETTC**

**Figure 1.10.** Chemical structures for 2-cyanopropyl dithiobenzoate (CPDB), 4-cyano-4-(2-phenylethanesulfanylthiocarbonyl)sulfanylpentanoic acid (PETTC) and 2-(dodecylthiocarbonothioylthio)-2-methylpropionic acid (DDMAT).

In addition to choosing an appropriate CTA for a given monomer, the choice of initiator, temperature and the CTA/initiator molar ratio also influences the outcome.[28] Moreover, the organosulfur RAFT groups are retained at the end of the polymer chains, which enables subsequent chain extension. Unfortunately, such end-groups confer unwanted color and malodor. However, RAFT end-group removal can be achieved *via* thermolysis, *via* reaction with suitable nucleophiles, oxidants or reducing agents, or by radical-induced reactions.[39–42]

## 1.4 Aqueous Dispersion Polymerization

In an aqueous dispersion polymerization, the monomer, initiator, and stabilizer are all fully soluble in water. Polymerization of the water-miscible monomer produces a water-insoluble polymer, which would form a macroscopic precipitate in the absence of an appropriate colloidal stability mechanism.[43] Unfortunately, only a few vinyl monomers fulfil this criterion. On the other hand, there are many literature examples of dispersion polymerization being conducted in non-aqueous media (e.g. lower alcohols, *n*-alkanes, supercritical $CO_2$ etc.).[44–48]

The general mechanism for dispersion polymerization is summarized in **Figure 1.11**.[49,50] Initially, the reaction mixture comprises a homogeneous solution containing monomer, an initiator and a suitable stabilizer (Stage 1). Thermal decomposition of the initiator occurs to form radicals, which react with soluble monomer to form oligomers (Stage 2). The soluble chains continue to grow until they attain a certain critical molecular weight, whereupon they become insoluble and aggregate to form nascent particles (Stage 3). The polymeric stabilizer then begins to either physically adsorb or chemically graft onto these unstable particle nuclei (Stage 4). Further adsorption leads to colloidally stable nanoparticles, and no new nuclei are formed. Instead, the monomer-swollen particles continue to grow as the polymerization proceeds within them (Stage 5). Finally, particle growth ends once all the monomer is consumed, producing a colloidal dispersion of sterically-stabilized latex particles (Stage 6).

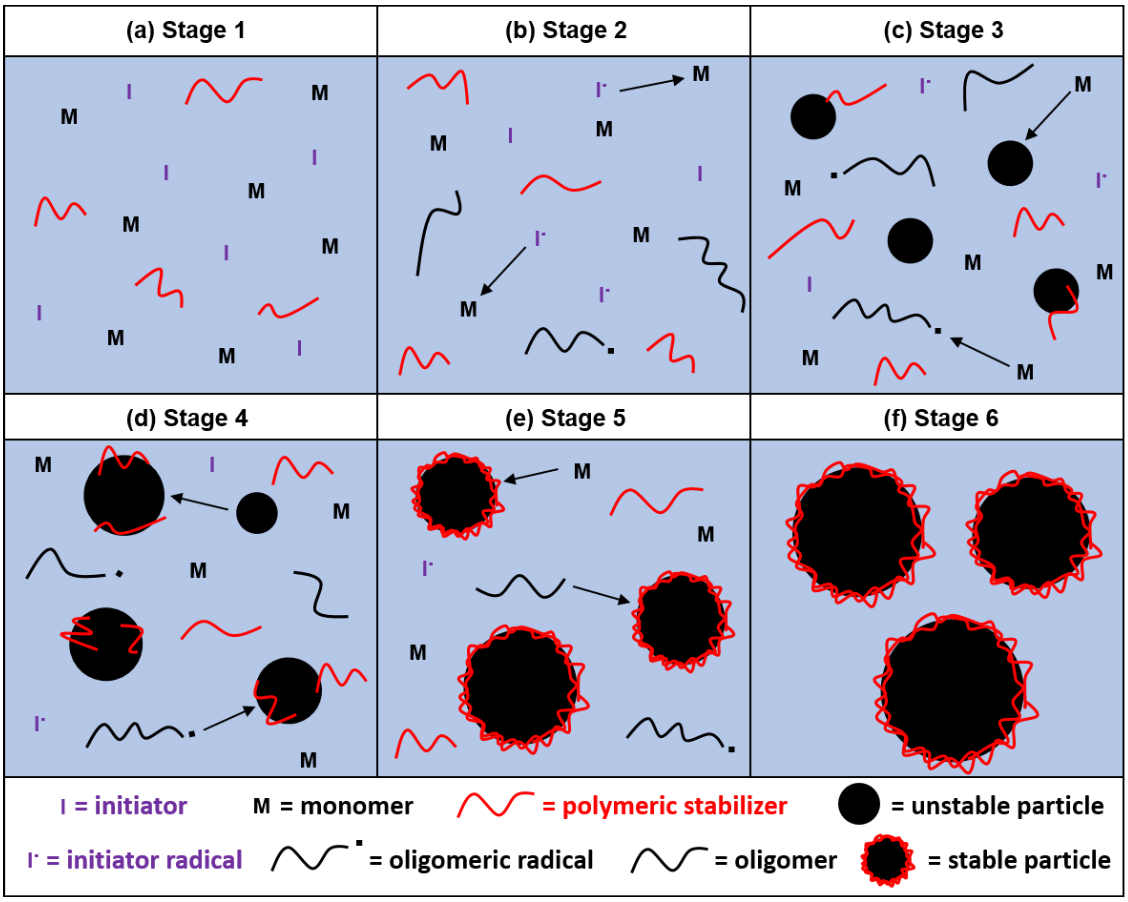

**Figure 1.11.** Schematic representation of the generic mechanism for a dispersion polymerization.[49,50]

As previously discussed, there are very few examples of suitable monomers for aqueous dispersion polymerization. Armes and co-workers have reported the synthesis of polypyrrole latexes with various steric stabilizers such as poly(*N*-vinylpyrrolidone) (PNVP),[51] poly(vinyl alcohol) (PVA),[51] poly(ethylene oxide) (PEO)[52] or sodium dodecylbenzenesulfonate.[53] In the context of vinyl monomers, Ali and co-workers reported the aqueous dispersion polymerization of 2-hydroxypropyl methacrylate (HPMA) using PNVP as the steric stabilizer to produce PHPMA latexes.[54]

## 1.5 Aqueous Emulsion Polymerization

Aqueous emulsion polymerization typically requires a water-immiscible monomer, a water-soluble initiator, a suitable surfactant (or polymeric stabilizer) and water. Emulsion polymerization enables rapid polymerization and the generation of high molecular weight polymers with low solution viscosity.[55] Furthermore, the use of water as a solvent is appealing since it is cheap, environmentally-friendly and has a high specific heat capacity, which enables efficient heat dissipation. As a result, emulsion polymerization has been widely used for the industrial manufacture of latex particles for adhesives, paints and coatings applications.[55] The mechanism for emulsion polymerization can be divided into three stages, which are known as Intervals I, II, and III (**Figure 1.12**).[56–59]

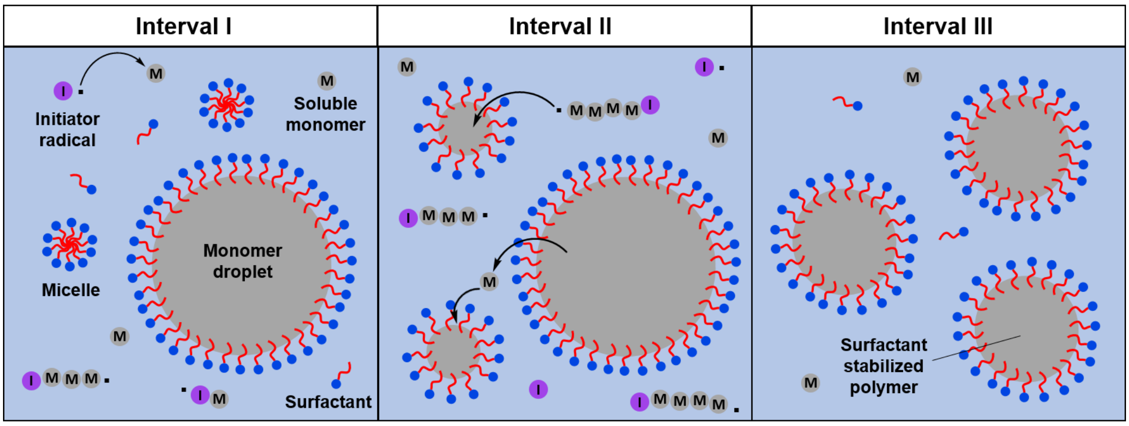

**Figure 1.12.** Schematic representation of the three main Intervals (I, II and III) that occur during conventional aqueous emulsion polymerization.[56–59]

Initially, the heterogeneous reaction mixture comprises many surfactant micelles and relatively few surfactant-stabilized monomer droplets of 1-10 µm diameter, with the latter being generated *via* stirring under high shear.[59] During Interval I, the initiator decomposes to form radicals that then react with monomer within the surfactant micelles, which is known as heterogeneous nucleation. Radicals generated *via* thermal decomposition of ionic initiators such as persulfate or water-soluble azo salts can preferentially migrate into surfactant micelles, which are much more numerous (and exhibit a much higher overall surface area) than the relatively hydrophobic monomer droplets. Alternatively, if the vinyl monomer has a relatively high background aqueous solubility, radicals may react with the relatively small amount of monomer dissolved within the aqueous phase. This is known as homogeneous nucleation, which leads to the formation of water-soluble oligomers. These oligomers become hydrophobic once they reach a certain critical chain length and subsequently migrate into the surfactant micelles if the surfactant concentration is above the critical micelle concentration (CMC). The growing particles become monomer-swollen, which leads to an enhanced rate of polymerization owing to the relatively high local monomer concentration (**Figure 1.13**). Interval I ends when the surfactant concentration in the aqueous phase falls below the CMC, whereupon all of the initial surfactant micelles have become nascent latex particles.[59]

In Interval II, the number of latex particles remains constant but they continue to grow in size as further monomer is consumed. The monomer dissolved within the aqueous phase is continuously replaced by diffusion from the surfactant-stabilized monomer droplets. Thus, a constant rate of polymerization is observed (**Figure 1.13**) until all the monomer droplets have disappeared, which signifies the end of Interval II.[58] During Interval III, there is a reduction in the rate of polymerization as the monomer present within the latex particles becomes depleted (**Figure 1.13**). This stage ends once all the monomer is consumed, leaving colloidally stable latex particles.

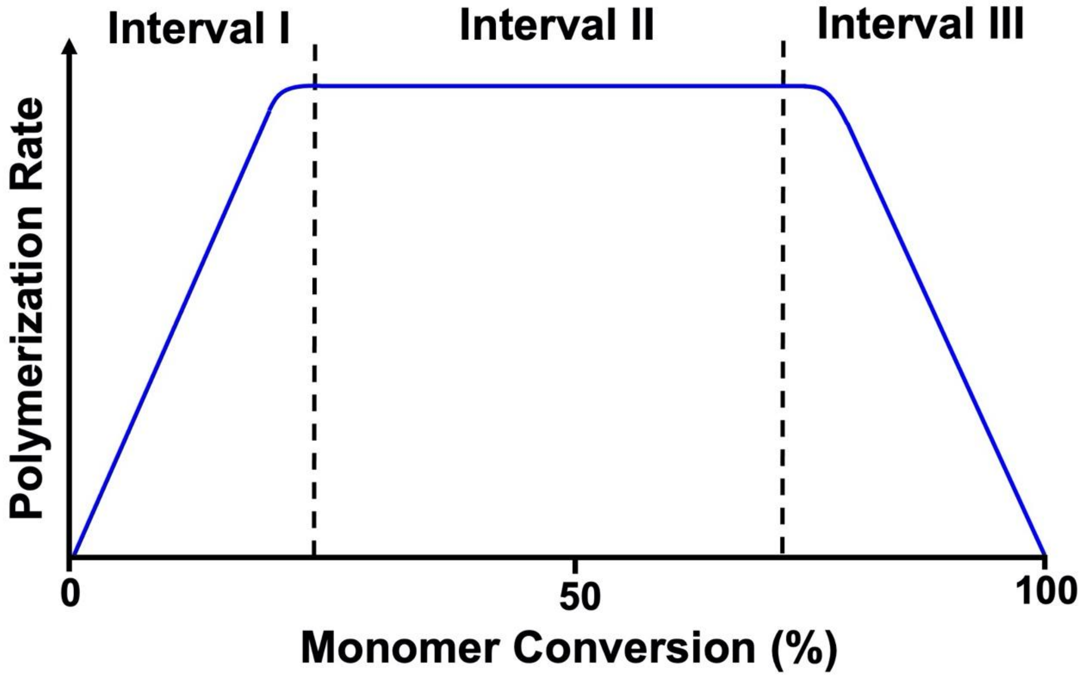

**Figure 1.13.** Rate of polymerization versus monomer conversion for a conventional aqueous emulsion polymerization during Intervals I, II and III.[58]

Latex particles can also be prepared by *surfactant-free* aqueous emulsion polymerization.[60–63] In this case, initiator decomposition generates charged water-soluble radicals (e.g. sulfate radicals), which react with monomer dissolved in the aqueous phase to give surface-active oligomer radicals, which form anionic micelles *in situ*. Monomer diffuses into these micelles and is polymerized therein to form small primary particles. These nascent particles possess insufficient surface charge for colloidal stability, so they aggregate to form larger particles. The gradual increase in surface charge density eventually leads to relatively large, colloidally stable latex particles.[62]

## 1.6 Self-Assembly

Self-assembly is described as the spontaneous ordering of components into patterns or structures without human intervention.[64] An important example within nature is the formation of cell membranes, which are formed by the self-assembly of amphiphilic phospholipids.[65]

### 1.6.1 Water and the Hydrophobic Effect

It is important to consider the unique properties of water when discussing self-assembly. It is known as a ‘universal solvent’ because of its ability to dissolve many ionic and polar solids.[66] This is primarily the result of hydrogen bonding between water molecules and hydrophilic solute molecules. In contrast, hydrophobic molecules are unable to form hydrogen bonds with water. Therefore, the loss of at least one intermolecular hydrogen bond occurs as the water molecules interact with such solutes. To minimize hydrogen bonding disruption, the water molecules form cage (or clathrate) structures around the hydrophobic molecules. This phenomenon is known as the hydrophobic effect.[67,68] Such reordering of water molecules is entropically unfavorable and explains why hydrophobic substrates are insoluble in water. On the other hand, *amphiphilic* molecules can undergo spontaneous self-assembly in aqueous solution to form a range of complex colloidal structures.

### 1.6.2 Self-assembly of Surfactants

Surfactants contain a hydrophilic head-group and a hydrophobic tail and constitute an important class of amphiphiles.[69] They can be classified as cationic, anionic, non-ionic or zwitterionic depending on the nature of the head-group. Surfactants spontaneously self-assemble in aqueous solution to form micelles if their concentration is above the CMC.[70] In aqueous solution, surfactant self-assembly is a thermodynamically-driven process. Micelles are produced when the energy required to form them is less than the entropic cost of individual surfactant molecules (unimers) remaining in solution. This typically occurs at relatively low surfactant concentrations owing to the hydrophobic effect (see **section 1.6.1**).

Surfactants can form spherical micelles, worm-like micelles, vesicles or bilayers depending on the surfactant concentration, temperature, solution pH and the electrolyte concentration. The final morphology can be directly related to the geometric packing of individual surfactant molecules. Two opposing forces must be considered: (i) mutual repulsion between neighboring hydrophilic (and often charged) head-groups and (ii) mutual attraction between hydrophobic tails at the hydrocarbon-water interface. This affects in turn the surface area occupied by each head-group, $a_o$, at the interface. Israelachvii *et al*.[71] defined the dimensionless packing parameter, $P$, according to **Equation 1.15**.

$$P = \frac{v}{a_0 l_c} \qquad \textbf{(1.15)}$$

Here $a_o$ is defined as the optimal surface area occupied by the head-group at the interface, $l_c$ is the maximum critical length of the hydrocarbon chain and $v$ is the volume of the hydrocarbon chain. **Figure 1.14** summarizes the relationship between the surfactant morphology and packing parameter. Characteristic numerical values for the fractional packing parameter corresponding to the formation of spheres ($P \leq 1/3$), cylinders ($1/3 < P \leq 1/2$) and vesicles ($1/2 < P \leq 1$) are indicated.

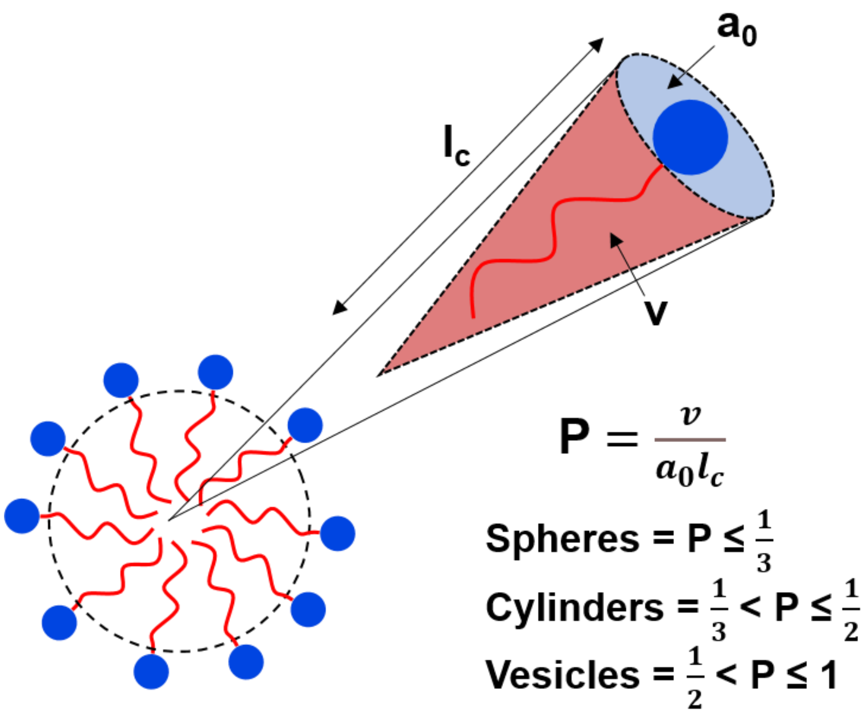

**Figure 1.14.** Schematic representation of the packing of surfactant amphiphiles within a spherical micelle. The range of values for the packing parameter *P* corresponding to the formation of spheres, cylinders and vesicles is indicated.[72]

### 1.6.3 Block Copolymer Self-assembly

Diblock copolymers can undergo self-assembly either in the bulk (i.e. in the absence of solvent) or in solution. In the bulk, the enthalpic incompatibility between the two blocks drives microphase separation.[73] [N.B. Macroscopic phase separation – which is invariably observed for pairs of homopolymers - cannot occur because the two blocks are linked by a covalent bond]. Microphase separation is observed if the Gibbs energy of mixing, $\Delta G_{mix}$, is negative in **Equation 1.16**. This requires the $\Delta H_{mix}$ term to be sufficiently negative to outweigh the positive entropic term.

$$\Delta G_{mix} = \Delta H_{mix} - T\Delta S_{mix} \tag{1.16}$$

Flory and Huggins independently developed a lattice model theory to calculate $\Delta G_{mix}$ when mixing two enthalpically incompatible homopolymers (**Equation 1.17**). The copolymer morphology is dictated by three parameters: (i) the relative volume fractions of the two blocks ($\varphi_A$ and $\varphi_B$), (ii) the overall degree of polymerization of each block ($N_A$ and $N_B$), and (iii) the Flory-Huggins interaction parameter, $\chi_{AB}$.

$$\frac{\Delta G_{mix}}{k_B T} = \left(\frac{\varphi_A ln\varphi_A}{N_A}\right) + \left(\frac{\varphi_B ln\varphi_B}{N_B}\right) + \varphi_A \varphi_B \chi_{AB} \qquad \textbf{(1.17)}$$

The $\chi_{AB}$ parameter represents the degree of enthalpic incompatibility between the two blocks and is defined by **Equation 1.18**.[74–76]

$$\chi_{AB} = \left(\frac{z}{k_B T}\right)\left[\varepsilon_{AB} - \frac{1}{2}(\varepsilon_{AA} + \varepsilon_{BB})\right] \qquad \textbf{(1.18)}$$

Here $z$ is the number of nearest neighbours per molecule, $k_B$ is the Boltzmann constant, $T$ is the absolute temperature and $\varepsilon_{AB}$, $\varepsilon_{AA}$ and $\varepsilon_{BB,}$ are the three respective interaction energies for the A and B blocks. According to **Equation 1.18**, spontaneous mixing of A and B occurs if $\chi_{AB}$ is negative. In contrast, a positive $\chi_{AB}$ value indicates enthalpic incompatibility between the two blocks and results in demixing. Furthermore, $\chi_{AB}$ is inversely related to temperature, thus diblock copolymers often exhibit an order-disorder transition (ODT) at a specific temperature.[76] The extent of microphase separation exhibited by diblock copolymers is determined by the $\chi N$ term.[77] Self-consistent mean-field theory has been used to predict diblock copolymer behaviour in the bulk.[78] Given a sufficiently high $\chi N$ term, systematic variation of the relative volume fraction of block A ($f_A$) can generate various morphologies, as summarized in the phase diagram shown in **Figure 1.15**. Strong segregation occurs if $\chi N > 100$, resulting in nearly pure phases. In contrast, weak segregation is observed if $\chi N < 10$, which is close to the ODT. **Figure 1.15** illustrates the various order-order transitions (OOT) that can be observed as the relative volume fraction $f_A$, is varied at a fixed $\chi N$ while above the ODT.[73]

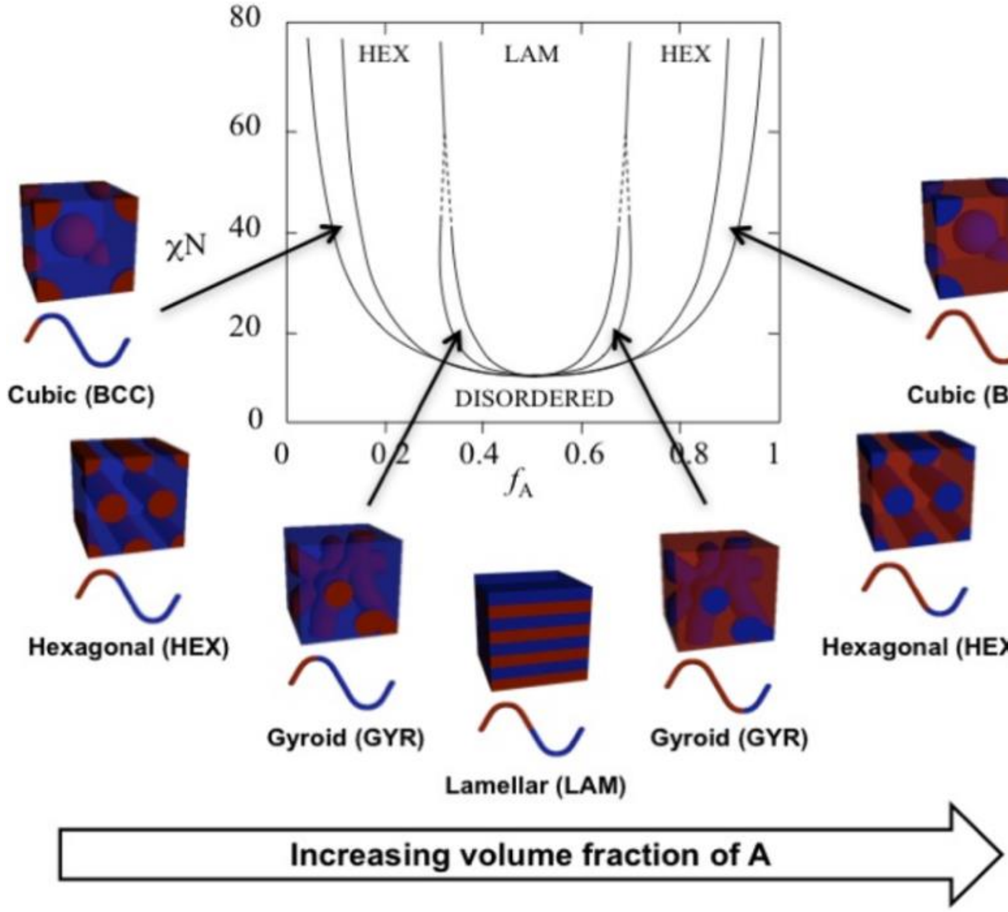

**Figure 1.15.** Theoretical phase diagram and morphology for an AB diblock copolymer, where $N$ is the overall degree of polymerization, $\chi$ is the Flory-Huggins interaction parameter and $f_A$ is the volume fraction of block A. Morphological phases and abbreviations are denoted as follows: body-centred cubic (BCC), hexagonal cylinders (HEX), gyroid (GRY), and lamellar (LAM).[73]

Introducing a solvent increases complexity as its interaction between each block must be considered. Nevertheless, there are examples of amphiphilic diblock copolymers that undergo self-assembly in a solvent which is selective for one of the two blocks.[79,80] Examples of diblock copolymer self-assembly achieved by traditional post-polymerization techniques include direct dissolution,[81] a solvent switch,[82,83] a pH switch,[84,85] or thin film rehydration.[45] However, these techniques are usually performed at relatively low copolymer concentrations (typically < 1% w/w), which severely limits their potential utility for industrial applications.

## 1.7 Polymerization-Induced Self-Assembly (PISA)

Within the last decade, many research groups have explored the preparation of block copolymer nanoparticles *via* polymerization-induced self-assembly (PISA).[86–88] This approach has mainly involved the use of RAFT polymerization, although other RDRP techniques are also applicable. It is particularly attractive because syntheses are usually efficient and can be performed at relatively high solids (25-50% w/w).[89–91]

PISA typically involves chain extension of a soluble homopolymer with a second monomer. The second polymer block gradually becomes insoluble, which drives *in situ* self-assembly to form AB diblock copolymer nanoparticles (**Figure 1.16**). It should be noted that PISA does not require the addition of any stabilizer (e.g. a surfactant) because the precursor block confers steric stabilization. Systematic variation of the copolymer concentration and the mean DP of each block can result in the formation of spheres, worms and vesicles.[27] Although these are the most commonly reported copolymer morphologies, more complex structures have also been reported (e.g. lamellae, jellyfish and framboidal vesicles). In principle, the final morphology is dictated by the relative volume fractions of the two blocks, as described by the packing parameter ($P$).[88] In practice, other parameters can lead to morphological constraints (see below). RAFT polymerization enables a wide range of monomers to be used in various solvents, including water,[89] polar solvents (alcohols),[92,93] and non-polar solvents (e.g. *n*-alkanes or mineral oil).[94,95] However, only block copolymer self-assembly *via* aqueous PISA formulations will be discussed in this Thesis.

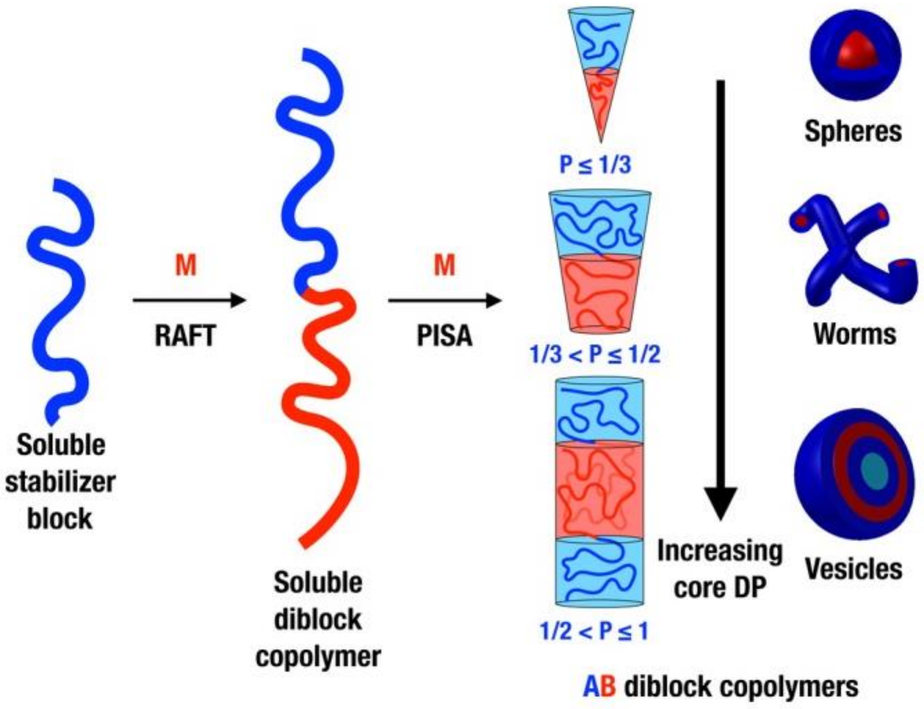

**Figure 1.16.** Schematic representation of polymerization-induced self-assembly (PISA) as illustrated for an AB diblock copolymer.[27]

### 1.7.1 RAFT Aqueous Dispersion Polymerization

RAFT aqueous dispersion polymerization involves chain extension of a water-soluble precursor using a water-miscible monomer to generate a water-insoluble polymer as the second block.[87,96] Initially, this block is soluble in the reaction mixture but once a critical DP is attained it becomes insoluble and *in situ* self-assembly occurs. The first example of RAFT aqueous dispersion polymerization was reported by Hawker *et al*., who described the chain extension of a poly(N,N'-dimethylacrylamide) (PDMAC) precursor with *N*-isopropylacrylamide (NIPAM) to form spherical nanoparticles at 70 °C.[97] Introduction of a bisacrylamide cross-linker enabled the formation of stable nanogels on cooling to room temperature. In the absence of any cross-linker, the nanoparticles formed at 70 °C simply dissociated on cooling to 20 °C, since this is below the LCST of the thermoresponsive PNIPAM chains.[98]

Many RAFT aqueous dispersion polymerization formulations have utilized the commodity monomer, HPMA. For example, in 2010 Li and Armes reported that chain extension of a poly(glycerol monomethacrylate) (PGMA) precursor with HPMA at 10% w/w solids led to kinetically-trapped spherical nanoparticles.[99] Systematically increasing the target PHPMA DP from 30 to 300 gave spheres of increasing size as judged by dynamic light scattering (DLS) (**Figure 1.17**). However, vesicles were obtained when targeting a $PGMA_{65}$-$PHPMA_{300}$ diblock copolymer at 20% w/w solids.

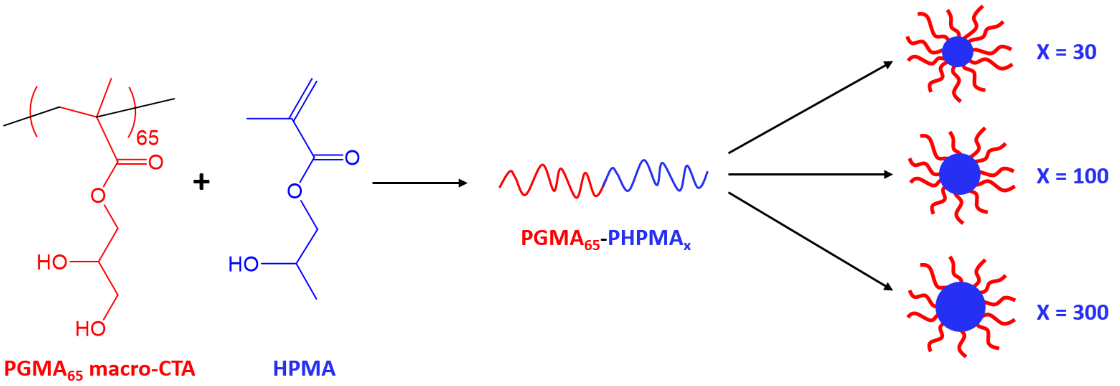

**Figure 1.17.** Synthesis of $PGMA_{65}$-$PHPMA_x$ diblock copolymer spheres (where x = 30-300) by RAFT aqueous dispersion polymerization of HPMA.[99]

In a follow-up study, Blanazs *et al*. examined the evolution of copolymer morphology that occurs during PISA when targeting $PGMA_{47}$-$PHPMA_{200}$ vesicles.[100] Aliquots were extracted regularly from the reaction solution to determine the monomer conversion by $^1H$ NMR spectroscopy while the copolymer morphology was assessed by transmission electron microscopy (TEM). Initially a transition from molecularly-dissolved chains, to spheres, to dimers and trimers was observed. This was followed by the formation of highly anisotropic linear worms, which evolved into vesicles *via* various intermediate structures such as branched worms, octopi and jellyfish, see **Figure 1.18**.

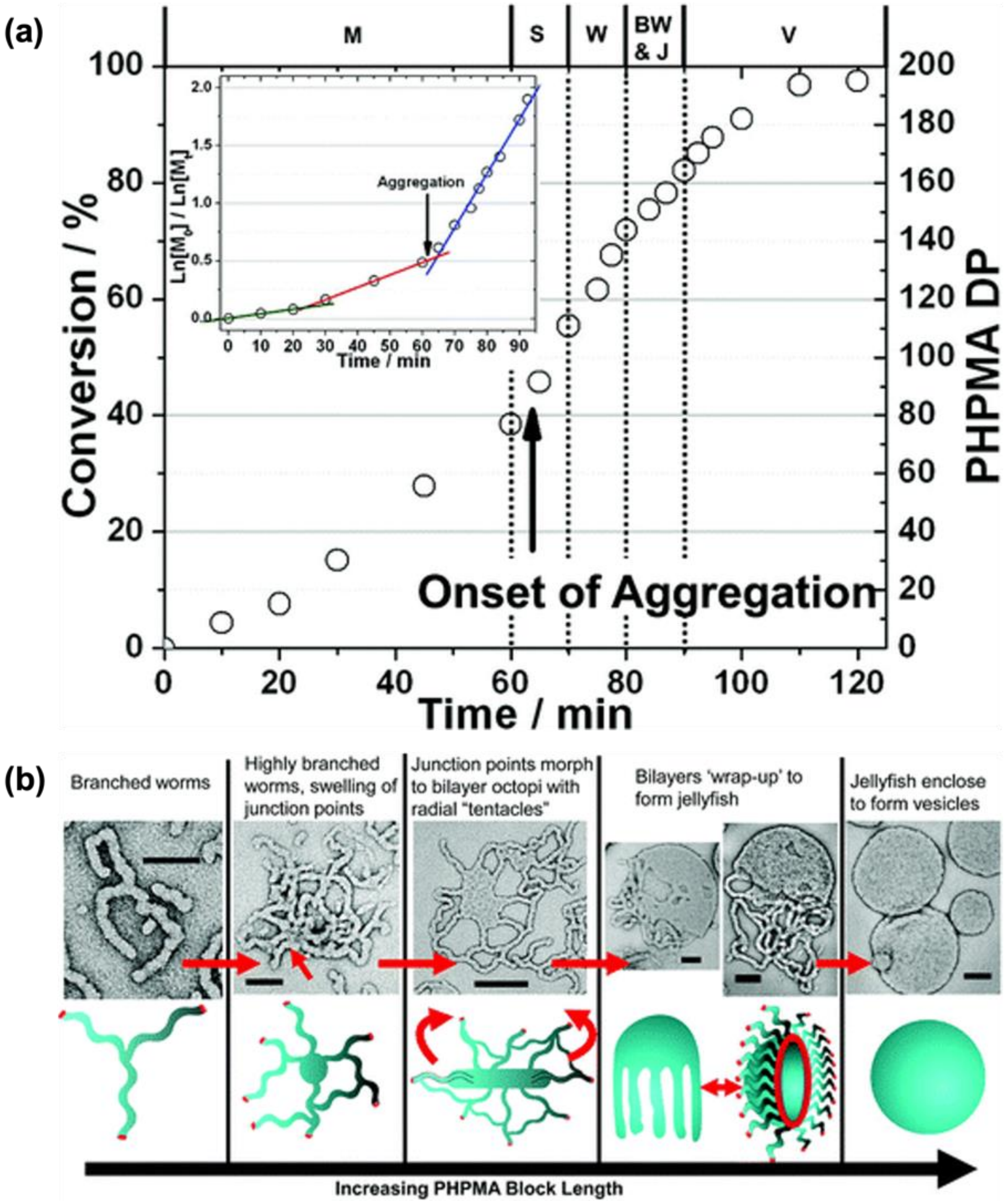

**Figure 1.18. (a)** $^1$H NMR studies of the RAFT aqueous dispersion polymerization of HPMA at 70 °C when targeting PGMA$_{47}$-PHPMA$_{200}$ vesicles at 10% w/w solids. The conversion vs. time plot indicates five morphological regimes: molecularly-dissolved chains (M), spheres (S), worms (W), branched worms (BW), jellyfish (J), and vesicles (V). The semilogarithmic plot (see inset) indicates a five-fold rate enhancement after nucleation; **(b)** TEM images illustrating the mechanism for the worm-to-vesicle transition during the synthesis of PGMA$_{47}$-PHPMA$_{200}$ vesicles by RAFT aqueous dispersion polymerization.[100]

Further work by Blanazs *et al*. produced detailed pseudo-phase diagrams (**Figure 1.19**) when employing three PGMA precursors with DPs of 47, 78 or 112.[35] These diagrams (or morphology maps) illustrate the variation in morphology with copolymer concentration and the effect of varying the mean DP for both the PGMA stabilizer block and the core-forming PHPMA block.

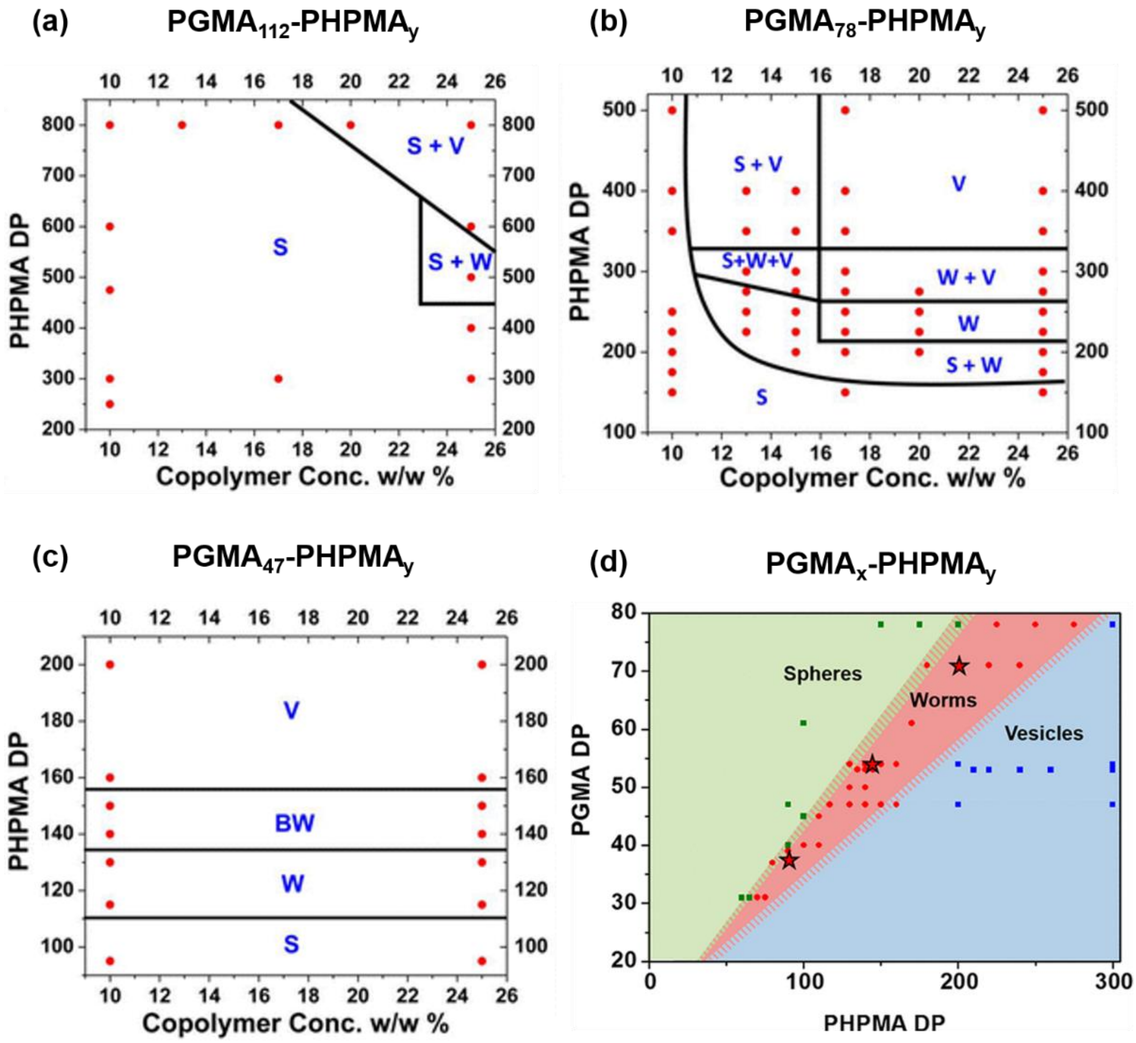

**Figure 1.19.** Phase diagrams constructed for $PGMA_x$-$PHPMA_y$ diblock copolymer nano-objects prepared at various copolymer concentrations (10-25% w/w) and PHPMA DP (y), when using a PGMA stabilizer DP of (a) 112, (b) 78 or (c) 47. (d) A master phase diagram constructed for the same PISA formulation for syntheses conducted at 20% w/w solids.[35,101]

**Figure 1.19a** indicates that employing the $PGMA_{112}$ precursor as the stabilizer block only produces kinetically-trapped spheres at lower copolymer concentrations. Higher order morphologies could be obtained above 20% w/w solids but only as mixed phases. This is because the relatively long $PGMA_{112}$ block confers effective steric stabilization and therefore impedes sphere-sphere fusion. A more interesting phase diagram is observed for the $PGMA_{78}$ precursor, see **Figure 1.19b**. A range of copolymer morphologies (spheres, worms or vesicles) can be accessed simply by varying the PHPMA DP. However, identical diblock copolymers produced different morphologies when adjusting the copolymer concentration. For example, targeting $PGMA_{78}$-$PHPMA_{500}$ produced a pure vesicle phase at 25% w/w solids but only kinetically-trapped spheres at 10% w/w solids. In contrast, using a relatively short $PGMA_{47}$ precursor yielded pure spheres, worms or vesicles as the target PHPMA DP was progressively increased, regardless of the copolymer concentration (see **Figure 1.19c**).

A master pseudo-phase diagram **(Figure 1.19d)** was constructed for this PGMA-PHPMA formulation at a fixed copolymer concentration of 20% w/w solids by Warren and co-workers.[101] This plot clearly shows the relationship between the core-forming block DP and stabilizer DP with regard to the final morphology and indicates that the worm phase is relatively narrow. It has become an essential tool for the Armes group when targeting specific morphologies using this aqueous PISA formulation.

Interesting properties and potential applications have been reported for higher order morphologies such as worms and vesicles. For example, a pure PGMA-PHPMA worm phase forms a soft, free-standing gel at ambient temperature owing to multiple inter-worm contacts.[102] Blanazs *et al*. demonstrated that cooling such worm dispersions to 4 °C led to degelation, with TEM studies indicating a worm-to-sphere transition (**Figure 1.20**). This transition proved to be fully reversible: regelation of the dispersion occurred upon heating to 25 °C.[103] Such thermoresponsive hydrogels may have useful biomedical applications, such as the cryopreservation of red blood cells[104] or as a cost-effective storage medium to enable the global transportation of human stem cells.[105] Core-crosslinked PGMA-PHPMA diblock copolymer worms can also be used as a Pickering emulsifier and offer some advantages over the equivalent spherical nanoparticles in this context.[106]

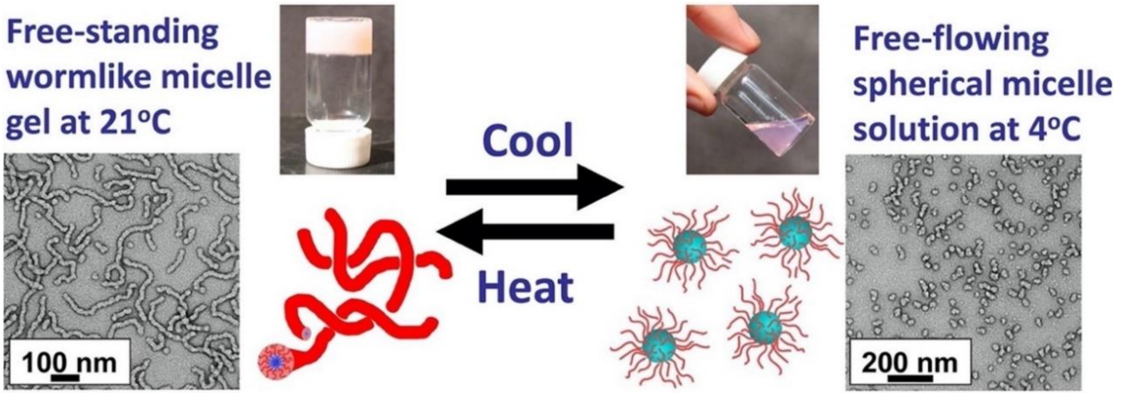

**Figure 1.20.** Thermoresponsive PGMA$_{54}$-PHPMA$_{140}$ diblock copolymer worms undergo a reversible worm-to-sphere transition when cooled to 4 °C, which leads to *in situ* degelation.[103]

Armes and co-workers have also investigated alternative water-soluble precursors for the RAFT aqueous dispersion polymerization of HPMA. These include poly(2-(methacryloyloxy) ethylphosphorylcholine (PMPC),[96] poly(ethylene glycol) (PEG),[107] poly(*N*-(2-methacryloyloxy)ethyl pyrrolidone) (PNMEP),[108] poly(2-(methacryloyloxy)ethyl trimethylammonium chloride) (PMETAC),[109] and poly(methacrylic acid) (PMAA).[110] Publications on alternative core-forming blocks are rather limited simply because there are relatively few vinyl monomers that are suitable for RAFT aqueous dispersion polymerization. However, some recent examples include 2-methoxyethyl acrylate (MEA),[111] *N,N′*-diethylacrylamide (DEAAm),[84] diacetone acrylamide (DAAM),[38] di(ethylene glycol) methyl ether methacrylate (DEGMA),[112] and 4-hydroxybutyl acrylate (HBA).[113,114]

In particular, Byard *et al.* reported the synthesis of PDMAC-PDAAM diblock copolymer nano-objects *via* RAFT aqueous dispersion polymerization of DAAM. A pseudo-phase diagram was constructed for this all-acrylamide PISA formulation, which enabled the reproducible targeting of pure spheres, worms or vesicles at 20% w/w solids (**Figure 1.21**).[38] With regard to this Thesis, this aqueous PISA formulation is used to prepare small well-defined spheres with a desired particle size.

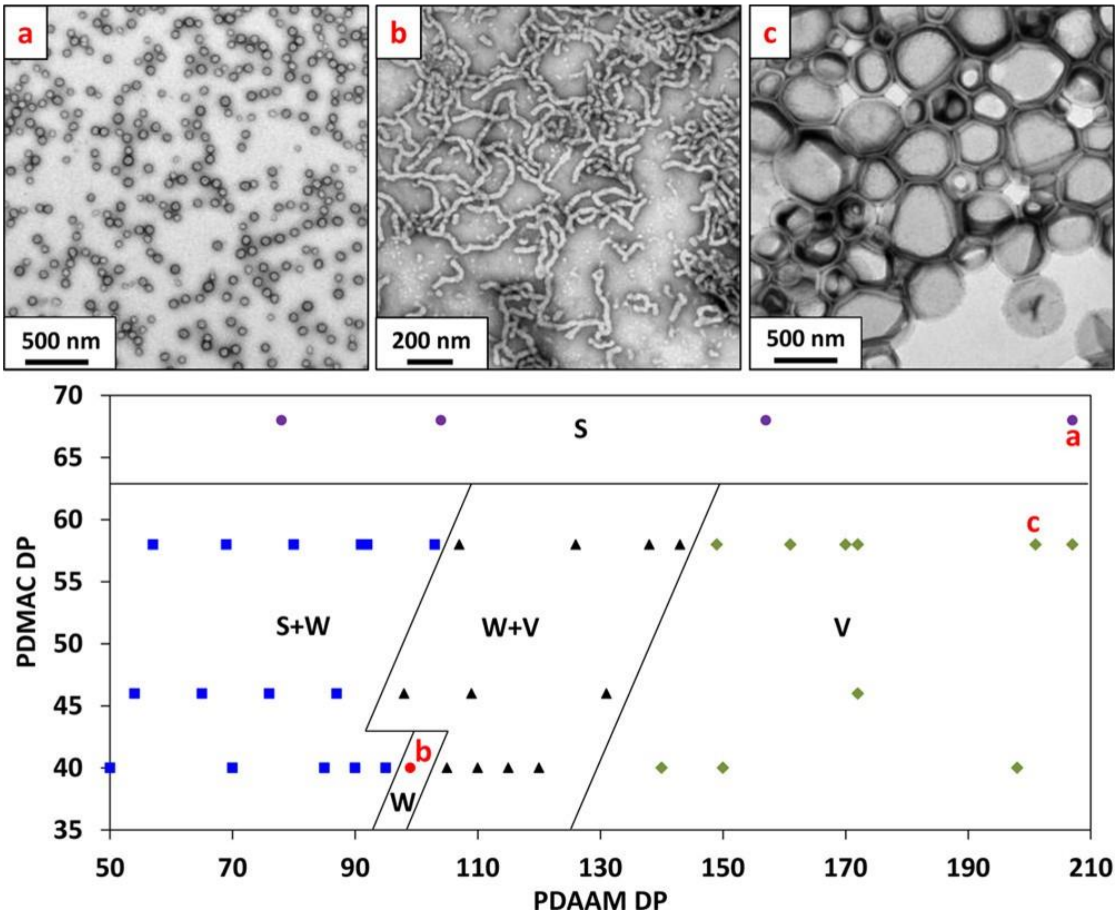

**Figure 1.21.** Pseudo-phase diagram constructed for a series of PDMAC$_x$–PDAAM$_y$ diblock copolymer nano-objects with representative TEM images shown for (a) spheres, (b) worms, and (c) vesicles.[38]

### 1.7.2 RAFT Aqueous Emulsion Polymerization

Initial attempts to develop RAFT aqueous emulsion polymerization formulations utilized conventional surfactants such as sodium dodecyl sulfate (SDS). However, these formulations suffered from poor monomer conversions, broad MWDs and colloidal instability. This was attributed to the inability of the RAFT agent to diffuse through the aqueous phase and interact with the growing polymer chains within the nascent nanoparticles.[115] The development of seeded RAFT emulsion polymerization addressed some of these issues. For example, Prescott *et al*. reported a well-controlled seeded emulsion polymerization of styrene using acetone as a co-solvent, which assisted diffusion of the RAFT agent to the polymer seed.[116] However, the initial seed particles were synthesized *via* FRP which inevitably produced relatively broad MWDs. Other obvious limitations of seeded emulsion polymerization include the undesirable use of water-miscible solvents such as acetone on an industrial scale. Furthermore, the presence of a suitable surfactant was still required for many of these formulations.

Hawkett *et al*. reported the first successful *ab initio* RAFT emulsion polymerization. A poly(acrylic acid) (PAA) precursor was chain-extended with *n*-butyl acrylate (nBA) in the absence of any surfactant.[117] High monomer conversions were achieved within 6 h at 60 °C and PAA-PnBA diblock copolymer nanoparticles with a mean diameter of 60 nm were obtained. A linear increase in molecular weight and relatively low dispersities were observed by gel permeation chromatography (GPC) analysis, see **Figure 1.22**. The same research group subsequently reported the synthesis of ABC triblock copolymer nanoparticles.[118] In this case, the B and C block comprised PnBA and polystyrene (PS), respectively.

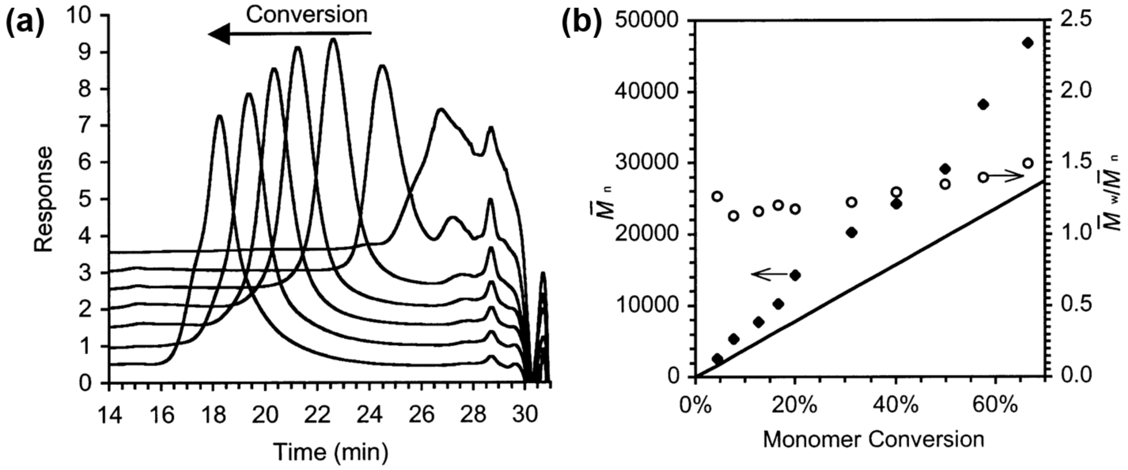

**Figure 1.22.** (a) THF GPC curves obtained during the synthesis of PAA-PnBA diblock copolymers by RAFT aqueous emulsion polymerization of *n*-butyl acrylate. (b) Evolution in $M_n$ (diamonds) and $M_w/M_n$ (circles) with nBA conversion as determined by GPC. The black solid line indicates the theoretical $M_n$.[117]

Since these seminal studies, there has been a significant increase in publications in this sub-field. For example, Charleux and co-workers prepared a trithiocarbonate-capped PEO-based precursor to serve as a RAFT agent and also a steric stabilizer. RAFT aqueous emulsion polymerization of styrene or nBA conducted in batch mode afforded core-shell nanoparticles. Kinetically-trapped spheres of up to 500 nm diameter were obtained and the final particle size depended on the PEO precursor/monomer molar ratio.[119,120] Subsequently, the same research group examined alternative steric stabilizer blocks (e.g. acrylic,[121–123] methacrylic,[124] acrylamide[90]), as well as core-forming blocks [e.g. poly(benzyl methacrylate) (PBzMA),[125] PMMA,[126] PS,[121,123,127] or PnBA[90]].

The Davis group reported the synthesis of ultrahigh molecular weight polystyrene-based diblock copolymer nanoparticles with relatively low dispersities *via* RAFT emulsion polymerization.[128] First, poly(ethylene glycol) methyl ether acrylate (PEGA) was statistically copolymerized with *N*-hydroxyethyl acrylamide (HEAA) to produce a water-soluble precursor, which was then used as the steric stabilizer for the polymerization of styrene at 80 °C. High styrene conversions (> 91%) and relatively narrow weight distributions ($M_w/M_n < 1.40$) were obtained for such aqueous PISA formulations. DLS and TEM studies indicated that only kinetically-trapped spheres of varying size were produced when adjusting the target DP of the core-forming block.

As mentioned previously, Armes and co-workers have utilized PGMA as a steric stabilizer block for RAFT aqueous dispersion polymerization. However, this non-ionic water-soluble homopolymer has also been used for the RAFT aqueous emulsion polymerization of various hydrophobic vinyl monomers. For example, Cunningham *et al*. produced a series of PGMA-PBzMA spherical nanoparticles with conversions of more than 99% being achieved after 6 h at 70 °C. TEM studies indicated that the mean particle diameter varied between 20 and 193 nm depending on the target DP for the core-forming PBzMA block (**Figure 1.23**). Furthermore, these PGMA-PBzMA nanoparticles were used to prepare Pickering emulsions using several model oils and their selective adsorption onto a patterned planar substrate was also demonstrated using phenylboronic acid chemistry.[89]

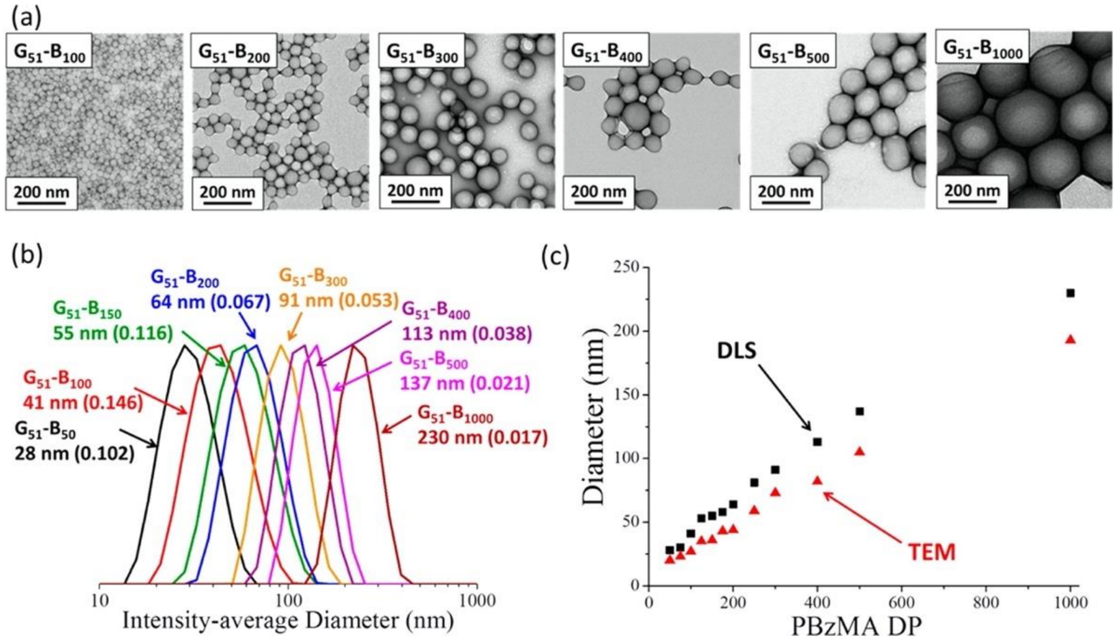

**Figure 1.23.** (a) TEM and (b) DLS studies on a series of $PGMA_{51}$-$PBzMA_x$ diblock copolymer nanoparticles synthesized *via* RAFT aqueous emulsion polymerization of BzMA, where the target DP for the core-forming PBzMA block was systematically varied between 50 and 1000. (c) A linear relationship between the mean particle diameter and PBzMA DP is indicated by both TEM and DLS studies.[89]

Subsequently, Akpinar *et al*. investigated the chain extension of four PGMA precursors (DP = 28, 43, 63 or 98) *via* the RAFT aqueous emulsion polymerization of 2,2,2-trifluoroethyl methacrylate (TFEMA) (**Figure 1.24**).[129] In this case, the target DP for the PTFEMA core-forming block was systematically varied between 100 and 1400. Very high TFEMA conversions (> 99%) were achieved after 20 h at 70 °C and narrow, unimodal MWDs were observed by UV GPC analysis. Spherical nanoparticles with a mean particle diameter of between 34 and 246 nm (judged by DLS) were prepared by systematically varying the DP of each block. By fixing the DP of the PGMA stabilizer, progressively increasing the target PTFEMA DP led to a monotonic increase in particle diameter. In contrast, when the target PTFEMA DP was fixed at 400, a reduction in particle size was observed when increasing the DP of the PGMA stabilizer block. This aqueous PISA formulation is of particular relevance to the work presented later in this Thesis.

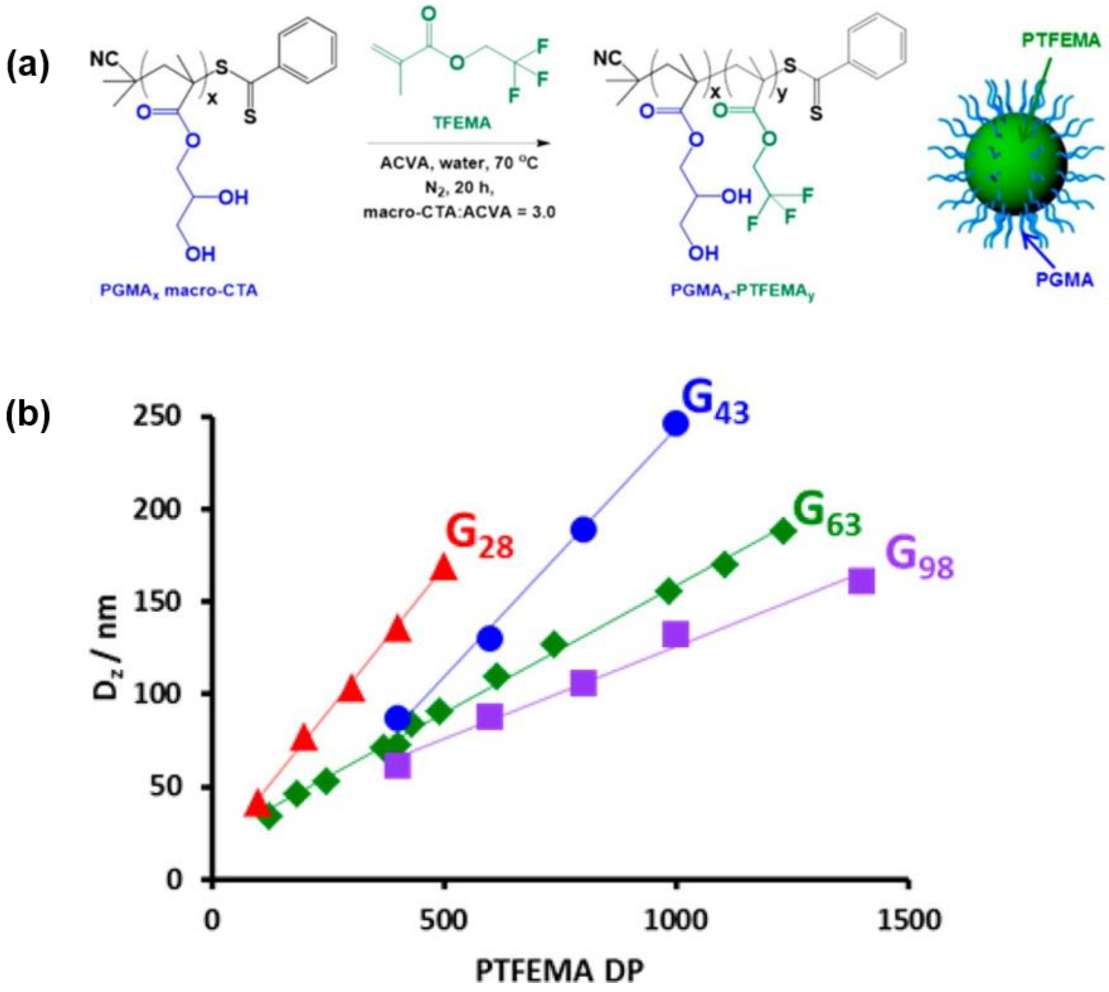

**Figure 1.24.** (a) Synthesis of PGMA$_x$-PTFEMA$_y$ diblock copolymer spheres by RAFT aqueous emulsion polymerization of TFEMA. (b) Plot of DLS intensity-average particle diameter versus DP of the PTFEMA core-forming block for four PGMA precursors (G) with DPs of 28, 43, 63 and 98.[129]

Similar PGMA stabilizers have been chain-extended using isopropylideneglycerol methacrylate (IPGMA)[130] or glycidyl methacrylate (GlyMA)[131] to form diblock copolymer nanoparticles. However, it is often observed that only kinetically-trapped spheres can be obtained by RAFT aqueous emulsion polymerization. This is a particularly perplexing observation since similar diblock copolymers prepared *via* RAFT alcoholic dispersion polymerization can form either worms or vesicles. Nevertheless, it is possible to avoid kinetically-trapped spheres for at least some RAFT aqueous emulsion polymerization formulations. For example, Charleux *et al*. reported using a poly[(acrylic acid)-co-poly(ethylene glycol methyl ether acrylate)] (P(AA-co-PEGA)) stabilizer for the polymerization of styrene. This approach enabled access to higher order morphologies.[121] The same group evaluated poly[methacrylic acid-co-poly(ethylene oxide) methyl ether methacrylate] (P(MAA-co-PEOMA)) as an alternative stabilizer block.[132] Empirically, it was found that a solution pH of 5-6 was optimal for high blocking efficiencies and low dispersities ($M_w/M_n < 1.35$). Interestingly, worms and vesicles were formed when targeting a DP of more than 200 for the core-forming PS block. Kinetic studies confirmed a morphological evolution from spheres to worms to vesicles with increasing PS DP. The effect of varying the stabilizer block DP on the final copolymer morphology was also explored. When targeting a PS DP of 300, a relatively long P(MAA-co-PEOMA) precursor ($M_n$ = 15 kg mol$^{-1}$) led to mainly worms, whereas a relatively short P(MAA-co-PEOMA) precursor ($M_n$ = 11.8 kg mol$^{-1}$) produced vesicles.

In closely-related work, Zhang *et al*. reported the synthesis of P(MAA-co-PEOMA)-PS nanoparticles in two steps using a one-pot protocol.[133] This is attractive for industrial scale-up because it eliminates the need for additional purification steps. Interestingly, this formulation also enabled the preparation of spheres, worms and vesicles. The pseudo-phase diagram shown in **Figure 1.25** indicates that the final copolymer morphology depends on both the PS DP and the steric stabilizer DP. In a further study, the core-forming PS block was replaced with PMMA. P(MAA-co-PEOMA)-PMMA spheres, worms or vesicles could be accessed simply by increasing the target DP for the hydrophobic block. This morphological evolution was observed irrespective of pH. However, syntheses conducted at pH 3.5 gave better controlled polymerizations with higher blocking efficiencies compared to those conducted at either pH 5 or pH 7. Interestingly, a core-forming statistical block containing both styrene and MMA only led to kinetically-trapped spheres.[126]

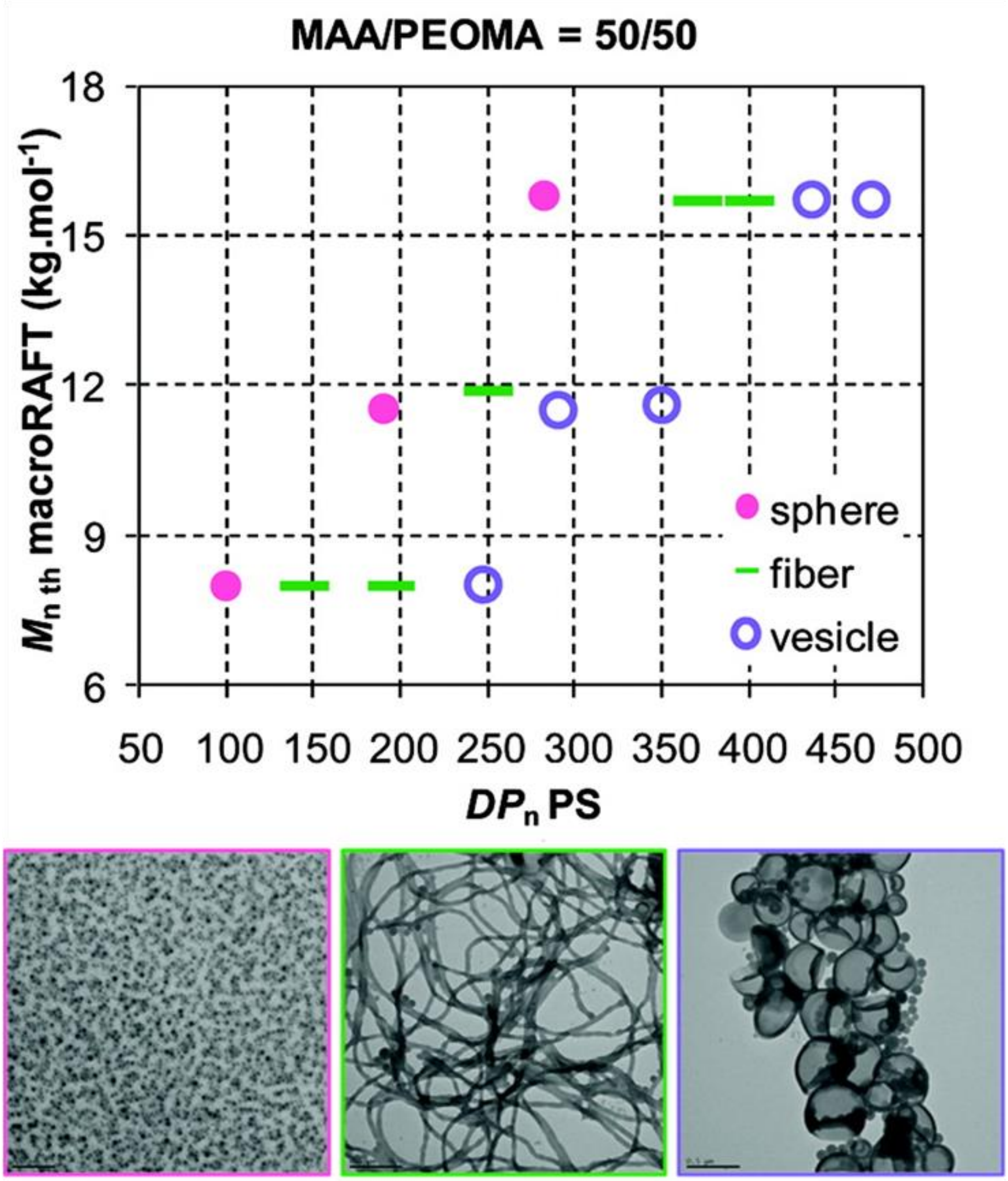

**Figure 1.25.** Pseudo-phase diagram constructed for the synthesis of P(MAA-co-PEOMA)-PS diblock copolymer nano-objects *via* RAFT aqueous emulsion polymerization of styrene. Preparation of spheres, worms and vesicles (shown by TEM) were possible by systematically varying the molecular mass of the stabilizer and the DP of the core PS block.[133]

Davis and co-workers also reported the synthesis of spheres, worms and vesicles *via* RAFT aqueous emulsion polymerization.[134] All three morphologies could be obtained when polymerizing styrene using two different poly[*N*-hydroxyethyl acrylamide-co-poly(ethylene glycol) methyl ether acrylate] (poly(HEAA-co-PEGA)) precursors. Moreover, it was demonstrated that the chemical nature of the RAFT end-groups and the initiator concentration also influenced the final copolymer morphology. For example, switching from a carboxylic acid end-group to a methyl ester end-group resulted in the formation of vesicles instead of spheres. Furthermore, an identical synthetic protocol employing half the radical initiator concentration produced spheres rather than vesicles. Formation of a worm-rich phase was achieved by lowering the target DP for the structure-directing PS block when using a carboxylic acid-functionalized P(HEAA-co-PEGA) macro-CTA.

Armes and co-workers have also obtained higher order morphologies *via* RAFT aqueous emulsion polymerization by targeting core-forming monomers that exhibit relatively high aqueous solubility. For example, Cockram *et al*. reported that the polymerization of 2-hydroxybutyl methacrylate (HBMA) using a PMAA precursor resulted in an unusual 'monkey nut' morphology.[135] It was suggested that the higher aqueous solubility of HBMA (20 g $dm^{-3}$ at 70 °C) enabled more efficient mass transport of monomer from the emulsion droplets to the growing diblock copolymer nanoparticles during this relatively fast polymerization. This increases the degree of solvation (and hence mobility) of the growing polymer chains by the HBMA monomer, which most likely facilitates an evolution in copolymer morphology during PISA.[27,87] This hypothesis also led to exploration of the RAFT aqueous emulsion polymerization of GlyMA, since this monomer has a comparable aqueous solubility (24-25 g $dm^{-3}$ at 80 °C) to that of HBMA.[136] Indeed, using a relatively short PGMA precursor provided convenient access to well-defined worms using an efficient one-pot protocol. More recently, Brotherton *et al*. reported the chain extension of PGMA *via* RAFT aqueous emulsion polymerization of 2-methoxyethyl methacrylate (MOEMA).[137] This system constitutes a third example of a vinyl monomer with a moderately high aqueous solubility (19.6 g $dm^{-3}$ at 70 °C). Again, systematic variation of the target PGMA-PMOEMA diblock composition and copolymer concentration provided access to spheres, worms and vesicles (**Figure 1.26**). In summary, several empirical approaches have been developed to avoid the formation of kinetically-trapped spheres *via* RAFT aqueous emulsion polymerization. However, it should be emphasized that kinetically-trapped spheres are highly desirable for certain applications. For example, this morphology ensures minimal dispersion viscosity when preparing nanoparticles at relatively high solids, which makes such formulations much more amenable to potential industrial scale-up.

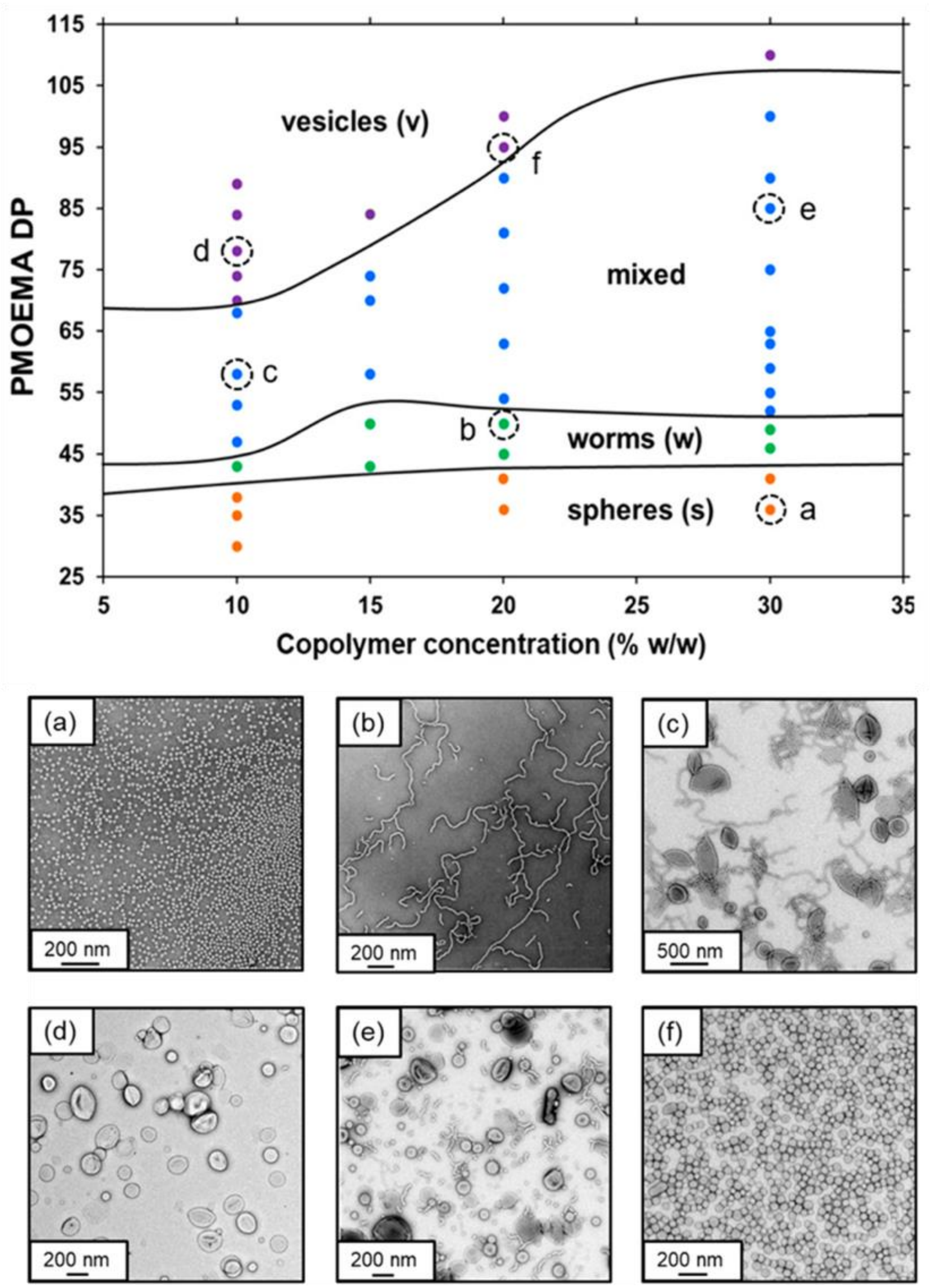

**Figure 1.26.** Representative TEM images and corresponding pseudo-phase diagram for a series of PGMA$_{29}$-PMOEMA$_{30-110}$ diblock copolymer nano-objects prepared by RAFT aqueous emulsion polymerization of MOEMA.[137]

## 1.8 Colloidal Dispersions

Colloidal dispersions are commonly found in various industrial products such as agrochemical formulations,[138] cement,[139] paint,[140] paper[141] and pharmaceutics.[142] By definition, colloidal dispersions comprises particles that lie between 1 nm and 1 μm. A repulsive force must be introduced to counteract the ever-present van der Waals forces between particles to ensure colloidal stability. In principle, this can be achieved by introducing either surface charge or an adsorbed layer of solvated polymer chains. This leads to stable colloidal particles *via* either an electrostatic or a steric stabilization mechanism, respectively.[143]

### 1.8.1 Electrostatic Stabilization

If a colloidal particle acquires surface charge in aqueous media, an electrical double layer (EDL) containing an excess of oppositely charged ions is formed around it.[144] Close approach of two such particles inevitably leads to overlap between their respective EDLs. This overlap is energetically unfavorable and hence gives rise to a strong repulsive force that offsets the ever-present van der Waals attractive forces between the two particles. A quantitative theory to describe this situation was developed by Derjaguin, Verwey, Landau and Overbeek in the 1940s and is now known as DLVO theory.[145,146] The total potential energy curve can be calculated by summing the attractive and repulsive forces (**Figure 1.27**). The van der Waals attractive forces dominate at sufficiently close range, which produces a deep potential well known as the primary minimum. At greater distances, the repulsive forces arising from EDL overlap dominate, which leads to a local energy maximum ($\Delta E_{max}$). This is the energy barrier that the two particles must overcome prior to aggregation. If the mean kinetic energy ($k_BT$) of the particles is not sufficient to traverse this barrier, then no particle aggregation can occur. Thus the criterion for colloidal stability is $\Delta E_{max} >> k_BT$.[144] On the other hand, if $\Delta E_{max} \sim kT$ then particle aggregation can occur. The magnitude of $\Delta E_{max}$ depends on the surface potential and the electrolyte concentration. Addition of salt shrinks the EDL and hence lowers $\Delta E_{max}$, which leads to particle aggregation. This electrostatic stabilization mechanism is restricted to highly polar solvents such as water or lower alcohols, because this enables the particles to acquire sufficient surface charge to form

EDLs. Such colloidal dispersions are only kinetically stable but they may still exhibit long-term stability.

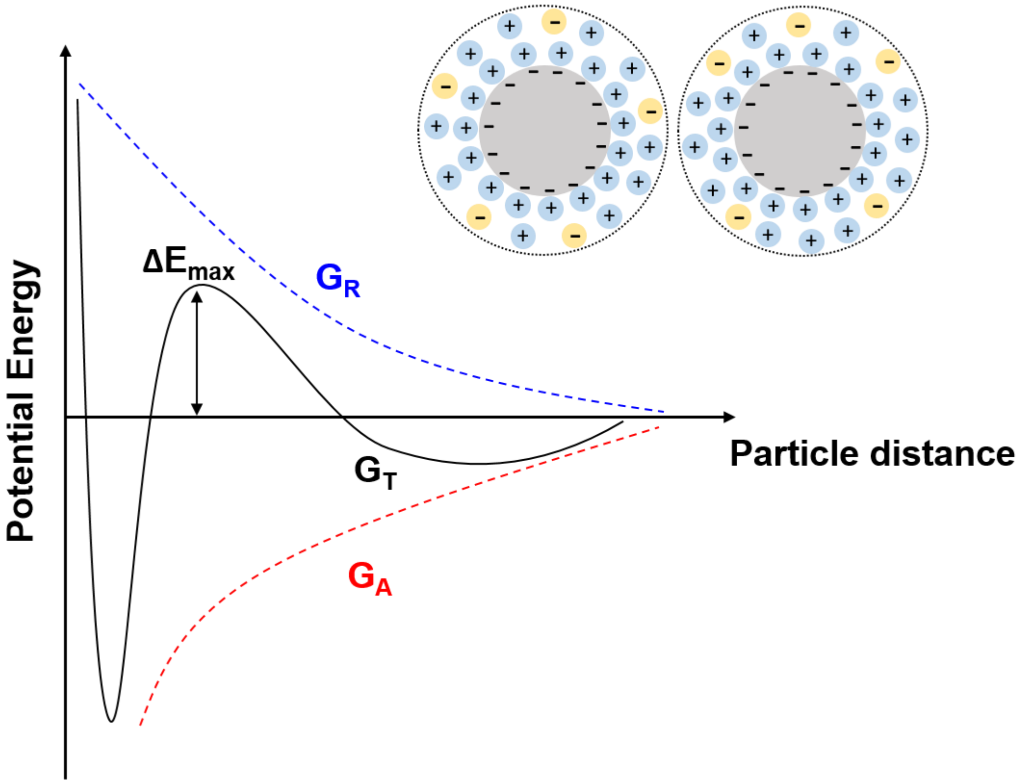

**Figure 1.27.** Potential energy curve for electrostatic stabilization where the total energy, $G_T$, is the sum of the repulsive and attractive energies ($G_T = G_R + G_A$). The schematic cartoon depicts two mutually repulsive particles owing to their respective electrical double layers.[147]

### 1.8.2 Steric Stabilization

An alternative stability mechanism becomes relevant if the colloidal particles are coated with a relatively thick adsorbed layer of well-solvated polymer chains. As two such particles approach one another, the adsorbed polymer chains begin to interpenetrate. This is energetically unfavorable in terms of both enthalpy (in a good solvent environment, polymer segments prefer to remain solvated rather than interact with segments on other chains) and entropy (because fewer chain conformations become accessible). The resulting build-up of osmotic pressure forces solvent between the approaching particles, which leads to their repulsion.[148] The total potential energy curve, $G_T$, for steric stabilization is calculated by combining the attractive and repulsive energy potentials (**Figure 1.28**). This produces a relatively shallow minimum, $\Delta E_{min}$, at approximately twice the mean thickness of the adsorbed polymer layer (2δ). The criterion for colloidal stability is $\Delta E_{min} << k_BT$. Thus, the particles must possess sufficient kinetic energy to escape from this shallow minimum if interparticle collisions are to remain elastic (non-sticky). The depth of this local minimum depends on the particle size, the Hamaker constant and the thickness of the adsorbed polymer layer.[144] Compared to electrostatic stabilization, steric stabilization is much less sensitive to electrolytes, is effective at high particle concentrations and is applicable over a wide range of solvents. Unlike electrostatic stabilization, it produces thermodynamically stable colloidal dispersions.

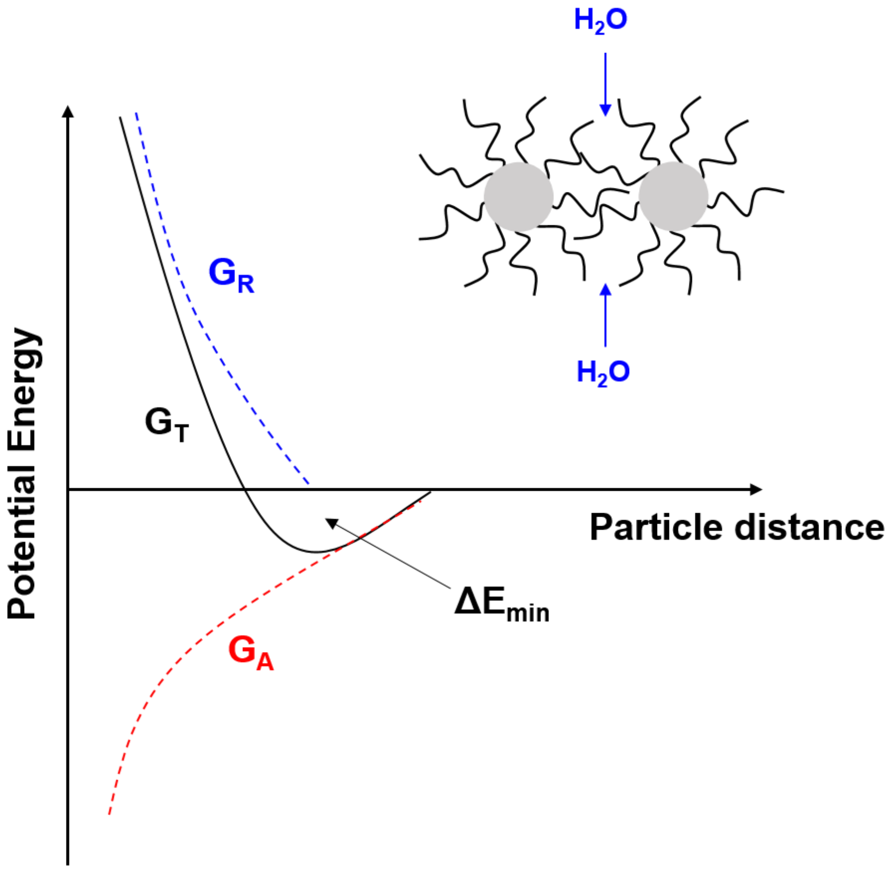

**Figure 1.28.** Potential energy curve for the case of steric stabilization, whereby the total energy, $G_T$, is the sum of the repulsive and attractive curves ($G_T = G_R + G_A$). The schematic cartoon depicts unfavorable overlap between adsorbed polymer chains during the close approach of a pair of particles, which generates an osmotic pressure between them.[147]

### 1.8.3 Polymers in Colloidal Dispersions

As previously mentioned, polymers can be utilized as dispersants to enable the preparation of colloidally stable dispersions. However, it may be advantageous for some industrial formulations to exhibit weak, reversible flocculation. For example, weakly flocculated pigment particles in paint formulations form a structured fluid or weak gel, which minimizes gravitational settling and confers the desired rheological properties.[149] Similarly, a network of weakly flocculated particles can prevent caking during the long-term storage of pesticide formulations.[150]

Rührwein and Ward introduced the concept of bridging flocculation, whereby high molecular weight polymers adsorb onto more than one particle.[151] This mechanism operates at relatively low polymer concentration. At higher polymer concentrations, the particles become sterically stabilized because there is sufficient polymer to achieve high surface coverage (**section 1.8.2**).

At still higher polymer concentrations, depletion interactions can occur owing to the presence of non-adsorbed polymer chains in solution. Asakura and Oosawa were the first to report the phenomenon of depletion flocculation, which involves the exclusion of free polymer chains between particles as they approach one another.[152] As a result, there is a build-up of osmotic pressure that generates interparticle attractive forces and hence causes flocculation. A further increase in polymer concentration can cause depletion stabilization. This differs from steric stabilization because depletion stabilization confers stability through non-adsorbed polymer, whereas the latter phenomenon involves adsorbed polymer.[153] Depletion interactions exhibit both a short-range attractive minimum and a long-range repulsive barrier. At sufficiently high polymer concentration, the long-range repulsive energy barrier produces kinetically-stabilized particles *via* depletion stabilization.[154] Although its mechanism is not well understood, depletion stabilization has been observed in several experimental studies.[155–157]

### 1.8.4 Adsorption and Adsorption Isotherms

Polymer adsorption may occur *via* either physisorption or chemisorption. Physisorption involves relatively weak van der Waals interactions and/or hydrogen bonding. In contrast, chemisorption involves the formation of surface covalent bonds. Adsorption isotherms are a convenient method for determining the amount of surface-adsorbed polymer.[158] Typically, the amount of adsorbed polymer ($\Gamma$) is plotted against the equilibrium concentration of polymer remaining in solution after adsorption.

Many adsorption isotherm models have been reported over the past century: some well-known examples include the Langmuir model,[159] the Freundlich model,[160] and the Brunauer-Emmett-Teller (BET) model.[161] However, only the Langmuir isotherm model will be discussed in this Thesis. The Langmuir model was originally used to describe the adsorption of gases on solids. It is based on the following assumptions: (i) the surface is treated as a lattice and all adsorption sites are equivalent; (ii) each site may only adsorb one molecule; (iii) there are no interactions between adsorbed molecules; (iv) maximum adsorption is restricted to monolayer coverage.

The Langmuir adsorption isotherm model can also be used to describe polymer adsorption onto colloidal substrates.[162] For example, a Langmuir isotherm was observed for poly(ethylene oxide)-poly(propylene oxide) (PEO-PPO) block copolymers adsorbed from aqueous solution onto carbon black.[163] Similarly, a star diblock copolymer adsorbed from *n*-dodecane onto the same substrate gave a low-affinity Langmuir isotherm.[164] The Langmuir adsorption model has also been utilized to analyse the adsorption of nanoparticles on various substrates.[165–167]

If monolayer coverage can be assumed for polymer adsorption, then it is appropriate to use the Langmuir adsorption isotherm model. The adsorbed amount of polymer can be calculated using **Equation 1.19**.

$$\Gamma = \frac{q_m K_a C_{eq}}{1 + K_a C_{eq}} \tag{1.19}$$

Here $\Gamma$ is the adsorbed amount (mg $m^{-2}$), $q_m$ is the monolayer capacity, $K_a$ is the equilibrium constant and $C_{eq}$ is the equilibrium concentration of the adsorbate that remains in solution. To calculate $q_m$, the surface area of the substrate must be known.[159]

Giles *et al.* classified solid/solute adsorption isotherms into four main groups: Langmuir (L), S-shaped (S), high affinity (H), and constant partition (C).[168] The adsorption mechanism can be determined by the isotherm shape when plotting the adsorbed amount against the equilibrium concentration (**Figure 1.29**).

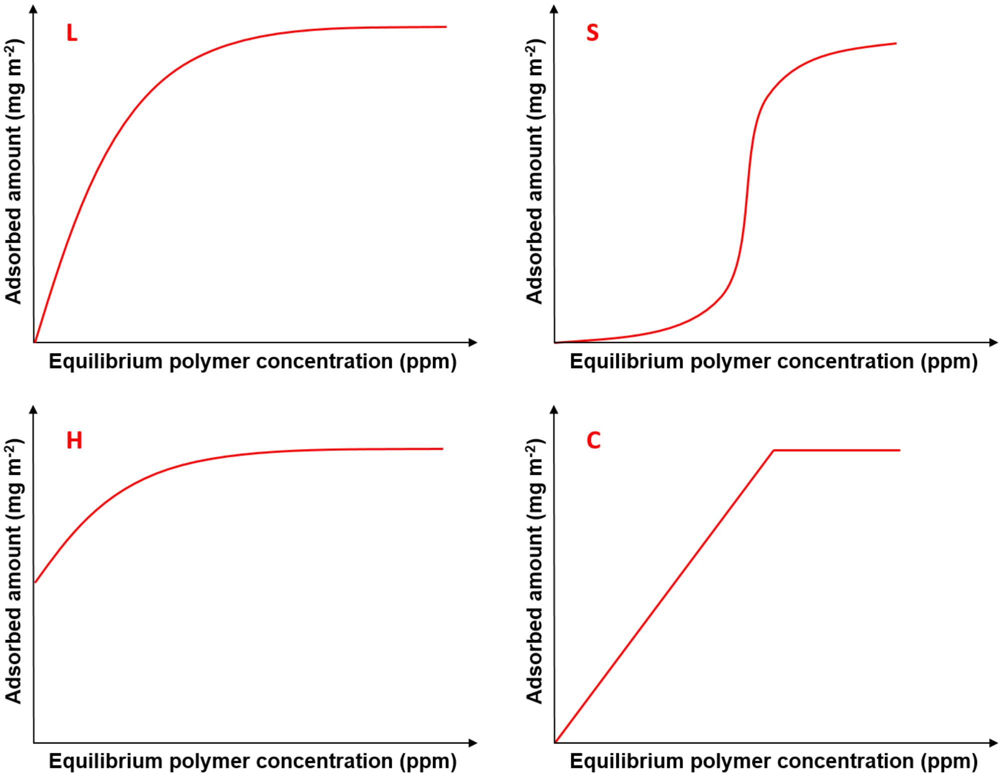

**Figure 1.29.** Four types of adsorption isotherm (L, S, H and C-type) for the adsorption of a solute onto a solid substrate from solution, as reported by Giles *et al*.[168]

For Langmuir isotherms (L-type), the adsorbed amount increases rapidly at low solute (polymer) concentrations. This is followed by an adsorption ‘knee’ and then a plateau region that corresponds to monolayer coverage. For S-type isotherms, greater adsorption occurs at higher concentrations owing to co-operative interactions between adjacent adsorbed molecules. H-type isotherms are similar to L-type isotherms but exhibit strong adsorption at even low concentrations. C-type isotherms exhibit a constant slope until a certain saturation point is attained and thereafter the adsorption remains constant.[168]

In practice, the adsorbed amount of polymer is often determined using an indirect approach known as a supernatant assay. This requires determining the solute concentration in the continuous phase before and after adsorption, with the difference corresponding to the adsorbed amount. In principle, centrifugation can be used to separate the colloidal substrate from any non-adsorbed polymer, which enables the adsorbed amount of polymer to be calculated. If the polymer has an appropriate spectroscopic signature, its solution concentration before and after adsorption can be assessed using either UV spectroscopy[169] or IR spectroscopy.[170]

### 1.8.5 Block Copolymer Dispersants

Block copolymers have been proven to be effective dispersants for a wide range of applications,[171–175] particularly for the dispersion of pigments for paints, coatings and inks.[176–180] For example, Duivenvoorde *et al.* reported the synthesis of a novel block copolymer comprising poly(2-vinylpyridine) and poly(ε-caprolactone). Such dispersants displayed high affinity for $TiO_2$, an inorganic pigment commonly used for high-quality white paint.[180,181] In addition, block copolymers have also been found to be effective dispersants for organic pigments.[177,182] In related work, Growney and co-workers reported the physical adsorption of hydrogenated polyisoprene-polystyrene star diblock copolymers onto carbon black. This system exhibited bridging flocculation at low polymer concentrations but steric stabilization of the carbon black particles was observed at a critical copolymer concentration of approximately 5.5% w/w.[164]

North *et al.* reported the electrostatic adsorption of cationic poly(2-(dimethylamino)ethyl methacrylate)-poly(benzyl methacrylate) ($PDMA_{71}$-$PBzMA_{100}$) spherical nanoparticles onto anionic silica particles.[169] Aqueous electrophoresis and TEM studies were consistent with nanoparticle adsorption (**Figure 1.30**). Recently, the same first author reported the wholly aqueous one-pot synthesis of PDMA-PMAA diblock copolymers. This zwitterionic diblock copolymer proved to be an effective dispersant for yellow iron oxide nanoparticles.[183]

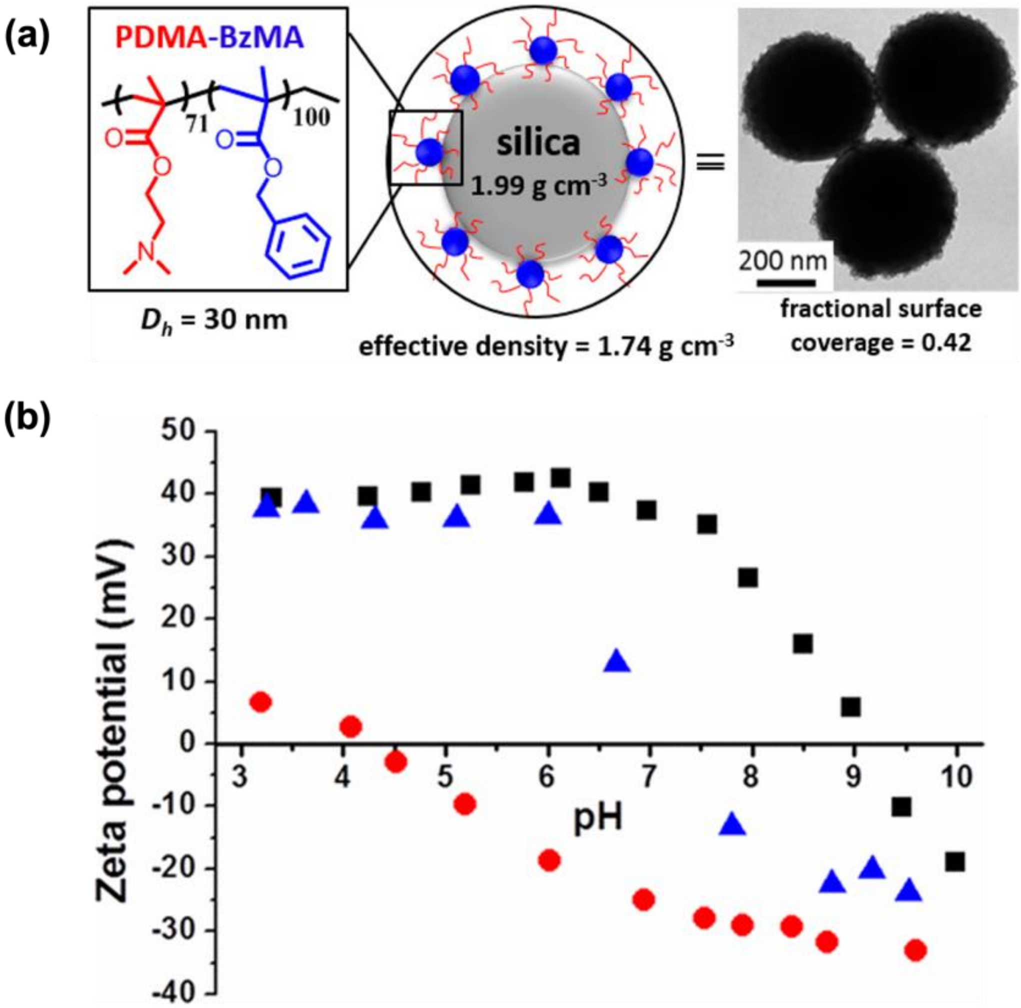

**Figure 1.30.** (a) Schematic representation of 30 nm diameter $PDMA_{71}$-$PBzMA_{100}$ nanoparticles adsorbed onto silica particles with a corresponding TEM image. (b) Zeta potential vs. pH curves recorded for $PDMA_{71}$–$PBzMA_{100}$ nanoparticles (black), bare silica (red), and nanoparticle-coated silica (blue). An intermediate isoelectric point at pH 7 is observed for the nanoparticle-coated silica particles, which is consistent with the adsorption of cationic nanoparticles onto anionic silica.[169]

Alexandridis and co-workers investigated the use of Pluronic dispersants, an important class of non-ionic ABA-type triblock copolymers consisting of PEO and PPO. More specifically, they reported the adsorption of PEO–PPO–PEO copolymers onto both carbon black and silica nanoparticles.[184,185] Fernandes *et al.* demonstrated that the same copolymer type could disperse single-walled carbon nanotubes. Here the hydrophobic PPO block adsorbs onto the surface of the nanotubes, while the hydrophilic PEO block confers effective steric stabilization.[186]

## 1.9 Colloid Dispersions in Agriculture

With an increase in global population and changes to dietary habits, the agrochemical sector has played an essential role in enabling improved food yields, whilst controlling a wide range of crop pests. Pesticides are chemical compounds that are designed to either kill or deter pests.[187,188] Some well-known examples of pesticides include fungicides, herbicides and insecticides, which can be formulated as solid particles within liquid dispersions.[189]

Two techniques for preparing generic solid/liquid dispersions are the condensation method and the dispersion method. The former involves the nucleation and growth of small molecules, e.g. the preparation of polymer latexes *via* emulsion or dispersion polymerization (**section 1.4 and 1.5**). In contrast, the latter approach involves preparing suspensions of preformed particles and typically requires a significant reduction in the initial particle size. This can be achieved *via* ball milling in the presence of a suitable surfactant or copolymer dispersant.[147]

### 1.9.1 Preparation of Suspension Concentrates *via* Ball Milling

A suspension concentrate (SC) is a type of pesticide formulation which is typically prepared using the dispersion method. SCs are dispersions consisting of insoluble hydrophobic crystals suspended in water. They offer advantages such as high solids, relatively low cost, ease of handling and are generally safer for the end-user.[190] The organic crystalline particles within the dispersion constitute an active ingredient (AI) that delivers the desired biological activity. The AI must have certain properties for it to be suitable for SC formulations. It needs to be easily milled, chemically stable in its crystal form and must be chemically stable in the presence of water. In addition, a relatively high melting point (> 80°C) prevents in situ melting of the crystals during ball milling, which can generate excess heat. Finally, the AI must possess relatively low water solubility (< 200 ppm) to minimize crystal growth by the phenomenon known as Ostwald ripening.[191]

SCs can be readily prepared using a wet milling process in the presence of a suitable surfactant or polymer dispersant. Shaker mills or planetary ball mills are typically used for high-energy milling (**Figure 1.31**). Ball or bead-milling provides sufficient mechanical energy to reduce the mean diameter of the AI crystals to approximately 1-2 µm. Collisions between crystals and beads or between individual crystals are completely random. As a result, only a fraction of the inputted energy is actually used for particle size reduction; the rest is lost as heat, vibrational or friction energy. Furthermore, the ideal milling conditions for a particular SC are usually established through trial and error. It is also quite rare for an AI to be processed in the absence of other inert compounds, known as adjuvants. These ensure efficient delivery of AIs to the appropriate crop or plant, while improving handling, storage or application properties. Examples of widely-used adjuvants include surfactants, rheological modifiers, pH buffers, biocides and antifreeze additives.[192]

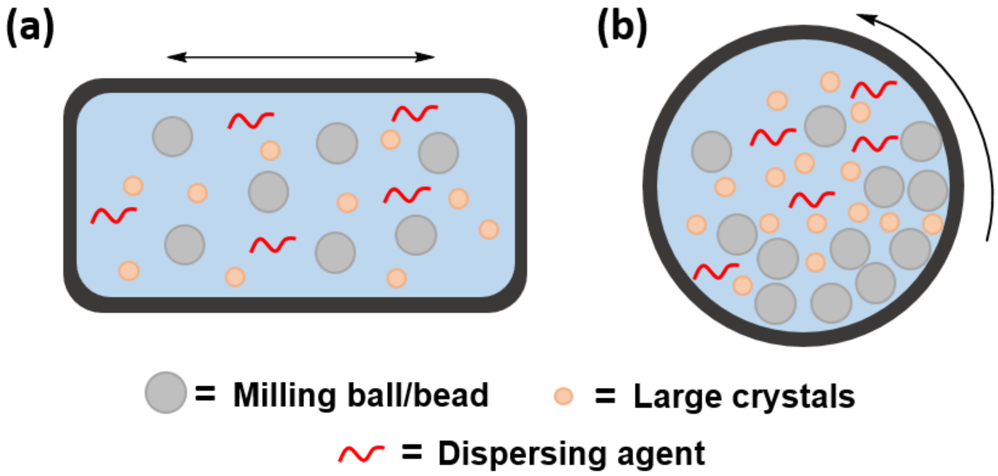

**Figure 1.31.** Schematic representation of milling using (a) a shaker mill and (b) a planetary ball mill.

### 1.9.2 Suspension Concentrate Failure Mechanisms

SC instability can occur through three failure mechanisms: sedimentation, crystallization and gross flocculation (see **Figure 1.32**).[191] Ideally, the particles are uniformly dispersed within the liquid phase, but gravitational settling can occur over time. Minimization of such sedimentation and improved physical stability can be achieved by adding appropriate polymeric dispersants and rheological modifiers. SCs are also prone to crystal growth through Ostwald ripening. This phenomenon is driven by small differences in solubility between smaller and larger particles. In addition, Ostwald ripening can occur because AIs may be present as several polymorphs with slightly differing aqueous solubilities. The formation of larger particles over time can lead to unstable suspensions and a concomitant reduction in AI efficiency. One method to combat Ostwald ripening is to use polymeric surfactants that adsorb onto the AI surface and therefore prevent particle growth. Finally, SCs can be susceptible to gross flocculation upon storage or dilution. This can be avoided with the addition of an effective dispersing agent, which must strongly adsorb onto the crystal surface. It must also resist displacement due to a change in temperature, application of shear forces or interactions with other components.[193]

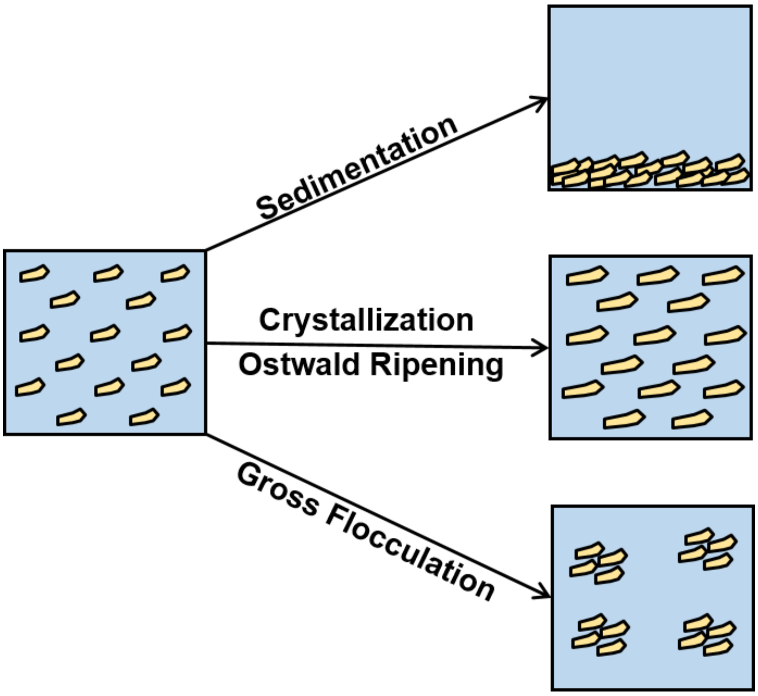

**Figure 1.32.** Schematic representation of potential failure mechanisms for SCs.[191]

### 1.9.3 Dispersing Agents in Agrochemicals

A dispersing agent (or dispersant) is an essential requirement for formulating pesticide dispersions such as SCs. The dispersing agent is required to: (i) be a good wetting agent in order to aid the dispersion of the aggregates or agglomerates that are formed in the dry state, (ii) enable break-up of large agglomerates during milling and (iii) provide good long-term stability for the final SC.[144]

Several types of dispersing agents have been used to form stable aqueous dispersions of AIs. For example, non-ionic ethoxylate-based surfactants (e.g. $R(CH_2CH_2O)_nH$) can stabilize various pesticide formulations. The hydrophobic *n*-alkyl component promotes adsorption, while the ethylene oxide-based head-group confers effective steric stabilization.[175] Alternatively, polycarboxylate-based dispersants can anchor onto the particle surface and confer *electrosteric* stabilization.[194] For example, Yang *et al*. recently reported on the synthesis of three polycarboxylate terpolymers and found that longer alkyl side-chains provided more efficient stabilization of imidacloprid-based SCs.[195] Moreover, they found that adding only 2.0 wt% dispersant caused a sharp reduction in the overall zeta potential, which indicates effective adsorption of dispersant onto the particle surface. Only relatively small changes in the zeta potential were observed beyond 2.0 wt%, suggesting that a saturation point was attained (**Figure 1.33**).

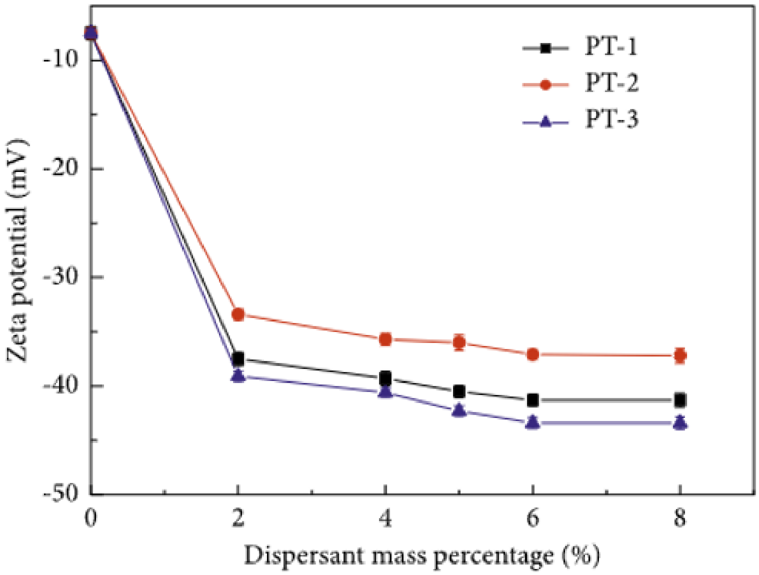

**Figure 1.33.** Zeta potential vs. mass of dispersant (%) for imidacloprid-based SCs prepared using three different polycarboxylate terpolymers.[195]

Heath *et al.* investigated using a poly(methyl methacrylate-methacrylic acid/methoxy-capped poly(ethylene oxide) methacrylate) graft copolymer as a dispersant for a well-known fungicide (ethirimol). The steric stabilization conferred by this strongly-adsorbed graft copolymer enables preparation of highly concentrated dispersions (volume fraction > 0.60).[196] Recently, Zhang and co-workers reported on the synthesis of novel comb-like copolymer dispersants consisting of poly(styrene-co-acrylic acid-co-polyethylene glycol methyl ether maleate). The additional non-ionic side branches are believed to provide improved dispersibility and thermal storage capabilities for a widely-used insecticide, pymetrozine.[197]

Polyelectrolytes such as naphthalene-formaldehyde sulfonate condensates (e.g. the well-known anionic dispersant, Morwet D-425) are commonly used as polymeric dispersants for the preparation of SCs and other pesticide formulations, such as wettable powders and water-dispersible granules.[198] Lignosulfonates are another type of polyelectrolyte that is commonly used as a dispersing agent for pesticides,[199] dyes,[200] coal–water slurries[201] and concrete.[202] It is an industrially attractive cost-effective option since it is a highly water-soluble derivative of lignin, which is derived from plant biomass.

### 1.9.4 Model Organic Crystals for Suspension Concentrates

The toxicity and/or the IP associated with some agrochemical AIs suggests that a model AI could be an attractive alternative. For example, pharmaceutical AIs such as ibuprofen and cholesterol have relatively low water solubilities and sufficiently high melting points, which suggests that they might be useful as model AIs for the production of SC formulations. Similarly, the well-known simple polyaromatic hydrocarbon (PAH), anthracene, also meets the same criteria and might therefore be a useful model AI.

Unfortunately, ibuprofen and cholesterol proved to be unsuitable model AIs and hence are not discussed further in this Thesis. However, the preparation of model SCs by subjecting macroscopic anthracene crystals to wet ball milling led to interesting new microparticles with potential space science applications. This additional work forms part of this Thesis (see Chapter 5).

## 1.10 Particle Size Analysis

Reliable determination of the SC particle size distribution is important to ensure that the desired AI particle diameter has been achieved after milling. Furthermore, such measurements can be useful for assessing the dispersant performance and also monitoring the long-term stability of such aqueous suspensions.

### 1.10.1 Laser Diffraction

Laser diffraction is suitable for measuring particles sizes of between 0.01 µm and 3 mm. A laser beam is passed through a dispersion or suspension of particles, which causes light scattering. Larger particles typically scatter light at smaller angles relative to the incident light beam, while the opposite is true for smaller particles. As a result, particle size distributions can be calculated based on the unique angular scattering patterns that are observed.[203] Traditionally, laser diffraction relied on Fraunhofer diffraction to determine the particle size. However, this theory is limited to particle sizes larger than approximately 20 µm. This is because the particle size must be at least ten times that of the incident wavelength and particles were only observed at a relatively small scattering angle.[204] In contrast, modern laser diffraction instruments use Mie theory to assess a wider range of particle sizes, but this more sophisticated approach requires knowledge of the optical properties (e.g., refractive and absorptive indices) of both the particles and the solvent.[141] Both mathematical models assume a spherical morphology to calculate a mean particle diameter.[205] However, this technique is also applicable for strictly non-spherical particles such as agrochemical SCs and typically reports a sphere-equivalent volume-average diameter.

### 1.10.2 Dynamic Light Scattering

Dynamic light scattering (DLS), also known as photon correlation spectroscopy (PCS), is a well-established particle size analysis technique in colloid science.[206] In this technique, light intensity fluctuations of the scattered incident light are measured as a function of time. The mean diffusion coefficient, *D*, is calculated from the auto-correlation function. Assuming that the particles are spherical, perfectly monodisperse and non-interacting, the mean hydrodynamic particle radius ($R$) can be determined at a known temperature (T) and solution viscosity (η) by using the Stokes-Einstein equation (**Equation 1.20**).[207]

$$D = \frac{k_B \mathrm{T}}{6\pi\eta R} \qquad \textbf{(1.20)}$$

DLS reports the *z*-average diameter for particles that range in size from 1 nm to 10 μm.[204] Compared to laser diffraction, DLS is well-suited for determining particle size distributions for the relatively small diblock copolymer nanoparticles that can be prepared by RAFT aqueous emulsion polymerization. In contrast, laser diffraction is a useful technique for sizing the micron-sized organic crystals within SCs.

### 1.10.3 Electron Microscopy

Scanning electron microscopy (SEM) and transmission electron microscopy (TEM) are useful techniques for determining the particle size of both diblock copolymer nanoparticles and micron-sized crystals.[208] In SEM, a sample is scanned with a focused electron beam, which interacts with the sample surface to generate back-scattered electrons, secondary electrons and X-rays. The latter can provide useful elemental information but images are produced by analysing the secondary electrons, which are emitted from the sample surface *via* inelastic interactions.[209] The volume and regions within a sample from which X-rays and electrons originate is illustrated in **Figure 1.34**.

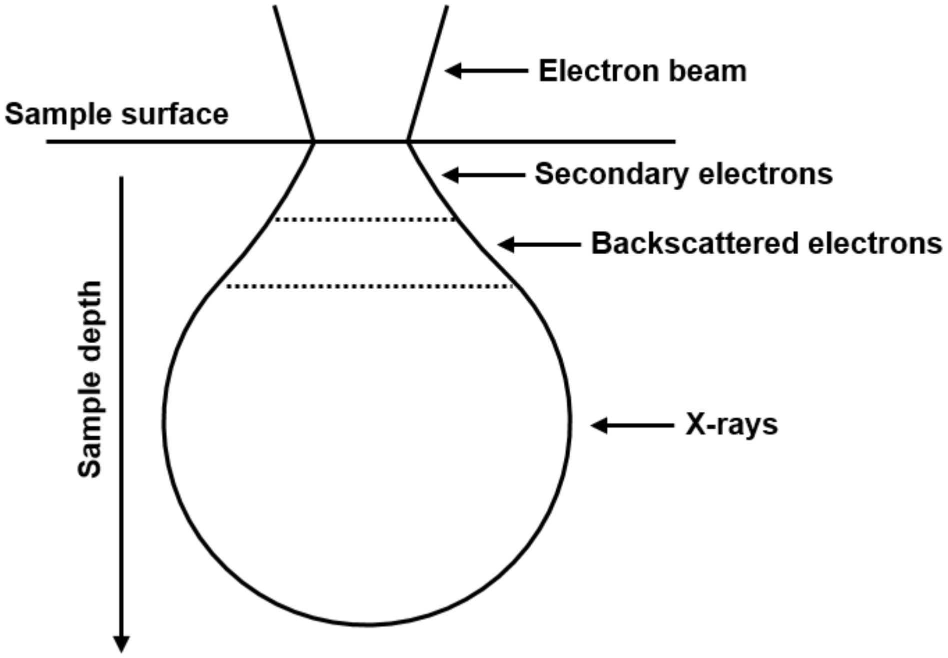

**Figure 1.34.** Schematic representation of the various regions within a sample from which secondary electrons, back-scattered electrons and X-rays originate during scanning electron microscopy.[210]

Like SEM, TEM uses a high-energy electron gun to generate a monochromatic beam of electrons. A condenser lens focuses this electron beam before it reaches the sample. An image is produced based on the electrons that are transmitted through the sample grid.[211]

A mean sphere-equivalent particle diameter and a corresponding standard deviation can be calculated using image analysis software (e.g. ImageJ) to examine high resolution images.[212] Non-spherical particle morphologies can also be readily identified.[213] However, if statistically meaningful particle size distributions are required then electron microscopy is certainly more labour-intensive than either DLS or laser diffraction. Moreover, it is often susceptible to drying artifacts. Furthermore, typically only hundreds of particles are analyzed by electron microscopy, which may be not truly representative of the actual sample. In contrast, light scattering techniques report mean diameters that are averaged over (at least) tens of thousands of particles.[207,214]

## 1.11 Thesis Outline

This Thesis focuses on the synthesis of various types of sterically-stabilized diblock copolymer nanoparticles *via* RAFT aqueous solution polymerization, RAFT aqueous emulsion polymerization and RAFT aqueous dispersion polymerization. These nanoparticles are evaluated as dispersants for the preparation of aqueous suspension concentrates (SCs) comprising various agrochemical actives. In Chapter 2, the polymerization of MMA using a PGMA precursor is examined. Some unexpected constraints in terms of colloidal stability are observed when using this non-ionic steric stabilizer block. As a result, an anionic PMAA precursor and a cationic PMETAC precursor are also investigated. Furthermore, RAFT end-group removal *via* visible light irradiation using a blue LED source is also briefly explored. In Chapter 3, both PGMA-PMMA and PGMA-PTFEMA diblock copolymer nanoparticles are tested as dispersants for SC formulations based on azoxystrobin, a widely-used fungicide. Ball milling led to a substantial reduction in size and produced azoxystrobin microparticles of around 2 µm diameter as judged by laser diffraction and optical microscopy studies. Evidence for nanoparticle adsorption at the surface of these azoxystrobin microparticles was obtained by TEM, SEM, solution densitometry, aqueous electrophoresis and X-ray photoelectron spectroscopy (XPS). In Chapter 4, azoxystrobin is ball milled in the presence of a wide range of alternative diblock copolymer nanoparticles. The effect of varying the nature of the stabilizer block, the core-forming block, the mean nanoparticle diameter, and the glass transition temperature of the core-forming block are investigated. Moreover, the performance of core cross-linked nanoparticles is compared to that of the corresponding linear nanoparticles. Finally, PGMA-PMMA nanoparticles were evaluated as dispersants for five other common agrochemical actives. In Chapter 5, a similar ball milling technique is used to prepare SCs comprising polyaromatic hydrocarbon (PAH) microparticles. Macroscopic crystals of the simplest PAH, anthracene, were ball milled and the resulting microparticles were coated with polypyrrole (PPy), an air-stable conducting polymer. Laser diffraction, optical microscopy, IR spectroscopy, Raman microscopy, SEM and XPS were used to characterize the PPy-coated anthracene microparticles and the corresponding uncoated precursor microparticles. The PPy-coated microparticles are expected to serve as useful synthetic mimics for PAH-rich cosmic dust. In principle, the electrical conductive PPy coating should enable their efficient acceleration up to hypervelocities using a van de Graaff accelerator for impact ionization experiments.

## 1.12 References

(1) Odian, G. *Principles of Polymerization*, 4th ed.; Wiley: New York, 2004.

(2) Staudinger, H. Über Polymerisation. *Berichte der Dtsch. Chem. Gesellschaft (A B Ser.* **1920**, *53*, 1073–1085.

(3) Chanda, M.; Roy, S. K. *Industrial Polymers, Specialty Polymers, and Their Applications*; CRC Press: Boca Raton, 2008.

(4) Carothers, W. H. Studies on Polymerization and Ring Formation. An Introduction to the General Theory of Condensation Polymers. *J. Am. Chem. Soc.* **1929**, *51*, 2548–2559.

(5) Flory, P. J. *Principles of Polymer Chemistry*; Cornell University Press: New York, 1953.

(6) Ebewele, R. O. *Polymer Science and Technology*; CRC Press: Boca Raton, 2000.

(7) Hiemenz, P. C., Lodge, T. P. *Polymer Chemistry*, 2nd ed.; CRC Press: Boca Raton, 2007.

(8) Matyjaszewski, K.; Gnanou, Y.; Leibler, L. *Macromolecular Engineering: Precise Synthesis, Materials Properties, Applications*; Wiley-VCH: Weinheim, 2011.

(9) Matyjaszewski K.; Davis T. P. *Handbook of Radical Polymerization*; John Wiley & Sons: Hoboken, 2002.

(10) Cowie, J. M. G.; Arrighi, V. *Polymers: Chemistry and Physics of Modern Materials*, 3rd ed.; CRC Press: New York, 2007.

(11) Ravve, A. *Principles of Polymer Chemistry*, 3rd ed.; Springer: New York, 2012.

(12) Moad, G.; Solomon, D. H. *The Chemistry of Radical Polymerization*; Elsevier: Oxford, 2005.

(13) Szwarc, M.; Levy, M.; Milkovich, R. Polymerization Initiated by Electron Transfer to Monomer. A New Method of Formation of Block Polymers. *J. Am. Chem. Soc.* **1956**, *78*, 2656–2657.

(14) Szwarc, M. "Living" Polymers. *Nature* **1956**, *178*, 1168–1169.

(15) Jenkins, A. D.; Jones, R. G.; Moad, G. Terminology for Reversible-Deactivation Radical Polymerization Previously Called "Controlled" Radical or "Living" Radical Polymerization (IUPAC Recommendations 2010). *Pure Appl. Chem.* **2009**, *82*, 483–491.

(16) Hadjichristidis, N.; Iatrou, H.; Pitsikalis, M.; Mays, J. Macromolecular Architectures by Living and Controlled/Living Polymerizations. *Prog. Polym. Sci.* **2006**, *31*, 1068–1132.

(17) Matyjaszewski, K. Architecturally Complex Polymers with Controlled Heterogeneity. *Science* **2011**, *333*, 1104–1105.

(18) Goto, A.; Fukuda, T. Kinetics of Living Radical Polymerization. *Prog. Polym. Sci.* **2004**, *29*, 329–385.

(19) Braunecker, W. A.; Matyjaszewski, K. Controlled/Living Radical Polymerization: Features, Developments, and Perspectives. *Prog. Polym. Sci.* **2007**, *32*, 93–146.

(20) Wang, J. S.; Matyjaszewski, K. Controlled/"Living" Radical Polymerization. Atom

Transfer Radical Polymerization in the Presence of Transition-Metal Complexes. *J. Am. Chem. Soc.* **1995**, *117*, 5614–5615.

(21) Kato, M.; Kamigaito, M.; Sawamoto, M.; Higashimura, T. Polymerization of Methyl Methacrylate with the Carbon Tetrachloride/Dichlorotris-(Triphenylphosphine)Ruthenium(II)/ Methylaluminum Bis(2,6-Di-Tert-Butylphenoxide) Initiating System: Possibility of Living Radical Polymerization. *Macromolecules* **1995**, *28*, 1721–1723.

(22) Hawker, C. J.; Bosman, A. W.; Harth, E. New Polymer Synthesis by Nitroxide Mediated Living Radical Polymerizations. *Chem. Rev.* **2001**, *101*, 3661–3688.

(23) Moad, G.; Rizzardo, E.; Thang, S. H. Living Radical Polymerization by the RAFT Process. *Aust. J. Chem.* **2005**, *58*, 379–410.

(24) Fischer, H. The Persistent Radical Effect: A Principle for Selective Radical Reactions and Living Radical Polymerizations. *Chem. Rev.* **2001**, *101*, 3581–3610.

(25) Moad, G.; Rizzardo, E.; Thang, S. H. Toward Living Radical Polymerization. *Acc. Chem. Res.* **2008**, *41*, 1133–1142.

(26) Chiefari, J.; Chong, Y. K. B.; Ercole, F.; Krstina, J.; Jeffery, J.; Le, T. P. T.; Mayadunne, R. T. A.; Meijs, G. F.; Moad, C. L.; Moad, G.; Rizzardo, E.; Thang, S. H. Living Free-Radical Polymerization by Reversible Addition-Fragmentation Chain Transfer: The RAFT Process. *Macromolecules* **1998**, *31*, 5559–5562.

(27) Canning, S. L.; Smith, G. N.; Armes, S. P. A Critical Appraisal of RAFT-Mediated Polymerization-Induced Self-Assembly. *Macromolecules* **2016**, *49*, 1985–2001.

(28) Perrier, S. 50th Anniversary Perspective: RAFT Polymerization - A User Guide. *Macromolecules* **2017**, *50*, 7433–7447.

(29) Rizzardo, E.; Chiefari, J.; Chong, B. Y. K.; Ercole, F.; Krstina, J.; Jeffrey, J.; Le, T. P. T.; Mayadunne, R. T. A.; Meijs, G. F.; Moad, C. L.; Moad, G.; Thang, S. H. Tailored Polymers by Free Radical Processes. *Macromol. Symp.* **1999**, *143*, 291–307.

(30) Grubbs, R. B. Nitroxide-Mediated Radical Polymerization: Limitations and Versatility. *Polym. Rev.* **2011**, *51*, 104–137.

(31) Matyjaszewski, K. Comparison and Classification of Controlled/Living Radical Polymerizations. *ACS Symp. Ser.* **2000**, *768*, 2–26.

(32) Moad, G.; Rizzardo, E.; Thang, S. H. Living Radical Polymerization by the RAFT Process - A First Update. *Aust. J. Chem.* **2006**, *59*, 669–692.

(33) Moad, G.; Rizzardo, E.; Thang, S. H. Living Radical Polymerization by the RAFT Process – A Second Update. *Aust. J. Chem* **2009**, *62*, 1402–1472.

(34) Moad, G.; Rizzardo, E.; Thang, S. H. Living Radical Polymerization by the RAFT Process - A Third Update. *Aust. J. Chem.* **2012**, *65*, 985–1076.

(35) Blanazs, A.; Ryan, A. J.; Armes, S. P. Predictive Phase Diagrams for RAFT Aqueous

Dispersion Polymerization: Effect of Block Copolymer Composition, Molecular Weight, and Copolymer Concentration. *Macromolecules* **2012**, *45*, 5099–5107.

(36) Lovett, J. R.; Warren, N. J.; Ratcliffe, L. P. D.; Kocik, M. K.; Armes, S. P. pH-Responsive Non-Ionic Diblock Copolymers: Ionization of Carboxylic Acid End-Groups Induces an Order-Order Morphological Transition. *Angew. Chemie - Int. Ed.* **2015**, *54*, 1279–1283.

(37) Deane, O. J.; Musa, O. M.; Fernyhough, A.; Armes, S. P. Synthesis and Characterization of Waterborne Pyrrolidone- Functional Diblock Copolymer Nanoparticles Prepared via Surfactant-Free RAFT Emulsion Polymerization. *Macromolecules* **2020**, *53*, 1422–1434.

(38) Byard, S. J.; Williams, M.; McKenzie, B. E.; Blanazs, A.; Armes, S. P. Preparation and Cross-Linking of All-Acrylamide Diblock Copolymer Nano-Objects via Polymerization-Induced Self-Assembly in Aqueous Solution. *Macromolecules* **2017**, *50*, 1482–1493.

(39) Chong, B.; Moad, G.; Rizzardo, E.; Skidmore, M.; Thang, S. H. Thermolysis of RAFT-Synthesized Poly (Methyl Methacrylate). *Aust. J. Chem* **2006**, *59*, 755–762.

(40) Willcock, H.; O'Reilly, R. K. End Group Removal and Modification of RAFT Polymers. *Polym. Chem.* **2010**, *1*, 149–157.

(41) Moad, G.; Rizzardo, E.; Thang, S. H. End-Functional Polymers, Thiocarbonylthio Group Removal/Transformation and Reversible Addition-Fragmentation-Chain Transfer (RAFT) Polymerization. *Polym. Int.* **2011**, *60*, 9–25.

(42) Jesson, C. P.; Pearce, C. M.; Simon, H.; Werner, A.; Cunningham, V. J.; Lovett, J. R.; Smallridge, M. J.; Warren, N. J.; Armes, S. P. $H_2O_2$ Enables Convenient Removal of RAFT End-Groups from Block Copolymer Nano-Objects Prepared via Polymerization-Induced Self- Assembly in Water. *Macromolecules* **2017**, *50*, 182–191.

(43) Arshady, R. Suspension, Emulsion, and Dispersion Polymerization: A Methodological Survey. *Colloid Polym. Sci.* **1992**, *270*, 717–732.

(44) Baines, F. L.; Dionisio, S.; Billingham, N. C.; Armes, S. P. Use of Block Copolymer Stabilizers for the Dispersion Polymerization of Styrene in Alcoholic Media. *Macromolecules* **1996**, *29*, 3096–3102.

(45) Richez, A. P.; Yow, H. N.; Biggs, S.; Cayre, O. J. Dispersion Polymerization in Non-Polar Solvent: Evolution toward Emerging Applications. *Prog. Polym. Sci.* **2013**, *38*, 897–931.

(46) Dawkins, J. V.; Taylor, G. Nonaqueous Poly(Methyl Methacrylate) Dispersions: Radical Dispersion Polymerization in the Presence of AB Block Copolymers of Polystyrene and Poly(Dimethyl Siloxane). *Polymer* **1979**, *20*, 599–604.

(47) Zong, M.; Thurecht, K. J.; Howdle, S. M. Dispersion Polymerisation in Supercritical $CO_2$ Using Macro-RAFT Agents. *Chem. Commun.* **2008**, 5942–5944.

(48) DeSimone, J. M.; Guan, Z.; Elsbernd, C. S. Synthesis of Fluoropolymers in Supercritical Carbon Dioxide. *Science* **1992**, *257*, 945–947.

(49) Kawaguchi, S.; Ito, K. Dispersion Polymerization. *Adv. Polym. Sci.* **2005**, *175*, 299–328.

(50) Shen, S.; Sudol, E. D.; El-Aasser, M. S. Dispersion Polymerization of Methyl Methacrylate: Mechanism of Particle Formation. *J. Polym. Sci. Part A Polym. Chem.* **1994**, *32*, 1087–1100.

(51) Armes, S. P.; Vincent, B. Dispersions of Electrically Conducting Polypyrrole Particles in Aqueous Media. *J. Chem. Soc. Chem. Commun.* **1987**, 288–290.

(52) Armes, S. P.; Aldissi, M.; Idzorek, G. C.; Keaton, P. W.; Rowton, L. J.; Stradling, G. L.; Collopy, M. T.; McColl, D. B. Particle Size Distributions of Polypyrrole Colloids. *J. Colloid Interface Sci.* **1991**, *141*, 119–126.

(53) DeArmitt, C.; Armes, S. P. Colloidal Dispersions of Surfactant-Stabilized Polypyrrole Particles. *Langmuir* **1993**, *9*, 652–654.

(54) Ali, A. M. I.; Pareek, P.; Sewell, L.; Schmid, A.; Fujii, S.; Armes, S. P.; Shirley, I. M. Synthesis of Poly(2-Hydroxypropyl Methacrylate) Latex Particles via Aqueous Dispersion Polymerization. *Soft Matter* **2007**, *3*, 1003–1013.

(55) Lovell, P. A.; El-Aasser, M. S. *Emulsion Polymerization and Emulsion Polymers*; Wiley, Chichester, 1997.

(56) Smith, W. V.; Ewart, R. H. Kinetics of Emulsion Polymerization. *J. Chem. Phys.* **1948**, *16*, 592–599.

(57) Harkins, W. D. A General Theory of the Mechanism of Emulsion Polymerization. *J. Am. Chem. Soc.* **1947**, *69*, 1428–1444.

(58) Chern, C. S. Emulsion Polymerization Mechanisms and Kinetics. *Prog. Polym. Sci.* **2006**, *31*, 443–486.

(59) Gilbert, R. G. *Emulsion Polymerization: A Mechanistic Approach*; Academic Press: London, 1995.

(60) Priest, W. J. Particle Growth in the Aqueous Polymerization of Vinyl Acetate. *J. Phys. Chem.* **1952**, *56*, 1077–1082.

(61) Ottewill, R. H.; Shaw, J. N. Studies on the Preparation and Characterization of Monodisperse Polystyrene Latices - I. Preparation. *Kolloid-Zeitschrift und Zeitschrift für Polym.* **1967**, *215*, 161–166.

(62) Goodwin, J. W.; Hearn, J.; Ho, C. C.; Ottewill, R. H. Studies on the Preparation and Characterisation of Monodisperse Polystyrene Laticee - III. Preparation without Added Surface Active Agents. *Colloid Polym. Sci.* **1974**, *252*, 464–471.

(63) Goodwin, J. W.; Hearn, J.; Ho, C. C.; Ottewill, R. H. The Preparation and Characterisation of Polymer Latices Formed in the Absence of Surface Active Agents. *Br Polym J* **1973**, *5*, 347–362.

(64) Whitesides, G. M.; Grzybowski, B. Self-Assembly at All Scales. *Science* **2002**, *295*, 2418–2421.

(65) Marsh, D. Thermodynamics of Phospholipid Self-Assembly. *Biophys. J.* **2012**, *102*, 1079–

1087.

(66) Reid, D. S.; Levine, H. Beyond Water Activity: Recent Advances Based on an Alternative Approach to the Assessment of Food Quality and Safety. *Crit. Rev. Food Sci. Nutr.* **1991**, *30*, 115–360.

(67) Tanford, C. The Hydrophobic Effect and the Organization of Living Matter. *Science* **1978**, *200*, 1012–1018.

(68) Chandler, D. Interfaces and the Driving Force of Hydrophobic Assembly. *Nature* **2005**, *437*, 640–647.

(69) Puvvada, S.; Blankschtein, D. Molecular-Thermodynamic Approach to Predict Micellization, Phase Behavior and Phase Separation of Micellar Solutions. I. Application to Nonionic Surfactants. *J. Chem. Phys.* **1990**, *92*, 2710–3724.

(70) Lombardo, D.; Kiselev, M. A.; Magazù, S.; Calandra, P. Amphiphiles Self-Assembly: Basic Concepts and Future Perspectives of Supramolecular Approaches. *Adv. Condens. Matter Phys.* **2015**, *11*, 1–22.

(71) Israelachvili, J. N.; Mitchell, D. J.; Ninham, B. W. Theory of Self-Assembly of Hydrocarbon Amphiphiles into Micelles and Bilayers. *J. Chem. Soc. Faraday Trans. 2 Mol. Chem. Phys.* **1976**, *72*, 1525–1568.

(72) Israelachvili, J. *Intermolecular and Surface Forces*; Elsevier: Amsterdam, 2011.

(73) Swann, J. M. G.; Topham, P. D. Design and Application of Nanoscale Actuators Using Block-Copolymers. *Polymer* **2010**, *2*, 454–469.

(74) Bates, F. S. Polymer-Polymer Phase Behavior. *Science* **1991**, *4996*, 898–905.

(75) Mai, Y.; Eisenberg, A. Self-Assembly of Block Copolymers. *Chem. Soc. Rev.* **2012**, *41*, 5969–5985.

(76) Bates, F. S.; Fredrickson, G. H. Block Copolymers-Designer Soft Materials. *Phys. Today* **1999**, *52*, 32–38.

(77) Leibler, L. Theory of Microphase Separation in Block Copolymers. *Macromolecules* **1980**, *13*, 1602–1617.

(78) Vavasour, J. D.; Whitmore, M. D. Self-Consistent Mean Field Theory of the Microphases of Diblock Copolymers. *Macromolecules* **1992**, *25*, 5477–5486.

(79) Zhang, L.; Eisenberg, A. Multiple Morphologies of “Crew-Cut” Aggregates of Polystyrene-b-Poly(Acrylic Acid) Block Copolymers. *Science* **1995**, *268*, 1728–1731.

(80) Yu, K.; Eisenberg, A. Multiple Morphologies in Aqueous Solutions of Aggregates of Polystyrene-Block-Poly(Ethylene Oxide) Diblock Copolymers. *Macromolecules* **1996**, *29*, 6359–6361.

(81) Won, Y. Y.; Ted Davis, H.; Bates, F. S. Giant Wormlike Rubber Micelles. *Science* **1999**, *283*, 960–963.

(82) Paine, A. J.; Deslandes, Y.; Gerroir, P.; Henrissat, B. Dispersion Polymerization of

Styrene in Polar Solvents. II. Visualization of Surface Layers of Steric Stabilizer on Dispersion-Polymerized and Precipitated Polystyrene Latex Particles by Transmission Electron Microscopy. *J. Colloid Interface Sci.* **1990**, *138*, 170–181.

(83) Bellomo, E. G.; Wyrsta, M. D.; Pakstis, L.; Pochan, D. J.; Deming, T. J. Stimuli-Responsive Polypeptide Vesicles by Conformation-Specific Assembly. *Nat. Mater.* **2004**, *3*, 244–248.

(84) Rieger, J.; Grazon, C.; Charleux, B.; Alaimo, D.; Jérôme, C. Pegylated Thermally Responsive Block Copolymer Micelles and Nanogels via In Situ RAFT Aqueous Dispersion Polymerization. *J. Polym. Sci. Part A Polym. Chem.* **2009**, *47*, 2373–2390.

(85) Almog, Y.; Reich, S.; Levy, M. Monodisperse Polymeric Spheres in the Micron Size Range by Single Step Process. *Br. Polym. J.* **1982**, *14*, 131–136.

(86) Charleux, B.; Delaittre, G.; Rieger, J.; D'Agosto, F. Polymerization-Induced Self-Assembly: From Soluble Macromolecules to Block Copolymer Nano-Objects in One Step. *Macromolecules* **2012**, *45*, 6753–6765.

(87) Warren, N. J.; Armes, S. P. Polymerization-Induced Self-Assembly of Block Copolymer Nano-Objects via RAFT Aqueous Dispersion Polymerization. *J. Am. Chem. Soc.* **2014**, *136*, 10174–10185.

(88) Derry, M. J.; Fielding, L. A.; Armes, S. P. Polymerization-Induced Self-Assembly of Block Copolymer Nanoparticles via RAFT Non-Aqueous Dispersion Polymerization. *Prog. Polym. Sci.* **2016**, *52*, 1–18.

(89) Cunningham, V. J.; Alswieleh, A. M.; Thompson, K. L.; Williams, M.; Leggett, G. J.; Armes, S. P.; Musa, O. M. Poly(Glycerol Monomethacrylate)-Poly(Benzyl Methacrylate) Diblock Copolymer Nanoparticles via RAFT Emulsion Polymerization: Synthesis, Characterization, and Interfacial Activity. *Macromolecules* **2014**, *47*, 5613–5623.

(90) Rieger, J.; Zhang, W.; Stoffelbach, F.; Charleux, B. Surfactant-Free RAFT Emulsion Polymerization Using Poly(N,N -Dimethylacrylamide) Trithiocarbonate Macromolecular Chain Transfer Agents. *Macromolecules* **2010**, *43*, 6302–6310.

(91) Derry, M. J.; Fielding, L. A.; Armes, S. P. Industrially-Relevant Polymerization-Induced Self-Assembly Formulations in Non-Polar Solvents: RAFT Dispersion Polymerization of Benzyl Methacrylate. *Polym. Chem.* **2015**, *6*, 3054–3062.

(92) Semsarilar, M.; Jones, E. R.; Blanazs, A.; Armes, S. P. Efficient Synthesis of Sterically-Stabilized Nano-Objects via RAFT Dispersion Polymerization of Benzyl Methacrylate in Alcoholic Media. *Adv. Mater.* **2012**, *24*, 3378–3382.

(93) Jones, E. R.; Semsarilar, M.; Blanazs, A.; Armes, S. P. Efficient Synthesis of Amine-Functional Diblock Copolymer Nanoparticles via RAFT Dispersion Polymerization of Benzyl Methacrylate in Alcoholic Media. *Macromolecules* **2012**, *45*, 5091–5098.

(94) Canning, S. L.; Cunningham, V. J.; Ratcliffe, L. P. D.; Armes, S. P. Phenyl Acrylate Is a

Versatile Monomer for the Synthesis of Acrylic Diblock Copolymer Nano-Objects: Via Polymerization-Induced Self-Assembly. *Polym. Chem.* **2017**, *8*, 4811–4821.

(95) Fielding, L. A.; Derry, M. J.; Ladmiral, V.; Rosselgong, J.; Rodrigues, A. M.; Ratcliffe, L. P. D.; Sugihara, S.; Armes, S. P. RAFT Dispersion Polymerization in Non-Polar Solvents: Facile Production of Block Copolymer Spheres, Worms and Vesicles in n-Alkanes. *Chem. Sci.* **2013**, *4*, 2081–2087.

(96) Sugihara, S.; Blanazs, A.; Armes, S. P.; Ryan, A. J.; Lewis, A. L. Aqueous Dispersion Polymerization: A New Paradigm for in Situ Block Copolymer Self-Assembly in Concentrated Solution. *J. Am. Chem. Soc.* **2011**, *133*, 15707–15713.

(97) An, Z.; Shi, Q.; Tang, W.; Tsung, C. K.; Hawker, C. J.; Stucky, G. D. Facile RAFT Precipitation Polymerization for the Microwave-Assisted Synthesis of Well-Defined, Double Hydrophilic Block Copolymers and Nanostructured Hydrogels. *J. Am. Chem. Soc.* **2007**, *129*, 14493–14499.

(98) Yamauchi, H.; Maeda, Y. LCST and UCST Behavior of Poly(N-Isopropylacrylamide) in DMSO/Water Mixed Solvents Studied by IR and Micro-Raman Spectroscopy. *J. Phys. Chem. B* **2007**, *111*, 12964–12968.

(99) Li, Y.; Armes, S. P. RAFT Synthesis of Sterically Stabilized Methacrylic Nanolatexes and Vesicles by Aqueous Dispersion Polymerization. *Angew. Chemie - Int. Ed.* **2010**, *49*, 4042–4046.

(100) Blanazs, A.; Madsen, J.; Battaglia, G.; Ryan, A. J.; Armes, S. P. Mechanistic Insights for Block Copolymer Morphologies: How Do Worms Form Vesicles? *J. Am. Chem. Soc.* **2011**, *133*, 16581–16587.

(101) Warren, N. J.; Derry, M. J.; Mykhaylyk, O. O.; Lovett, J. R.; Ratcliffe, L. P. D.; Ladmiral, V.; Blanazs, A.; Fielding, L. A.; Armes, S. P. Critical Dependence of Molecular Weight on Thermoresponsive Behavior of Diblock Copolymer Worm Gels in Aqueous Solution. *Macromolecules* **2018**, *51*, 8357–8371.

(102) Lovett, J. R.; Derry, M. J.; Yang, P.; Hatton, F. L.; Warren, N. J.; Fowler, P. W.; Armes, S. P. Can Percolation Theory Explain the Gelation Behavior of Diblock Copolymer Worms? *Chem. Sci.* **2018**, *9*, 7138–7144.

(103) Blanazs, A.; Verber, R.; Mykhaylyk, O. O.; Ryan, A. J.; Heath, J. Z.; Douglas, C. W. I.; Armes, S. P. Sterilizable Gels from Thermoresponsive Block Copolymer Worms. *J. Am. Chem. Soc.* **2012**, *134*, 9741–9748.

(104) Mitchell, D. E.; Lovett, J. R.; Armes, S. P.; Gibson, M. I. Combining Biomimetic Block Copolymer Worms with an Ice-Inhibiting Polymer for the Solvent-Free Cryopreservation of Red Blood Cells. *Angew. Chemie - Int. Ed.* **2016**, *55*, 2801–2804.

(105) Canton, I.; Warren, N. J.; Chahal, A.; Amps, K.; Wood, A.; Weightman, R.; Wang, E.; Moore, H.; Armes, S. P. Mucin-Inspired Thermoresponsive Synthetic Hydrogels Induce

Stasis in Human Pluripotent Stem Cells and Human Embryos. *ACS Cent. Sci.* **2016**, *2*, 65–74.

(106) Thompson, K. L.; Mable, C. J.; Cockram, A.; Warren, N. J.; Cunningham, V. J.; Jones, E. R.; Verber, R.; Armes, S. P. Are Block Copolymer Worms More Effective Pickering Emulsifiers than Block Copolymer Spheres? *Soft Matter* **2014**, *10*, 8615–8626.

(107) Warren, N. J.; Mykhaylyk, O. O.; Mahmood, D.; Ryan, A. J.; Armes, S. P. RAFT Aqueous Dispersion Polymerization Yields Poly(Ethylene Glycol)-Based Diblock Copolymer Nano-Objects with Predictable Single Phase Morphologies. *J. Am. Chem. Soc.* **2014**, *136*, 1023–1033.

(108) Gibson, R. R.; Armes, S. P.; Musa, O. M.; Fernyhough, A. End-Group Ionisation Enables the Use of Poly(: N -(2-Methacryloyloxy)Ethyl Pyrrolidone) as an Electrosteric Stabiliser Block for Polymerisation-Induced Self-Assembly in Aqueous Media. *Polym. Chem.* **2019**, *10*, 1312–1323.

(109) Williams, M.; Penfold, N. J. W.; Lovett, J. R.; Warren, N. J.; Douglas, C. W. I.; Doroshenko, N.; Verstraete, P.; Smets, J.; Armes, S. P. Bespoke Cationic Nano-Objects: Via RAFT Aqueous Dispersion Polymerisation. *Polym. Chem.* **2016**, *7*, 3864–3873.

(110) North, S. M.; Armes, S. P. Aqueous Solution Behavior of Stimulus-Responsive Poly(Methacrylic Acid)-Poly(2-Hydroxypropyl Methacrylate) Diblock Copolymer Nanoparticles. *Polym. Chem.* **2020**, *11*, 2147–2156.

(111) Sugihara, S.; Ma'Radzi, A. H.; Ida, S.; Irie, S.; Kikukawa, T.; Maeda, Y. In Situ Nano-Objects via RAFT Aqueous Dispersion Polymerization of 2-Methoxyethyl Acrylate Using Poly(Ethylene Oxide) Macromolecular Chain Transfer Agent as Steric Stabilizer. *Polymer* **2015**, *76*, 17–24.

(112) Shen, W.; Chang, Y.; Liu, G.; Wang, H.; Cao, A.; An, Z. Biocompatible, Antifouling, and Thermosensitive Core-Shell Nanogels Synthesized by RAFT Aqueous Dispersion Polymerization. *Macromolecules* **2011**, *44*, 2524–2530.

(113) Byard, S. J.; O'Brien, C. T.; Derry, M. J.; Williams, M.; Mykhaylyk, O. O.; Blanazs, A.; Armes, S. P. Unique Aqueous Self-Assembly Behavior of a Thermoresponsive Diblock Copolymer. *Chem. Sci.* **2020**, *11*, 396–402.

(114) Deane, O. J.; Jennings, J.; Neal, T. J.; Musa, O. M.; Fernyhough, A.; Armes, S. P. Synthesis and Aqueous Solution Properties of Shape-Shifting Stimulus-Responsive Diblock Copolymer Nano-Objects. *Chem. Mater.* **2021**, *33*, 7767–7779.

(115) Cunningham, M. F. Living/Controlled Radical Polymerizations in Dispersed Phase Systems. *Prog. Polym. Sci.* **2002**, *27*, 1039–1067.

(116) Prescott, S. W.; Ballard, M. J.; Rizzardo, E.; Gilbert, R. G. Successful Use of RAFT Techniques in Seeded Emulsion Polymerization of Styrene: Living Character, RAFT Agent Transport, and Rate of Polymerization. *Macromolecules* **2002**, *35*, 5417–5425.

(117) Ferguson, C. J.; Hughes, R. J.; Pham, B. T. T.; Hawkett, B. S.; Gilbert, R. G.; Serelis, A. K.; Such, C. H. Effective Ab Initio Emulsion Polymerization under RAFT Control. *Macromolecules* **2002**, *35*, 9243–9245.

(118) Ferguson, C. J.; Hughes, R. J.; Nguyen, D.; Pham, B. T. T.; Gilbert, R. G.; Serelis, A. K.; Such, C. H.; Hawkett, B. S. Ab Initio Emulsion Polymerization by RAFT-Controlled Self-Assembly. *Macromolecules* **2005**, *38*, 2191–2204.

(119) Rieger, J.; Stoffelbach, F.; Bui, C.; Alaimo, D.; Jérôme, C.; Charleux, B. Amphiphilic Poly(Ethylene Oxide) Macromolecular RAFT Agent as a Stabilizer and Control Agent in Ab Initio Batch Emulsion Polymerization. *Macromolecules* **2008**, *41*, 4065–4068.

(120) Rieger, J.; Osterwinter, G.; Bui, C.; Charleux, B. Surfactant-Free Controlled/Living Radical Emulsion (Co) Polymerization of n -Butyl Acrylate and Methyl Methacrylate via RAFT Using Amphiphilic Poly (Ethylene Oxide)-Based Trithiocarbonate Chain Transfer Agents. *Macromolecules* **2009**, *42*, 5518–5525.

(121) Boissé, S.; Rieger, J.; Belal, K.; Di-Cicco, A.; Beaunier, P.; Li, M. H.; Charleux, B. Amphiphilic Block Copolymer Nano-Fibers via RAFT-Mediated Polymerization in Aqueous Dispersed System. *Chem. Commun.* **2010**, *46*, 1950–1952.

(122) Chaduc, I.; Crepet, A.; Boyron, O.; Charleux, B.; D'Agosto, F.; Lansalot, M. Effect of the pH on the Raft Polymerization of Acrylic Acid in Water. Application to the Synthesis of Poly(Acrylic Acid)-Stabilized Polystyrene Particles by RAFT Emulsion Polymerization. *Macromolecules* **2013**, *46*, 6013–6023.

(123) Chaduc, I.; Girod, M.; Antoine, R.; Charleux, B.; D'Agosto, F.; Lansalot, M. Batch Emulsion Polymerization Mediated by Poly(Methacrylic Acid) MacroRAFT Agents: One-Pot Synthesis of Self-Stabilized Particles. *Macromolecules* **2012**, *45*, 5881–5893.

(124) Manguian, M.; Save, M.; Charleux, B. Batch Emulsion Polymerization of Styrene Stabilized by a Hydrophilic Macro-RAFT Agenta. *Macromol. Rapid Commun.* **2006**, *27*, 399–404.

(125) Zhang, X.; Rieger, J.; Charleux, B. Effect of the Solvent Composition on the Morphology of Nano-Objects Synthesized via RAFT Polymerization of Benzyl Methacrylate in Dispersed Systems. *Polym. Chem.* **2012**, *3*, 1502–1509.

(126) Zhang, W.; D'Agosto, F.; Dugas, P. Y.; Rieger, J.; Charleux, B. RAFT-Mediated One-Pot Aqueous Emulsion Polymerization of Methyl Methacrylate in Presence of Poly(Methacrylic Acid-Co-Poly(Ethylene Oxide) Methacrylate) Trithiocarbonate Macromolecular Chain Transfer Agent. *Polymer* **2013**, *54*, 2011–2019.

(127) Boissé, S.; Rieger, J.; Pembouong, G.; Beaunier, P.; Charleux, B. Influence of the Stirring Speed and $CaCl_2$ Concentration on the Nano-object Morphologies Obtained via RAFT-mediated Aqueous Emulsion Polymerization in the Presence of a Water-soluble MacroRAFT Agent. *J. Polym. Sci. Part A Polym. Chem.* **2011**, *49*, 3346–3354.

(128) Truong, N. P.; Dussert, M. V.; Whittaker, M. R.; Quinn, J. F.; Davis, T. P. Rapid Synthesis of Ultrahigh Molecular Weight and Low Polydispersity Polystyrene Diblock Copolymers by RAFT-Mediated Emulsion Polymerization. *Polym. Chem.* **2015**, *6*, 3865–3874.

(129) Akpinar, B.; Fielding, L. A.; Cunningham, V. J.; Ning, Y.; Mykhaylyk, O. O.; Fowler, P. W.; Armes, S. P. Determining the Effective Density and Stabilizer Layer Thickness of Sterically Stabilized Nanoparticles. *Macromolecules* **2016**, *49*, 5160–5171.

(130) Jesson, C. P.; Cunningham, V. J.; Smallridge, M. J.; Armes, S. P. Synthesis of High Molecular Weight Poly(Glycerol Monomethacrylate) via RAFT Emulsion Polymerization of Isopropylideneglycerol Methacrylate. *Macromolecules* **2018**, *51*, 3221–3232.

(131) Hatton, F. L.; Lovett, J. R.; Armes, S. P. Synthesis of Well-Defined Epoxy-Functional Spherical Nanoparticles by RAFT Aqueous Emulsion Polymerization. *Polym. Chem.* **2017**, *8*, 4856–4868.

(132) Zhang, X.; Boissé, S.; Zhang, W.; Beaunier, P.; D'Agosto, F.; Rieger, J.; Charleux, B. Well-Defined Amphiphilic Block Copolymers and Nano-Objects Formed in Situ via RAFT-Mediated Aqueous Emulsion Polymerization. *Macromolecules* **2011**, *44*, 4149–4158.

(133) Zhang, W.; D'Agosto, F.; Boyron, O.; Rieger, J.; Charleux, B. Toward a Better Understanding of the Parameters That Lead to the Formation of Nonspherical Polystyrene Particles via RAFT-Mediated One-Pot Aqueous Emulsion Polymerization. *Macromolecules* **2012**, *45*, 4075–4084.

(134) Khor, S. Y.; Truong, N. P.; Quinn, J. F.; Whittaker, M. R.; Davis, T. P. Polymerization-Induced Self-Assembly: The Effect of End Group and Initiator Concentration on Morphology of Nanoparticles Prepared via RAFT Aqueous Emulsion Polymerization. *ACS Macro Lett.* **2017**, *6*, 1013–1019.

(135) Cockram, A. A.; Neal, T. J.; Derry, M. J.; Mykhaylyk, O. O.; Williams, N. S. J.; Murray, M. W.; Emmett, S. N.; Armes, S. P. Effect of Monomer Solubility on the Evolution of Copolymer Morphology during Polymerization-Induced Self-Assembly in Aqueous Solution. *Macromolecules* **2017**, *50*, 796–802.

(136) Hatton, F. L.; Park, A. M.; Zhang, Y.; Fuchs, G. D.; Ober, C. K.; Armes, S. P. Aqueous One-Pot Synthesis of Epoxy-Functional Diblock Copolymer Worms from a Single Monomer: New Anisotropic Scaffolds for Potential Charge Storage Applications. *Polym. Chem.* **2019**, *10*, 194–200.

(137) Brotherton, E. E.; Hatton, F. L.; Cockram, A. A.; Derry, M. J.; Czajka, A.; Cornel, E. J.; Topham, P. D.; Mykhaylyk, O. O.; Armes, S. P. In Situ Small-Angle X-Ray Scattering Studies during Reversible Addition-Fragmentation Chain Transfer Aqueous Emulsion Polymerization. *J. Am. Chem. Soc.* **2019**, *141*, 13664–13675.

(138) Tadros, T. F. *Colloids in Agrochemicals*; Wiley: Weinheim, 2011.

(139) Ridi, F.; Fratini, E.; Baglioni, P. Cement: A Two Thousand Year Old Nano-Colloid. *J. Colloid Interface Sci.* **2011**, *357*, 255–264.

(140) Fujitani, T. Stability of Pigment and Resin Dispersions in Waterborne Paint. *Prog. Org. Coatings* **1996**, *29*, 97–105.

(141) Rowland, B. Colloid Chemistry in Paper Making. *J. Phys. Chem.* **1937**, *41*, 997–1005.

(142) Beija, M.; Salvayre, R.; Lauth-de Viguerie, N.; Marty, J. D. Colloidal Systems for Drug Delivery: From Design to Therapy. *Trends Biotechnol.* **2012**, *30*, 485–496.

(143) Shaw, D. J. *Introduction to Colloid and Surface Chemistry*, 4th ed.; Elsevier: Oxford, 1992.

(144) Tadros, T. *General Principles of Colloid Stability and the Role of Surface Forces*; Wiley-VCH: Weinheim, 2010.

(145) Derjaguin, B.; Landau, L. Theory of the Stability of Strongly Charged Lyophobic Sols and of the Adhesion of Strongly Charged Particles in Solutions of Electrolytes. *Prog. Surf. Sci.* **1993**, *43*, 30–59.

(146) Verwey, E. J. W. Theory of the Stability of Lyophobic Colloids. *J. Phys. Colloid Chem.* **1947**, *51*, 631–636.

(147) Tadros, T. F. *Interfacial Phenomena and Colloid Stability: Basic Principles*; De Gruyter: Berlin, 2015.

(148) Morgan, L. J. Polymeric Stabilization of Colloidal Dispersions. *Colloids and Surfaces* **1985**, *15*, 356–357.

(149) Kostansek, E. Using Dispersion/Flocculation Phase Diagrams to Visualize Interactions of Associative Polymers, Latexes, and Surfactants. *J. Coatings Technol.* **2003**, *75*, 1–8.

(150) Vincent, B. Weak, Reversible Flocculation Phenomena in Sterically-Stabilised Dispersions. *Croat. Chem. Acta* **1983**, *56*, 623–631.

(151) Ruehrwein, R. A.; Ward, D. W. Mechanism of Clay Aggregation by Polyelectrolytes. *Soil Sci.* **1952**, *73*, 485–492.

(152) Asakura, S.; Oosawa, F. Interaction between Particles Suspended in Solutions of Macromolecules. *J. Polym. Sci.* **1958**, *33*, 183–192.

(153) Feigin, R. I.; Napper, D. H. Depletion Stabilization and Depletion Flocculation. *J. Colloid Interface Sci.* **1980**, *75*, 525–541.

(154) Kim, S.; Hyun, K.; Moon, J. Y.; Clasen, C.; Ahn, K. H. Depletion Stabilization in Nanoparticle-Polymer Suspensions: Multi-Length-Scale Analysis of Microstructure. *Langmuir* **2015**, *31*, 1892–1900.

(155) Zhang, X.; Servos, M. R.; Liu, J. Ultrahigh Nanoparticle Stability against Salt, pH, and Solvent with Retained Surface Accessibility via Depletion Stabilization. *J. Am. Chem. Soc.* **2012**, *134*, 9910–9913.

(156) Ogden, A. L.; Lewis, J. A. Effect of Nonadsorbed Polymer on the Stability of Weakly

Flocculated Suspensions. *Langmuir* **1996**, *12*, 3413–3424.

(157) Liang, W.; Tadros, T. H. F.; Luckham, P. F. Flocculation of Sterically Stabilized Polystyrene Latex Particles by Adsorbing and Nonadsorbing Poly(Acrylic Acid). *Langmuir* **1994**, *10*, 441–446.

(158) Al-Ghouti, M. A.; Da'ana, D. A. Guidelines for the Use and Interpretation of Adsorption Isotherm Models: A Review. *J. Hazard. Mater.* **2020**, *393*, 1–22.

(159) Langmuir, I. The Constitution and Fundamental Properties of Solids and Liquids. Part I. Solids. *J. Am. Chem. Soc.* **1916**, *38*, 2221–2295.

(160) Freundlich, H. Uber Die Adsorption in Losungen. *Zeitschrift für Phys. Chemie* **1906**, *57*, 385–490.

(161) Brunauer, S.; Emmett, P. H.; Teller, E. Adsorption of Gases in Multimolecular Layers. *J. Am. Chem. Soc.* **1938**, *60*, 309–319.

(162) Cohen Stuart, M. A.; Cosgrove, T.; Vincent, B. Experimental Aspects of Polymer Adsorption at Solid/Solution Interfaces. *Adv. Colloid Interface Sci.* **1985**, *24*, 143–239.

(163) Yasin, S.; Luckham, P. F. Investigating the Effectiveness of PEO/PPO Based Copolymers as Dispersing Agents for Graphitic Carbon Black Aqueous Dispersions. *Colloids Surfaces A Physicochem. Eng. Asp.* **2012**, *404*, 25–35.

(164) Growney, D. J.; Mykhaylyk, O. O.; Derouineau, T.; Fielding, L. A.; Smith, A. J.; Aragrag, N.; Lamb, G. D.; Armes, S. P. Star Diblock Copolymer Concentration Dictates the Degree of Dispersion of Carbon Black Particles in Nonpolar Media: Bridging Flocculation versus Steric Stabilization. *Macromolecules* **2015**, *48*, 3691–3704.

(165) Hitchcock, J. P.; Tasker, A. L.; Stark, K.; Leeson, A.; Baxter, E. A.; Biggs, S.; Cayre, O. J. Adsorption of Catalytic Nanoparticles onto Polymer Substrates for Controlled Deposition of Microcapsule Metal Shells. *Langmuir* **2018**, *34*, 1473–1480.

(166) Park, J. J.; De Paoli Lacerda, S. H.; Stanley, S. K.; Vogel, B. M.; Kim, S.; Douglas, J. F.; Raghavan, D.; Karim, A. Langmuir Adsorption Study of the Interaction of CdSe/ZnS Quantum Dots with Model Substrates: Influence of Substrate Surface Chemistry and pH. *Langmuir* **2009**, *25*, 443–450.

(167) Rudrake, A.; Karan, K.; Horton, J. H. A Combined QCM and XPS Investigation of Asphaltene Adsorption on Metal Surfaces. *J. Colloid Interface Sci.* **2009**, *332*, 22–31.

(168) Giles, C. H.; Smith, D.; Huitson, A. A General Treatment and Classification of the Solute Adsorption Isotherm. I. Theoretical. *J. Colloid Interface Sci.* **1974**, *47*, 755–765.

(169) North, S. M.; Jones, E. R.; Smith, G. N.; Mykhaylyk, O. O.; Annable, T.; Armes, S. P. Adsorption of Small Cationic Nanoparticles onto Large Anionic Particles from Aqueous Solution: A Model System for Understanding Pigment Dispersion and the Problem of Effective Particle Density. *Langmuir* **2017**, *33*, 1275–1284.

(170) Thies, C. The Adsorption of Polystyrene-Poly (Methyl Methacrylate) Mixtures at a Solid-

Liquid Interface. *J. Phys. Chem.* **1966**, *70*, 247–257.

(171) Zhang, Q.; Thompson, M. S.; Carmichael-Baranauskas, A. Y.; Caba, B. L.; Zalich, M. A.; Lin, Y. N.; Mefford, O. T.; Davis, R. M.; Riffle, J. S. Aqueous Dispersions of Magnetite Nanoparticles Complexed with Copolyether Dispersants: Experiments and Theory. *Langmuir* **2007**, *23*, 6927–6936.

(172) Loos, M. R.; Yang, J.; Feke, D. L.; Manas-Zloczower, I. Effect of Block-Copolymer Dispersants on Properties of Carbon Nanotube/Epoxy Systems. *Compos. Sci. Technol.* **2012**, *72*, 482–488.

(173) Trojer, M. A.; Holmberg, K.; Nydén, M. The Importance of Proper Anchoring of an Amphiphilic Dispersant for Colloidal Stability. *Langmuir* **2012**, *28*, 4047–4050.

(174) Bishop, J. F.; Mourey, T. H.; Texter, J. Adsorption of Triblock Copolymers on Nanoparticulate Pharmaceutical Imaging Agents. *ACS Symp. Ser.* **1996**, *615*, 205–216.

(175) Tadros, T. F. Disperse Systems in Pesticidal Formulations. *Adv. Colloid Interface Sci.* **1990**, *32*, 205–234.

(176) Auschra, C.; Eckstein, E.; Mühlebach, A.; Zink, M. O.; Rime, F. Design of New Pigment Dispersants by Controlled Radical Polymerization. *Prog. Org. Coatings* **2002**, *45*, 83–93.

(177) Creutz, S.; Jérôme, R.; Kaptijn, G. M. P.; Van Der Werf, A. W.; Akkerman, J. M. Design of Polymeric Dispersants for Waterborne Coatings. *J. Coatings Technol.* **1998**, *70*, 41–46.

(178) Saindane, P.; Jagtap, R. N. RAFT Copolymerization of Amphiphilic Poly (Ethyl Acrylate-b-Acrylicacid) as Wetting and Dispersing Agents for Water Borne Coating. *Prog. Org. Coatings* **2015**, *79*, 106–114.

(179) Ma, S.; Rodriguez-Parada, J. Block Copolymers of Oxazolines and Oxazines as Pigment Dispersants and Their Use in Ink Jet Inks. *US Pat. 5,854,331* **1998**.

(180) Duivenvoorde, F. L.; Van Nostrum, C. F.; Van Der Linde, R. The Pigmentation of Powder Coatings with the Use of Block Copolymer Dispersants. *Prog. Org. Coatings* **1999**, *36*, 225–230.

(181) Duivenvoorde, F. L.; Van Nostrum, C. F.; Laven, J.; Van Der Linde, R. Improving Pigment Dispersing in Powder Coatings with Block Copolymer Dispersants. *J. Coatings Technol.* **2000**, *72*, 145–152.

(182) Wijting, W. K.; Laven, J.; van Benthem, R. A. T. M.; de With, G. Adsorption of Ethoxylated Styrene Oxide and Polyacrylic Acid and Mixtures There of on Organic Pigment. *J. Colloid Interface Sci.* **2008**, *327*, 1–8.

(183) North, S. M.; Armes, S. P. Aqueous One-Pot Synthesis of Well-Defined Zwitterionic Diblock Copolymers by RAFT Polymerization: An Efficient and Environmentally-Friendly Route to a Useful Dispersant for Aqueous Pigments. *Green Chem.* **2021**, *23*, 1248–1258.

(184) Lin, Y.; Alexandridis, P. Temperature-Dependent Adsorption of Pluronic F127 Block

Copolymers onto Carbon Black Particles Dispersed in Aqueous Media. *J. Phys. Chem. B* **2002**, *106*, 10834–10844.

(185) Sarkar, B.; Venugopal, V.; Tsianou, M.; Alexandridis, P. Adsorption of Pluronic Block Copolymers on Silica Nanoparticles. *Colloids Surfaces A Physicochem. Eng. Asp.* **2013**, *422*, 155–164.

(186) Fernandes, R. M. F.; Dai, J.; Regev, O.; Marques, E. F.; Furó, I. Block Copolymers as Dispersants for Single-Walled Carbon Nanotubes: Modes of Surface Attachment and Role of Block Polydispersity. *Langmuir* **2018**, *34*, 13672–13679.

(187) Sparks, T. C.; Lorsbach, B. A. Perspectives on the Agrochemical Industry and Agrochemical Discovery. *Pest Manag. Sci.* **2017**, *73*, 672–677.

(188) Aktar, W.; Sengupta, D.; Chowdhury, A. Impact of Pesticides Use in Agriculture: Their Benefits and Hazards. *Interdiscip. Toxicol.* **2009**, *2*, 1–12.

(189) Tadros, T. F. Physical Stability of Suspension Concentrates. *Adv. Colloid Interface Sci.* **1980**, *12*, 141–261.

(190) Knowles, A. Recent Developments of Safer Formulations of Agrochemicals. *Environmentalist* **2008**, *28*, 35–44.

(191) Luckham, P. F. The Physical Stability of Suspension Concentrates with Particular Reference to Pharmaceutical and Pesticide Formulations. *Pestic. Manag. Sci.* **1989**, *25*, 25–34.

(192) Viets, A. K.; Tann, R. S.; Mueninghoff, J. C. *Pesticide Formulations and Application Systems: A New Century for Agricultural Formualtions*; ASTM International: Philadelphia, 2001.

(193) Haas, S.; Hässlin, H. W.; Schlatter, C. Influence of Polymeric Surfactants on Pesticidal Suspension Concentrates: Dispersing Ability, Milling Efficiency and Stabilization Power. *Colloids Surfaces A Physicochem. Eng. Asp.* **2001**, *183*, 785–793.

(194) Fritz, G.; Schädler, V.; Willenbacher, N.; Wagner, N. J. Electrosteric Stabilization of Colloidal Dispersions. *Langmuir* **2002**, *18*, 6381–6390.

(195) Yang, X.; Ren, T.; Zhang, B. Dispersion Performance of Polycarboxylate Terpolymers with Different Alkyl Side-Chain Lengths in Pesticide Suspension Concentrate. *Int. J. Chem. Eng.* **2021**, 9, 1-7.

(196) Heath, D.; Tadros, T. F.; Knott, R. D.; Knowles, D. A. Stabilization of Aqueous Pesticidal Suspensions by Graft Copolymers. *ACS Symp. Ser.* **1984**, *254*, 11–28.

(197) Zhang, S.; Zhang, L.; Yang, X.; Hua, W.; Qiu, J.; Zhang, M.; Zhang, B.; Ren, T. Novel Comb-like Anion-Nonionic Copolymer for Improving the Stability of Pymetrozine Suspension Concentrate. *J. Appl. Polym. Sci.* **2021**, *138*, 1–10.

(198) Narayanan, K. S.; Jon, D. I.; Patel, J. New Value-Added Polymeric Dispersants and Uses Thereof in Agricultural Formulations. *J. ASTM Int.* **2005**, *2*, 299–312.

(199) Pang, Y.; Li, X.; Zhou, M.; Li, Y.; Gao, W.; Qiu, X. Relationship between the Hydrophilicity of Lignin Dispersants and Their Performance towards Pesticide Particles. *Holzforschung* **2016**, *70*, 653–660.

(200) Qin, Y.; Yang, D.; Qiu, X. Hydroxypropyl Sulfonated Lignin as Dye Dispersant: Effect of Average Molecular Weight. *ACS Sustain. Chem. Eng.* **2015**, *3*, 3239–3244.

(201) Qin, Y.; Yang, D.; Gu, F.; Li, X.; Xiong, W.; Zhu, J. Y. Biorefinery Lignosulfonates as a Dispersant for Coal Water Slurry. *Sustain. Chem. Process.* **2016**, *4*, 1–8.

(202) Arel, H. Ş.; Aydin, E. Effects of Ca-, Mg-, K-, and Na-Lignosulfonates on the Behavior of Fresh Concrete. *Constr. Build. Mater.* **2017**, *157*, 1084–1091.

(203) Eshel, G.; Levy, G. J.; Mingelgrin, U.; Singer, M. J. Critical Evaluation of the Use of Laser Diffraction for Particle-Size Distribution Analysis. *Soil Sci. Soc. Am. J.* **2004**, *68*, 736–743.

(204) Li, H.; Li, J.; Bodycomb, J.; Patience, G. S. Experimental Methods in Chemical Engineering: Particle Size Distribution by Laser Diffraction—PSD. *Can. J. Chem. Eng.* **2019**, *97*, 1974–1981.

(205) de Boer, G. B. J.; de Weerd, C.; Thoenes, D.; Goossens, H. W. J. Laser Diffraction Spectrometry: Fraunhofer Diffraction Versus Mie Scattering. *Part. Part. Syst. Charact.* **1987**, *4*, 14–19.

(206) Hassan, P. A.; Rana, S.; Verma, G. Making Sense of Brownian Motion: Colloid Characterization by Dynamic Light Scattering. *Langmuir* **2015**, *31*, 3–12.

(207) Bhattacharjee, S. DLS and Zeta Potential - What They Are and What They Are Not? *J. Control. Release* **2016**, *235*, 337–351.

(208) Ning, Y.; Fielding, L. A.; Andrews, T. S.; Growney, D. J.; Armes, S. P. Sulfate-Based Anionic Diblock Copolymer Nanoparticles for Efficient Occlusion within Zinc Oxide. *Nanoscale* **2015**, *7*, 6691–6702.

(209) Stokes, D. J. *Principles and Practice of Variable Pressure/Environmental Scanning Electron Microscopy (VP-ESEM)*; Wiley, Chichester, 2008.

(210) Goodhew, P. J.; Humphreys, J. *Electron Microscopy and Analysis, Third Edition*; CRC Press: New York, 2014.

(211) Williams, D. B.; Carter, C. B. *Transmission Electron Microscopy: A Textbook for Materials Science*; Springer: New York, 2009.

(212) Rice, S. B.; Chan, C.; Brown, S. C.; Eschbach, P.; Han, L.; Ensor, D. S.; Stefaniak, A. B.; Bonevich, J.; Vladár, A. E.; Walker, A. R. H.; Zheng, J.; Starnes, C.; Stromberg, A.; Ye, J.; Grulke, E. A. Particle Size Distributions by Transmission Electron Microscopy: An Interlaboratory Comparison Case Study. *Metrologia* **2013**, *50*, 663–678.

(213) Bootz, A.; Vogel, V.; Schubert, D.; Kreuter, J. Comparison of Scanning Electron Microscopy, Dynamic Light Scattering and Analytical Ultracentrifugation for the Sizing

of Poly(Butyl Cyanoacrylate) Nanoparticles. *Eur. J. Pharm. Biopharm.* **2004**, *57*, 369–375.

(214) Pyrz, W. D.; Buttrey, D. J. Particle Size Determination Using TEM: A Discussion of Image Acquisition and Analysis for the Novice Microscopist. *Langmuir* **2008**, *24*, 11350–11360.

# Chapter 2

# RAFT Aqueous Emulsion Polymerization of Methyl Methacrylate

Reproduced in full with permission from [Chan, D. H. H.; Cockram, A. A.; Gibson, R. R.; Kynaston, E. L.; Lindsay, C.; Taylor, P.; Armes, S. P. RAFT Aqueous Emulsion Polymerization of Methyl Methacrylate: Observation of Unexpected Constraints When Employing a Non-Ionic Steric Stabilizer Block. *Polym. Chem.* **2021**, *12*, 5760–5769.]

## 2.1 Introduction

RAFT polymerization is exceptionally tolerant of monomer functionality and is usually conducted in either organic solvents or aqueous solution to afford soluble polymer chains.[1] However, it is equally well-suited to heterogeneous conditions such as suspension,[2] dispersion[3–7] or emulsion[8–10] polymerization. In particular, RAFT aqueous emulsion polymerization – which is an important example of polymerization-induced self-assembly (PISA)[11,12]– enables the controlled polymerization of a wide range of water-immiscible vinyl monomers in aqueous media.[12–14] Typically, spherical nanoparticles of tunable particle size can be readily prepared at high solids,[11] although so-called 'higher order' copolymer morphologies (e.g. worms or vesicles) are also accessible for at least some formulations.[13–15] Potential applications for such nano-objects include surface modifiers for cellulose fibres,[16] viscosity modifiers,[17] organic opacifiers for paints[18] and additives for the reinforcement of latex films.[19]

There are many reports of the RAFT aqueous emulsion polymerization of commodity monomers such as styrene,[7,18,20–22] *n*-butyl acrylate[8,23–25] or vinyl acetate.[26] Moreover, there are also various reports of the use of speciality vinyl monomers such as benzyl methacrylate,[27] 2,2,2-trifluoroethyl methacrylate,[28] isopropylideneglycerol monomethacrylate,[29] 2-methoxyethyl methacrylate,[30] glycidyl methacrylate,[31–34] or hydroxybutyl methacrylate.[35] However, given its undoubted importance as a commodity monomer, there are surprisingly few literature reports of the RAFT aqueous emulsion polymerization of methyl methacrylate (MMA).[16,24,36,37,38] Moreover, given the moderately high aqueous solubility of this monomer (15.9 g dm$^{-3}$ at 20 °C), such PISA formulations might be expected to provide convenient access to a wide range of block copolymer nano-objects (e.g. spheres, worms and vesicles).[30,34,35,39]

Chaduc *et al.* reported the polymerization of MMA using a poly(methacrylic acid) (PMAA) precursor using a one-pot protocol. Good molecular weight control was obtained with only a slight broadening of the MWD being observed after 80% conversion. Moreover, essentially full MMA conversion (> 99%) was achieved after only 1 h at 80 °C. Colloidally stable diblock copolymer spheres were formed with a hydrodynamic diameter of 69 nm.[24]

Carlsson and co-workers reported the RAFT aqueous emulsion polymerization of MMA using a poly(2-(dimethylamino)ethyl methacrylate)-*co*-methacrylic acid) [P(DMAEMA-co-MAA)] statistical block as a steric stabilizer. This P(DMAEMA-co-MAA) precursor comprised mainly protonated DMAEMA units and just a few MAA units so it exhibited strongly cationic character at pH 7. The DP of the core-forming PMMA block was varied to produce a series of cationic block copolymers with *z*-average particle diameters ranging between 50 and 146 nm, as judged by DLS. Interestingly, quartz crystal microbalance with dissipation (QCM-D) experiments confirmed that these cationic nanoparticles adsorbed onto model cellulose substrates.[16]

Glycerol monomethacrylate (GMA) is a relatively expensive specialty monomer that has been used for the manufacture of soft contact lenses.[40] GMA-based copolymers have been examined for biomedical applications such as drug delivery,[41] human cell storage[42] and hydrogels acting as corneal substitutes.[43] GMA is usually synthesized from glycerol by a multi-step process that leads to a mixture of 1,3- and 2,3-hydroxy isomers.[44] An alternative method includes the use of the relatively cheap commodity monomer, glycidyl methacrylate (GlyMA). GMA can be obtained directly from GlyMA using either acetic acid or $H_2SO_4$ as an acid catalyst.[45,46] However, Radcliffe *et al.* demonstrated that full conversion of GlyMA to GMA could be achieved by simply heating an aqueous *emulsion* of GlyMA to 80 ˚C for 9 h in the absence of any catalyst.[47]

This Chapter will examine the RAFT emulsion polymerization of MMA using PGMA as a water-soluble precursor, which is known to act as an effective non-ionic steric stabilizer for various other water-immiscible vinyl monomers under such conditions.[27–31] In view of the unexpected limited utility of this PISA formulation, a PGMA stabilizer containing an anionic carboxylate end-group, an anionic PMAA stabilizer and a cationic poly(2-(methacryloyloxy)ethyl trimethylammonium chloride) (PMETAC) were also evaluated for the RAFT emulsion polymerization of MMA. Finally, visible light irradiation is investigated as a method for end-group removal on PGMA-PMMA diblock copolymers containing either dithiobenzoate or trithiocarbonate end-groups.

## 2.2 Experimental

### 2.2.1 Materials

Glycerol monomethacrylate (GMA) was donated by GEO Specialty Chemicals (Hythe, UK). Methyl methacrylate (MMA; 99%), 4,4′-azobis(4-cyanopentanoic acid) (ACVA; 98%), methacrylic acid (MAA; 99%), [2-(methacryloyloxy)ethyl] trimethylammonium chloride (METAC; 80% solution), 2-cyanopropyl dithiobenzoate (CPDB; 97%) and trimethylsilyl diazomethane solution (2.0 M in hexanes) were each purchased from Sigma-Aldrich (UK) and used as received. $d_6$-Dimethyl sulfoxide was purchased from Goss Scientific Instruments Ltd (Crewe, UK). 4-Cyano-4-(2-phenylethanesulfanylthiocarbonyl)sulfanylpentanoic acid (PETTC) was prepared according to a literature protocol.[48] Deionized water from an Elga Medica DV25 water purification unit was used in all the experiments.

### 2.2.2 Synthesis of the PGMA$_{50}$ Precursor by RAFT Aqueous Solution Polymerization

GMA monomer (30.0 g, 187 mmol), CPDB RAFT agent (0.589 g, 2.66 mmol; target PGMA DP = 70) and ACVA initiator (0.149 g, 0.53 mmol; CPDB/ACVA molar ratio = 5.0) were weighed into a 250 mL round-bottom flask. Ethanol (46.5 g, 60% w/w) was added and the flask was cooled by immersing in an ice bath while degassed with $N_2$ gas for 30 min. The flask was then immersed in an oil bath at 70 °C for 165 min. The polymerization was quenched by exposing the reaction mixture to air and cooling the flask to 20 °C. $^1$H NMR spectroscopy indicated a final GMA conversion of 71%. The reaction solution was diluted with methanol (30 mL) and then precipitated into a ten-fold excess of dichloromethane (three times). End-group analysis *via* $^1$H NMR spectroscopy indicated a mean degree of polymerization (DP) of 50 (the integrated aromatic proton signals at 7.4–7.8 ppm were compared to the integrated methacrylic backbone proton signals at 0.7–2.5 ppm).

### 2.2.3 Synthesis of the HOOC-PGMA$_{54}$ Precursor by RAFT Aqueous Solution Polymerization

GMA monomer (10.0 g, 62.4 mmol), PETTC RAFT agent (0.302 g, 0.892 mmol; target PGMA DP = 70) and ACVA initiator (0.050 g, 0.18 mmol; PETTC/ACVA molar ratio = 5.0) were weighed into a 100 mL round-bottom flask. Ethanol (15.5 g, 60% w/w) was added and the flask was cooled by immersing in an ice bath while degassed with $N_2$ gas for 30 min. The flask was then immersed in an oil bath at 70 °C for 120 min. The polymerization was quenched by exposing the reaction mixture to air and cooling the flask to 20 °C. $^1$H NMR spectroscopy indicated a final GMA conversion of 77%. The solution was diluted with methanol (10 mL) and then precipitated into a ten-fold excess of dichloromethane (three times). End-group analysis *via* $^1$H NMR spectroscopy indicated a mean DP of 54.

### 2.2.4 Synthesis of PGMA$_{50}$-PMMA$_x$ Diblock Copolymer Nanoparticles by RAFT Aqueous Emulsion Polymerization

A typical protocol for the synthesis of PGMA$_{50}$-PMMA$_x$ diblock copolymer nanoparticles was as follows. PGMA$_{50}$ precursor (0.150 g, 18.2 µmol), MMA monomer (0.146 g, 1.46 mmol, target DP = 80), ACVA initiator (1.00 mg, 3.65 µmol, PGMA$_{50}$/ACVA molar ratio = 5.0) and deionized water (2.675 g, 10% w/w solution) were added to a 20 mL round-bottom flask. The mixture was adjusted to pH 7 using 1 M NaOH. The flask was then placed in an ice bath and degassed with $N_2$ gas for 30 min, before immersing the flask in an oil bath set at 70 °C. After 3 h, the polymerization was quenched by exposing the reaction mixture to air while cooling the flask to 20 °C. $^1$H NMR spectroscopy analysis in d$_6$-dimethyl sulfoxide was used to calculate monomer conversion. Essentially the same protocol was employed for the synthesis of HOOC-PGMA$_{54}$-PMMA$_x$ diblock copolymer nanoparticles but in this case the HOOC-PGMA$_{54}$ precursor was used instead of the PGMA$_{50}$ precursor.

### 2.2.5 Synthesis of the $PMAA_{56}$ Precursor by RAFT Aqueous Solution Polymerization

MAA monomer (45.0 g, 0.523 mol), PETTC RAFT agent (3.165 g, 9.34 mmol; target DP = 56), ACVA initiator (0.523 g, 1.87 mmol; PETTC/ACVA molar ratio = 5.0) and ethanol (73.0 g, 40% w/w) were weighed into a 500 mL round-bottom flask. The solution was placed in an ice bath and degassed with $N_2$ gas for 30 min, before the flask was immersed in an oil bath at 70 °C. The polymerization was quenched after 3 h by exposing the reaction mixture to air while cooling the flask to 20 °C. The crude polymer was then precipitated into a ten-fold excess of diethyl ether. The insoluble polymer was redissolved in ethanol prior to a second precipitation step and then freeze-dried overnight. End-group analysis by $^1H$ NMR spectroscopy indicated a DP of 56 for this PMAA precursor.

### 2.2.6 Synthesis of $PMAA_{56}$-$PMMA_x$ Diblock Copolymer Nanoparticles by RAFT Aqueous Emulsion Polymerization

A typical protocol for the synthesis of $PMAA_{56}$-$PMMA_x$ diblock copolymer nanoparticles was conducted as follows. $PMAA_{56}$ precursor (0.100 g, 19.4 μmol), MMA monomer (0.194 g, 1.94 mmol, target DP = 100), ACVA initiator (1.10 mg, 3.88 μmol, $PMAA_{56}$/ACVA molar ratio = 5.0) and deionized water (1.18 g, 20% w/w solution) were added to a 20 mL round-bottom flask. The mixture was adjusted to pH 5 using 1 M HCl. The reaction mixture was then placed in an ice bath and degassed with $N_2$ gas for 30 min, before immersing in an oil bath set at 70 °C. The polymerization was allowed to proceed at this temperature for 6 h and then quenched by exposing the reaction mixture to air while cooling the flask to 20 °C.

### 2.2.7 Methylation of $PMAA_{56}$-$PMMA_x$ Diblock Copolymer Nanoparticles

Methylation of the carboxylic acid groups on the PMAA block was performed before THF GPC analysis. $PMAA_{56}$-$PMMA_x$ diblock copolymer powder (20 mg) was diluted in THF (2.0 mL). Excess trimethylsilyldiazomethane was then gradually added to this solution until it turned yellow. The reaction mixture was stirred overnight, dried and analyzed by THF GPC.

### 2.2.8 Synthesis of the $PMETAC_{46}$ Precursor by RAFT Aqueous Solution Polymerization

METAC monomer (5.0 g, 19.3 mmol; supplied as an 80% w/w aqueous solution), PETTC RAFT agent (0.131 g, 0.385 mmol, target DP = 50) and ACVA initiator (21.6 mg, 0.08 mmol; PETTC/ACVA molar ratio = 5.0) were weighed into a 50 mL round-bottom flask. After addition of ethanol (7.79 g, 60 % w/w), the solution was degassed with $N_2$ gas for 30 min in an ice bath, before immersing the sealed flask in an oil bath at 70 °C. After 3 h, the polymerization was quenched by exposing the reaction mixture to air while cooling the flask to 20 °C. The crude polymer was isolated by slowly pouring the reaction mixture into a ten-fold excess of acetonitrile. The precipitated polymer was dissolved in water prior to a second precipitation using excess acetonitrile. The purified polymer was then freeze-dried overnight. End-group analysis *via* $^1H$ NMR spectroscopy indicated a mean DP of 46 for this PMETAC precursor.

### 2.2.9 Synthesis of $PMETAC_{46}$-$PMMA_x$ Diblock Copolymer Nanoparticles by RAFT Aqueous Emulsion Polymerization

A typical protocol for the synthesis of $PMETAC_{46}$-$PMMA_x$ diblock copolymer nanoparticles was conducted as follows. The dithiobenzoate-capped $PMETAC_{46}$ precursor (0.150 g, 15.2 µmol), MMA monomer (0.152 g, 1.52 mmol, target DP = 100), ACVA initiator (0.800 mg, 3.03 µmol, $PMETAC_{46}$/ACVA molar ratio = 5.0) and deionized water (1.211 g, 20 % w/w solution) were added in turn to a 20 mL round-bottom flask. This flask was then placed in an ice bath and the reaction mixture was degassed with $N_2$ gas for 30 min, before immersing in an oil bath set at 70 °C. After 6 h, the polymerization was quenched by exposing the reaction mixture to air while cooling the flask to 20 °C. An MMA conversion of 99% was determined by $^1H$ NMR spectroscopy studies in $d_6$-DMSO. Other DPs were targeted by adjusting the relative amounts of MMA and $PMETAC_{46}$ precursor as required.

### 2.2.10 Protocols for Cleavage of RAFT End-groups

The dithiobenzoate end-groups within $PGMA_{50}$-$PMMA_{80}$ nanoparticles were cleaved using the following protocol. A 10% w/w copolymer dispersion (1.00 g) was placed in a water-jacketed Schlenk tube wrapped in blue LED light strips ($\lambda = 405$ nm, 0.37 mW cm$^{-2}$) with the temperature of the water within the recirculating jacket set to 80 °C. Aliquots of this reaction mixture were extracted periodically and analyzed using UV GPC (with the UV detector set at $\lambda = 308$ nm). As a control experiment, the same protocol was used but without the blue LED light strips (*i.e.* no visible light irradiation). The same 10% w/w dispersion of $PGMA_{50}$-$PMMA_{80}$ nanoparticles was also treated with $H_2O_2$ (using a five-fold excess relative to the concentration of dithiobenzoate end-groups, as reported by Jesson and co-workers[49]) at 80 °C with no visible light irradiation. The same protocol was used for cleaving trithiocarbonate RAFT end-groups from a 10% w/w aqueous dispersion of HOOC-$PGMA_{54}$-$PMMA_{80}$ nanoparticles. This included cleavage at 80 °C using blue LED strips, $H_2O_2$ or no visible light irradiation for 24 h.

### 2.2.11 Characterization Techniques

#### Dynamic Light Scattering and Aqueous Electrophoresis

DLS and aqueous electrophoresis studies were conducted on 0.50% w/w aqueous dispersions using a Malvern Zetasizer NanoZS instrument. The hydrodynamic *z*-average diameter was determined at 20 °C at a scattering angle of 173° and averaged over three measurements. Aqueous electrophoresis studies were conducted in the presence of 1 mM KCl as background electrolyte. The solution pH was adjusted using either NaOH or HCl. Zeta potentials (also averaged over three measurements) were calculated *via* the Henry equation using the Smoluchowski approximation.

#### Gel Permeation Chromatography (GPC)

Molecular weight distributions of the $PGMA_{50}$ and HOOC-$PGMA_{54}$ precursors and a series of $PGMA_{50}$-$PMMA_{80}$ diblock copolymers were assessed using DMF eluent (containing 10 mM LiBr) at 60 °C. Two Polymer Laboratories PL gel 5 μm Mixed-C columns were connected in series to a Varian 290-LC pump injection module and a Varian 390-LC multidetector suite (refractive index detector) at a flow rate of 1.0 mL $\text{min}^{-1}$. Near-monodisperse poly(methyl methacrylate) standards with $M_\text{p}$ values ranging from 645 g $\text{mol}^{-1}$ to 618 000 g $\text{mol}^{-1}$ were used for calibration. Molecular weights distributions of methylated $PMAA_{56}$-$PMMA_x$ diblock copolymers were assessed using THF eluent (containing 0.05% w/v butylhydroxytoluene and 2.0% v/v trimethylamine). Two Polymer Laboratories PL gel 5 μm Mixed-C columns were connected in series to a WellChrom K-2301 refractive index detector at a flow rate of 1.0 mL min$^{-1}$. Near-monodisperse poly(methyl methacrylate) standards were used for calibration.

### Transmission Electron Microscopy (TEM)

Copper/palladium TEM grids (Agar Scientific, UK) were coated with a thin film of amorphous carbon. Grids were treated with a plasma glow discharge for 30 s to produce a hydrophilic surface. A 10 µL droplet of a 0.10% w/w aqueous dispersion was placed on a grid and left for 1 min before blotting. The adsorbed nanoparticles were then stained using uranyl formate (9.0 µL of a 0.75% w/w aqueous solution) for 20 s followed by blotting to remove excess stain. Grids were carefully dried under vacuum and images were recorded at 100 kV using a Philips CM100 instrument equipped with a Gatan 1k CCD camera.

### Small-angle X-ray Scattering (SAXS)

SAXS patterns were collected using a Xeuss 2.0 (Xenocs) SAXS instrument equipped with a Dectris Pilatus 1 M detector and an Excillum liquid gallium MetalJet X-ray source ($\lambda$ = 1.34 Å). SAXS patterns were recorded for 1.0% w/w aqueous dispersions of PGMA$_{50}$-PMMA$_x$ nanoparticles over a scattering vector $q$ range of 0.04–0.4 Å$^{-1}$ using 2.0 mm diameter glass capillary cells. The scattering of deionized water was used for absolute intensity calibration. Irena SAS macros for Igor Pro software were used to perform background subtraction, normalization and data analysis.[50]

## 2.3 Results and Discussion

### 2.3.1 Synthesis of a PGMA$_{50}$ Precursor *via* RAFT Solution Polymerization

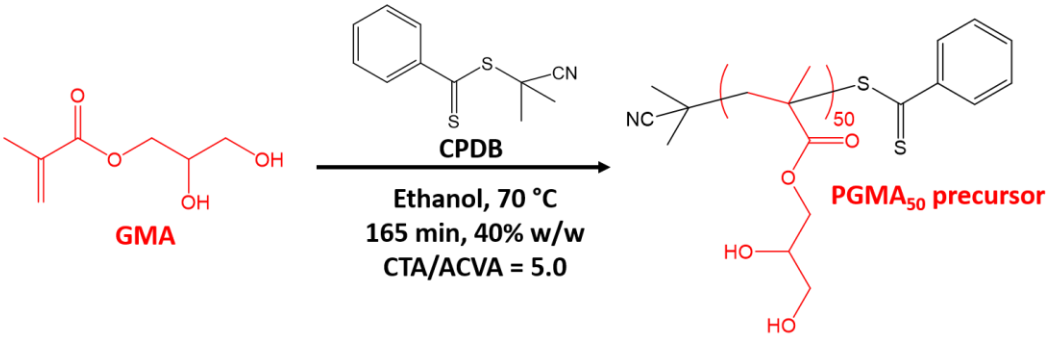

**Scheme 2.1.** Synthesis of a PGMA$_{50}$ precursor *via* RAFT solution polymerization of GMA using CPDB.

A PGMA precursor was prepared by RAFT solution polymerization of GMA in ethanol at 70 °C using 2-cyanopropyl dithiobenzoate (CPDB) as the RAFT chain transfer agent (CTA) (see **Scheme 2.1**). This reaction was allowed to proceed for 165 min, which resulted in a GMA conversion of 71%. Avoiding monomer-starved conditions was considered desirable so as to retain maximum RAFT chain-end fidelity. In principle, this approach should ensure high blocking efficiencies when chain-extending this PGMA homopolymer with a second monomer. The crude precursor was purified by precipitation into excess dichloromethane to remove unreacted monomer. The polymer was then dissolved in water and freeze-dried overnight to yield a pink powder. End-group analysis by $^1$H NMR spectroscopy indicated a mean DP of 50 (**Figure 2.1**).

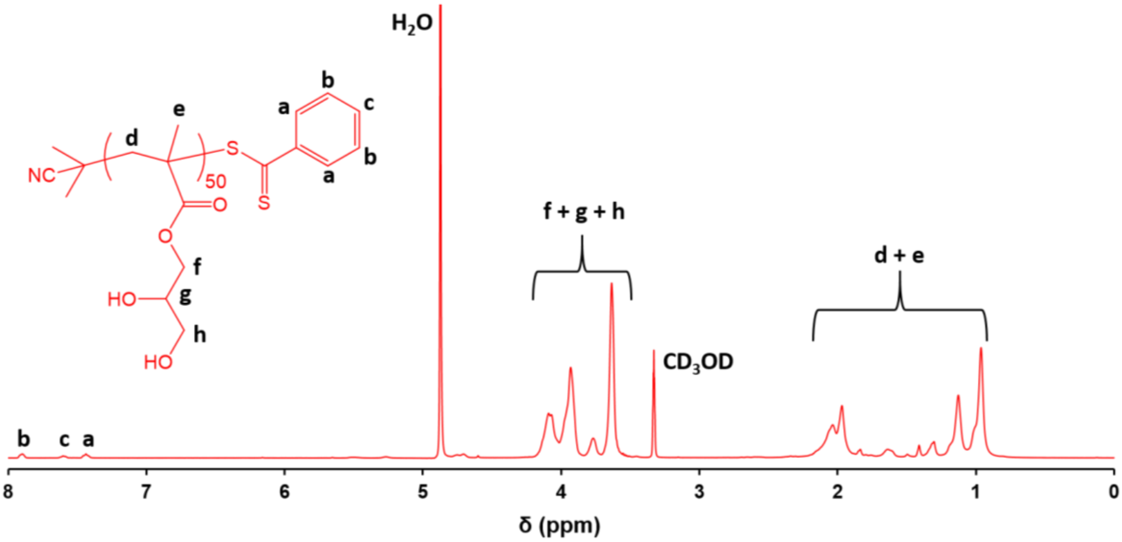

**Figure 2.1.** $^1$H NMR spectra recorded in d$_4$-methanol for the PGMA$_{50}$ precursor prepared using CPDB as the RAFT CTA.

### 2.3.2 RAFT Aqueous Emulsion Polymerization Kinetics for the Synthesis of PGMA$_{50}$-PMMA$_{80}$ Diblock Copolymer Nanoparticles

This PGMA$_{50}$ precursor was subsequently chain-extended *via* RAFT aqueous emulsion polymerization of MMA (**Scheme 2.2**). The kinetics of this reaction was studied at 70 °C by $^1$H NMR spectroscopy when targeting PGMA$_{50}$-PMMA$_{80}$ diblock copolymer spheres at 10% w/w solids. The PGMA$_{50}$/ACVA molar ratio was varied from 3.0 to 7.0 to determine the effect on both the reaction kinetics (**Figure 2.2**) and the dispersity of the final PGMA$_{50}$-PMMA$_{80}$ chains (**Figure 2.3**).

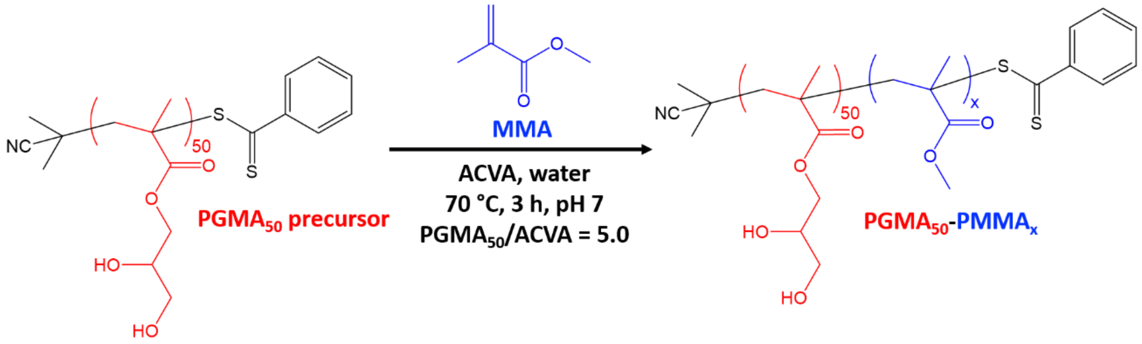

**Scheme 2.2.** Synthesis of PGMA$_{50}$-PMMA$_x$ diblock copolymer nanoparticles by RAFT aqueous emulsion polymerization of methyl methacrylate MMA at 70 °C using a dithiobenzoate-capped PGMA$_{50}$ precursor at pH 7.

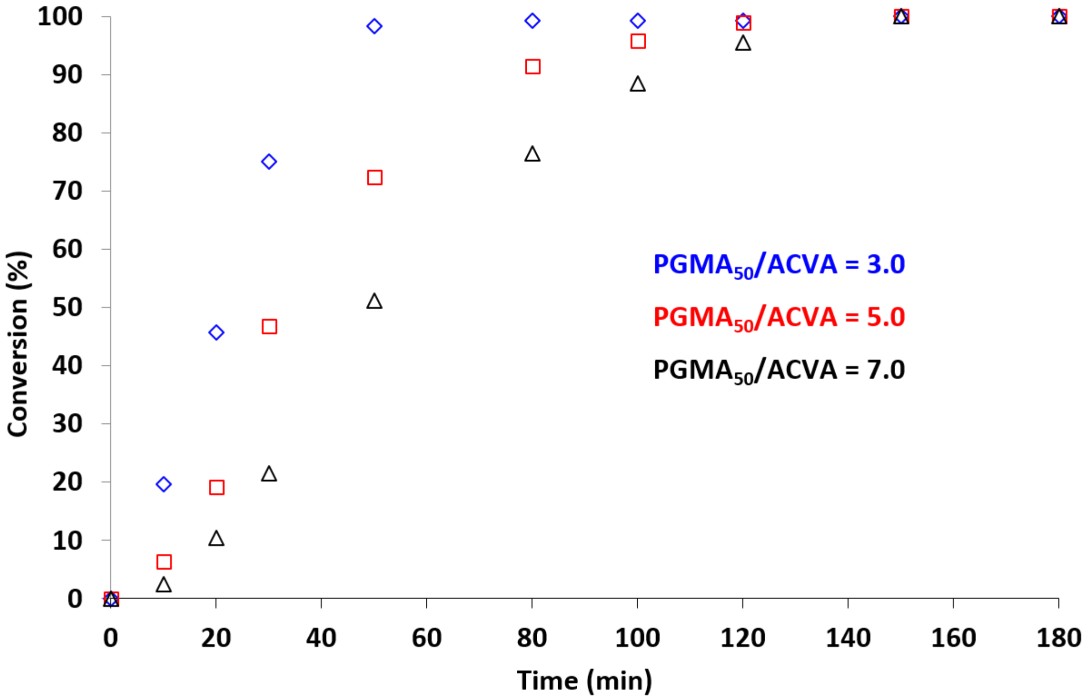

**Figure 2.2.** Kinetics of polymerization of MMA at 70 °C when using a PGMA$_{50}$ macro-CTA/ACVA molar ratio of 3.0, 5.0 or 7.0 when targeting PGMA$_{50}$-PMMA$_{80}$ diblock copolymer nanoparticles at 10% w/w solids. $^1$H NMR spectroscopy analysis in d$_6$-dimethyl sulfoxide was used to calculate monomer conversion.

**Figure 2.2** indicates that very high conversions were achieved at all three PGMA$_{50}$/ACVA molar ratios. As expected, the fastest polymerization was obtained using a PGMA$_{50}$/ACVA molar ratio of 3.0, with > 99% conversion being attained within ~60 min. As this molar ratio was increased to 5.0 and 7.0, essentially full conversion was achieved after 120 min and 160 min, respectively. In principle, a low macro-CTA/initiator ratio should cause an increase in dispersity owing to a reduction in living character.[51] Hence these three reactions were analyzed by DMF GPC and the chromatograms are shown in **Figure 2.3**. Perhaps surprisingly, comparable molecular weights and only very slight differences in the dispersities were observed for these three polymerizations. Similar observations were reported by Cunningham and co-workers for the RAFT aqueous emulsion polymerization of benzyl methacrylate.[27] Somewhat arbitrarily, a PGMA$_{50}$/ACVA molar ratio of 5.0 was selected for subsequent reactions.

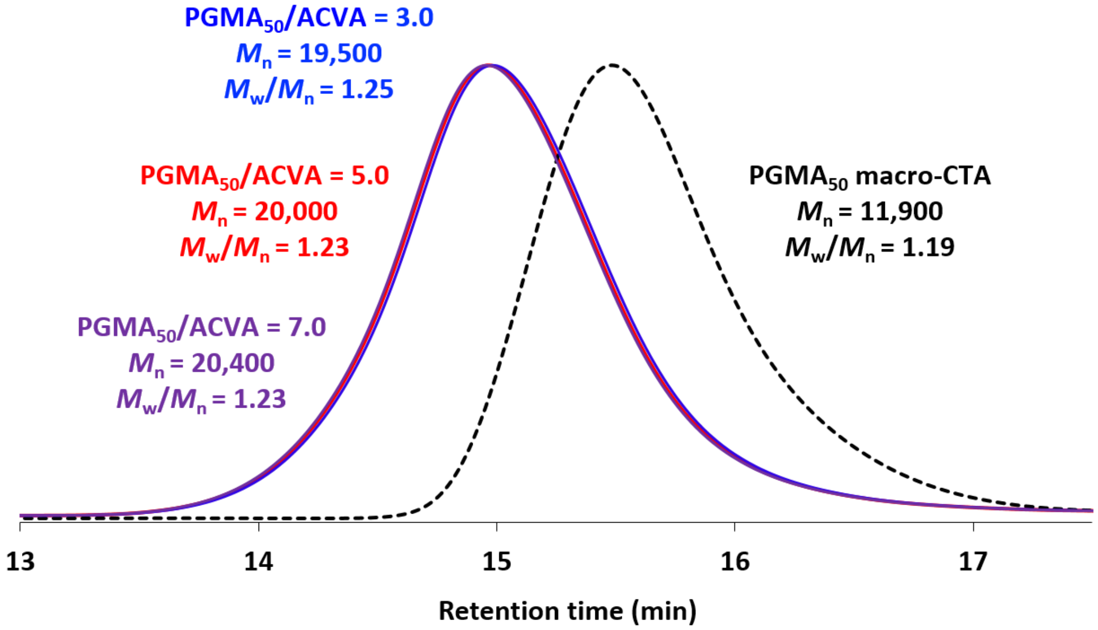

**Figure 2.3.** DMF GPC curves recorded for a PGMA$_{50}$ precursor and three PGMA$_{50}$-PMMA$_{80}$ diblock copolymers synthesized when varying the macro-CTA/initiator molar ratio between 3.0 and 7.0.

### 2.3.3 Synthesis of a Series of PGMA$_{50}$-PMMA$_x$ Diblock Copolymer Nanoparticles *via* RAFT Aqueous Emulsion Polymerization

A series of PGMA$_{50}$-PMMA$_x$ nanoparticles were obtained by systematically varying the target DP of the PMMA core-forming block. High MMA conversions were achieved within 3 h at 70 °C for all syntheses (**Table 2.1**). Digital photographs taken at the end of each polymerization are shown in **Figure 2.4**. These images show that these dispersions became more viscous and opaque when targeting higher PMMA DPs, with a paste-like dispersion being obtained at a PMMA DP of 130.

**Table 2.1.** Summary of monomer conversions and mean particle diameters obtained for the synthesis of a series of $PGMA_{50}$-$PMMA_{20–130}$ nanoparticles *via* RAFT aqueous emulsion polymerization of MMA at 70 °C targeting 10% w/w solids.

| Target PMMA DP | Conversion (%) | DLS *z*-average diameter (nm) | DLS polydispersity | TEM morphology | SAXS core diameter (nm) |
|---|---|---|---|---|---|
| 20 | > 99 | 18 | 0.04 | spheres | 14 |
| 40 | > 99 | 20 | 0.04 | spheres | 15 |
| 60 | > 99 | 29 | 0.08 | spheres | 18 |
| 80 | > 99 | 38 | 0.10 | spheres | 21 |
| 100 | > 99 | 66 | 0.12 | spheres | 24 |
| 130 | 99 | 422 | 0.49 | spheres | 30 |

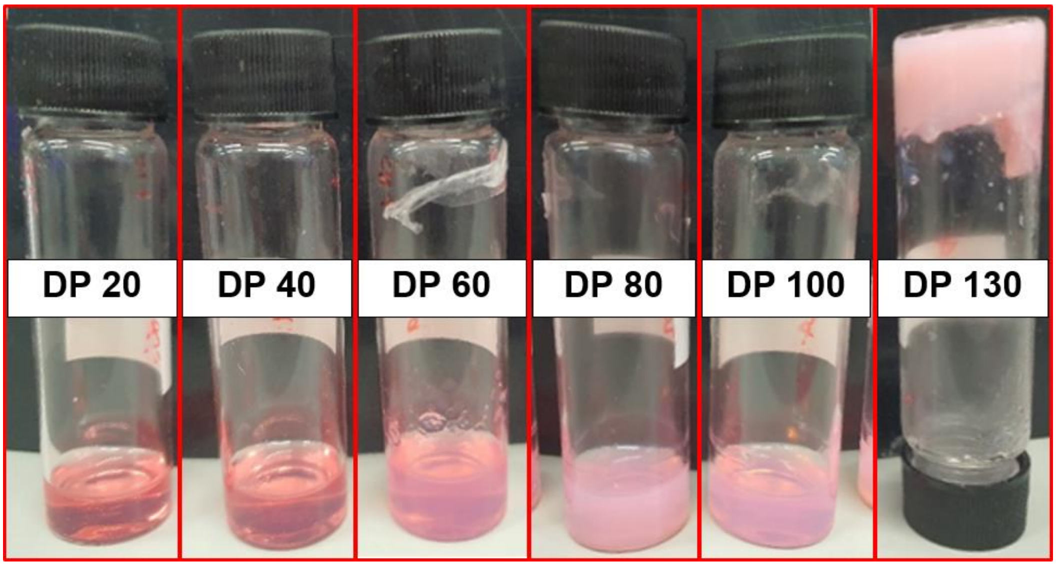

**Figure 2.4.** Digital photographs recorded for a series of $PGMA_{50}$-$PMMA_{20–130}$ nanoparticles *via* RAFT aqueous emulsion polymerization of MMA at 70 °C when targeting 10% w/w solids.

DMF GPC analysis indicated relatively high blocking efficiencies and unimodal molecular weight distributions in each case (**Figure 2.5**). Increasing the target PMMA DP led to progressively higher $M_n$ values, albeit with a gradual increase in dispersity (from $M_w/M_n$ = 1.17 for $PGMA_{50}$-$PMMA_{20}$ up to $M_w/M_n$ = 1.37 for $PGMA_{50}$-$PMMA_{130}$). Similar observations have been reported for various other PISA formulations in the literature.[16,24,36]

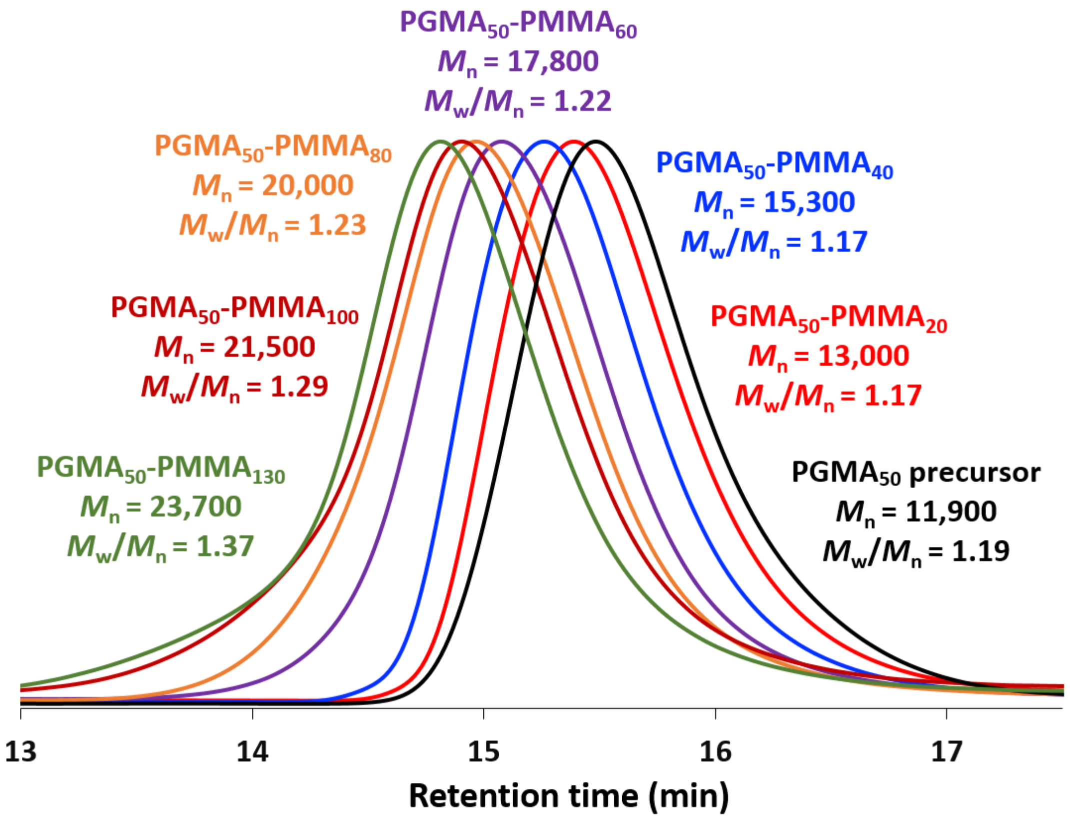

**Figure 2.5.** DMF GPC curves recorded for the $PGMA_{50}$ precursor and a series of $PGMA_{50}$-$PMMA_x$ nanoparticles for which the target PMMA DP ($x$) is 20, 40, 60, 80, 100 or 130 (see **Table 2.1** for further details).

TEM studies confirmed that kinetically-trapped spherical nanoparticles of increasing size were obtained when systematically varying the DP of the core-forming PMMA block ($x$) from 20 to 130 (**Figure 2.6a**). Furthermore, dynamic light scattering (DLS) studies revealed a systematic increase in the hydrodynamic *z*-average diameter while DLS polydispersities remained reasonably low up to $x = 100$, signifying relatively narrow particle size distributions (see **Table 2.1** and **Figure 2.6b**). However, a substantial increase in both the apparent *z*-average diameter and DLS polydispersity was observed when targeting $x = 130$. Moreover, the TEM image recorded for this PISA synthesis indicates aggregates or clusters of nanoparticles on the grid, suggesting colloidal instability. Various PISA syntheses were conducted targeting $x > 100$ and similar results were invariably obtained (data not shown). This was an unexpected limitation, not least because we had previously reported that non-ionic dithiobenzoate-based PGMA precursors with similar (or lower) DPs were effective when performing RAFT aqueous emulsion polymerization syntheses with more hydrophobic methacrylic monomers. For example, Akpinar and co-workers[28] were able to prepare $PGMA_{28}$-$PTFEMA_{500}$ and $PGMA_{43}$-$PTFEMA_{1000}$ spherical nanoparticles with no loss in colloidal stability. Similar results were also obtained by Jesson and co-workers when preparing $PGMA_{39}$-$PIPGMA_{1000}$ spheres[29] and by Cunningham *et al*. when preparing $PGMA_{51}$-$PBzMA_{1000}$ spheres.[27]

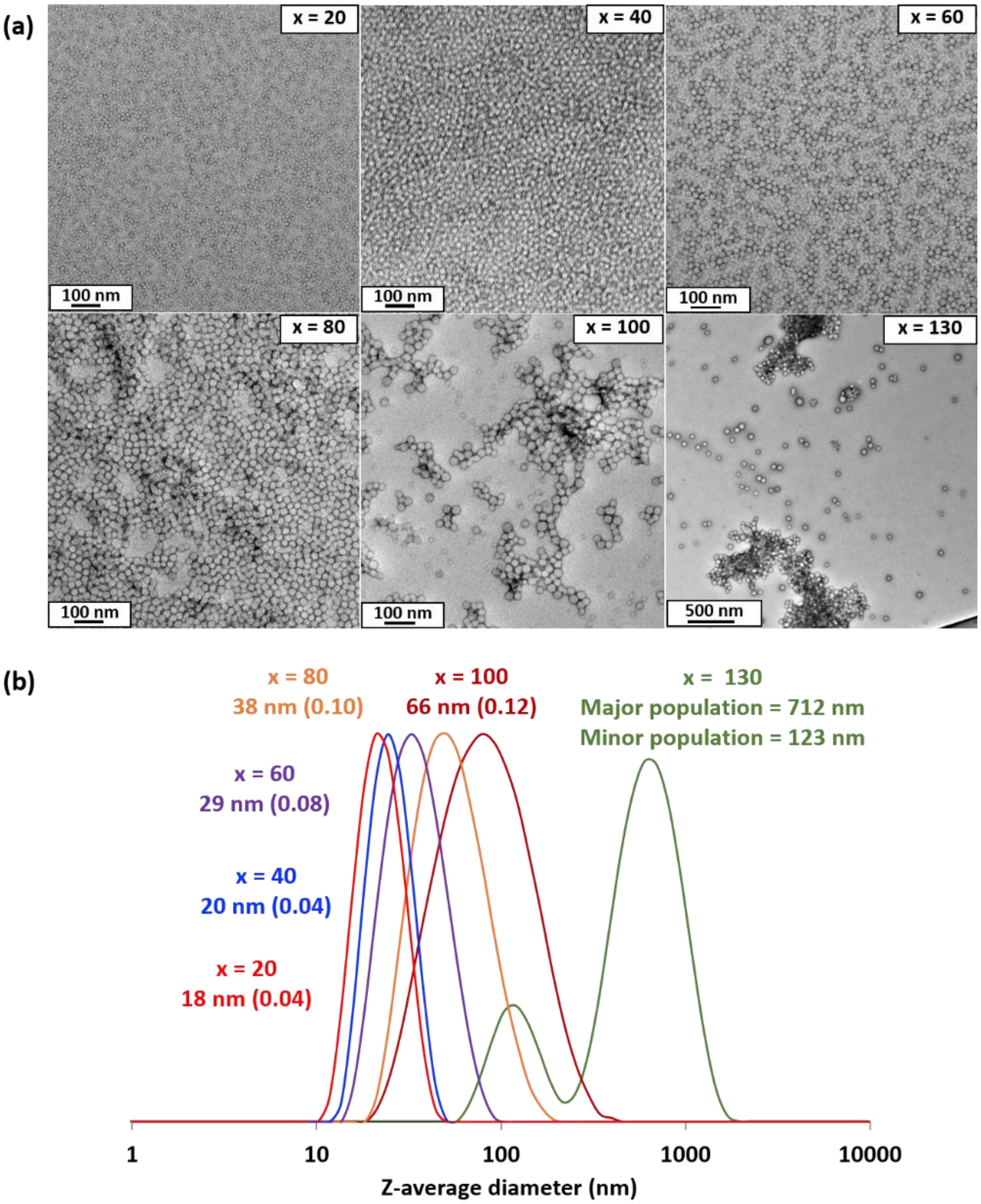

**Figure 2.6.** (a) Representative TEM images and (b) DLS particle size distributions obtained for a series of $PGMA_{50}$-$PMMA_{x}$ nanoparticles prepared by RAFT aqueous emulsion polymerization of MMA where the target PMMA DP ($x$) is 20, 40, 60, 80, 100 or 130. DLS indicates a bimodal particle size distribution in the latter case owing to nanoparticle flocculation.

Thus, at first sight, this unforeseen limitation appeared more likely to be associated with the choice of PMMA as the core-forming block, rather than the use of PGMA as a non-ionic stabilizer block. A few additional experiments were conducted using a longer $PGMA_{101}$ block as a steric stabilizer. However, nanoparticle aggregation was still observed when targeting PMMA DPs above 100. For example, DLS studies indicated incipient flocculation for $PGMA_{101}$-$PMMA_{200}$ nanoparticles prepared at 70 °C when targeting 10% w/w solids using the CPDB RAFT agent (**Figure 2.7a**). An apparent hydrodynamic *z*-average diameter of 189 nm (PDI = 0.30) was determined for this particular nanoparticle dispersion. In contrast, a hydrodynamic *z*-average diameter of 41 nm (PDI = 0.10) was obtained for the $PGMA_{101}$-$PMMA_{100}$ nanoparticle dispersion, suggesting good colloidal stability in this case. These observations are supported by TEM images of each dispersion (**Figure 2.7b**).

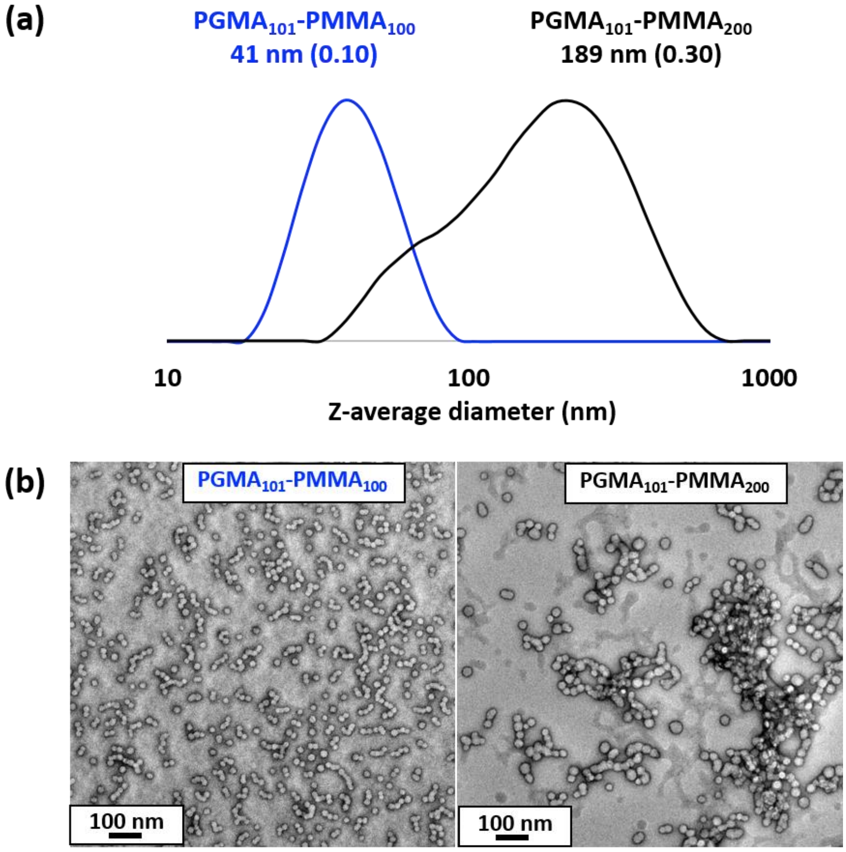

**Figure 2.7.** (a) DLS intensity-average particle size distributions for $PGMA_{101}$-$PMMA_{100}$ and $PGMA_{101}$-$PMMA_{200}$ nanoparticles prepared *via* RAFT aqueous emulsion polymerization at 10% w/w solids at 70 °C using the CPDB RAFT agent. (b) TEM images recorded for $PGMA_{101}$-$PMMA_{100}$ and $PGMA_{101}$-$PMMA_{200}$ nanoparticles, suggesting that the former dispersion is colloidally stable whereas the latter dispersion is weakly flocculated.

SAXS patterns were recorded for 1.0% w/w aqueous dispersions of the $PGMA_{50}$-$PMMA_{20–130}$ nanoparticles. Representative $I(q)$ *vs.* $q$ plots for six dispersions are shown in **Figure 2.8**. The local minimum observed for each pattern is shifted to lower $q$ as higher PMMA DPs are targeted. This indicates a systematic increase in the nanoparticle core diameter, $d$, according to the well-known relation $q = 2\pi/d$.[52] These findings are consistent with the TEM and DLS data discussed above. Moreover, it is well-known that the low $q$ gradient can be used to infer the predominant copolymer morphology.[53] More specifically, a low $q$ gradient of zero indicates a spherical morphology, which is indeed observed when targeting PMMA DPs of between 20 and 80. However, non-zero low $q$ gradients are observed for $PGMA_{50}$-$PMMA_{100}$ and $PGMA_{50}$-$PMMA_{130}$, which suggests incipient nanoparticle aggregation and the formation of mass fractals for these two dispersions. Again, this is consistent with the corresponding TEM and DLS data shown in **Figure 2.6**. Fitting the SAXS patterns using a well-established spherical micelle model[54] and also a unified fit[55–57] (to account for nanoparticle aggregation) enables the volume-average diameter of the PMMA cores to be determined in each case (**Table 2.1**).

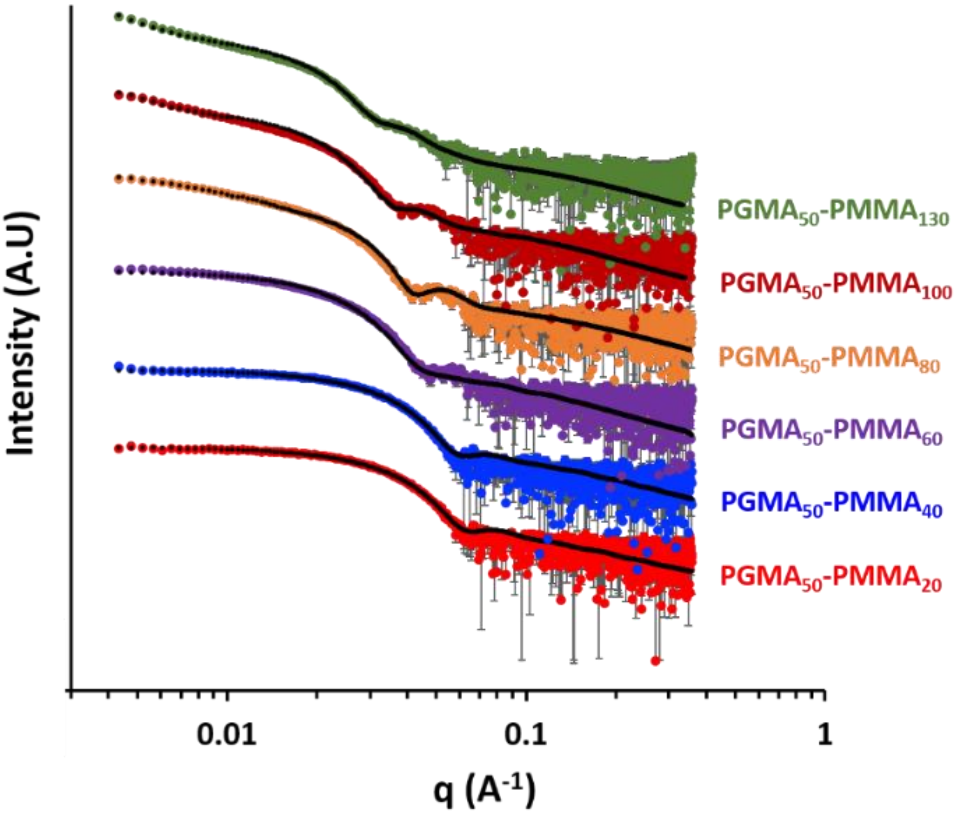

**Figure 2.8.** SAXS patterns recorded for a series of 1.0% w/w aqueous dispersions of $PGMA_{50}$-$PMMA_x$ nanoparticles for which the target PMMA DP has been systematically varied from 20 to 130.

Aqueous electrophoresis studies were performed on $PGMA_{50}$-$PMMA_{80}$ nanoparticles prepared using the dithiobenzoate-capped $PGMA_{50}$ precursor (**Figure 2.9a**). These nanoparticles exhibited zeta potentials close to zero (approximately −3 mV) across the whole pH range, which is consistent with the non-ionic nature of this steric stabilizer block. Given the unexpected colloidal stability problems associated with this PISA formulation, an alternative PGMA stabilizer bearing a carboxylic acid end-group[58] and an anionic poly(methacrylic acid) stabilizer[24] were also evaluated for the RAFT aqueous emulsion polymerization of MMA (see **Scheme 2.3**).

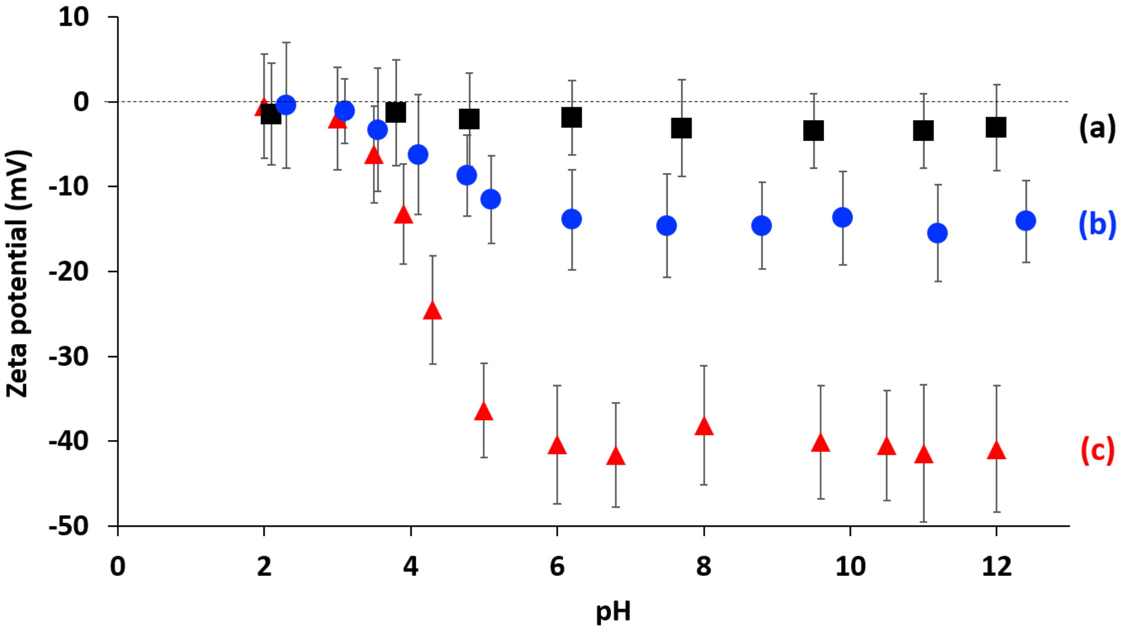

**Figure 2.9.** Zeta potential *vs*. pH curves obtained for dilute aqueous dispersions of: (a) $PGMA_{50}$-$PMMA_{80}$ spheres prepared using the non-ionic dithiobenzoate-based $PGMA_{50}$ precursor shown in **Scheme 2.2**; (b) HOOC-$PGMA_{54}$-$PMMA_{80}$ spheres prepared using the carboxylic acid-functionalized trithiocarbonate-based $PGMA_{54}$ precursor shown in **Scheme 2.3a**; (c) $PMAA_{56}$-$PMMA_{100}$ spheres prepared using the anionic PMAA precursor shown in **Scheme 2.3b.**

### 2.3.4 RAFT Aqueous Emulsion Polymerization of MMA Using a HOOC-PGMA$_{54}$ Precursor, a PMAA$_{56}$ Precursor and a PMETAC$_{46}$ Precursor in Turn

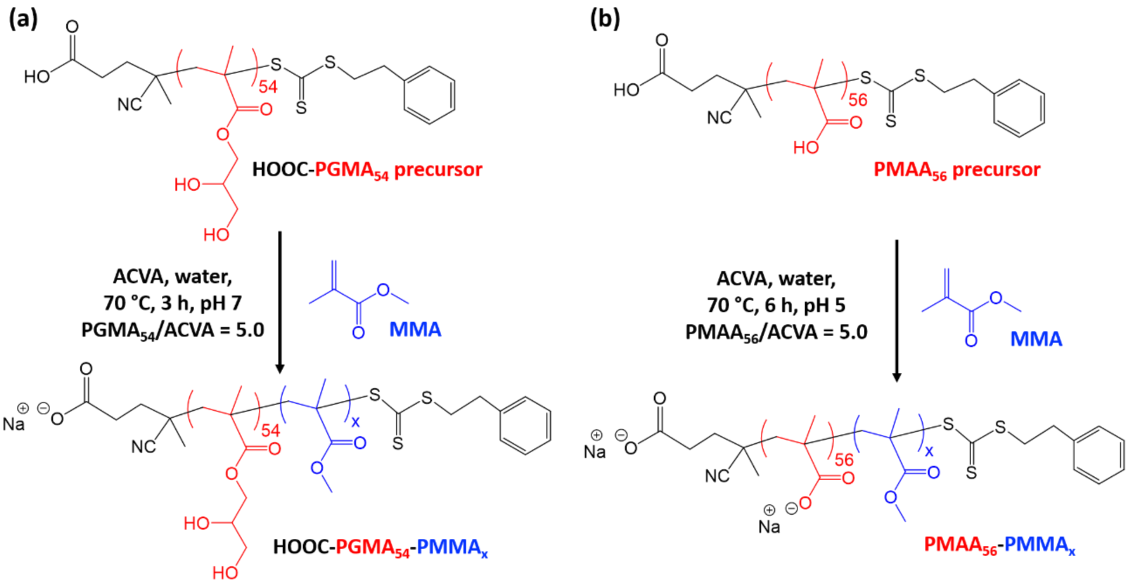

**Scheme 2.3.** (a) Synthesis of HOOC-PGMA$_{54}$-PMMA$_x$ diblock copolymer nanoparticles by RAFT aqueous emulsion polymerization of methyl methacrylate using a trithiocarbonate-based HOOC-PGMA$_{54}$ precursor at 70 °C and targeting $x = 80$ or 150 at pH 7. (b) Synthesis of PMAA$_{56}$-PMMA$_x$ diblock copolymer nanoparticles by RAFT aqueous emulsion polymerization of methyl methacrylate at 70 °C targeting $x = 50$ to 2000 at pH 5.

A trithiocarbonate-based RAFT agent, PETTC, was used to prepare a carboxylic acid-capped PGMA$_{54}$ precursor, which was then chain-extended *via* RAFT aqueous emulsion polymerization of MMA at pH 7 to produce either HOOC-PGMA$_{54}$-PMMA$_{80}$ or HOOC-PGMA$_{54}$-PMMA$_{150}$ spherical nanoparticles (**Scheme 2.3a**). The associated DLS, TEM and GPC data for these two dispersions are summarized in **Figure 2.10.** The anionic charge conferred by the terminal ionized carboxylic group led to significant anionic character under the PISA synthesis conditions (pH 7) as judged by aqueous electrophoresis studies (see **Figure 2.9b**). More specifically, the nanoparticles become progressively more anionic between pH 2 and 6, before a maximum zeta potential of approximately −14 mV is observed at or above pH 6. DLS studies confirmed the formation of relatively small nanoparticles with a *z*-average diameter of 26 nm when targeting a PMMA DP of 80, which indicated good colloidal stability in this case (**Figure 2.10a**). However, such anionic character was not sufficient to allow the PISA synthesis of colloidally stable spherical nanoparticles when targeting a PMMA DP of 150. In this case, DLS and TEM studies indicated extensive nanoparticle aggregation similar to that observed for the non-ionic PGMA$_{50}$-PMMA$_{130}$ nanoparticles. DMF GPC analysis indicated a relatively high blocking efficiency for both copolymers**,** but a significant increase in dispersity ($M_w/M_n$ = 1.35) was observed for the HOOC-PGMA$_{54}$-PMMA$_{150}$ nanoparticles (**Figure 2.10c**).

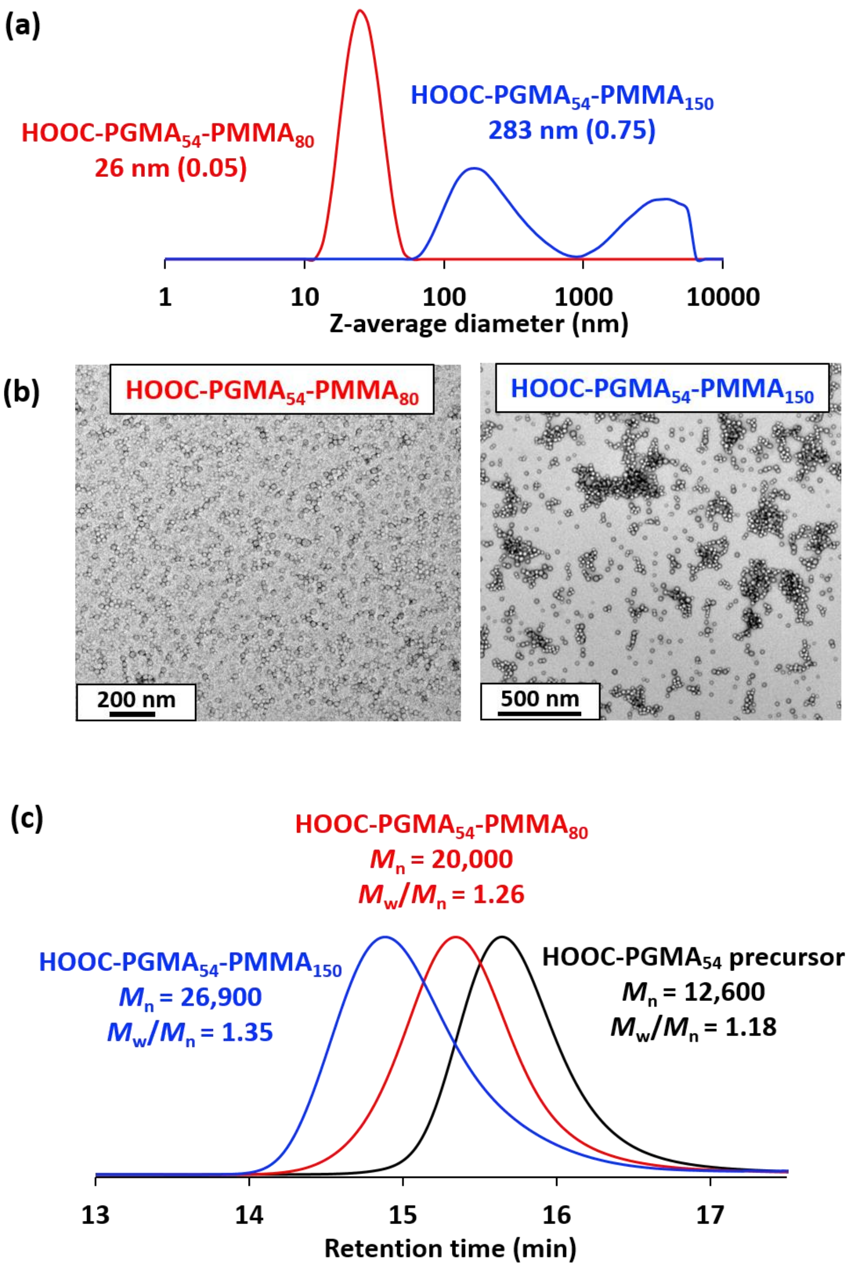

**Figure 2.10.** (a) DLS intensity-average size distributions and (b) corresponding TEM images obtained for HOOC-PGMA$_{54}$-PMMA$_{80}$ and HOOC-PGMA$_{54}$-PMMA$_{150}$ nanoparticles. (c) DMF GPC curves recorded for the HOOC-PGMA$_{54}$ precursor and the corresponding HOOC-PGMA$_{54}$-PMMA$_{80}$ and HOOC-PGMA$_{54}$-PMMA$_{150}$ nanoparticles.

As a result, a poly(methacrylic acid) (PMAA) precursor was evaluated for the RAFT aqueous emulsion polymerization of MMA.[24] A series of $PMAA_{56}$-$PMMA_x$ nanoparticles was prepared using this polyelectrolytic steric stabilizer by systematic variation of the target PMMA DP from 50 to 2000 (see **Scheme 2.3b**). All syntheses were performed at pH 5 targeting 20% w/w solids, as reported by Cockram and co-workers for aqueous PISA syntheses using a PMAA steric stabilizer.[35] $^1$H NMR spectroscopy studies confirmed that relatively high conversions (94–99%) were obtained in each case, with a modest reduction in the final conversion being observed when targeting DPs above 500 (**Table 2.2**). Mean hydrodynamic diameters determined by DLS are summarized in **Table 2.2** and the relationship between DLS diameter and the PMMA DP is shown in **Figure 2.11**.

**Table 2.2.** Summary of monomer conversions and *z*-average diameters obtained for a series of $PMAA_{56}$-$PMMA_{50-2000}$ nanoparticles prepared *via* RAFT aqueous emulsion polymerization of MMA at 70 °C when targeting 20% w/w solids at pH 5.

| Target PMMA DP | Conversion (%) | Actual PMMA DP | DLS Diameter (nm) | DLS PDI | TEM Morphology |
|---|---|---|---|---|---|
| 50 | 99 | 50 | 29 | 0.14 | spheres |
| 100 | 99 | 99 | 35 | 0.13 | spheres |
| 200 | 99 | 198 | 42 | 0.16 | spheres |
| 300 | 99 | 297 | 54 | 0.14 | spheres |
| 400 | 99 | 396 | 59 | 0.10 | spheres |
| 500 | 99 | 495 | 73 | 0.11 | spheres |
| 800 | 98 | 784 | 84 | 0.19 | spheres |
| 1000 | 97 | 970 | 92 | 0.17 | spheres |
| 1500 | 94 | 1410 | 94 | 0.20 | spheres |
| 2000 | 95 | 1900 | 99 | 0.24 | spheres |

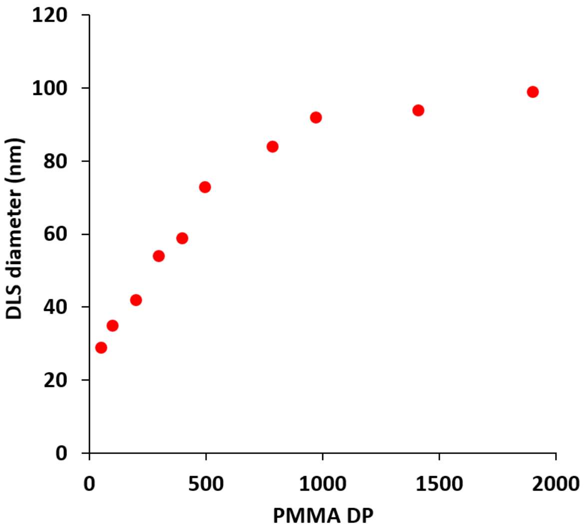

**Figure 2.11.** Variation in *z*-average diameter with PMMA DP ($x$; corrected for the final monomer conversion) for a series of $PMAA_{56}$-$PMMA_x$ diblock copolymer nanoparticles prepared *via* RAFT aqueous emulsion polymerization of MMA at 70 °C targeting 20% w/w solids at pH 5.

As expected, the particle size increases monotonically as the target DP is increased from 50 to 2000. Indeed, an approximate linear relationship is observed between DP 50 (29 nm) and DP 500 (73 nm). Above DP 500, the particle size continues to increase up to DP 2000, albeit more slowly. TEM images for selected $PMAA_{56}$-$PMMA_x$ nanoparticles are shown in **Figure 2.12** when targeting $x$ = 50 to 2000. As expected, a kinetically-trapped spherical morphology was obtained in each case.

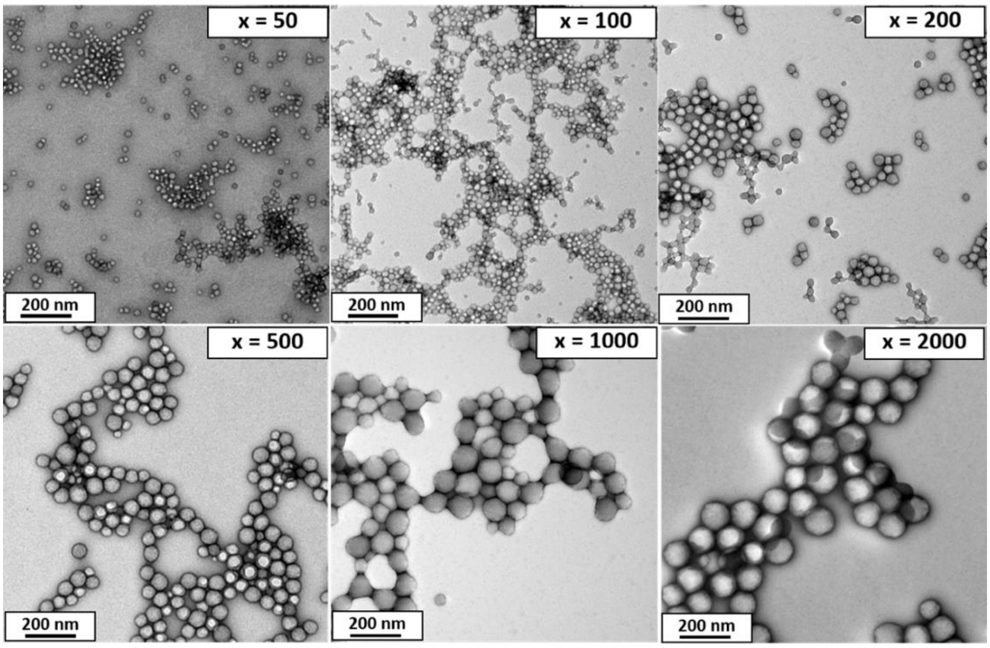

**Figure 2.12.** TEM images recorded for a series of $PMAA_{56}$-$PMMA_y$ diblock copolymer nanoparticles prepared by RAFT aqueous emulsion polymerization of MMA when targeting a PMMA DP ($x$) of 50, 100, 200, 500, 1000 or 2000 (see **Table 2.2** for further details).

Selected PMAA$_{56}$-PMMA$_x$ diblock copolymers were methylated to convert such copolymers into the corresponding PMMA$_{56+x}$ homopolymers for THF GPC analysis using PMMA calibration standards (see **Figure 2.13**). In each case, unimodal MWDs and high blocking efficiencies were observed and targeting higher PMMA DPs led to the expected monotonic increase in the GPC $M_n$. Notably, no systematic GPC error was incurred for this particular data set and the $M_n$ values were reasonably close to the expected theoretical values. However, dispersities were relatively high ($M_w/M_n$ = 1.51–1.76). Similar GPC data were reported by Chaduc and co-workers for the RAFT aqueous emulsion polymerization of MMA using a PMAA precursor at pH 3.5.[24] Clearly, this aqueous PISA formulation does not suffer from colloidal instability problems when targeting relatively high PMMA DPs. This is perhaps not surprising, because aqueous electrophoresis studies of PMAA$_{56}$-PMMA$_{100}$ nanoparticles (**Figure 2.9c**) indicated highly negative zeta potentials (approximately −40 mV at or above pH 5) owing to the strongly anionic nature of the ionized PMAA$_{56}$ chains.

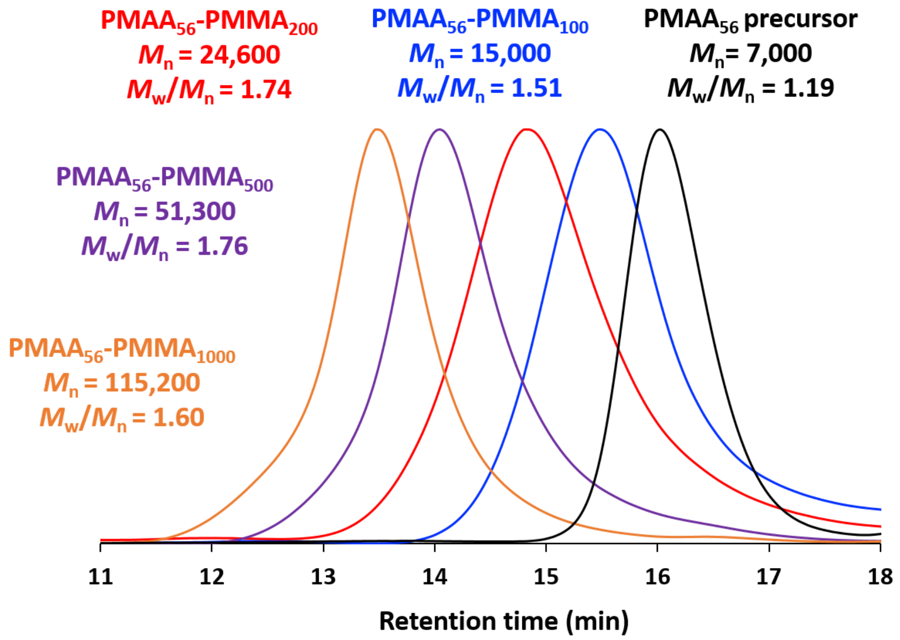

**Figure 2.13.** THF GPC curves recorded for the methylated PMAA$_{56}$ precursor and a series of methylated PMAA$_{56}$-PMMA$_x$ diblock copolymer nanoparticles for which the target PMMA DP ($x$) was 100, 200, 500 or 1000.

Similar results were obtained when employing a cationic steric stabilizer comprising poly(2-(methacryloyloxy)ethyl trimethylammonium chloride) [PMETAC], see **Figure 2.14**. DLS studies indicate a systematic increase in the hydrodynamic *z*-average diameter from 36 nm to 115 nm when targeting a PMMA DP of between 50 and 500. Furthermore, DLS polydispersities remained reasonably low (PDI < 0.15) in each case. The gradual increase in particle diameter is confirmed by TEM but a minor population of smaller spheres is also observed when targeting DPs of 400 or 500. Nevertheless, higher core-forming PMMA DPs could be targeted when using this cationic stabilizer and this particular formulation may be of interest for future studies, particularly if narrower particle size distributions can be obtained. In summary, if relatively large PMMA-core nanoparticles are required for a given application, it is clear that polyelectrolytic stabilizers offer a decisive advantage over non-ionic stabilizers such as PGMA.

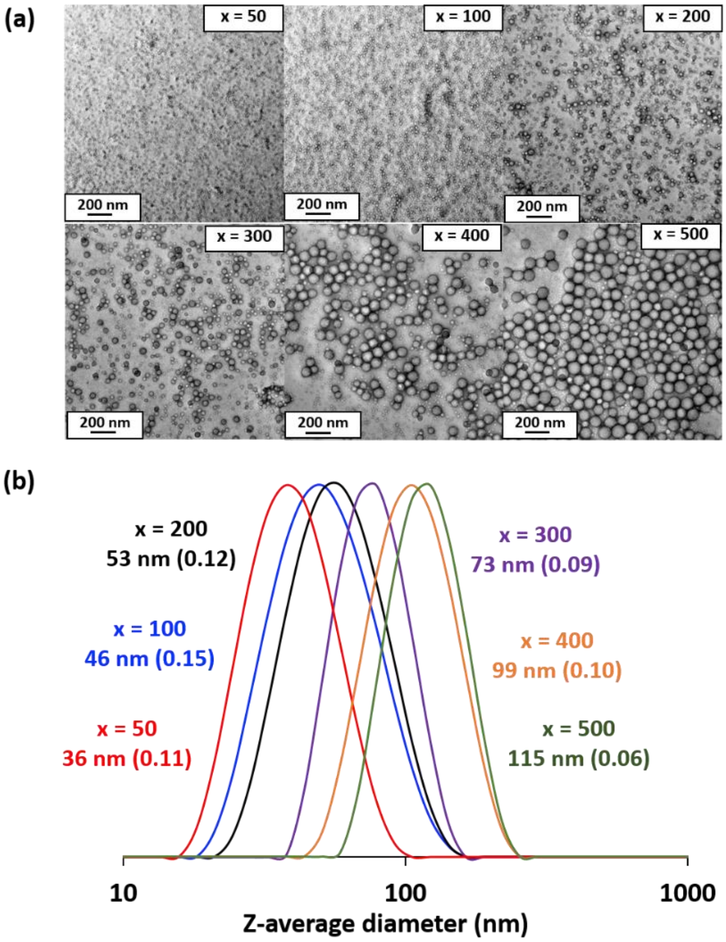

**Figure 2.14.** (a) Representative TEM images and (b) DLS intensity-average size distributions obtained for a series of cationic $PMETAC_{46}$-$PMMA_x$ nanoparticles prepared by RAFT aqueous emulsion polymerization of MMA where the target PMMA DP (x) is 50, 100, 200, 300, 400 or 500.

### 2.3.5 End-group Removal from PGMA-PMMA Nanoparticles Using Visible Light Irradiation

For many potential applications, it is desirable to remove the RAFT end-groups after the polymerization because these organosulfur groups confer color and malodour.[51] For soluble copolymers, this is readily achieved using various chemistries.[59–61] However, there are rather few studies of the removal of RAFT end-groups from diblock copolymer nanoparticles. In 2015, Destarac and co-workers demonstrated that xanthate groups could be efficiently cleaved from aqueous poly(*n*-butyl acrylate) latexes using ozone at ambient temperature.[62]

Subsequently, Jesson *et al.*[49] reported that dithiobenzoate end-groups can be efficiently removed from $PGMA_{52}$-$PHPMA_{135}$ (where PHPMA denotes poly(2-hydroxypropyl methacrylate)) diblock copolymer worms after treatment with $H_2O_2$ at 70 °C for 3 h using a $H_2O_2$/dithiobenzoate molar ratio of 5.0. However, removal of a trithiocarbonate end-group from essentially the same diblock copolymer proved to be much slower, with around 24% organosulfur groups remaining after 8 h under the same reaction conditions. Furthermore, the removal of dithiobenzoate end-groups from $PGMA_{61}$-$PBzMA_{100}$ (where PBzMA denotes poly(benzyl methacrylate)) spheres using this $H_2O_2$ protocol was relatively ineffective, with UV GPC analysis indicating that more than 60% of the original end-groups remained intact after 8 h. This was attributed to the relatively hydrophobic nature of the core-forming PBzMA block, which is likely to impede ingress of the $H_2O_2$ into the nanoparticle cores.

More recently, Gibson and co-workers[63] reported that visible light irradiation (blue LED; $\lambda$ = 405 nm) at 50 °C removed dithiobenzoate end-groups from aqueous dispersions of $PNMEP_{28}$-$PLMA_{87}$ [where PNMEP denotes poly(*N*-(2-methacryloyloxy)ethyl pyrrolidone) and PLMA denotes poly(lauryl methacrylate)] diblock copolymer vesicles. In principle, this approach is attractive because it should not suffer from the retarded diffusion of reagents observed by Jesson and co-workers.[49] Thus, the removal of dithiobenzoate end-groups from 10% w/w aqueous dispersions of $PGMA_{50}$-$PMMA_{80}$ nanoparticles using similar visible light irradiation conditions as those reported by Gibson and co-workers[63] is studied here. Bearing in mind the aqueous solubilities of the respective monomers at room temperature, the hydrophobic character of the core-forming PMMA block is significantly greater than that of PHPMA but rather less than that of either PBzMA or PLMA. Moreover, it is perhaps worth emphasizing that PMMA has a significantly higher glass transition temperature ($T_g$) than these three alternative core-forming blocks and it is not obvious whether the glassy nature of the PMMA nanoparticle cores might impede removal of the RAFT end-groups.

In initial RAFT end-group removal studies, visible light irradiation experiments were conducted at 70 °C. However, only rather slow and incomplete end-group cleavage (86% within 24 h; data not shown) was achieved under such conditions for $PGMA_{50}$-$PMMA_{80}$ nanoparticles prepared using CPDB. Fortunately, we found that significantly higher rates of end-group cleavage could be achieved at 80 °C. Accordingly, the kinetics of dithiobenzoate end-group removal by visible light irradiation (blue LED source; $\lambda$ = 405 nm) of a 10% w/w aqueous dispersion of $PGMA_{50}$-$PMMA_{80}$ nanoparticles at 80 °C was monitored by periodic sampling of the reaction mixture followed by DMF GPC analysis using a UV detector set at 309 nm. Unlike visible absorption spectrophotometry, this technique enables the RAFT end-groups that remain attached to the copolymer chains to be distinguished from those that have been cleaved to produce small molecule by-products.[49]

Representative UV GPC curves are shown in **Figure 2.15a** and the fraction of remaining dithiobenzoate end-groups is plotted against time in **Figure 2.15b**. Initially, relatively rapid cleavage occurs, with 87% of the original end-groups being removed within 12 h at 80 °C. After continuous irradiation for 24 h, 94% end-group removal can be achieved and the initial pink copolymer dispersion is converted into a colorless dispersion (see inset digital photographs). As a comparison, $H_2O_2$ was employed for oxidative end-group removal under the same conditions, as previously reported.[49] However, this only led to 24% end-group removal within 12 h and 58% after 24 h (**Figure 2.15b** and **Figure 2.16a**). This is presumably because this water-soluble reagent cannot readily diffuse into the glassy hydrophobic PMMA cores. The extent of end-group removal was also monitored for the $PGMA_{50}$-$PMMA_{80}$ nanoparticles at 80 °C in the absence of either visible light irradiation or $H_2O_2$. For this control experiment, UV GPC studies (**Figure 2.16b**) indicated that 92% end-groups remained intact after 24 h, suggesting minimal thermally-induced hydrolysis.

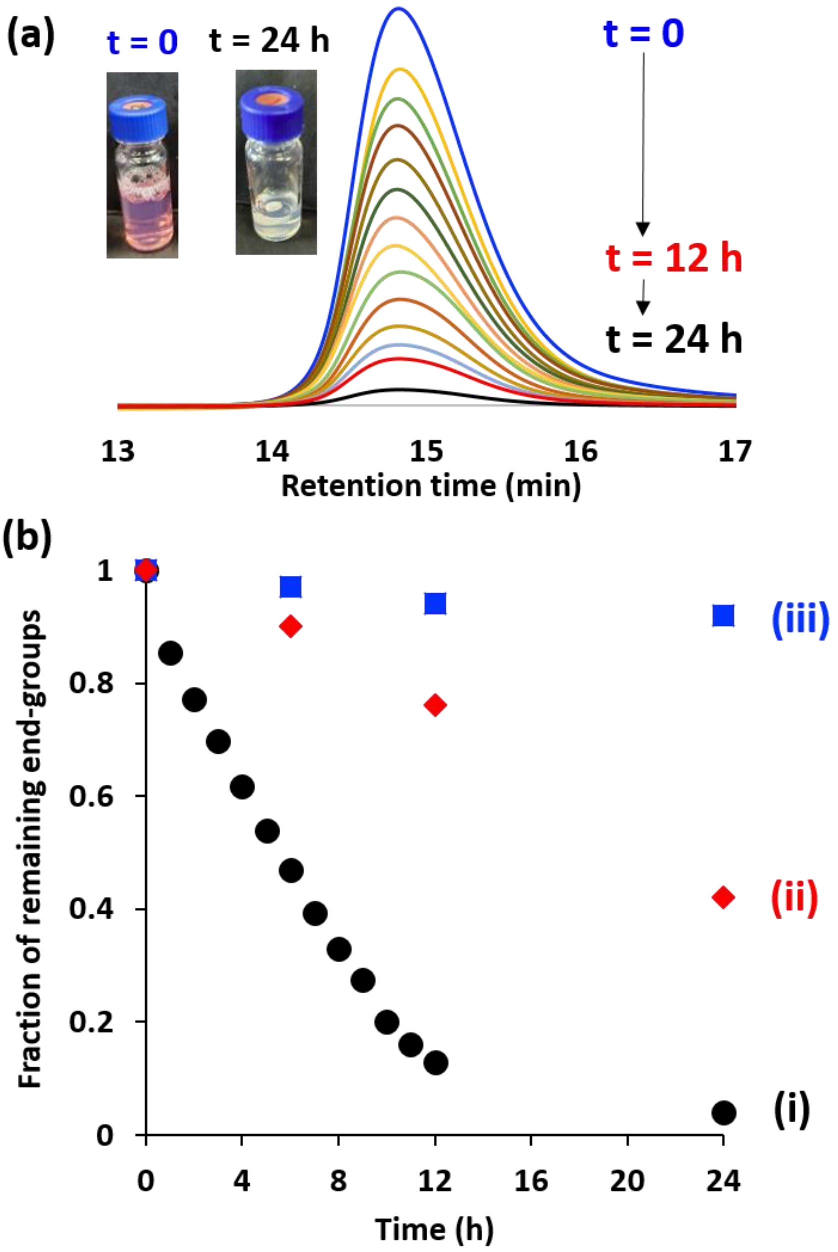

**Figure 2.15.** (a) Representative UV GPC curves ($\lambda = 309$ nm) recorded during kinetic studies of the cleavage of dithiobenzoate end-groups for a 10% w/w aqueous dispersion of $PGMA_{50}$-$PMMA_{80}$ spherical nanoparticles at 80 °C. (b) Fraction of remaining dithiobenzoate RAFT end-groups over time determined by UV GPC analysis when a 10% w/w aqueous dispersion of $PGMA_{50}$-$PMMA_{80}$ spherical nanoparticles at 80 °C is exposed to: (i) continuous visible light irradiation ($\lambda = 405$ nm), (ii) $H_2O_2$ (using a $H_2O_2$/dithiobenzoate molar ratio of 5.0) and (iii) neither visible light nor $H_2O_2$ (control).

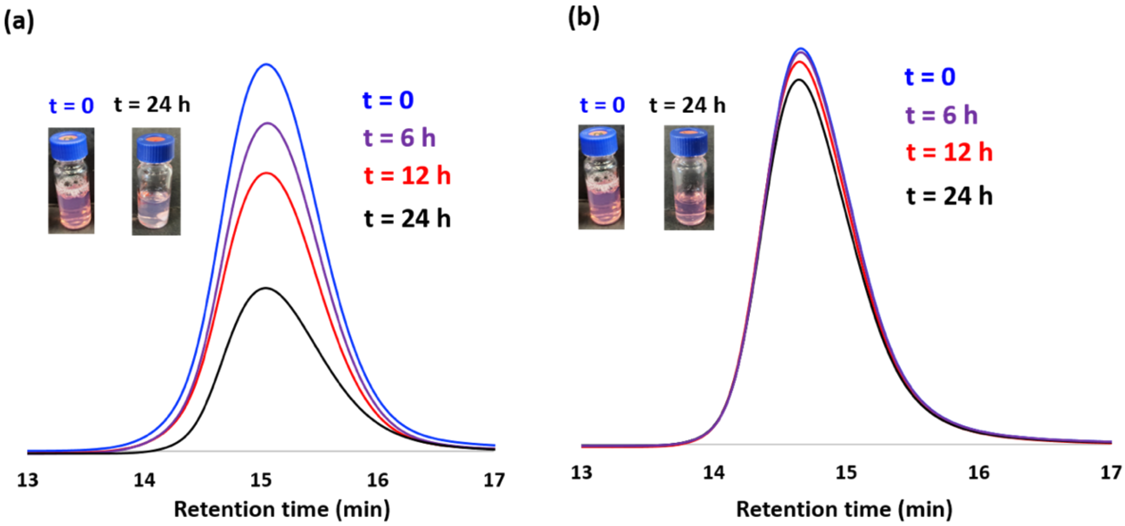

**Figure 2.16.** UV GPC curves (λ = 309 nm) recorded during kinetic studies of the removal of dithiobenzoate end-groups from an aqueous dispersion of PGMA$_{50}$-PMMA$_{80}$ spherical nanoparticles at 80 °C using (a) $H_2O_2$ (using a $H_2O_2$/dithiobenzoate molar ratio of 5.0) and (b) in the absence of either visible light irradiation or $H_2O_2$ (control).

Precisely the same protocol was adopted when studying trithiocarbonate end-group removal from a 10% w/w aqueous dispersion of HOOC-PGMA$_{54}$-PMMA$_{80}$ nanoparticles. The GPC curves and kinetics are summarized in **Figure 2.17**. Cleavage of trithiocarbonate end-groups was achieved, albeit at a somewhat slower rate than that found for the dithiobenzoate end-groups. More specifically, 72% of the original trithiocarbonate groups were cleaved within 12 h at 80 °C with 87% being removed after 24 h. As a control experiment, the trithiocarbonate-capped HOOC-PGMA$_{54}$-PMMA$_{80}$ nanoparticles were exposed to $H_2O_2$ at 80 °C using a $H_2O_2$/trithiocarbonate molar ratio of 5.0. However, UV GPC studies indicated that more than 80% of the original RAFT end-groups remained intact within 24 h. Similarly, a control experiment conducted in the absence of either $H_2O_2$ or visible light irradiation indicated that 96% trithiocarbonate end-groups survived intact after 24 h at 80 °C **(Figure 2.17b)**.

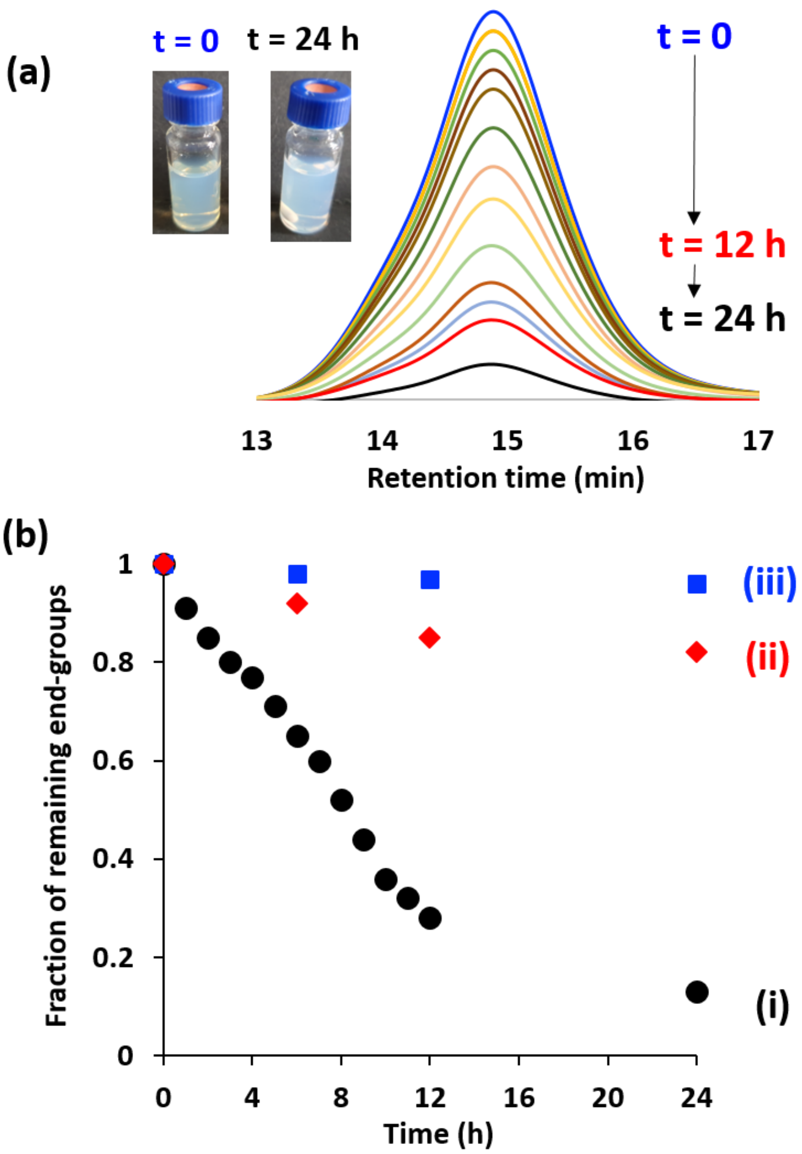

**Figure 2.17.** (a) UV GPC curves (λ = 309 nm) recorded during kinetic studies of the removal of trithiocarbonate end-groups from a 10% w/w aqueous dispersion of HOOC-PGMA$_{54}$-PMMA$_{80}$ spherical nanoparticles at 80 °C. (b) Fraction of remaining trithiocarbonate RAFT end-groups over time determined by UV GPC when a 10% w/w aqueous dispersion of HOOC-PGMA$_{54}$-PMMA$_{80}$ spherical nanoparticles at 80 °C is exposed to: (i) continuous visible light irradiation (λ = 405 nm), (ii) $H_2O_2$ ($H_2O_2$/trithiocarbonate molar ratio = 5.0) and (iii) no visible light irradiation or $H_2O_2$ (control).

Clearly, visible light irradiation can be a highly effective means of removing trithiocarbonate end-groups as well as dithiobenzoate end-groups. This approach works well for both high $T_g$ core-forming blocks such as PMMA (as demonstrated herein) and low $T_g$ core-forming blocks such as PLMA.[63] The only disadvantage appears to be the relatively long reaction time required at 80 °C but presumably this could be reduced by increasing the intensity of the visible light source.

## 2.4 Conclusions

Sterically-stabilized diblock copolymer nanoparticles are prepared by RAFT aqueous emulsion polymerization of MMA using PGMA as a non-ionic steric stabilizer block. For a target PMMA DP of 20 to 100, kinetically-trapped spherical nanoparticles ranging in size from 17 nm to 31 nm are obtained. However, highly flocculated spherical nanoparticles are produced when targeting DPs above 100. Similar flocculation problems are encountered when employing a PGMA stabilizer block that possesses a terminal anionic carboxylate group. Moreover, this unexpected limitation does not appear to apply to various other RAFT aqueous emulsion polymerization formulations: core-forming block DPs of up to 1000 can be targeted without any loss of colloidal stability when employing alternative (and more hydrophobic) water-immiscible monomers such as benzyl methacrylate, 2,2,2-trifluoroethyl methacrylate or isopropylideneglycerol monomethacrylate when using a non-ionic PGMA stabilizer block. This perplexing constraint appears to be related to the high $T_g$ of the PMMA block, which exceeds the reaction temperature of 70 °C used for such PISA syntheses. However, we demonstrate that colloidally stable dispersions can be obtained when targeting PMMA DPs of up to 2000 using a highly anionic PMAA stabilizer block. Similarly, PMMA DPs of up to 500 could also be achieved without any loss in colloidal stability when using a cationic PMETAC stabilizer block. Finally, visible light irradiation is used to cleave dithiobenzoate end-groups from a 10% w/w aqueous dispersion of $PGMA_{50}$-$PMMA_{80}$ nanoparticles. UV GPC studies indicated 87% end-group removal from such nanoparticles within 12 h at 80 °C. In contrast, using excess $H_2O_2$ only led to 24% end-group removal under the same conditions. This striking difference is attributed to the water-soluble reagent having restricted access to the hydrophobic PMMA nanoparticle cores. Furthermore, the same visible light irradiation protocol can be used to remove trithiocarbonate end-groups from HOOC-$PGMA_{54}$-$PMMA_{80}$ nanoparticles.

## 2.5 References

(1) Keddie, D. J.; Moad, G.; Rizzardo, E.; Thang, S. H. RAFT Agent Design and Synthesis. *Macromolecules* **2012**, *45*, 5321–5342.

(2) Biasutti, J. D.; Davis, T. P.; Lucien, F. P.; Heuts, J. P. A. Reversible Addition-Fragmentation Chain Transfer Polymerization of Methyl Methacrylate in Suspension. *J. Polym. Sci. Part A Polym. Chem.* **2005**, *43*, 2001–2012.

(3) Wan, W.; Pan, C. One-Pot Synthesis of Polymeric Nanomaterials via RAFT Dispersion Polymerization Induced Self-Assembly and Re-Organization. *Polym. Chem.* **2010**, *1*, 1475–1484.

(4) Li, Y.; Armes, S. P. RAFT Synthesis of Sterically Stabilized Methacrylic Nanolatexes and Vesicles by Aqueous Dispersion Polymerization. *Angew. Chemie - Int. Ed.* **2010**, *49*, 4042–4046.

(5) Fielding, L. A.; Derry, M. J.; Ladmiral, V.; Rosselgong, J.; Rodrigues, A. M.; Ratcliffe, L. P. D.; Armes, S. P. RAFT Dispersion Polymerization in Non-Polar Solvents: Facile Production of Block Copolymer Spheres, Worms and Vesicles in n-Alkanes. *Chem. Sci.* **2013**, *4*, 2081–2087.

(6) Zhang, X.; Rieger, J.; Charleux, B. Effect of the Solvent Composition on the Morphology of Nano-Objects Synthesized via RAFT Polymerization of Benzyl Methacrylate in Dispersed Systems. *Polym. Chem.* **2012**, *3*, 1502–1509.

(7) Deane, O. J.; Musa, O. M.; Fernyhough, A.; Armes, S. P. Synthesis and Characterization of Waterborne Pyrrolidone- Functional Diblock Copolymer Nanoparticles Prepared via Surfactant-Free RAFT Emulsion Polymerization. *Macromolecules* **2020**, *53*, 1422–1434.

(8) Ferguson, C. J.; Hughes, R. J.; Pham, B. T. T.; Hawkett, B. S.; Gilbert, R. G.; Serelis, A. K.; Such, C. H. Effective Ab Initio Emulsion Polymerization under RAFT Control. *Macromolecules* **2002**, *35*, 9243–9245.

(9) Ferguson, C. J.; Hughes, R. J.; Nguyen, D.; Pham, B. T. T.; Gilbert, R. G.; Serelis, A. K.; Such, C. H.; Hawkett, B. S. Ab Initio Emulsion Polymerization by RAFT-Controlled Self-Assembly. *Macromolecules* **2005**, *38*, 2191–2204.

(10) Rieger, J.; Stoffelbach, F.; Bui, C.; Alaimo, D.; Jérôme, C.; Charleux, B. Amphiphilic Poly(Ethylene Oxide) Macromolecular RAFT Agent as a Stabilizer and Control Agent in Ab Initio Batch Emulsion Polymerization. *Macromolecules* **2008**, *41*, 4065–4068.

(11) Charleux, B.; Delaittre, G.; Rieger, J.; D'Agosto, F. Polymerization-Induced Self-Assembly: From Soluble Macromolecules to Block Copolymer Nano-Objects in One Step. *Macromolecules* **2012**, *45*, 6753–6765.

(12) Canning, S. L.; Smith, G. N.; Armes, S. P. A Critical Appraisal of RAFT-Mediated Polymerization-Induced Self-Assembly. *Macromolecules* **2016**, *49*, 1985–2001.

(13) Zhang, X.; Boissé, S.; Zhang, W.; Beaunier, P.; D'Agosto, F.; Rieger, J.; Charleux, B. Well-Defined Amphiphilic Block Copolymers and Nano-Objects Formed in Situ via RAFT-Mediated Aqueous Emulsion Polymerization. *Macromolecules* **2011**, *44*, 4149–4158.

(14) Boissé, S.; Rieger, J.; Pembouong, G.; Beaunier, P.; Charleux, B. Influence of the Stirring Speed and $CaCl_2$ Concentration on the Nano-object Morphologies Obtained via RAFT-mediated Aqueous Emulsion Polymerization in the Presence of a Water-soluble MacroRAFT Agent. *J. Polym. Sci. Part A Polym. Chem.* **2011**, *49*, 3346–3354.

(15) Zhang, W.; D'Agosto, F.; Boyron, O.; Rieger, J.; Charleux, B. Toward a Better Understanding of the Parameters That Lead to the Formation of Nonspherical Polystyrene Particles via RAFT-Mediated One-Pot Aqueous Emulsion Polymerization. *Macromolecules* **2012**, *45*, 4075–4084.

(16) Carlsson, L.; Fall, A.; Chaduc, I.; Wågberg, L.; Charleux, B.; Malmström, E.; D'Agosto, F.; Lansalot, M.; Carlmark, A. Modification of Cellulose Model Surfaces by Cationic Polymer Latexes Prepared by RAFT-Mediated Surfactant-Free Emulsion Polymerization. *Polym. Chem.* **2014**, *5*, 6076–6086.

(17) Zhang, W.; Charleux, B.; Cassagnau, P. Viscoelastic Properties of Water Suspensions of Polymer Nanofibers Synthesized via RAFT-Mediated Emulsion Polymerization. *Macromolecules* **2012**, *45*, 5273–5280.

(18) Pham, B. T. T.; Nguyen, D.; Huynh, V. T.; Pan, E. H.; Shirodkar-Robinson, B.; Carey, M.; Serelis, A. K.; Warr, G. G.; Davey, T.; Such, C. H.; Hawkett, B. S. Aqueous Polymeric Hollow Particles as an Opacifier by Emulsion Polymerization Using Macro-RAFT Amphiphiles. *Langmuir* **2018**, *34*, 4255–4263.

(19) Albigès, R.; Klein, P.; Roi, S.; Stoffelbach, F.; Creton, C.; Bouteiller, L.; Rieger, J. Water-Based Acrylic Coatings Reinforced by PISA-Derived Fibers. *Polym. Chem.* **2017**, *8*, 4992–4995.

(20) Truong, N. P.; Dussert, M. V.; Whittaker, M. R.; Quinn, J. F.; Davis, T. P. Rapid Synthesis of Ultrahigh Molecular Weight and Low Polydispersity Polystyrene Diblock Copolymers by RAFT-Mediated Emulsion Polymerization. *Polym. Chem.* **2015**, *6*, 3865–3874.

(21) Zhao, W.; Gody, G.; Dong, S.; Zetterlund, P. B.; Perrier, S. Optimization of the RAFT Polymerization Conditions for the in Situ Formation of Nano-Objects via Dispersion Polymerization in Alcoholic Medium. *Polym. Chem.* **2014**, *5*, 6990–7003.

(22) Chaduc, I.; Boyron, O.; Charleux, B.; Agosto, F. D.; Lansalot, M. Effect of the pH on the RAFT Polymerization of Acrylic Acid in Water. Application to the Synthesis of Poly(Acrylic Acid)-Stabilized Polystyrene Particles by RAFT Emulsion Polymerization. *Macromolecules* **2013**, *46*, 6013–6023.

(23) Rieger, J.; Osterwinter, G.; Bui, C.; Charleux, B. Surfactant-Free Controlled/Living

Radical Emulsion (Co) Polymerization of n-Butyl Acrylate and Methyl Methacrylate via RAFT Using Amphiphilic Poly (Ethylene Oxide)-Based Trithiocarbonate Chain Transfer Agents. *Macromolecules* **2009**, *42*, 5518–5525.

(24) Chaduc, I.; Girod, M.; Antoine, R.; Charleux, B.; D’Agosto, F.; Lansalot, M. Batch Emulsion Polymerization Mediated by Poly(Methacrylic Acid) MacroRAFT Agents: One-Pot Synthesis of Self-Stabilized Particles. *Macromolecules* **2012**, *45*, 5881–5893.

(25) Chenal, M.; Véchambre, C.; Chenal, J. M.; Chazeau, L.; Humblot, V.; Bouteiller, L.; Creton, C.; Rieger, J. Mechanical Properties of Nanostructured Films with an Ultralow Volume Fraction of Hard Phase. *Polymer* **2017**, *109*, 187–196.

(26) Binauld, S.; Delafresnaye, L.; Charleux, B.; Dagosto, F.; Lansalot, M. Emulsion Polymerization of Vinyl Acetate in the Presence of Different Hydrophilic Polymers Obtained by RAFT/MADIX. *Macromolecules* **2014**, *47*, 3461–3472.

(27) Cunningham, V. J.; Alswieleh, A. M.; Thompson, K. L.; Williams, M.; Leggett, G. J.; Armes, S. P.; Musa, O. M. Poly(Glycerol Monomethacrylate)-Poly(Benzyl Methacrylate) Diblock Copolymer Nanoparticles via RAFT Emulsion Polymerization: Synthesis, Characterization, and Interfacial Activity. *Macromolecules* **2014**, *47*, 5613–5623.

(28) Akpinar, B.; Fielding, L. A.; Cunningham, V. J.; Ning, Y.; Mykhaylyk, O. O.; Fowler, P. W.; Armes, S. P. Determining the Effective Density and Stabilizer Layer Thickness of Sterically Stabilized Nanoparticles. *Macromolecules* **2016**, *49*, 5160–5171.

(29) Jesson, C. P.; Cunningham, V. J.; Smallridge, M. J.; Armes, S. P. Synthesis of High Molecular Weight Poly(Glycerol Monomethacrylate) via RAFT Emulsion Polymerization of Isopropylideneglycerol Methacrylate. *Macromolecules* **2018**, *51*, 3221–3232.

(30) Brotherton, E. E.; Hatton, F. L.; Cockram, A. A.; Derry, M. J.; Czajka, A.; Cornel, E. J.; Topham, P. D.; Mykhaylyk, O. O.; Armes, S. P. In Situ Small-Angle X-Ray Scattering Studies during Reversible Addition-Fragmentation Chain Transfer Aqueous Emulsion Polymerization. *J. Am. Chem. Soc.* **2019**, *141*, 13664–13675.

(31) Hatton, F. L.; Lovett, J. R.; Armes, S. P. Synthesis of Well-Defined Epoxy-Functional Spherical Nanoparticles by RAFT Aqueous Emulsion Polymerization. *Polym. Chem.* **2017**, *8*, 4856–4868.

(32) Tan, J.; Liu, D.; Huang, C.; Li, X.; He, J.; Xu, Q.; Zhang, L. Photoinitiated Polymerization-Induced Self-Assembly of Glycidyl Methacrylate for the Synthesis of Epoxy-Functionalized Block Copolymer Nano-Objects. *Macromol. Rapid Commun.* **2017**, *38*, 1–7.

(33) Hatton, F. L.; Park, A. M.; Zhang, Y.; Fuchs, G. D.; Ober, C. K.; Armes, S. P. Aqueous One-Pot Synthesis of Epoxy-Functional Diblock Copolymer Worms from a Single Monomer: New Anisotropic Scaffolds for Potential Charge Storage Applications. *Polym. Chem.* **2019**, *10*, 194–200.

(34) Hatton, F. L.; Derry, M. J.; Armes, S. P. Rational Synthesis of Epoxy-Functional Spheres, Worms and Vesicles by RAFT Aqueous Emulsion Polymerisation of Glycidyl Methacrylate. *Polym. Chem.* **2020**, *11*, 6343–6355.

(35) Cockram, A. A.; Neal, T. J.; Derry, M. J.; Mykhaylyk, O. O.; Williams, N. S. J.; Murray, M. W.; Emmett, S. N.; Armes, S. P. Effect of Monomer Solubility on the Evolution of Copolymer Morphology during Polymerization-Induced Self-Assembly in Aqueous Solution. *Macromolecules* **2017**, *50*, 796–802.

(36) Zhang, W.; D'Agosto, F.; Dugas, P. Y.; Rieger, J.; Charleux, B. RAFT-Mediated One-Pot Aqueous Emulsion Polymerization of Methyl Methacrylate in Presence of Poly(Methacrylic Acid-Co-Poly(Ethylene Oxide) Methacrylate) Trithiocarbonate Macromolecular Chain Transfer Agent. *Polymer* **2013**, *54*, 2011–2019.

(37) Hatton, F. L.; Ruda, M.; Lansalot, M.; Agosto, F. D.; Malmstro, E.; Carlmark, A. Xyloglucan-Functional Latex Particles via RAFT-Mediated Emulsion Polymerization for the Biomimetic Modification of Cellulose. *Biomacromolecules* **2016**, *17*, 1414–1424.

(38) Engström, J.; Asem, H.; Brismar, H.; Zhang, Y.; Malkoch, M.; Malmström, E. In Situ Encapsulation of Nile Red or Doxorubicin during RAFT-Mediated Emulsion Polymerization via Polymerization-Induced Self-Assembly for Biomedical Applications. *Macromol. Chem. Phys.* **2020**, *221*, 1900443.

(39) Hunter, S. J.; Lovett, J. R.; Mykhaylyk, O. O.; Jones, E. R.; Armes, S. P. Synthesis of Diblock Copolymer Spheres, Worms and Vesicles via RAFT Aqueous Emulsion Polymerization of Hydroxybutyl Methacrylate. *Polym. Chem.* **2021**, *12*, 3629–3639.

(40) Chatterjee, S.; Upadhyay, P.; Mishra, M.; Srividya, M.; Akshara, M. R.; Kamali, N.; Zaidi, Z. S.; Iqbal, S. F.; Misra, S. K. Advances in Chemistry and Composition of Soft Materials for Drug Releasing Contact Lenses. *RSC Adv.* **2020**, *10*, 36751–36777.

(41) Giacomelli, C.; Schmidt, V.; Borsali, R. Nanocontainers Formed by Self-Assembly of Poly(Ethylene Oxide)-b-Poly(Glycerol Monomethacrylate) - Drug Conjugates. *Macromolecules* **2007**, *40*, 2148–2157.

(42) Canton, I.; Warren, N. J.; Chahal, A.; Amps, K.; Wood, A.; Weightman, R.; Wang, E.; Moore, H.; Armes, S. P. Mucin-Inspired Thermoresponsive Synthetic Hydrogels Induce Stasis in Human Pluripotent Stem Cells and Human Embryos. *ACS Cent. Sci.* **2016**, *2*, 65–74.

(43) Hassan, E.; Deshpande, P.; Claeyssens, F.; Rimmer, S.; Macneil, S. Amine Functional Hydrogels as Selective Substrates for Corneal Epithelialization. *Acta Biomater.* **2014**, *10*, 3029–3037.

(44) Save, M.; Weaver, J. V. M.; Armes, S. P.; McKenna, P. Atom Transfer Radical Polymerization of Hydroxy-Functional Methacrylates at Ambient Temperature: Comparison of Glycerol Monomethacrylate with 2-Hydroxypropyl Methacrylate.

*Macromolecules* **2002**, *35*, 1152–1159.

(45) Olszewski-Ortar, A.; Gros, P.; Fort, Y. Selective Ring-Opening of ω-Epoxyalkyl (Meth)Acrylates. An Efficient Access to Bifunctional Monomers. *Tetrahedron Lett.* **1997**, *38*, 8699–8702.

(46) Shaw, S. E.; Russo, T.; Solomon, D. H.; Qiao, G. G. An Alternative Pathway for the Hydrolysis of Epoxy Ester Compounds. *Polymer* **2006**, *47*, 8247–8252.

(47) Ratcliffe, L. P. D.; Ryan, A. J.; Armes, S. P. From a Water-Immiscible Monomer to Block Copolymer Nano-Objects via a One-Pot RAFT Aqueous Dispersion Polymerization Formulation. *Macromolecules* **2013**, *46*, 769–777.

(48) Semsarilar, M.; Ladmiral, V.; Blanazs, A.; Armes, S. P. Cationic Polyelectrolyte-Stabilized Nanoparticles via RAFT Aqueous Dispersion Polymerization. *Langmuir* **2013**, *29*, 7416–7424.

(49) Jesson, C. P.; Pearce, C. M.; Simon, H.; Werner, A.; Cunningham, V. J.; Lovett, J. R.; Smallridge, M. J.; Warren, N. J.; Armes, S. P. $H_2O_2$ Enables Convenient Removal of RAFT End-Groups from Block Copolymer Nano-Objects Prepared via Polymerization-Induced Self- Assembly in Water. *Macromolecules* **2017**, *50*, 182–191.

(50) Ilavsky, J.; Jemian, P. R. Irena: Tool Suite for Modeling and Analysis of Small-Angle Scattering. *J. Appl. Crystallogr.* **2009**, *42*, 347–353.

(51) Perrier, S. 50th Anniversary Perspective: RAFT Polymerization - A User Guide. *Macromolecules* **2017**, *50*, 7433–7447.

(52) Guinier, A.; Fournet, G. *Small-Angle Scattering of X-Rays*; John Wiley & Sons: New York, 1955.

(53) Glatter, O.; Kratky, O. *Small-Angle X-Ray Scattering*; Academic Press: London, 1982.

(54) Pedersen, J. S. Form Factors of Block Copolymer Micelles with Spherical, Ellipsoidal and Cylindrical Cores. *J. Appl. Crystallogr.* **2000**, *33*, 637–640.

(55) Beaucage, G.; Schaefer, D. W. Structural Studies of Complex Systems Using Small-Angle Scattering: A Unified Guinier/Power-Law Approach. *J. Non. Cryst. Solids* **1994**, *172–174*, 797–805.

(56) Beaucage, G. Approximations Leading to a Unified Exponential/Power-Law Approach to Small-Angle Scattering. *J. Appl. Crystallogr.* **1995**, *28*, 717–728.

(57) Beaucage, G. Small-Angle Scattering from Polymeric Mass Fractals of Arbitrary Mass-Fractal Dimension. *J. Appl. Crystallogr.* **1996**, *29*, 134–146.

(58) Lovett, J. R.; Warren, N. J.; Ratcliffe, L. P. D.; Kocik, M. K.; Armes, S. P. pH-Responsive Non-Ionic Diblock Copolymers: Ionization of Carboxylic Acid End-Groups Induces an Order-Order Morphological Transition. *Angew. Chemie - Int. Ed.* **2015**, *54*, 1279–1283.

(59) Perrier, S.; Takolpuckdee, P. Macromolecular Design via Reversible Addition-Fragmentation Chain Transfer (RAFT)/Xanthates (MADIX) Polymerization. *J. Polym.*

*Sci. Part A Polym. Chem.* **2005**, *43*, 5347–5393.

(60) Willcock, H.; O'Reilly, R. K. End Group Removal and Modification of RAFT Polymers. *Polym. Chem.* **2010**, *1*, 149–157.

(61) Quiclet-Sire, B.; Zard, S. Z. A Convenient, High Yielding Cleavage of the Thiocarbonyl Group in Xanthates. *Bull. Korean Chem. Soc.* **2010**, *31*, 543–544.

(62) Matioszek, D.; Dufils, P. E.; Vinas, J.; Destarac, M. Selective and Quantitative Oxidation of Xanthate End-Groups of RAFT Poly(n-Butyl Acrylate) Latexes by Ozonolysis. *Macromol. Rapid Commun.* **2015**, *36*, 1354–1361.

(63) Gibson, R. R.; Cornel, E. J.; Musa, O. M.; Fernyhough, A.; Armes, S. P. RAFT Dispersion Polymerisation of Lauryl Methacrylate in Ethanol-Water Binary Mixtures: Synthesis of Diblock Copolymer Vesicles with Deformable Membranes. *Polym. Chem.* **2020**, *11*, 1785–1796.

# Chapter 3

# Block Copolymer Nanoparticles are Effective Dispersants for Micrometer-Sized Organic Crystalline Particles

Reproduced in full with permission from [Chan, D. H. H.; Kynaston, E. L.; Lindsay, C.; Taylor, P.; Armes, S. P. Block Copolymer Nanoparticles Are Effective Dispersants for Micrometer-Sized Organic Crystalline Particles. *ACS Appl. Mater. Interfaces* **2021**, *13*, 30235–30243.]

## 3.1 Introduction

Azoxystrobin is a broad spectrum strobilurin fungicide that is widely used for the control of a range of diseases in cereals, brassicae, beans, asparagus, peas, oil seed rape, potatoes, carrots, alliums, strawberries, lettuce and other food crops.[1,2] This molecule preferentially binds at the quinol outer binding site of the cytochrome b-c1 complex relative to ubiquinone (coenzyme Q10), which transports electrons to this protein. This prevents ATP production and hence inhibits mitochondrial respiration.[3] The chemical structure of azoxystrobin is shown in **Figure 3.1**. It is an organic crystalline compound with a melting point of 116 °C, and it has a relatively low aqueous solubility of 6.7 mg $dm^{-3}$. Consequently, azoxystrobin is usually formulated as a concentrated aqueous dispersion of micron-sized particles (also known as ‘suspension concentrates’ or SC) using various water-soluble synthetic polymers or biopolymers as dispersants.[4] Recently, submicrometer-sized azoxystrobin particles have been prepared and shown to exhibit greater efficacy.[5,6] Such colloidal dispersions were reported to be “self-dispersible” but in fact a commercial *Pluronic*-type block copolymer was used for their preparation.[5]

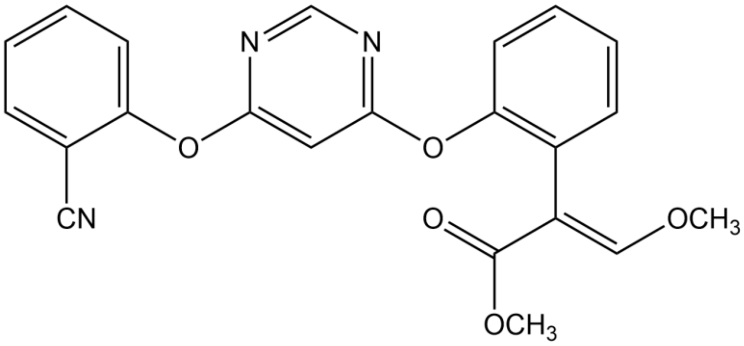

**Figure 3.1.** Chemical structure of azoxystrobin, a member of the strobilurin family. This broad-spectrum fungicide is used to prevent a wide range of crop diseases.

In the colloid science literature, there are many examples of the physical adsorption of small particles onto large particles. Often, such studies involve model systems,[7–12] but potential applications include new routes to (i) core-shell particles for paints and coatings applications[13,14] and (ii) polymer-silica nanocomposite particles.[15–17] In addition, North and co-workers reported that 30 nm diameter diblock copolymer nanoparticles can act as a particulate dispersant for 470 nm diameter silica particles, which serve as a model pigment. At pH 7, the weakly basic nanoparticles acquired cationic character and their electrostatic adsorption onto the anionic silica particles led to a fractional surface coverage of 0.51 as judged by XPS.[18]

As discussed in Chapter 1, PISA is as a powerful and versatile platform technology for the rational synthesis of sterically stabilized diblock copolymer nanoparticles of controllable size and shape.[19–26] Of particular relevance to the present study, PISA can be conducted in aqueous media using reversible addition–fragmentation chain transfer (RAFT) polymerization.[26–28] Depending on the aqueous solubility of the vinyl monomer, this may involve either an aqueous emulsion or an aqueous dispersion formulation.[29–31]

According to the PISA literature, a wide range of non-ionic, anionic, cationic, and zwitterionic polymers can be used as water-soluble stabilizer blocks.[31–39] Indeed, Chapter 2 describes the use of non-ionic, anionic or cationic blocks for the RAFT aqueous emulsion polymerization of methyl methacrylate (MMA). Similarly, various other water-insoluble core-forming blocks have been examined, including polystyrene, poly(benzyl methacrylate) and poly(*n*-butyl acrylate).[32,33,40,41] In many cases, the copolymer morphology comprises solely kinetically-trapped spheres, even if highly asymmetric diblock compositions are targeted.[32,42–45] Such nanoparticles have been evaluated for coatings applications[40] and as Pickering emulsifiers for the preparation of oil-in-water emulsions.[46]

Herein, similar diblock copolymer nanoparticles to those prepared in Chapter 2 are utilized. More specifically, a non-ionic PGMA$_{50}$ precursor is chain-extended *via* RAFT aqueous emulsion polymerization of MMA to produce PGMA$_{50}$-PMMA$_{80}$ spherical nanoparticles. Such sterically-stabilized nanoparticles are then evaluated as a putative dispersant for organic crystalline microparticles produced *via* ball milling. This aqueous SC formulation is exemplified for azoxystrobin, one of the world’s most widely used fungicides (see **Scheme 3.1**). To aid characterization of such azoxystrobin microparticles, sterically-stabilized nanoparticles of comparable size were prepared *via* RAFT aqueous emulsion polymerization of 2,2,2-trifluoroethyl methacrylate (TFEMA) using the same $PGMA_{50}$ precursor.[47] This is because the corresponding semi-fluorinated PTFEMA block should offer superior electron contrast when characterizing the nanoparticle-coated microparticles by transmission electron microscopy.

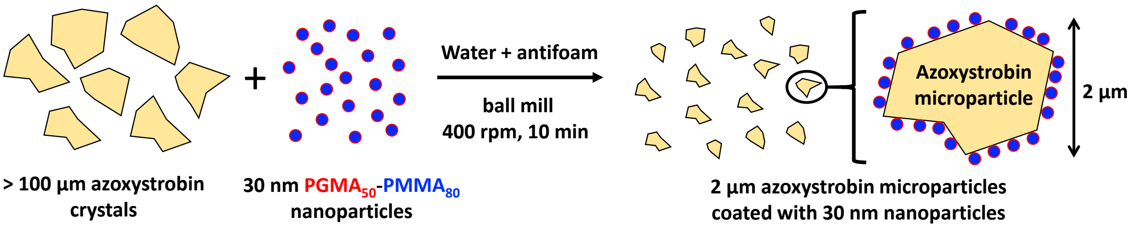

**Scheme 3.1.** Schematic representation of the preparation of 2 µm azoxystrobin microparticles in the form of a 20% w/w aqueous suspension concentrate by ball milling macroscopic azoxystrobin crystals in the presence of an aqueous dispersion of approximately 30 nm diameter nanoparticles [N.B. Individual components are not drawn to scale].

## 3.2 Experimental

### 3.2.1 Materials

MMA (99%), TFEMA (99%), 4,4′-azobis(4-cyanopentanoic acid) (ACVA; 98%), 2-cyanopropyl dithiobenzoate (CPDB; 97%), and Triton X-100 were purchased from Sigma-Aldrich (UK) and used as received. Glycerol monomethacrylate (GMA) was donated by GEO Specialty Chemicals (Hythe, UK), and the commercial dispersant Morwet D-425 was obtained from AkzoNobel (Sweden). Azoxystrobin was provided by Syngenta (Jealott's Hill, UK). The antifoaming agent silicone SAG1572 was purchased from Momentive (Germany), and 1.0 mm zirconium aluminum oxide beads were purchased from Sigmund-Lindner (Germany). Deionized water from an Elga Medica DV25 water purification unit was used in all the experiments.

### Synthesis Protocols

### 3.2.2 Synthesis of the $PGMA_{50}$ Precursor by RAFT Aqueous Solution Polymerization

See Chapter 2, **section 2.2.2** for full details.

### 3.2.3 Synthesis of $PGMA_{50}$-$PMMA_{80}$ Diblock Copolymer Nanoparticles by RAFT Aqueous Emulsion Polymerization

An aqueous emulsion comprising the $PGMA_{50}$ precursor (0.150 g, 18.2 μmol), MMA monomer (0.146 g, 1.46 mmol), ACVA initiator (1.0 mg, 3.65 μmol, CTA/ACVA molar ratio = 5.0), and deionized water (2.675 g, 10% w/w solution) was made up in a 20 mL round-bottom flask. This flask was immersed in an ice bath and the emulsion was deoxygenated using a stream of $N_2$ gas for 30 min. The flask was then placed in an oil bath set at 70 °C, and the ensuing polymerization was quenched after 3 h by exposing the flask contents to air while cooling to 20 °C.

### 3.2.4 Synthesis of $PGMA_{50}$-$PTFEMA_{80}$ Diblock Copolymer Nanoparticles by RAFT Aqueous Emulsion Polymerization

An aqueous emulsion comprising the $PGMA_{50}$ precursor (0.150 g, 18.2 μmol), TFEMA monomer (0.245 g, 1.46 mmol), ACVA initiator (1.0 mg, 3.65 μmol, CTA/ACVA molar ratio = 5.0), and deionized water (3.568 g, 10% w/w solution) was made up in a 20 mL round-bottom flask. This flask was immersed in an ice bath, and the emulsion was deoxygenated using a stream of $N_2$ gas for 30 min. The flask was then placed in an oil bath set at 70 °C, and the ensuing polymerization was quenched after 6 h by exposing the flask contents to air while cooling to 20 °C.

### 3.2.5 Preparation of Suspension Concentrates by Ball Milling

Azoxystrobin (3.00 g), $PGMA_{50}$-$PMMA_{80}$ nanoparticles (0.375 g, 2.5% w/w), SAG1572 antifoaming agent (0.15 g, 1.0% w/w), and deionized water (11.48 g, 76.5%) were added to a 50 mL Retsch zirconium oxide-coated jar along with 1.0 mm ceramic beads (15.0 g). A Retsch PM 100 planetary ball mill was used to mill this suspension at 400 rpm for 10 min. The beads were removed by filtration to afford a 20% w/w suspension concentrate.

### 3.2.6 Centrifugal Purification of Suspension Concentrates

SCs were centrifuged for 5 min at 5 000 rpm using a Thermo Heraeus Biofuge Pico centrifuge and the aqueous supernatant containing excess copolymer nanoparticles was carefully decanted. The sedimented microparticles were redispersed using deionized water. Two further centrifugation/redispersion cycles were performed prior to characterization of the purified nanoparticle-coated azoxystrobin microparticles.

### 3.2.7 Examination of the Stability of Suspension Concentrates Using a Surfactant Challenge

The suspension concentrates (1.0 g) and Triton X-100 surfactant (10.0 mg, 1.0% w/w) were weighed into a 5 mL vial, which was placed on a roller mixer for 24 h at 20 °C prior to transmission electron microscopy (TEM) analysis.

### 3.2.8 Characterization Techniques

**Dynamic Light Scattering and Aqueous Electrophoresis**

A Malvern Zetasizer NanoZS instrument was used to perform both DLS and aqueous electrophoresis studies with an aqueous dispersion concentration of 0.50% w/w being used in each case. Hydrodynamic *z*-average diameters were determined at 20 °C using a scattering angle of 173°, and measurements were averaged over three runs. Aqueous electrophoresis experiments utilized 1 mM KCl as background salt, and the solution pH being adjusted as required with either HCl or NaOH. The Smoluchkowski approximation was used to calculate zeta potentials (also averaged over three measurements) *via* the Henry equation.

**Gel Permeation Chromatography**

Molecular weight distributions were assessed for the $PGMA_{50}$ precursor, the $PGMA_{50}$-$PMMA_{80}$ diblock copolymer, and the $PGMA_{50}$-$PTFEMA_{80}$ diblock copolymer by GPC analysis at 60 °C using DMF eluent (containing 10 mM LiBr), two Agilent PL gel 5 μm Mixed-C columns connected to a Varian 290-LC pump injection module, and a Varian 390-LC multidetector suite (refractive index detector). A series of near-monodisperse poly(methyl methacrylate) standards ranging from $M_n$ = 645 g mol$^{-1}$ to 618 000 g mol$^{-1}$ were used for calibration at a flow rate of 1.0 mL min$^{-1}$.

### Optical Microscopy

A Cole-Palmer optical microscope fitted with a Moticam camera and an LCD tablet was used for imaging both the original coarse azoxystrobin crystals and the much finer azoxystrobin microparticles obtained after milling.

### Transmission Electron Microscopy

Copper/palladium TEM grids (Agar Scientific, UK) were coated with a thin film of amorphous carbon and then treated with a plasma glow discharge for 30 s. A 10 μL droplet of a 0.10% w/w aqueous dispersion (or SC) was placed on each grid for 60 s before blotting. Each particle-loaded grid was stained for 20 s using uranyl formate (9.0 μL of 0.75% w/w solution) before removing excess stain and drying under vacuum. TEM studies were performed at 100 kV using a Philips CM100 instrument equipped with a Gatan 1 k CCD camera.

### Laser Diffraction

The initial coarse active ingredients and final milled microparticles were sized by laser diffraction using a Malvern Mastersizer 3000 instrument equipped with a Hydro EV wet dispersion unit set at 2 000 rpm, a red HeNe laser (λ = 633 nm) and a light-emitting blue light source (λ = 470 nm). The volume-average particle diameter, d(0.5), was calculated by averaging over five measurements. After each measurement, the instrument was thoroughly rinsed with deionized water (three times) to prevent contamination.

### Scanning Electron Microscopy

Scanning electron microscopy (SEM) images were recorded using an FEI Inspect-F instrument at an accelerating voltage of 10 kV. Samples were allowed to dry overnight on thin glass slides and then sputter-coated with a thin overlayer of gold before imaging.

**Solution Densitometry**

An Anton Paar DMA 4500 M density meter was used to determine the solution densities of 0.50–5.00% w/w aqueous dispersions of $PGMA_{50}$-$PMMA_{80}$ nanoparticles and also various aqueous supernatants obtained after centrifugation of a series of SCs at 20 °C. The adsorbed amount of polymer, $\Gamma$ (in mg $m^{-2}$) could be calculated assuming 2 μm azoxystrobin microparticles had a surface area of 2.2 $m^2$ $g^{-1}$.

**X-ray Photoelectron Spectroscopy**

Azoxystrobin, $PGMA_{50}$-$PTFEMA_{80}$ nanoparticles, $PGMA_{50}$-$PMMA_{80}$ nanoparticles, and the two types of nanoparticle-coated azoxystrobin microparticles were placed in turn on indium foil and analyzed using a Kratos Axis Supra X-ray photoelectron spectrometer. Survey spectra were recorded for each sample using a step size of 0.50 eV. High resolution core-line spectra were recorded for each element of interest using a step size of 0.05 eV.

## 3.3 Results and Discussion

### 3.3.1 Synthesis of $PGMA_{50}$-$PMMA_{80}$ and $PGMA_{50}$-$PTFEMA_{80}$ Diblock Copolymer Nanoparticles by RAFT Aqueous Emulsion Polymerization

A $PGMA_{50}$ precursor was synthesized by RAFT solution polymerization of GMA in methanol using a dithiobenzoate-based RAFT agent (CPDB). After purification, $^1$H NMR spectroscopy was used to calculate a mean DP of 50 for this homopolymer by end-group analysis (See Chapter 2, **section 2.3.1** for details) This precursor was then chain-extended *via* RAFT aqueous emulsion polymerization of MMA to afford $PGMA_{50}$-$PMMA_{80}$ nanoparticles, with essentially full conversion being achieved within 3 h at 70 °C (**Scheme 3.2a**). A similar protocol was also used to prepare the equivalent $PGMA_{50}$-$PTFEMA_{80}$ nanoparticles and full conversion was achieved within 6 h at 70 °C (**Scheme 3.2b**).

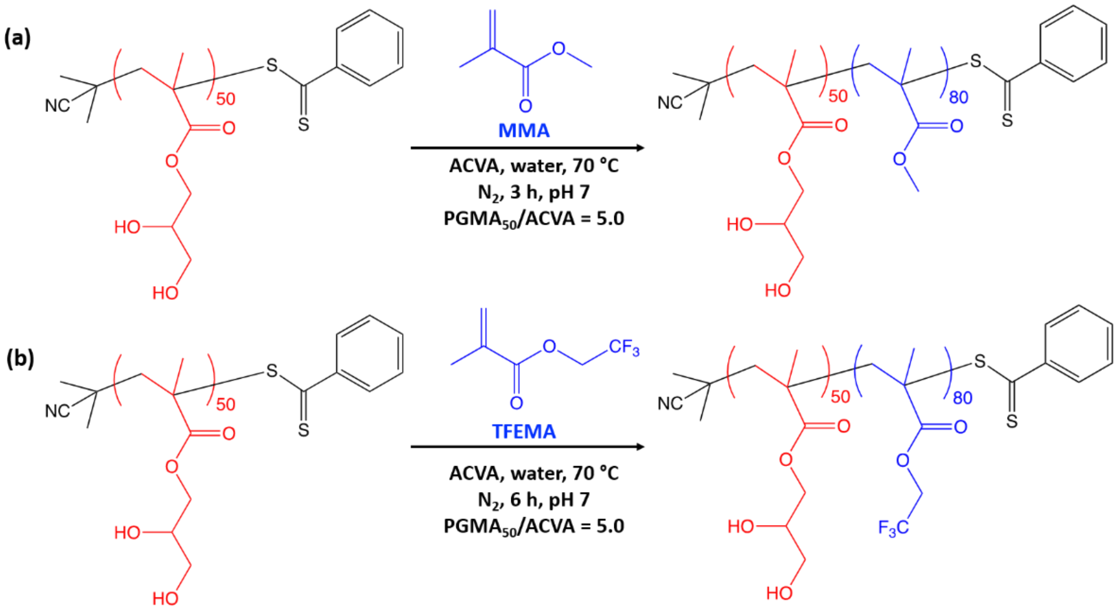

**Scheme 3.2.** Synthesis of (a) $PGMA_{50}$-$PMMA_{80}$ and (b) $PGMA_{50}$-$PTFEMA_{80}$ diblock copolymer nanoparticles by RAFT aqueous emulsion polymerization using a water-soluble poly(glycerol monomethacrylate) ($PGMA_{50}$) precursor at 70 °C.

DMF GPC analysis (**Figure 3.2a**) confirmed the expected increase in molecular weight for the $PGMA_{50}$-$PMMA_{80}$ diblock copolymer chains relative to the $PGMA_{50}$ homopolymer precursor, and the relatively low dispersity ($M_w/M_n = 1.15$) is consistent with a well-controlled RAFT polymerization. The $PGMA_{50}$-$PMMA_{80}$ diblock copolymer nanoparticles were characterized in terms of their particle size using DLS and TEM (see **Figure 3.2b,c**). DLS studies indicated a *z*-average diameter of 29 ± 4 nm, while TEM analysis confirmed a spherical morphology and a number-average diameter of 25 ± 3 nm.

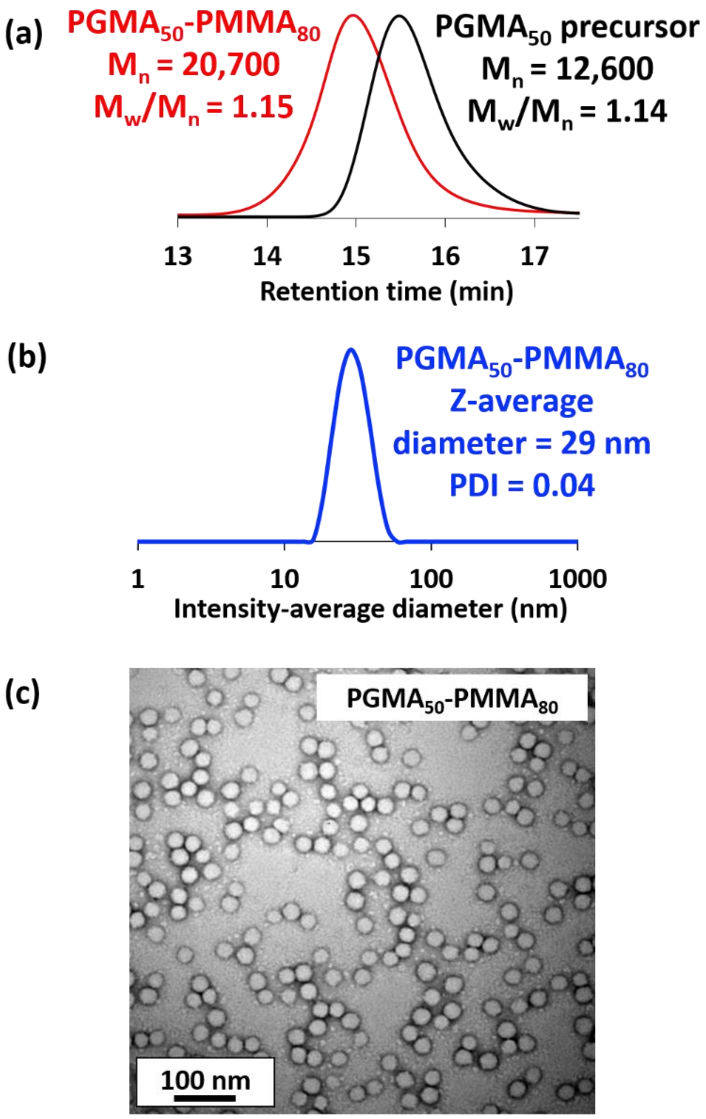

**Figure 3.2.** (a) GPC curves recorded for the $PGMA_{50}$ precursor and $PGMA_{50}$-$PMMA_{80}$ nanoparticles; (b) DLS intensity-average particle size distribution (plus *z*-average diameter and polydispersity, PDI); and (c) TEM image recorded for $PGMA_{50}$-$PMMA_{80}$ spherical nanoparticles.

Similar GPC, DLS and TEM analyses were performed on the $PGMA_{50}$-$PTFEMA_{80}$ nanoparticles (**Figure 3.3**). DMF GPC confirmed the expected increase in molecular weight for the diblock copolymer chains relative to the $PGMA_{50}$ precursor, and a relatively low dispersity was obtained ($M_w/M_n$ = 1.12). DLS studies indicated a *z*-average diameter of 33 ± 4 nm, while TEM analysis confirmed a spherical morphology and a number-average diameter of 30 ± 3 nm.

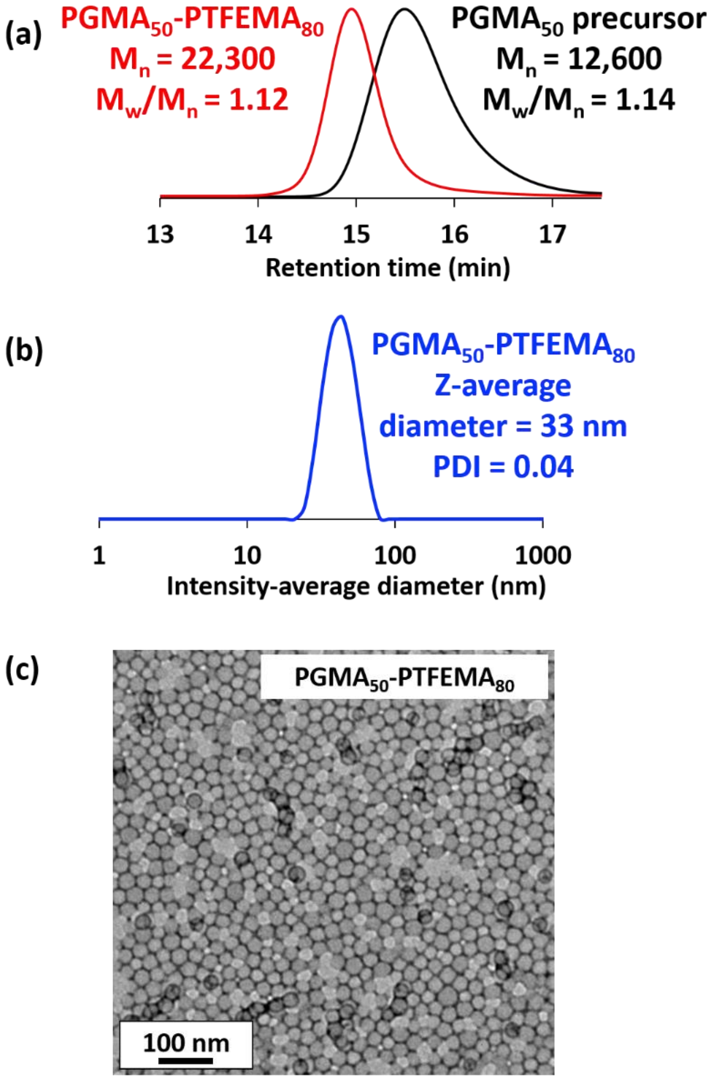

**Figure 3.3.** (a) GPC curves recorded for the $PGMA_{50}$ precursor and $PGMA_{50}$-$PTFEMA_{80}$ nanoparticles; (b) DLS intensity-average particle size distribution (plus *z*-average diameter and polydispersity, PDI); and (c) TEM image recorded for $PGMA_{50}$-$PTFEMA_{80}$ spherical nanoparticles.

Thus, diblock copolymer nanoparticles with differing core-forming blocks can be used as dispersants for the preparation of azoxystrobin SCs *via* ball milling. MMA is a much more cost-effective choice than TFEMA, but the $PGMA_{50}$-$PTFEMA_{80}$ nanoparticles are expected to offer superior electron contrast for TEM characterization. Furthermore, studying the effect of changing the core-forming block on both the milling efficiency and the final azoxystrobin particle size is of fundamental scientific interest. These initial studies utilize diblock copolymer nanoparticles with comparable *z*-average diameters (see **Figures 3.2 and 3.3)**: the effect of systematically adjusting the nanoparticle diameter will be discussed in Chapter 4.

### 3.3.2 Preparation of Suspension Concentrates by Ball Milling

In the context of agrochemical science, hydrophobic organic crystalline compounds are typically milled in the presence of a suitable dispersant to prepare SC formulations.[48,49] Accordingly, ball milling of azoxystrobin crystals was performed in the presence of an aqueous dispersion of $PGMA_{50}$-$PMMA_{80}$ nanoparticles, which was used instead of a conventional water-soluble copolymer dispersant (**Scheme 3.1**). The size distributions obtained by laser diffraction for the initial azoxystrobin crystals and the final azoxystrobin microparticles after milling in the presence of such nanoparticles are shown in **Figure 3.4**. A substantial reduction in the volume-average particle diameter from 76 μm to approximately 2 μm was achieved after milling for just 10 min under the stated conditions. These laser diffraction data were supported by optical microscopy studies, which also indicated a marked reduction in the mean size of the azoxystrobin crystals (**Figure 3.5a,b**). Clearly, the $PGMA_{50}$-$PMMA_{80}$ nanoparticles can act as both a wetting agent and an effective dispersant, which enables a free-flowing SC to be obtained at 20% w/w solids.

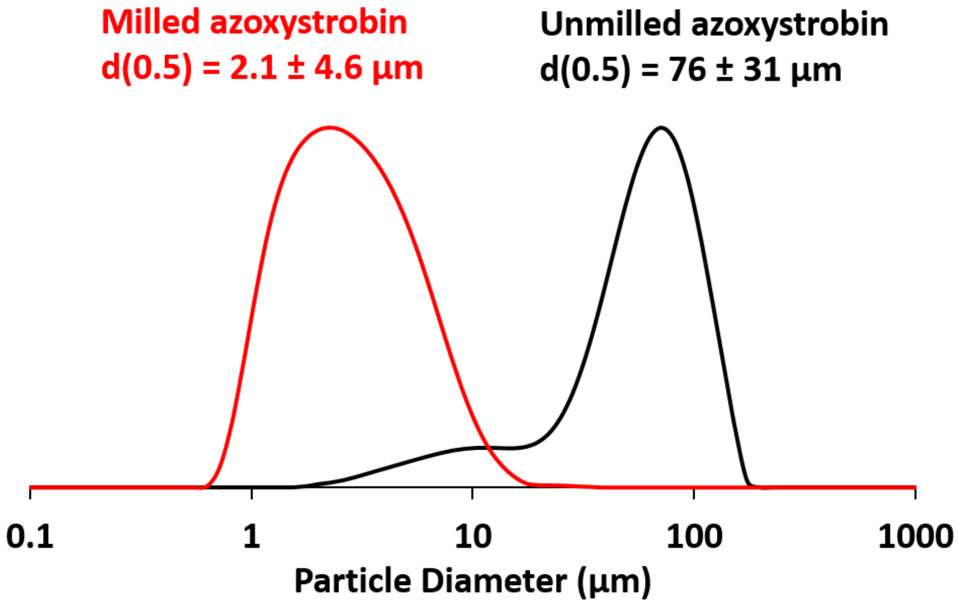

**Figure 3.4.** Laser diffraction particle size distribution curves (based on a volume-weighted average) recorded for the original coarse azoxystrobin particles and the much finer $PGMA_{50}$-$PMMA_{80}$ nanoparticle-coated azoxystrobin microparticles obtained after ball milling.

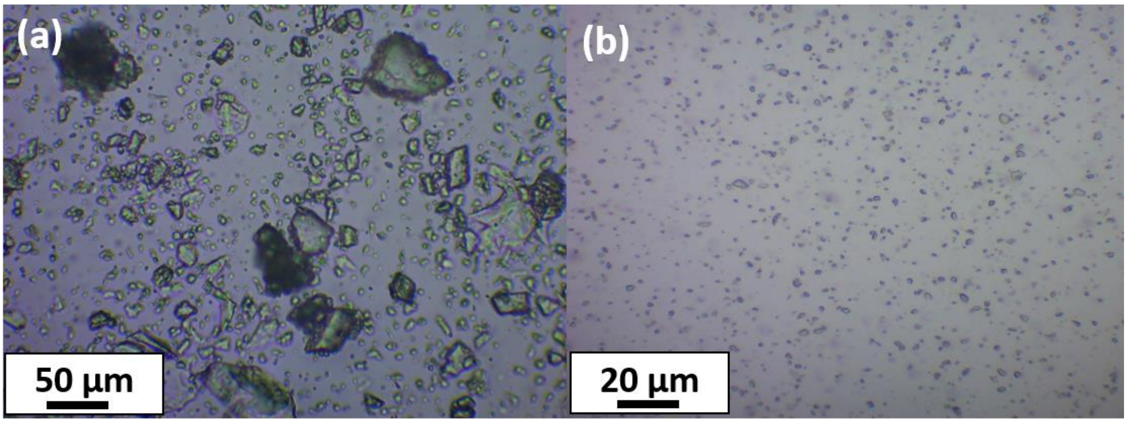

**Figure 3.5.** Optical microscopy images of (a) unmilled azoxystrobin crystals and (b) azoxystrobin microparticles after ball milling in the presence of PGMA$_{50}$-PMMA$_{80}$ nanoparticles.

Similarly, azoxystrobin crystals were milled in the presence of PGMA$_{50}$-PTFEMA$_{80}$ nanoparticles. Under the same milling conditions, azoxystrobin microparticles of approximately 2 µm diameter were produced within 10 min (see **Figure 3.6**). Therefore, switching the core-forming block from PMMA to PTFEMA seems to have little or no effect on the milling efficiency, at least for azoxystrobin.

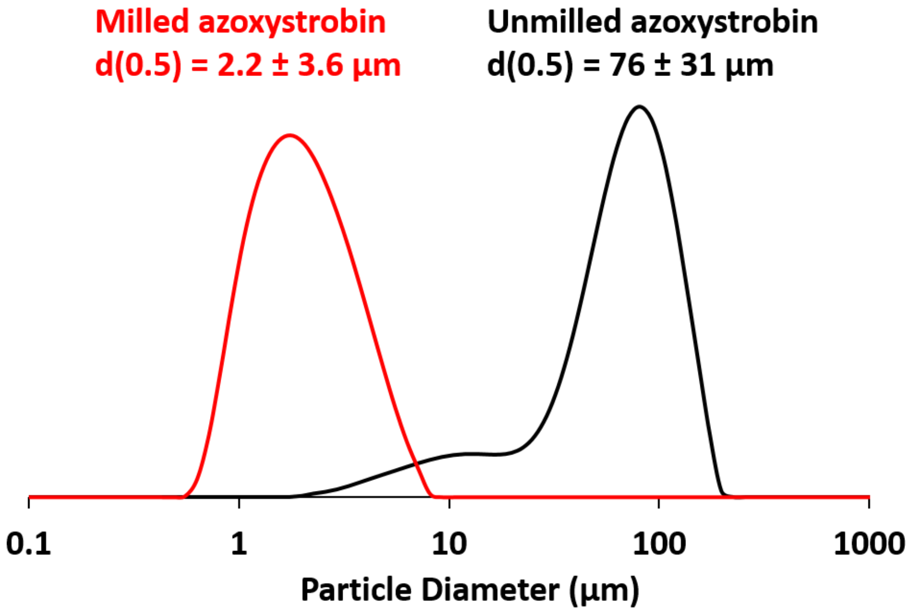

**Figure 3.6.** Laser diffraction particle size distribution curves (based on a volume-weighted average) recorded for the original coarse azoxystrobin particles and the much finer PGMA$_{50}$-PTFEMA$_{80}$ nanoparticle-coated azoxystrobin microparticles obtained after ball milling.

### 3.3.3 Nanoparticle Adsorption Studies *via* Characterization of Suspension Concentrates

A TEM image recorded for the as-prepared azoxystrobin microparticles is shown in **Figure 3.7a**. The resulting $PGMA_{50}$-$PMMA_{80}$ nanoparticles were clearly present both on the crystal surface and also in the background. This SC was then subjected to three centrifugation–redispersion cycles, and each supernatant was carefully decanted and discarded to remove any excess (non-adsorbed) nanoparticles. A TEM image recorded for the resulting purified azoxystrobin microparticles is shown in **Figure 3.7b**. Excess nanoparticles are no longer detected in the background, and the azoxystrobin microparticles are clearly coated with an adsorbed layer of $PGMA_{50}$-$PMMA_{80}$ nanoparticles. Similar observations were made for azoxystrobin microparticles milled in the presence of $PGMA_{50}$-$PTFEMA_{80}$ nanoparticles. Again, a relatively uniform layer of adsorbed nanoparticles is discernible at the surface of the azoxystrobin microparticles (**Figure 3.7c**).

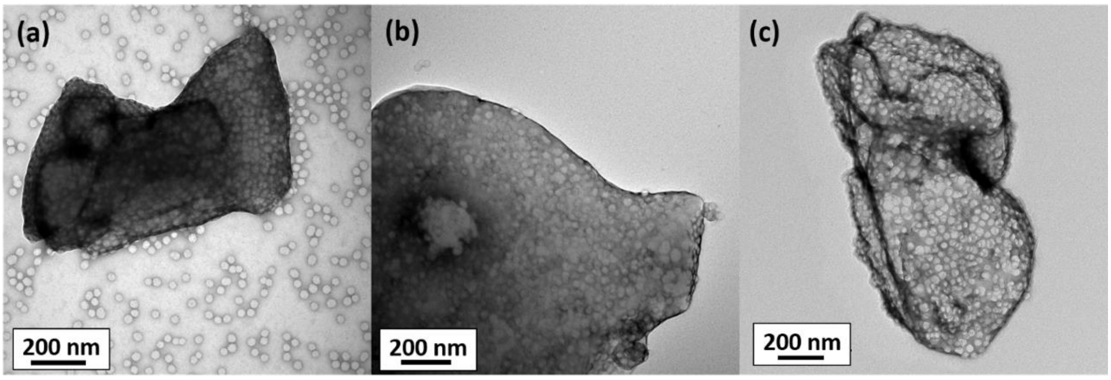

**Figure 3.7.** (a) TEM image recorded for azoxystrobin microparticles prepared by milling in the presence of $PGMA_{50}$-$PMMA_{80}$ nanoparticles before removal of excess non-adsorbed nanoparticles by centrifugation. (b) TEM image recorded for azoxystrobin microparticles prepared by milling in the presence of $PGMA_{50}$-$PMMA_{80}$ nanoparticles after removal of excess non-adsorbed nanoparticles by centrifugation. (c) TEM image recorded for azoxystrobin microparticles prepared by milling in the presence of $PGMA_{50}$-$PTFEMA_{80}$ nanoparticles after removal of excess non-adsorbed nanoparticles by centrifugation.

The nanoparticle-coated azoxystrobin microparticles were also characterized by scanning electron microscopy (see **Figure 3.8**). A relatively uniform layer of adsorbed $PGMA_{50}$-$PMMA_{80}$ or $PGMA_{50}$-$PTFEMA_{80}$ nanoparticles (*z*-average diameter = 29 or 33 nm, respectively) is discernible at the surface of the micron-sized azoxystrobin crystals. Such SEM studies confirm that the nanoparticles survive the ball milling, regardless of the nature of the core-forming block.

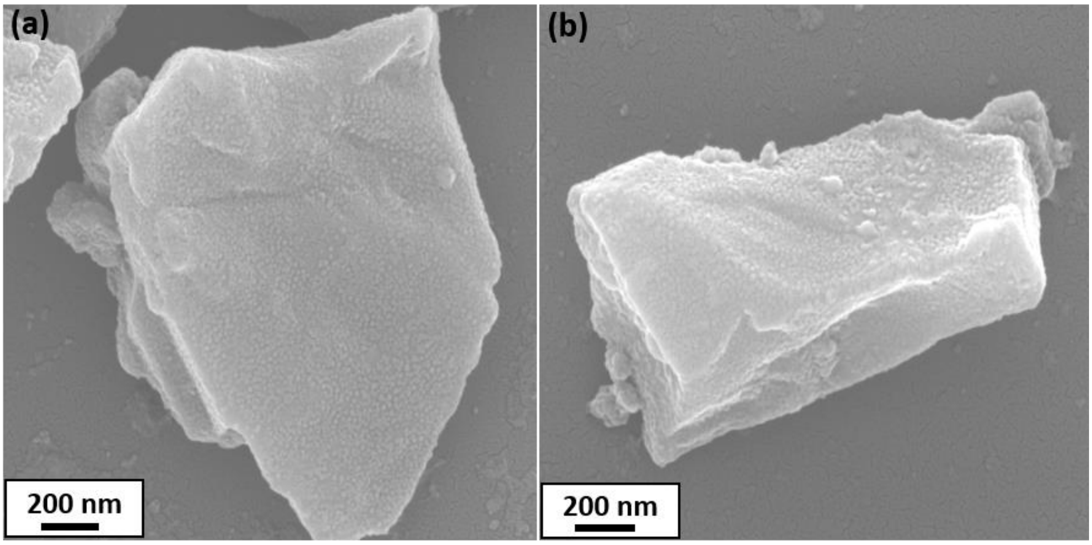

**Figure 3.8.** SEM images recorded for azoxystrobin microparticles coated with (a) PGMA$_{50}$-PMMA$_{80}$ nanoparticles and (b) PGMA$_{50}$-PTFEMA$_{80}$ nanoparticles. Both images were obtained after centrifugal purification to remove any excess non-adsorbed nanoparticles.

The solution densities of aqueous dispersions of PGMA$_{50}$-PMMA$_{80}$ nanoparticles were determined at various concentrations using a solution densitometer to afford a linear calibration plot (see **Figure 3.9**). This enabled nanoparticle adsorption onto the azoxystrobin microparticles to be assessed indirectly using a supernatant depletion assay after sedimentation of the relatively large azoxystrobin microparticles by centrifugation, followed by analysis of the solution density of the remaining aqueous supernatant. **Figure 3.10** shows the Langmuir-type adsorption isotherm constructed from such measurements.

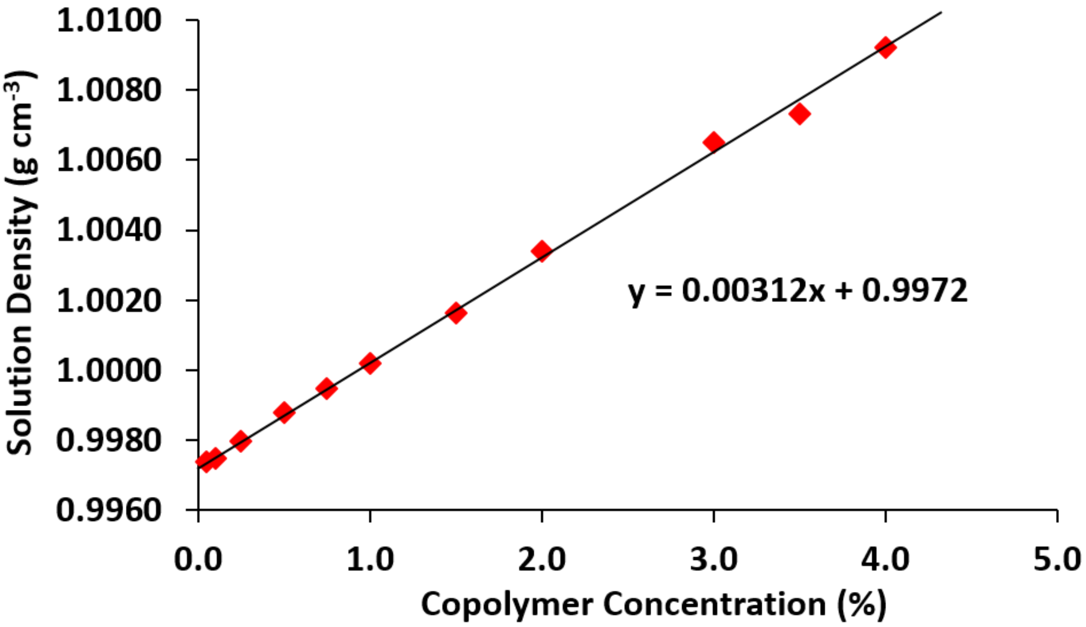

**Figure 3.9.** Calibration plot constructed for solution density vs. concentration for an aqueous dispersion of PGMA$_{50}$-PMMA$_{80}$ nanoparticles. This linear relationship was employed to calculate the concentration of nanoparticles remaining in the aqueous supernatant after milling various suspension concentrates followed by centrifugal sedimentation of the microparticles. The y-intercept corresponds to the density of pure water at 20 °C.

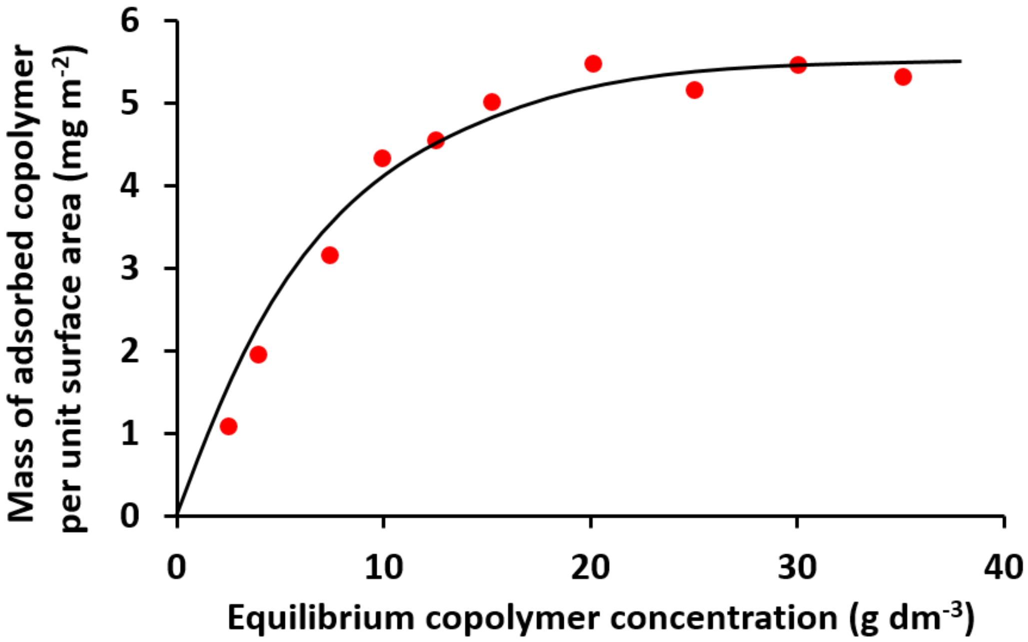

**Figure 3.10.** Langmuir-type adsorption isotherm constructed for PGMA$_{50}$-PMMA$_{80}$ nanoparticles adsorbed onto azoxystrobin microparticles at 20 °C as determined by a supernatant depletion assay based on solution densitometry.

From the plateau region of the adsorption isotherm (**Figure 3.10**), the maximum adsorbed amount, Γ, is estimated to be around 5.5 mg $m^{-2}$. A theoretical fractional surface coverage was calculated from this adsorbed amount using **Equation 3.1**.

$$\theta = \frac{3\Gamma}{4r\rho_p} \qquad \textbf{(3.1)}$$

Here Γ is the adsorbed amount of nanoparticles per unit area (g $m^{-2}$), $r$ is the mean nanoparticle radius (m) and $\rho_p$ is the nanoparticle density (g $m^{-3}$). For the $PGMA_{50}$-$PMMA_{80}$ nanoparticles, $\rho_p$ was taken to be 1.1 x $10^6$ g $m^{-3}$ and $r$ is estimated to be 1.5 x $10^{-8}$ m.

This approach indicated a maximum fractional coverage of 0.25 for the $PGMA_{50}$-$PMMA_{80}$ nanoparticles. This value is comparable to that determined by Hayes and co-workers for the physical adsorption of 40 nm diameter silica nanoparticles onto a planar aminated silicon wafer at pH 5.6 in the presence of 0.01 M $KNO_3$ using optical reflectometry.[50]

Zeta potential versus pH curves were determined for the $PGMA_{50}$-$PMMA_{80}$ nanoparticles, the nanoparticle-coated azoxystrobin microparticles, and the original azoxystrobin crystals (see **Figure 3.11**). The latter relatively coarse particles exhibited a zeta potential of around −23 mV above pH 9. In contrast, the $PGMA_{50}$-$PMMA_{80}$ nanoparticles exhibited zeta potentials close to zero (approximately −3 mV) across the whole pH range owing to the non-ionic nature of the PGMA steric stabilizer chains.[51] Clearly, nanoparticle adsorption is not driven by electrostatics in the present study, which differentiates it from our earlier model system.[18] Moreover, the significant reduction in the zeta potential (around −8 mV at pH 9–10) observed for the nanoparticle-coated anionic azoxystrobin microparticles provides further evidence for the partial surface coverage of the azoxystrobin microparticles by the near-neutral nanoparticles.

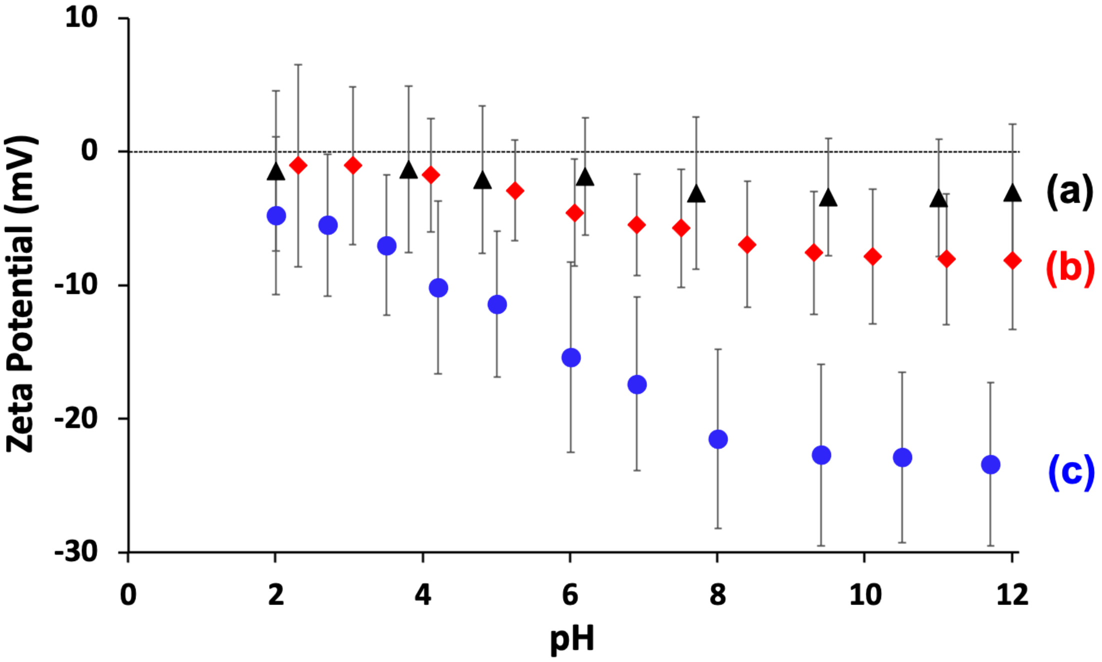

**Figure 3.11.** Zeta potential versus pH curves recorded for (a) aqueous dispersion of the PGMA$_{50}$-PMMA$_{80}$ nanoparticles alone, (b) diluted suspension concentrate comprising PGMA$_{50}$-PMMA$_{80}$ nanoparticle-coated azoxystrobin microparticles, and (c) coarse aqueous suspension comprising azoxystrobin crystals only. Thus, physical adsorption of the non-ionic PGMA$_{50}$-PMMA$_{80}$ nanoparticles significantly reduces the anionic surface character of azoxystrobin.

Similar observations were made when using PGMA$_{50}$-PTFEMA$_{80}$ nanoparticles in place of the PGMA$_{50}$-PMMA$_{80}$ nanoparticles (**Figure 3.12**). As expected, PGMA$_{50}$-PTFEMA$_{80}$ nanoparticles alone had zeta potentials close to zero (approximately −2 mV), while the PGMA$_{50}$-PTFEMA$_{80}$ nanoparticle-coated azoxystrobin microparticles exhibited intermediate zeta potentials of approximately −10 mV between pH 9 and pH 12.

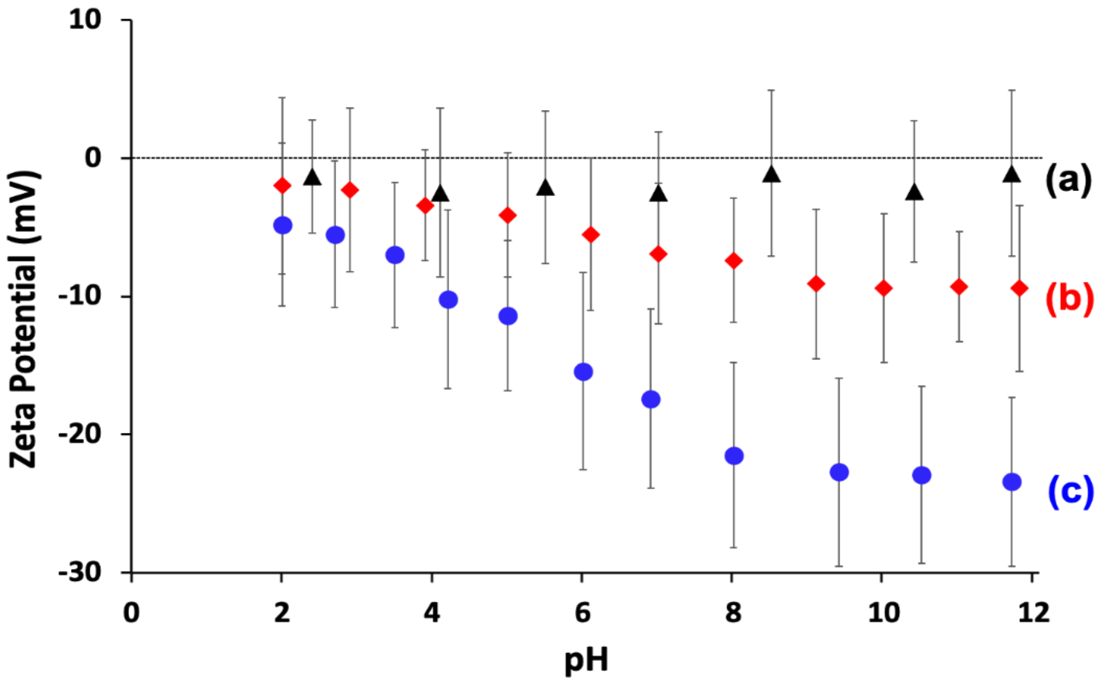

**Figure 3.12.** Zeta potential versus pH curves recorded for (a) aqueous dispersion of the PGMA$_{50}$-PTFEMA$_{80}$ nanoparticles alone, (b) diluted suspension concentrate comprising PGMA$_{50}$-PTFEMA$_{80}$ nanoparticle-coated azoxystrobin microparticles, and (c) coarse aqueous suspension comprising azoxystrobin crystals only. Thus, physical adsorption of the non-ionic PGMA$_{50}$-PTFEMA$_{80}$ nanoparticles significantly reduces the anionic surface character of azoxystrobin.

X-ray photoelectron survey spectra recorded for the azoxystrobin crystals, the PGMA$_{50}$-PMMA$_{80}$ nanoparticles alone, and the PGMA$_{50}$-PMMA$_{80}$ nanoparticle-coated azoxystrobin microparticles are shown in **Figure 3.13**. The chemical structure of azoxystrobin includes three nitrogen atoms (see **Figure 3.1**). In contrast, the PGMA$_{50}$-PMMA$_{80}$ nanoparticles contain no nitrogen atoms, so this element serves as a unique elemental marker for azoxystrobin (see **Figure 3.13**).[52] If the azoxystrobin microparticles are partially coated with such nanoparticles and the mean nanoparticle diameter exceeds the X-ray photoelectron spectroscopy (XPS) sampling depth of 2–5 nm,[52] then, the XPS N1s signal observed for the nanoparticle-coated azoxystrobin microparticles should be attenuated relative to that of azoxystrobin crystals alone. This is indeed the case: the former signal is 1.9 atom %, whereas the latter signal is 7.9 atom %. This implies a fractional surface coverage of approximately 1.9/7.9 = 0.24, which is consistent with the calculated theoretical surface coverage of 0.25 (see above). A comparable fractional surface coverage of 0.28 was calculated for the PGMA$_{50}$-PTFEMA$_{80}$ nanoparticle-coated azoxystrobin microparticles using the X-ray photoelectron survey spectra shown in **Figure 3.14**.

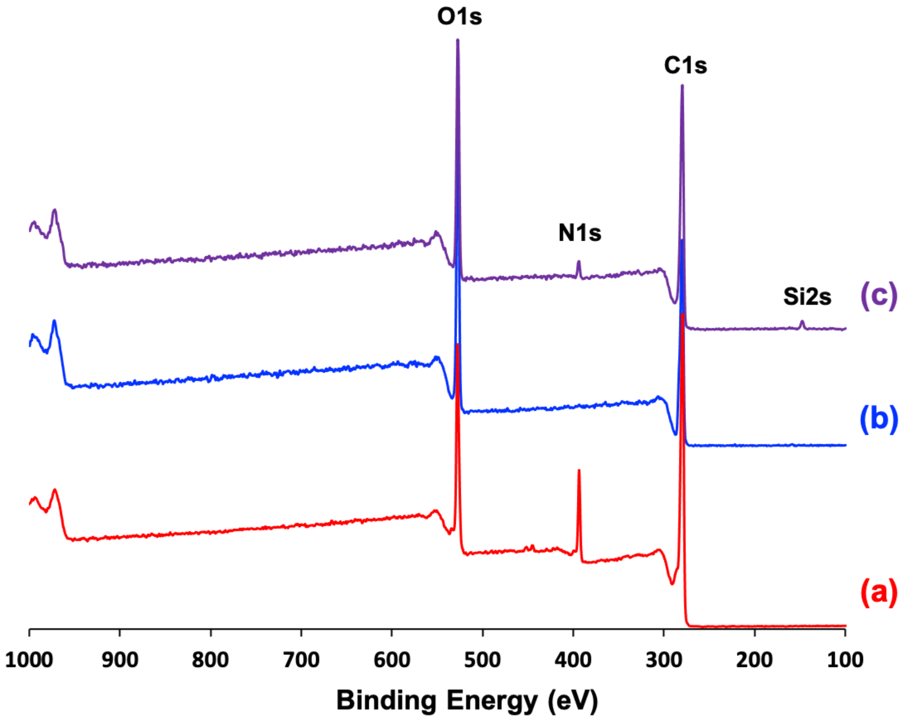

**Figure 3.13.** X-ray photoelectron survey spectra recorded for (a) pure azoxystrobin crystals, (b) PGMA$_{50}$-PMMA$_{80}$ nanoparticles alone, and (c) PGMA$_{50}$-PMMA$_{80}$ nanoparticle-coated azoxystrobin microparticles. These spectra confirm that the N1s signal may be used as a unique elemental marker for the azoxystrobin and that nanoparticle adsorption onto milled azoxystrobin microparticles leads to partial obscuration of this signal. Comparing the relative intensities of the N1s signals, the surface coverage of the azoxystrobin microparticles by the PGMA$_{50}$-PMMA$_{80}$ nanoparticles is estimated to be 0.24.

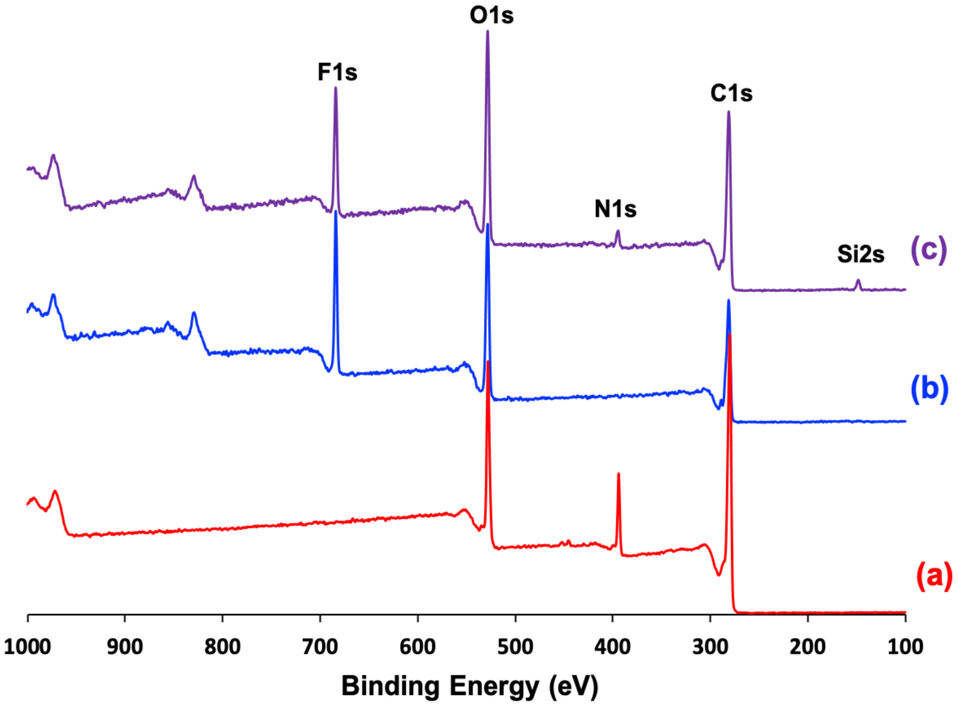

**Figure 3.14.** X-ray photoelectron survey spectra recorded for (a) azoxystrobin crystals, (b) the PGMA$_{50}$-PTFEMA$_{80}$ nanoparticles alone and (c) the PGMA$_{50}$-PTFEMA$_{80}$ nanoparticle-coated azoxystrobin microparticles. These spectra confirm that the N1s signal can be used as a unique elemental marker for the azoxystrobin and that nanoparticle adsorption onto milled azoxystrobin microparticles leads to partial obscuration of this signal. Inspecting the relative intensities of the N1s signals, the surface coverage of the azoxystrobin microparticles by the PGMA$_{50}$-PTFEMA$_{80}$ nanoparticles is estimated to be 0.28.

### 3.3.4 Preparation of Suspension Concentrates using Morwet D-425 as a Soluble Dispersant

A control experiment was conducted whereby a SC was prepared using a commercially available water-soluble polymer dispersant, Morwet D-425, rather than the nanoparticles described herein. Laser diffraction size distributions shown in **Figure 3.15a** confirm a similar reduction in the volume-average particle diameter to just under 2 µm for the azoxystrobin microparticles when using identical milling conditions. This mean size is consistent with images obtained by both optical microscopy and SEM **(Figure 3.15b,c**). Moreover, the latter technique indicates a smooth surface for the azoxystrobin microparticles, as expected when employing a soluble polymer as a comparable dispersant rather than nanoparticles. Clearly, sterically stabilized diblock copolymer nanoparticles offer dispersant performance to that achieved when using water-soluble polymers.

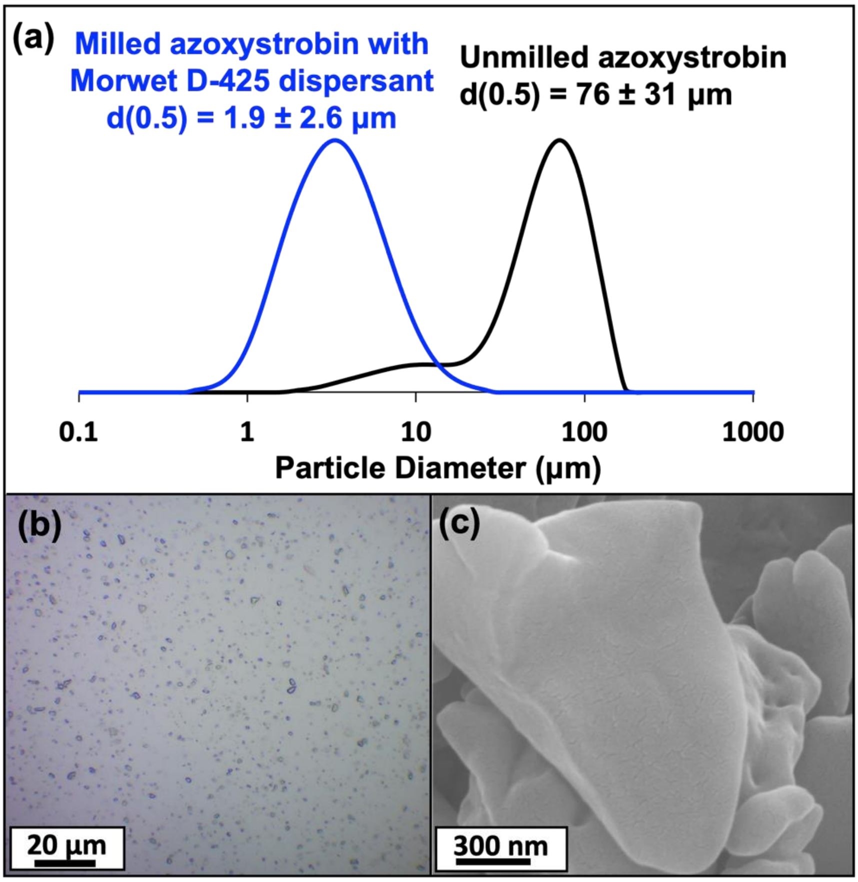

**Figure 3.15** (a) Laser diffraction particle size distributions recorded for the original coarse azoxystrobin particles and the much finer azoxystrobin microparticles obtained after ball milling in the presence of the commercial Morwet D-425 using the same conditions employed for the PGMA$_{50}$-PMMA$_{80}$ nanoparticles (see **Figure 3.4**). (b) Representative optical microscopy image and (c) SEM image recorded for azoxystrobin microparticles prepared using the Morwet D-425 dispersant. The latter technique confirms a smooth surface morphology, unlike that observed when using the nanoparticles as a particulate dispersant (see **Figures 3.7** and **3.8**).

### 3.3.5 Long-term Stability of Suspension Concentrates and Nanoparticle Displacement Studies

Finally, the nanoparticle-stabilized SCs reported herein were periodically sampled during storage at ambient temperature. Laser diffraction studies indicated no significant change in particle size over a 12-month period, suggesting good long-term stability (**Figure 3.16**). On the other hand, addition of a non-ionic surfactant (Triton X-100) led to partial displacement of the adsorbed nanoparticles from the surface of the azoxystrobin nanoparticles (**Figure 3.17**). Further long-term stability studies will be discussed in Chapter 4.

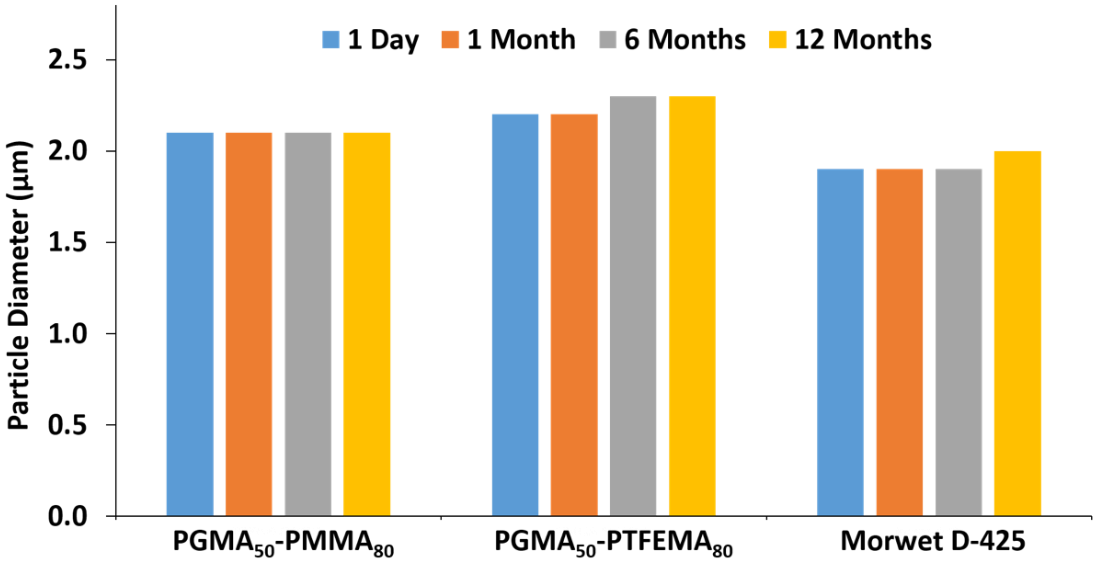

**Figure 3.16.** Volume-average particle diameter data obtained *via* laser diffraction for azoxystrobin-based aqueous SCs prepared using PGMA$_{50}$-PMMA$_{80}$ diblock copolymer nanoparticles, PGMA$_{50}$-PTFEMA$_{80}$ diblock copolymer nanoparticles or a commercial water-soluble Morwet D-425 dispersant. Laser diffraction measurements were conducted on the initial dispersion immediately after milling (day one) and after 1, 6 or 12 months storage at 20 °C.

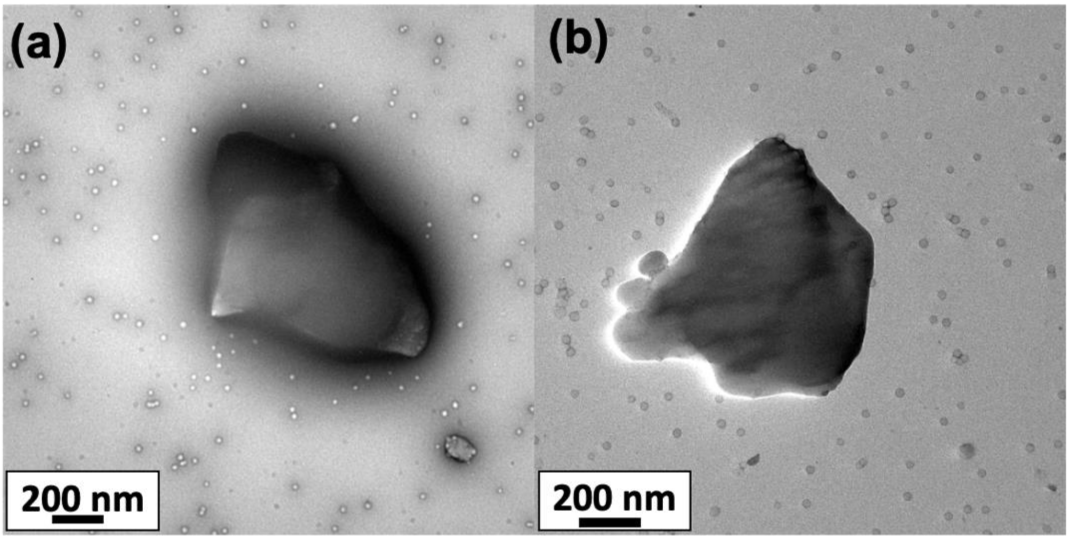

**Figure 3.17.** TEM images recorded for azoxystrobin microparticles prepared using (a) $PGMA_{50}$-$PMMA_{80}$ and (b) $PTFEMA_{50}$-$PMMA_{80}$ nanoparticles after addition of Triton X-100 surfactant. In each case, the presence of this non-ionic surfactant clearly leads to (partial) displacement of the adsorbed nanoparticles from the surface of the azoxystrobin microparticles.

## 3.4 Conclusions

Sterically stabilized diblock copolymer nanoparticles prepared by RAFT aqueous emulsion polymerization can be used as a dispersant for the preparation of micron-sized organic crystals *via* ball milling. This is exemplified for the specific case of azoxystrobin, a broad-spectrum fungicide that is widely used to prevent crop diseases. Laser diffraction studies indicate that both $PGMA_{50}$-$PMMA_{80}$ and $PGMA_{50}$-$PTFEMA_{80}$ nanoparticles enabled the convenient preparation of aqueous SCs containing azoxystrobin microparticles with a particle diameter of approximately 2 µm. Electron microscopy studies confirm that the nanoparticles adsorb onto the azoxystrobin microparticles and modify their electrophoretic behavior. The extent of nanoparticle adsorption can be quantified using a supernatant assay based on solution densitometry. This indicates a maximum adsorbed amount of approximately 5.5 mg $m^{-2}$ for the $PGMA_{50}$-$PMMA_{80}$ nanoparticles, which suggests a theoretical surface coverage of 0.25. Moreover, XPS studies enable an experimental fractional surface coverage of approximately 0.24 as calculated from the attenuation of the underlying N1s signal arising from the azoxystrobin microparticles. Furthermore, no significant differences were observed in the initial milling, extent of nanoparticle adsorption or overall long-term stability of the aqueous SC when switching the core-forming block from PMMA to PTFEMA. Overall, this study suggests that sterically stabilized diblock copolymer nanoparticles may offer a useful alternative to traditional water-soluble copolymer dispersants in the formulation of SCs for agrochemical applications.

## 3.5 References

(1) Steglich, W.; Schramm, G. The Strobilurins - New Antifungal Antibiotics from the Basidiomycete Strobilurus Tenacellus. *J. Antibiot.* **1977**, *30*, 806–810.

(2) Bartlett, D. W.; Clough, J. M.; Godwin, J. R.; Hall, A. A.; Hamer, M.; Parr-Dobrzanski, B. The Strobilurin Fungicides. *Pest Manag. Sci.* **2002**, *58*, 649–662.

(3) Becker, W. F.; Von Jagow, G.; Anke, T.; Steglich, W. Oudemansin, Strobilurin A, Strobilurin B and Myxothiazol: New Inhibitors of the Bc 1 Segment of the Respiratory Chain with an E-β-Methoxyacrylate System as Common Structural Element. *FEBS Lett.* **1981**, *132*, 329–333.

(4) Yao, J.; Cui, B.; Zhao, X.; Wang, Y.; Zeng, Z.; Sun, C.; Yang, D.; Liu, G.; Gao, J.; Cui, H. Preparation, Characterization, and Evaluation of Azoxystrobin Nanosuspension Produced by Wet Media Milling. *Appl. Nanosci.* **2018**, *8*, 297–307.

(5) Camiletti, B. X.; Camacho, N. M.; Paredes, A. J.; Allemandi, D. A.; Palma, S. D.; Grosso, N. R. Self-Dispersible Nanocrystals of Azoxystrobin and Cyproconazole with Increased Efficacy against Soilborne Fungal Pathogens Isolated from Peanut Crops. *Powder Technol.* **2020**, *372*, 455–465.

(6) Kah, M.; Hofmann, T. Nanopesticide Research: Current Trends and Future Priorities. *Environ. Int.* **2014**, *63*, 224–235.

(7) Harley, S.; Thompson, D. W.; Vincent, B. The Adsorption of Small Particles onto Larger Particles of Opposite Charge Direct Electron Microscope Studies. *Colloids and Surfaces* **1992**, *62*, 163–176.

(8) Hansen, F. K.; Matijevic, E. Heterocoagulation, Adsorption of a Carboxylated Polymer Latex on Monodispersed Hydrated Metal. *J. Chem. Soc. Faraday Trans. 1 Phys. Chem. Condens. Phases* **1980**, *76*, 1240–1262.

(9) Luckham, P.; Vincent, B.; Hart, C. A.; Tadros, T. F. The Controlled Flocculation of Particulate Dispersions Using Small Particles of Opposite Charge I. Sediment Volumes and Morphology. *Colloids and Surfaces* **1980**, *1*, 281–293.

(10) Vincent, B.; Young, C. A.; Tadros, T. F. Adsorption of Small, Positive Particles onto Large, Negative Particles in the Presence of Polymer: Part 1. - Adsorption Isotherms. *J. Chem. Soc. Faraday Trans. 1 Phys. Chem. Condens. Phases* **1980**, *76*, 665–673.

(11) Vincent, B.; Young, C. A.; Tadros, T. F. Adsorption of Small, Positive Particles onto

Large, Negative Particles in the Presence of Polymer: Part 2. - Adsorption Equilibrium and Kinetics as a Function of Temperature. *J. Chem. Soc. Faraday Trans. 1 Phys. Chem. Condens. Phases* **1980**, *76*, 674–682.

(12) Furusawa, K.; Anzai, C. Preparation of Composite Fine Particles by Heterocoagulation. *Colloid Polym. Sci.* **1987**, *265*, 882–888.

(13) Ottewill, R. H.; Schofield, A. B.; Waters, J. A. Preparation of Composite Latex Particles by Engulfment. *Colloid Polym. Sci.* **1996**, *274*, 763–771.

(14) Ottewill, R. H.; Schofield, A. B.; Waters, J. A.; Williams, N. S. J. Preparation of Core-Shell Polymer Colloid Particles by Encapsulation. *Colloid Polym. Sci.* **1997**, *275*, 274–283.

(15) Balmer, J. A.; Armes, S. P.; Fowler, P. W.; Tarnai, T.; Gáspár, Z.; Murray, K. A.; Williams, N. S. J. Packing Efficiency of Small Silica Particles on Large Latex Particles: A Facile Route to Colloidal Nanocomposites. *Langmuir* **2009**, *25*, 5339–5347.

(16) Balmer, J. A.; Mykhaylyk, O. O.; Patrick A Falrclough, J.; Ryan, A. J.; Armes, S. P.; Murray, M. W.; Murray, K. A.; Williams, N. S. J. Unexpected Facile Redistribution of Adsorbed Silica Nanoparticles between Latexes. *J. Am. Chem. Soc.* **2010**, *132*, 2166–2168.

(17) Balmer, J. A.; Mykhaylyk, O. O.; Armes, S. P.; Fairclough, J. P. A.; Ryan, A. J.; Gummel, J.; Murray, M. W.; Murray, K. A.; Williams, N. S. J. Time-Resolved Small-Angle X-Ray Scattering Studies of Polymer-Silica Nanocomposite Particles: Initial Formation and Subsequent Silica Redistribution. *J. Am. Chem. Soc.* **2011**, *133*, 826–837.

(18) North, S. M.; Jones, E. R.; Smith, G. N.; Mykhaylyk, O. O.; Annable, T.; Armes, S. P. Adsorption of Small Cationic Nanoparticles onto Large Anionic Particles from Aqueous Solution: A Model System for Understanding Pigment Dispersion and the Problem of Effective Particle Density. *Langmuir* **2017**, *33*, 1275–1284.

(19) Ferguson, C. J.; Hughes, R. J.; Pham, B. T. T.; Hawkett, B. S.; Gilbert, R. G.; Serelis, A. K.; Such, C. H. Effective Ab Initio Emulsion Polymerization under RAFT Control. *Macromolecules* **2002**, *35*, 9243–9245.

(20) Zetterlund, P. B.; Thickett, S. C.; Perrier, S.; Bourgeat-Lami, E.; Lansalot, M. Controlled/Living Radical Polymerization in Dispersed Systems: An Update. *Chem. Rev.* **2015**, *115*, 9745–9800.

(21) Charleux, B.; Delaittre, G.; Rieger, J.; D’Agosto, F. Polymerization-Induced Self-Assembly: From Soluble Macromolecules to Block Copolymer Nano-Objects in One Step. *Macromolecules* **2012**, *45*, 6753–6765.

(22) Canning, S. L.; Smith, G. N.; Armes, S. P. A Critical Appraisal of RAFT-Mediated Polymerization-Induced Self-Assembly. *Macromolecules* **2016**, *49*, 1985–2001.

(23) Rieger, J. Guidelines for the Synthesis of Block Copolymer Particles of Various

Morphologies by RAFT Dispersion Polymerization. *Macromol. Rapid Commun.* **2015**, *36*, 1458–1471.

(24) Penfold, N. J. W.; Yeow, J.; Boyer, C.; Armes, S. P. Emerging Trends in Polymerization-Induced Self-Assembly. *ACS Macro Lett.* **2019**, *8*, 1029–1054.

(25) Sun, J. T.; Hong, C. Y.; Pan, C. Y. Formation of the Block Copolymer Aggregates via Polymerization-Induced Self-Assembly and Reorganization. *Soft Matter* **2012**, *8*, 7753–7767.

(26) Warren, N. J.; Armes, S. P. Polymerization-Induced Self-Assembly of Block Copolymer Nano-Objects via RAFT Aqueous Dispersion Polymerization. *J. Am. Chem. Soc.* **2014**, *136*, 10174–10185.

(27) Ferguson, C. J.; Hughes, R. J.; Nguyen, D.; Pham, B. T. T.; Gilbert, R. G.; Serelis, A. K.; Such, C. H.; Hawkett, B. S. Ab Initio Emulsion Polymerization by RAFT-Controlled Self-Assembly. *Macromolecules* **2005**, *38*, 2191–2204.

(28) Boissé, S.; Rieger, J.; Belal, K.; Di-Cicco, A.; Beaunier, P.; Li, M. H.; Charleux, B. Amphiphilic Block Copolymer Nano-Fibers via RAFT-Mediated Polymerization in Aqueous Dispersed System. *Chem. Commun.* **2010**, *46*, 1950–1952.

(29) Li, Y.; Armes, S. P. RAFT Synthesis of Sterically Stabilized Methacrylic Nanolatexes and Vesicles by Aqueous Dispersion Polymerization. *Angew. Chemie - Int. Ed.* **2010**, *49*, 4042–4046.

(30) Blanazs, A.; Ryan, A. J.; Armes, S. P. Predictive Phase Diagrams for RAFT Aqueous Dispersion Polymerization: Effect of Block Copolymer Composition, Molecular Weight, and Copolymer Concentration. *Macromolecules* **2012**, *45*, 5099–5107.

(31) Sugihara, S.; Blanazs, A.; Armes, S. P.; Ryan, A. J.; Lewis, A. L. Aqueous Dispersion Polymerization: A New Paradigm for in Situ Block Copolymer Self-Assembly in Concentrated Solution. *J. Am. Chem. Soc.* **2011**, *133*, 15707–15713.

(32) Truong, N. P.; Dussert, M. V.; Whittaker, M. R.; Quinn, J. F.; Davis, T. P. Rapid Synthesis of Ultrahigh Molecular Weight and Low Polydispersity Polystyrene Diblock Copolymers by RAFT-Mediated Emulsion Polymerization. *Polym. Chem.* **2015**, *6*, 3865–3874.

(33) Cunningham, V. J.; Alswieleh, A. M.; Thompson, K. L.; Williams, M.; Leggett, G. J.; Armes, S. P.; Musa, O. M. Poly(Glycerol Monomethacrylate)-Poly(Benzyl Methacrylate) Diblock Copolymer Nanoparticles via RAFT Emulsion Polymerization: Synthesis, Characterization, and Interfacial Activity. *Macromolecules* **2014**, *47*, 5613–5623.

(34) Williams, M.; Penfold, N. J. W.; Armes, S. P. Cationic and Reactive Primary Amine-Stabilised Nanoparticles via RAFT Aqueous Dispersion Polymerisation. *Polym. Chem.* **2016**, *7*, 384–393.

(35) Semsarilar, M.; Ladmiral, V.; Blanazs, A.; Armes, S. P. Cationic Polyelectrolyte-Stabilized Nanoparticles via RAFT Aqueous Dispersion Polymerization. *Langmuir* **2013**,

*29*, 7416–7424.

(36) Ning, Y.; Fielding, L. A.; Doncom, K. E. B.; Penfold, N. J. W.; Kulak, A. N.; Matsuoka, H.; Armes, S. P. Incorporating Diblock Copolymer Nanoparticles into Calcite Crystals: Do Anionic Carboxylate Groups Alone Ensure Efficient Occlusion? *ACS Macro Lett.* **2016**, *5*, 311–315.

(37) Ladmiral, V.; Charlot, A.; Semsarilar, M.; Armes, S. P. Synthesis and Characterization of Poly(Amino Acid Methacrylate)-Stabilized Diblock Copolymer Nano-Objects. *Polym. Chem.* **2015**, *6*, 1805–1816.

(38) Chaduc, I.; Girod, M.; Antoine, R.; Charleux, B.; D’Agosto, F.; Lansalot, M. Batch Emulsion Polymerization Mediated by Poly(Methacrylic Acid) MacroRAFT Agents: One-Pot Synthesis of Self-Stabilized Particles. *Macromolecules* **2012**, *45*, 5881–5893.

(39) Doncom, K. E. B.; Warren, N. J.; Armes, S. P. Polysulfobetaine-Based Diblock Copolymer Nano-Objects via Polymerization-Induced Self-Assembly. *Polym. Chem.* **2015**, *6*, 7264–7273.

(40) Chenal, M.; Bouteiller, L.; Rieger, J. Ab Initio RAFT Emulsion Polymerization of Butyl Acrylate Mediated by Poly(Acrylic Acid) Trithiocarbonate. *Polym. Chem.* **2013**, *4*, 752–762.

(41) Fréai-Saison, S.; Save, M.; Bui, C.; Charleux, B.; Magnet, S. Emulsifier-Free Controlled Free-Radical Emulsion Polymerization of Styrene via RAFT Using Dibenzyltrithiocarbonate as a Chain Transfer Agent and Acrylic Acid as an Ionogenic Comonomer: Batch and Spontaneous Phase Inversion Processes. *Macromolecules* **2006**, *39*, 8632–8638.

(42) Rieger, J.; Stoffelbach, F.; Bui, C.; Alaimo, D.; Jérôme, C.; Charleux, B. Amphiphilic Poly(Ethylene Oxide) Macromolecular RAFT Agent as a Stabilizer and Control Agent in Ab Initio Batch Emulsion Polymerization. *Macromolecules* **2008**, *41*, 4065–4068.

(43) Manguian, M.; Save, M.; Charleux, B. Batch Emulsion Polymerization of Styrene Stabilized by a Hydrophilic Macro-RAFT Agenta. *Macromol. Rapid Commun.* **2006**, *27*, 399–404.

(44) Chaduc, I.; Zhang, W.; Rieger, J.; Lansalot, M.; D’Agosto, F.; Charleux, B. Amphiphilic Block Copolymers from a Direct and One-Pot RAFT Synthesis in Water. *Macromol. Rapid Commun.* **2011**, *32*, 1270–1276.

(45) Chaduc, I.; Crepet, A.; Boyron, O.; Charleux, B.; D’Agosto, F.; Lansalot, M. Effect of the Ph on the Raft Polymerization of Acrylic Acid in Water. Application to the Synthesis of Poly(Acrylic Acid)-Stabilized Polystyrene Particles by RAFT Emulsion Polymerization. *Macromolecules* **2013**, *46*, 6013–6023.

(46) Thompson, K. L.; Cinotti, N.; Jones, E. R.; Mable, C. J.; Fowler, P. W.; Armes, S. P. Bespoke Diblock Copolymer Nanoparticles Enable the Production of Relatively Stable

Oil-in-Water Pickering Nanoemulsions. *Langmuir* **2017**, *33*, 12616–12623.

(47) Akpinar, B.; Fielding, L. A.; Cunningham, V. J.; Ning, Y.; Mykhaylyk, O. O.; Fowler, P. W.; Armes, S. P. Determining the Effective Density and Stabilizer Layer Thickness of Sterically Stabilized Nanoparticles. *Macromolecules* **2016**, *49*, 5160–5171.

(48) Haas, S.; Hässlin, H. W.; Schlatter, C. Influence of Polymeric Surfactants on Pesticidal Suspension Concentrates: Dispersing Ability, Milling Efficiency and Stabilization Power. *Colloids Surfaces A Physicochem. Eng. Asp.* **2001**, *183*, 785–793.

(49) Stern, A. J.; Elsik, C. M. New Polymeric Comb Dispersants for Agricultural Formulations: A Comparison of Performance in Pesticide Suspension Concentrates. *J. ASTM Int.* **2007**, *4*, 34–42.

(50) Hayes, R. A.; Böhmer, M. R.; Fokkink, L. G. J. Study of Silica Nanoparticle Adsorption Using Optical Reflectometry and Streaming Potential Techniques. *Langmuir* **1999**, *15*, 2865–2870.

(51) Hatton, F. L.; Lovett, J. R.; Armes, S. P. Synthesis of Well-Defined Epoxy-Functional Spherical Nanoparticles by RAFT Aqueous Emulsion Polymerization. *Polym. Chem.* **2017**, *8*, 4856–4868.

(52) Watts, J. F.; Wolstenholme, J. *An Introduction to Surface Analysis by XPS and AES*; Wiley, Chichester, 2003.

# Chapter 4

# Using Alternative Diblock Copolymer Nanoparticles as Dispersants for Various Agrochemical Actives

Reproduced in full with permission from [Chan, D. H. H.; Deane, O. J.; Kynaston, E. L.; Lindsay, C.; Taylor, P.; Armes, S. P. Sterically-Stabilized Diblock Copolymer Nanoparticles Enable Facile Preparation of Suspension Concentrates Comprising Various Agrochemical Actives. *Langmuir* **2022**, *38*, 2885-2894.]

## 4.1 Introduction

Many types of agrochemicals, e.g. fungicides, herbicides or insecticides, are organic crystalline compounds with relatively low solubility in aqueous solution.[1] Traditionally, ball milling has been employed to produce crystalline microparticles of such active ingredients (AIs) in the form of so-called aqueous suspension concentrates (SCs).[2] This processing technique has been used for several decades to ensure the efficient delivery of AIs to various crops – indeed, this is probably the most widely used formulation within the agrochemical industry. The initial coarse particulates are subjected to wet milling in the presence of a suitable surfactant and/or water-soluble polymer, which acts as a dispersant. Such copolymers enhance the milling efficiency and are essential for conferring steric stabilization to prevent agglomeration or crystal growth.[3] The final mean microparticle diameter is usually targeted to be a few microns (or 1-2 µm).[4]

Haas and co-workers investigated the influence of a wide range of commercially-available copolymer surfactants on pesticidal SCs.[3] The effectiveness of each dispersant was assessed according to three criteria: (i) the final size of the microparticles (i.e. the degree of dispersion achieved), (ii) the milling efficiency and (iii) long-term stabilization against agglomeration. Firstly, an effective polymeric surfactant should provide sufficient 'wetting' of the hydrophobic AI crystals in water. Secondly, the target AI particle size should be achieved after ball milling for a relatively short time period while producing a low-viscosity dispersion [in contrast, a relatively slow reduction in particle size usually indicates poor milling efficiency for a given dispersant, especially if foaming is also observed]. Finally, the long-term stability of the resulting aqueous SC was studied by monitoring the mean particle size after storage at various temperatures.[3]

As previously discussed, polymerization-induced self-assembly (PISA) has become widely recognized as a powerful platform technology for the efficient synthesis of many types of block copolymer nano-objects in the form of concentrated dispersions in various solvents.[5-17] One of the most common PISA formulations reported in the literature is RAFT aqueous emulsion polymerization, which is applicable to various water-immiscible commodity vinyl monomers such as styrene (S), *n*-butyl acrylate (nBA), vinyl acetate (VAc) or methyl methacrylate (MMA).[18–28] Of particular importance for the present study, it enables the convenient and efficient synthesis of sterically-stabilized diblock copolymer spheres of tunable size with mean diameters ranging from 20 to 200 nm depending on the degree of polymerization (DP) that is targeted for the hydrophobic core-forming block.[29,30]

Another relevant study was reported by Deane and co-workers, who chain-extended a non-ionic poly(2-(*N*-acryloyloxy)ethyl pyrrolidone) (PNAEP) precursor with styrene, nBA or a statistical mixture thereof *via* RAFT aqueous emulsion (co)polymerization.[23] High conversions (> 99%) were achieved within 1 h and well-defined spherical nanoparticles were produced for all three types of core-forming blocks. As a result, a series of nanoparticles with differing glass transition temperatures ($T_g$) for the core-forming block were obtained. Thus, PS-based nanoparticles exhibited a relatively high $T_g$, whereas PnBA-based nanoparticles had a much lower $T_g$. As expected, the statistical copolymer exhibited an intermediate $T_g$ value.

As discussed in Chapter 3, diblock copolymer nanoparticles can serve as an effective dispersant to prepare SCs comprising micrometer-sized particles of a widely-used fungicide (azoxystrobin) *via* ball milling.[31] PGMA was employed as a non-ionic steric stabilizer block while the hydrophobic core-forming block was either PMMA or PTFEMA. It was shown that both types of nanoparticles survived the ball milling process and absorbed intact at the surface of the azoxystrobin microparticles.

Chapter 4 examines how varying the nature of the steric stabilizer block, adjusting the mean nanoparticle diameter and cross-linking the nanoparticle cores affects the size of the azoxystrobin microparticles. In addition, the effect of varying the $T_g$ of the core-forming block on the formation and colloidal stability of the final aqueous SC is examined. Moreover, this Chapter explores whether this approach is also applicable to a further five common agrochemicals, namely tebuconazole (TEB), difenoconazole (DFZ), cyproconazole (CCZ), isopyrazam (IZM) and pinoxaden (PXD), see **Figure 4.1**. Finally, the long-term stability of a series of SCs is assessed by using laser diffraction to monitor the mean particle diameter. The various types of diblock copolymer nanoparticles are characterized using TEM, DLS, aqueous electrophoresis and $^1$H NMR spectroscopy while the SCs comprising microparticles of the above six agrochemical actives are characterized using optical microscopy, laser diffraction and TEM.

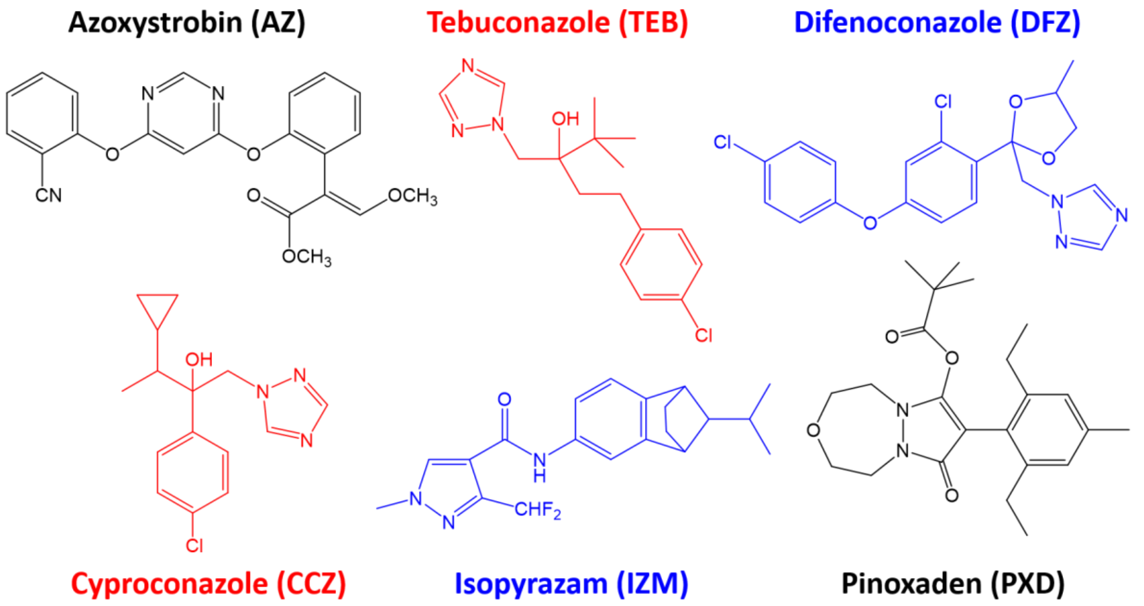

**Figure 4.1**. Chemical structures of the six agrochemical active compounds examined in this study: azoxystrobin, tebuconazole, difenoconazole, cyproconazole, isopyrazam and pinoxaden. The latter compound is a herbicide while the other five compounds are fungicides.

## 4.2 Experimental

### 4.2.1 Materials

Methyl methacrylate (MMA, 99%), 4,4′-azobis(4-cyanovaleric acid) (ACVA, 98%), 2-cyanopropyl dithiobenzoate (CPDB, 97%), *N*,*N*-dimethylacrylamide (DMAC, 99%), benzyl methacrylate (BzMA, 98%), styrene (S, 99%), *n*-butyl acrylate (nBA, 99%) and ethylene glycol dimethylacrylate (EGDMA, 98%) were purchased from Sigma-Aldrich (Gillingham, UK) and used as received. Diacetone acrylamide (DAAM, 99%) was purchased from Alfa Aesar (UK) while methyl-2 (dodecylthiocarbonothioylthio)-2-methylpropionate (Me-DDMAT) was prepared according to a literature protocol.[32] Glycerol monomethacrylate (GMA, 99.8%) was donated by GEO Specialty Chemicals (Hythe, UK). Azoxystrobin (AZ), tebuconazole (TEB), difenoconazole (DFZ), cyproconazole (CCZ), isopyrazam (IZM) and pinoxaden (PXD) were provided by

Syngenta (Jealott's Hill, UK). 1.0 mm zirconium aluminium oxide beads were purchased from Sigmund-Lindner (Germany). Silicone SAG1572 antifoam was purchased from Momentive (Germany). Deionized water from an Elga Medica DV25 water purification unit was used in all the experiments.

### 4.2.2 Synthesis of PGMA$_{50}$ Precursor by RAFT Aqueous Solution Polymerization of GMA

See Chapter 2, **section 2.2.2** for full details.

### 4.2.3 Synthesis of PGMA$_{50}$-PBzMA$_x$ Diblock Copolymer Nanoparticles by RAFT Aqueous Emulsion Polymerization

A typical synthesis of PGMA$_{50}$-PBzMA$_x$ nanoparticles was conducted according to the following protocol. PGMA$_{50}$ precursor (0.150 g, 18.2 µmol), BzMA monomer (0.161 g, 0.91 mmol; target DP = 50), ACVA initiator (1.0 mg, 3.65 µmol; PGMA$_{50}$/ACVA molar ratio = 5.0) and deionized water (2.806 g, 10 % w/w solution) were added to a 20 mL round-bottom flask. This flask was placed in an ice bath and the resulting aqueous solution was deoxygenated using a $N_2$ sparge for 30 min. The flask was then immersed in an oil bath set at 70 °C for 6 h. The BzMA polymerization was quenched by exposing the contents of the flask to air while cooling to 20 °C.

### 4.2.4 Synthesis of Linear PGMA$_{50}$-PMMA$_{80}$ Diblock Copolymer and Cross-linked PGMA$_{50}$-PMMA$_{80}$-PEGDMA$_{10}$ Triblock Copolymer Nanoparticles by RAFT Aqueous Emulsion Polymerization

Synthesis of linear PGMA$_{50}$-PMMA$_{80}$ diblock copolymer nanoparticles can be found in Chapter 3, **section 3.2.3**. The synthesis of cross-linked PGMA$_{50}$-PMMA$_{80}$ nanoparticles by RAFT aqueous emulsion polymerization was conducted as follows. PGMA$_{50}$ precursor (0.150 g, 18.2 µmol), MMA monomer (0.146 g, 1.46 mmol; target DP = 80), ACVA initiator (1.0 mg, 3.64 µmol; PGMA$_{50}$/ACVA molar ratio = 5.0) and deionized water (2.675 g, 10 % w/w solution) were added to a 20 mL round-bottom flask. The flask was placed in an ice bath and the aqueous emulsion was deoxygenated using a $N_2$ sparge for 30 min and then immersed in an oil bath set at 70 °C for 3 h. EGDMA (0.036 g, 0.182 mmol; target DP = 10) was added and the aqueous dispersion was stirred for 12 h at 70 °C to ensure full EGDMA conversion. The polymerization was quenched by exposing the contents of the flask to air while cooling to 20 °C.

### 4.2.5 Synthesis of $PDMAC_{67}$-$PDAAM_{50}$ Diblock Copolymer Nanoparticles by RAFT Aqueous Dispersion Polymerization

The poly(*N*,*N*-dimethylacrylamide) $PDMAC_{67}$ precursor was prepared *via* RAFT solution polymerization using a literature protocol.[32] The synthesis of $PDMAC_{67}$-$PDAAM_{50}$ nanoparticles by RAFT aqueous dispersion polymerization was conducted as follows. $PDMAC_{67}$ precursor (0.200 g, 28.4 µmol), DAAM monomer (0.241 g, 1.42 mmol; target DP = 50) and ACVA initiator (0.80 mg, 2.85 µmol; $PDMAC_{67}$/ACVA molar ratio = 10) were weighed into a 20 mL round-bottom flask. Deionized water (1.767 g) was adjusted to pH 2.5 using HCl and added to make up a 20% w/w solution. The flask was placed in an ice bath and the aqueous solution was deoxygenated using a $N_2$ sparge for 15 min prior to immersing the flask in an oil bath set at 70 °C. After 4 h, the polymerization was quenched by exposing the contents of the flask to air while cooling to 20 °C.

### 4.2.6 Synthesis of $PNAEP_{67}$, $PNAEP_{67}$-$PS_{75}$ Diblock Copolymer Nanoparticles and $PNAEP_{67}$ P(S-stat-PnBA)$_{100}$ Diblock Copolymer Nanoparticles by RAFT Aqueous Emulsion Polymerization

The synthesis of PNAEP precursors by RAFT aqueous solution polymerization and the preparation of both $PNAEP_{67}$-$PS_{75}$ and $PNAEP_{67}$-P(S-*stat*-PnBA)$_{100}$ diblock copolymer nanoparticles by RAFT aqueous emulsion polymerization have been previously reported by Deane and co-workers.[23] The same protocols were adopted in Chapter 4.

### 4.2.7 Preparation of Suspension Concentrates by Ball Milling

A typical protocol used for the preparation of a suspension concentrate at pH 7 was as follows. Azoxystrobin (2.00 g), $PGMA_{50}$-$PBzMA_{50}$ nanoparticles (0.25 g, 2.5% w/w), SAG1572 antifoam (0.10 g, 1.0% w/w) and deionized water (7.65 g) were added to a 30 mL tube containing 1.0 mm ceramic beads (10.0 g). An IKA Ultra-Turrax Tube Drive was used to mill this suspension at 6000 rpm for 15-40 min. The beads were removed by filtration to afford a 20% w/w suspension concentrate.

### 4.2.8 Centrifugal Purification of Suspension Concentrates

SCs were purified by centrifugation using a Thermo Heraeus Biofuge Pico centrifuge for 5 min at 5 000 rpm. The aqueous supernatant was carefully decanted and the sedimented microparticles were redispersed using deionized water. Two further centrifugation-redispersion cycles were performed before characterization to ensure removal of any excess non-adsorbed nanoparticles.

### 4.2.9 Characterization Techniques

#### Dynamic Light Scattering and Aqueous Electrophoresis

A Malvern Zetasizer NanoZS instrument was used to perform both DLS and aqueous electrophoresis studies on 0.10% w/w nanoparticle dispersions. Hydrodynamic *z*-average diameters were determined at 20 °C at a scattering angle of 173° and measurements were averaged over three runs. Aqueous electrophoresis experiments were conducted in the presence of 1 mM KCl as background electrolyte. The pH was adjusted as required with either HCl or NaOH. The Smoluchkowski approximation was used to calculate zeta potentials (also averaged over three measurements) *via* the Henry equation.

#### Optical Microscopy

A Cole-Palmer optical microscope fitted with a Moticam camera and an LCD tablet was used for imaging both the initial unmilled AIs and the final milled AI microparticles.

#### Transmission Electron Microscopy

Copper/palladium TEM grids (Agar Scientific, UK) were coated with a thin film of amorphous carbon and then treated with a plasma glow discharge for 30 s. Either an aqueous dispersion of nanoparticles or a suspension concentrate (10 µL, 0.10% w/w) was placed on each grid for 60 s before blotting to remove excess sample. Each grid was stained using uranyl formate (9.0 µL of a 0.75 % w/w solution) for 20 s before removing excess stain and drying under vacuum. Grid were imaged at 100 kV using a Philips CM100 TEM instrument equipped with a Gatan 1 k CCD camera.

### Laser Diffraction

The initial coarse active ingredients and final milled microparticles were sized by laser diffraction using a Malvern Mastersizer 3000 instrument equipped with a Hydro EV wet dispersion unit set at 2 000 rpm, a red HeNe laser ($\lambda = 633$ nm) and a light-emitting blue light source ($\lambda = 470$ nm). The volume-average particle diameter, d(0.5), was calculated by averaging over five measurements. After each measurement, the instrument was thoroughly rinsed with deionized water (three times) to prevent contamination.

### Scanning Electron Microscopy

SEM Images were recorded using an FEI Inspect-F instrument using an accelerating voltage of 10 kV and a beam current of 200 nA. Samples were dried onto thin glass slides and then sputter-coated with a thin overlayer of gold prior to imaging.

## 4.3 Results and Discussion

Initially, we sought to extend the work discussed in Chapter 3 by examining whether, and if so to what extent, adjusting various synthesis parameters affected the preparation of aqueous SCs comprising azoxystrobin, a widely used fungicide.[31] Preparation of SC formulations involves milling relatively coarse (20-76 µm diameter) hydrophobic organic crystals in the presence of a suitable polymeric dispersant. In Chapter 4, an IKA Ultra-Turrax Tube Drive was used for milling rather than a planetary ball mill. This approach enabled the convenient preparation of SCs on a relatively small scale (**Scheme 4.1**). Using the same general approach described in Chapter 3, a series of sterically-stabilized nanoparticles were employed as putative dispersants, rather than conventional commercially-available water-soluble polymers such as Morwet D-425.[31]

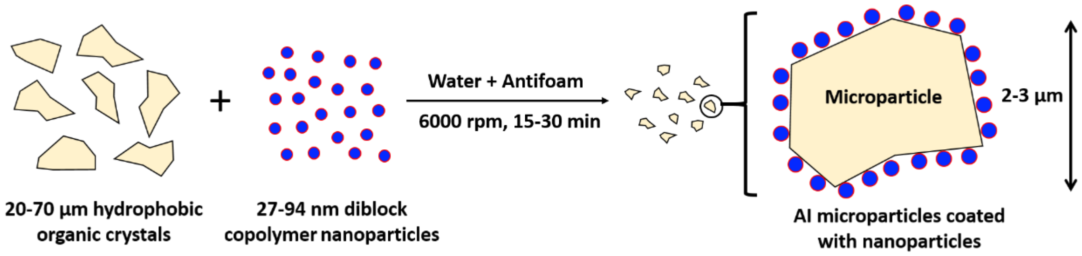

**Scheme 4.1.** Schematic cartoon of the preparation of a suspension concentrate comprising an agrochemical active ingredient (AI) in the form of microparticles using sterically-stabilized diblock copolymer nanoparticles as the sole dispersant. An IKA Ultra-Turrax Tube Drive containing 1.0 mm ceramic beads was used to mill the initial coarse AI crystals. [N.B. Individual components are not drawn to scale].

### 4.3.1 Effect of Varying the Chemical Nature of the Steric Stabilizer Block

Four different types of sterically-stabilized nanoparticles were prepared *via* RAFT polymerization using aqueous PISA formulations described in the literature.[23,29,32,33] Three non-ionic steric stabilizer blocks were employed and the relevant chemical structures for the resulting amphiphilic diblock copolymers ($PGMA_{50}$-$PMMA_{80}$, $PGMA_{50}$-$PBzMA_{50}$, $PDMAC_{67}$-$PDAAM_{50}$ and $PNAEP_{67}$-$PS_{75}$) are shown in **Figure 4.2a**. TEM studies confirmed that a well-defined spherical morphology was obtained in each case and DLS measurements indicated that these diblock copolymer nanoparticles had comparable hydrodynamic *z*-average diameters (27-33 nm) and relatively low polydispersities ($0.04 < PDI < 0.13$) (**Figure 4.2b**).

Coarse, polydisperse azoxystrobin crystals of approximately 76 µm diameter were milled in the presence of a 2.5% w/w aqueous dispersion of nanoparticles until a volume-average particle diameter of approximately 2 µm was achieved as judged by laser diffraction studies (**Figure 4.2c**). In Chapter 3, it was demonstrated that planetary ball milling of azoxystrobin crystals in the presence of $PGMA_{50}$-$PMMA_{80}$ nanoparticles produced the desired mean microparticle diameter within 10 min.[31] In the same study, it was found that switching the hydrophobic core-forming block from PMMA to PTFEMA had no discernible effect on either the milling efficiency or the final size of the azoxystrobin microparticles. Similar results were obtained herein when replacing the PMMA core-forming block with PBzMA. More specifically, a final azoxystrobin microparticle diameter of approximately 2 µm was produced within a milling time of 30 min when using $PGMA_{50}$-$PBzMA_{50}$ nanoparticles as a dispersant.

The effect of varying the nature of the (non-ionic) steric stabilizer was further examined by evaluating $PDMAC_{67}$-$PDAAM_{50}$ and $PNAEP_{67}$-$PS_{75}$ nanoparticles as putative dispersants. Using the former diblock copolymer led to a significant improvement in milling efficiency: a final particle size of 2.1 µm was achieved after a milling time of just 15 min. The latter diblock copolymer required a milling time of 30 min, which is comparable to the conditions required when using either the $PGMA_{50}$-$PMMA_{80}$ or $PGMA_{50}$-$PBzMA_{50}$ nanoparticles. Clearly, all four types of nanoparticles act as both a wetting agent and an effective dispersant: the chemical nature of the non-ionic stabilizer block has minimal effect on dispersant performance.

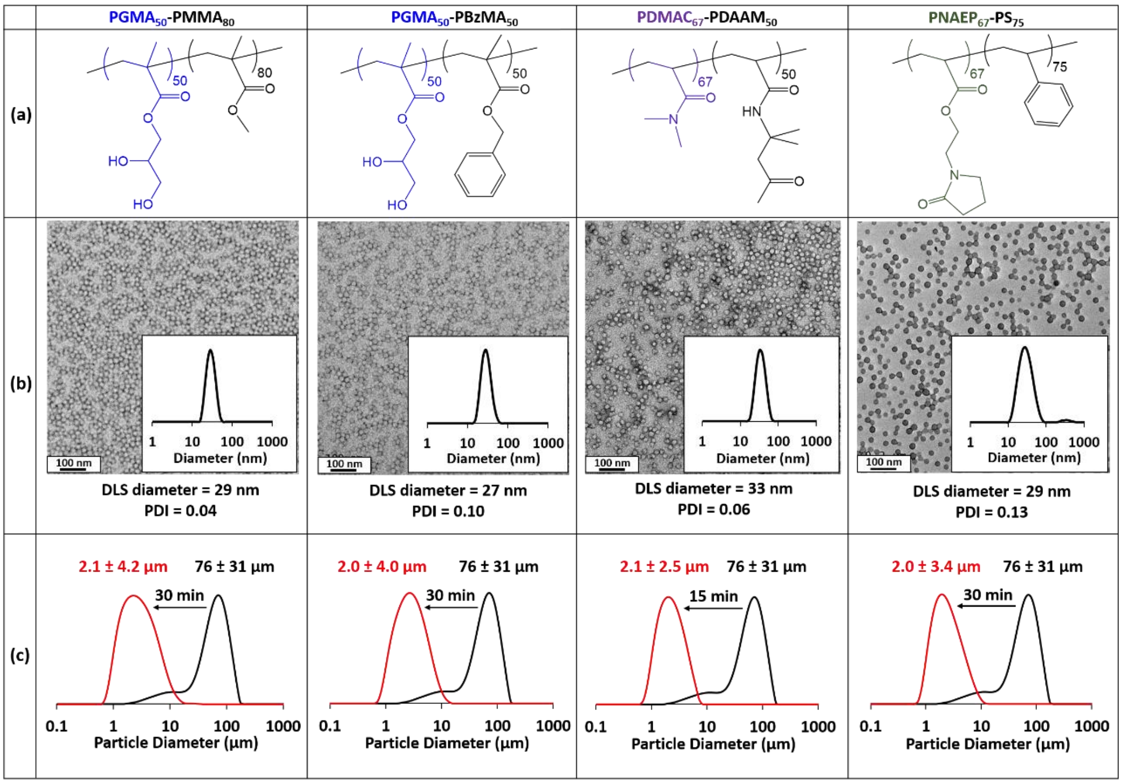

**Figure 4.2.** (a) Chemical structures of the four non-ionic sterically stabilized diblock copolymer nanoparticles used in this study; (b) TEM images and DLS intensity-average particle size distributions (see insets) recorded for each type of diblock copolymer nanoparticles; (c) Laser diffraction particle size distribution curves (and corresponding volume-average diameters) recorded for unmilled coarse azoxystrobin crystals (black trace) and milled azoxystrobin microparticles (red traces) prepared when using such nanoparticles as the sole dispersant.

Additional experiments were performed using amphiphilic diblock copolymer nanoparticles comprising either cationic poly(2-(methacryloyloxy)ethyl trimethylammonium chloride) [PMETAC] or anionic poly(methacrylic acid) [PMAA] as the steric stabilizer block (**Figure 4.3a**). Compared to sterically-stabilized nanoparticles prepared using non-ionic steric stabilizers, such nanoparticles exhibit comparable DLS diameters (35 nm and 29 nm respectively) but strikingly different electrophoretic footprints (**Figure 4.4**). For example, $PGMA_{50}$-$PMMA_{80}$ spheres exhibited zeta potentials close to zero (approximately −3 mV) throughout the whole pH range. As expected, the $PMAA_{56}$-$PMMA_{50}$ spheres become progressively more anionic between pH 2 and 6, before a maximum zeta potential of approximately −41 mV is observed above pH 6. In contrast, the $PMETAC_{46}$-$PMMA_{50}$ spheres retained their cationic character throughout the whole pH range with a maximum zeta potential of approximately +37 mV being observed.

However, in neither case was it possible to obtain a final volume-average diameter of 2 µm for azoxystrobin microparticles even after a milling time of 60 min at pH 7 (**Figure 4.3c**). Moreover, such formulations generated many air bubbles and/or foam, which could not be suppressed by adding an antifoam agent. Thus, polyelectrolytic steric stabilizers do not seem to be appropriate for the design of efficient nanoparticle dispersants, at least in the case of azoxystrobin. The adsorption of soluble polymer chains onto surfaces is a rather generic enthalpically driven phenomenon,[34] the same appears to be true for (non-ionic) sterically stabilized nanoparticles.

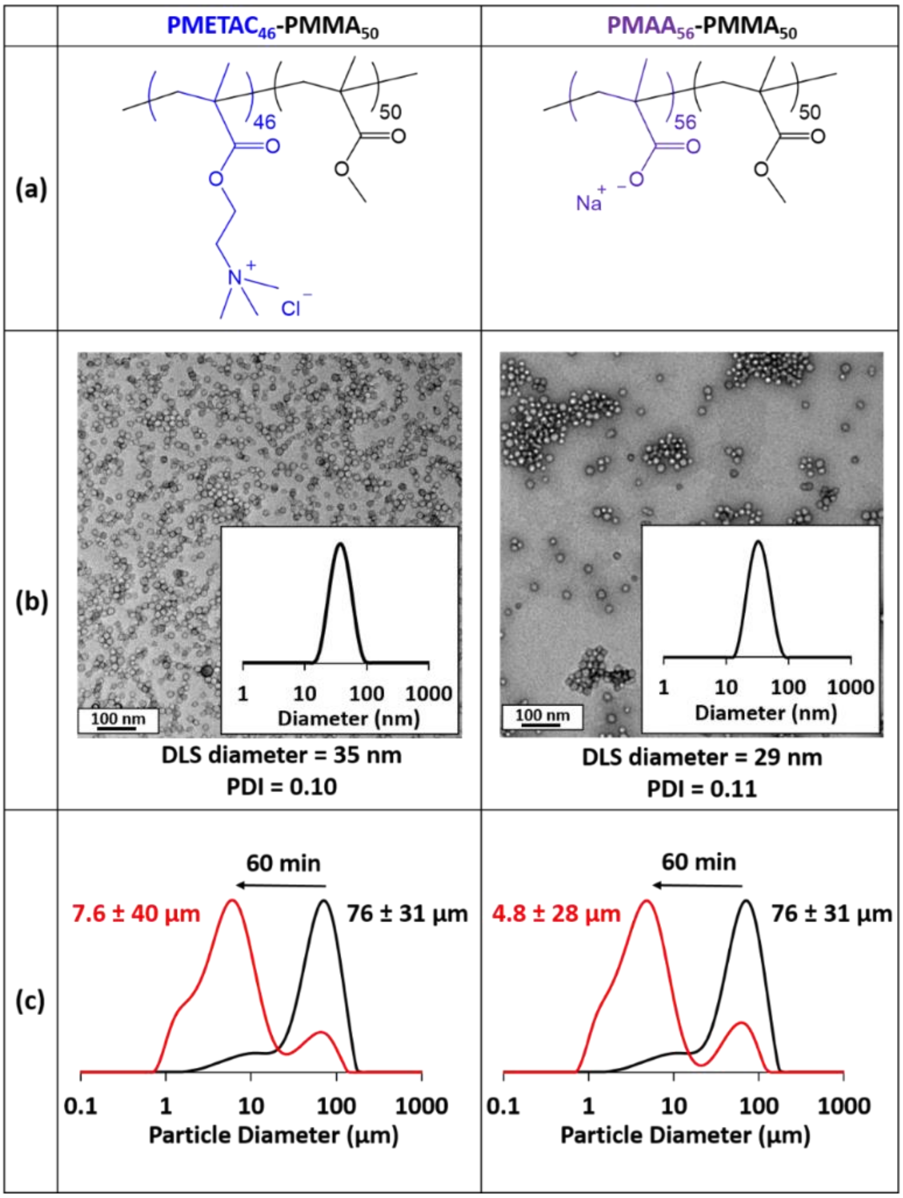

**Figure 4.3.** (a) Chemical structure, (b) representative TEM image and DLS intensity-average particle size distribution (see inset) for PMETAC$_{46}$-PMMA$_{50}$ and PMAA$_{56}$-PMMA$_{50}$ diblock copolymer nanoparticles; (c) Laser diffraction particle size distributions curves (and corresponding volume-average diameters) recorded for unmilled azoxystrobin (black) and milled azoxystrobin (red) in the presence of either (left) PMETAC$_{46}$-PMMA$_{50}$ or (right) PMAA$_{56}$-PMMA$_{50}$ nanoparticles at pH 7.

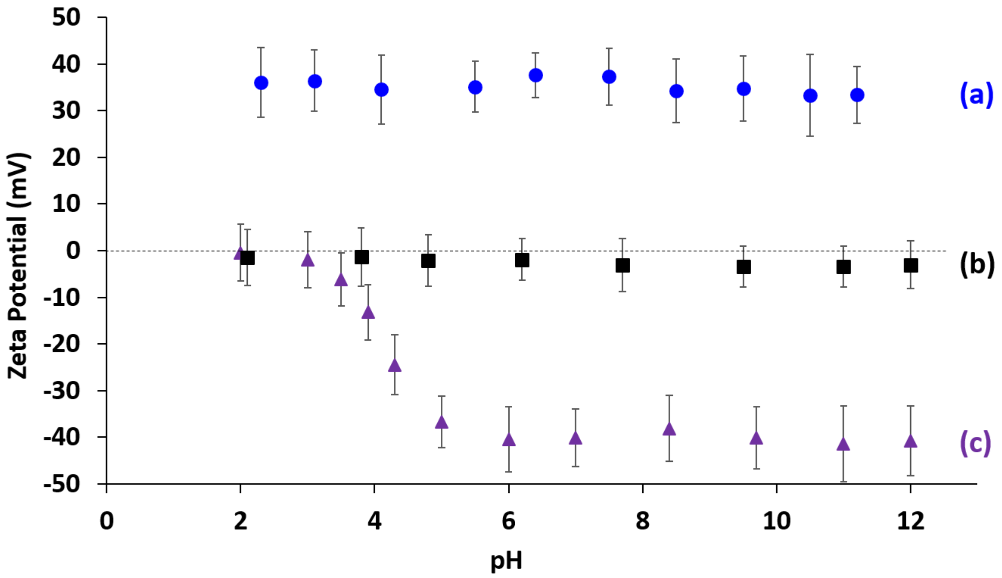

**Figure 4.4.** Zeta potential vs pH curves obtained for dilute aqueous dispersions of: (a) $PMETAC_{46}$-$PMMA_{50}$ spheres; (b) $PGMA_{50}$-$PMMA_{80}$ spheres; and (c) $PMAA_{56}$-$PMMA_{50}$ spheres.

### 4.3.2 Effect of Varying the Mean Nanoparticle Diameter

A series of $PGMA_{50}$-$PBzMA_x$ nanoparticles were prepared in which the mean diameter was systematically varied simply by increasing the target DP for the core-forming PBzMA block (**Scheme 4.2**). More specifically, targeting PBzMA DPs of 50 to 300 led to *z*-average diameters ranging from 27 to 94 nm as judged by DLS (**Figure 4.5a**). TEM studies indicated an increase in the number-average particle diameter (**Figure 4.5b-f**) and confirmed that only kinetically-trapped spheres were produced (as opposed to higher order morphologies such as worms or vesicles). Similar observations were reported by Cunningham and co-workers.[29]

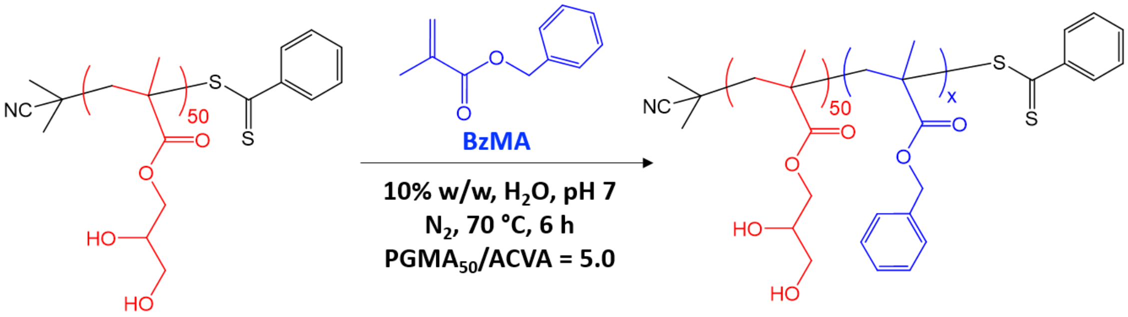

**Scheme 4.2.** Synthesis of $PGMA_{50}$-$PBzMA_x$ diblock copolymer nanoparticles by RAFT aqueous emulsion polymerization of BzMA using a $PGMA_{50}$ precursor under the stated conditions. Systematic variation of the target degree of polymerization of the PBzMA block (x) enables the mean nanoparticle diameter to be tuned (see main text for further details).

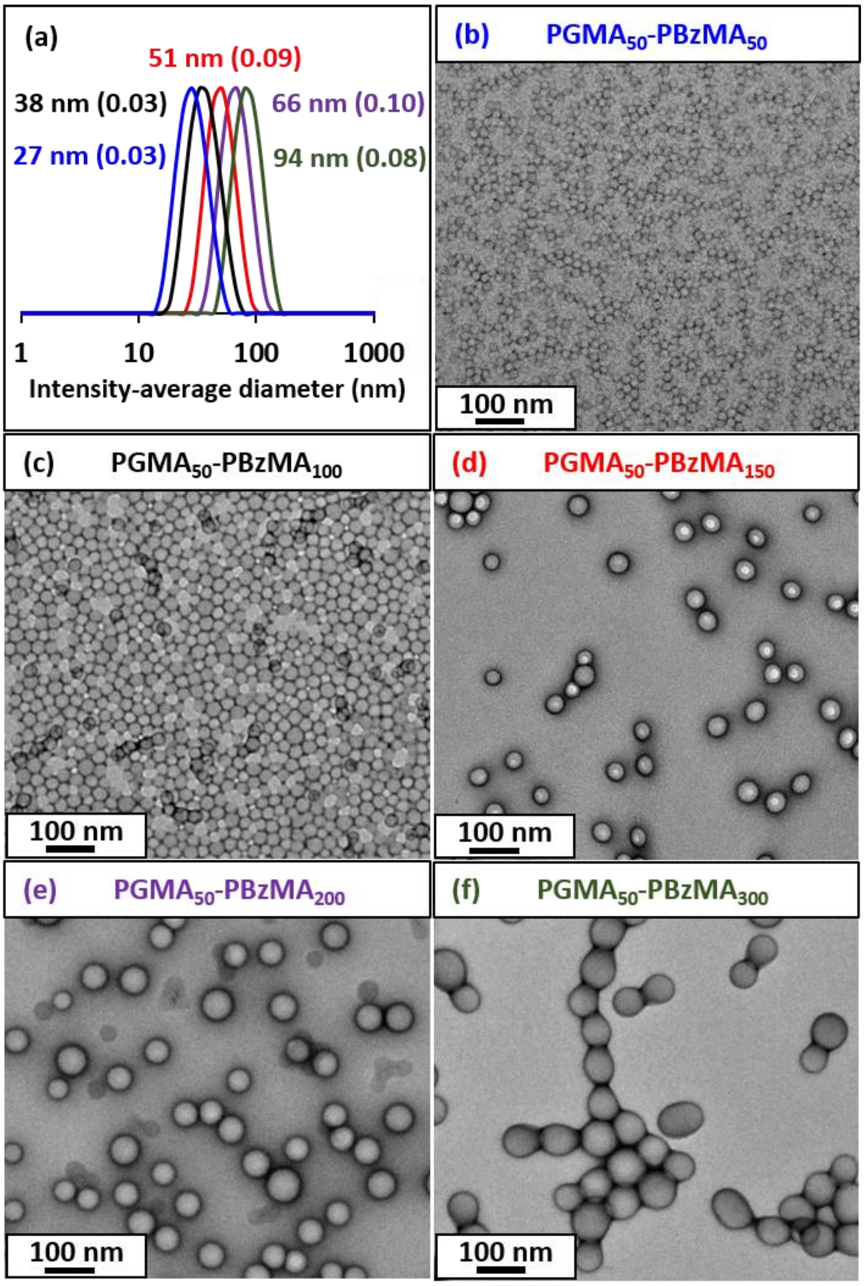

**Figure 4.5.** (a) DLS intensity-average particle size distributions recorded (plus *z*-average diameters and DLS polydispersities) for PGMA$_{50}$-PBzMA$_x$ nanoparticles, where x is varied from 50 to 300**.** (b-f) Corresponding TEM images obtained for the same series of five PGMA$_{50}$-PBzMA$_{50-300}$ nanoparticles prepared *via* RAFT aqueous emulsion polymerization of BzMA according to **Scheme 4.2**.

Azoxystrobin was milled in turn using five examples of PGMA$_{50}$-PBzMA$_x$ nanoparticles of varying *z*-average diameter. In this series of experiments, the dispersant concentration was adjusted to ensure that a constant total surface area of nanoparticles was used to prepare each SC. Full details of these formulations are summarized in **Table 4.1**.

**Table 4.1.** Summary of suspension concentrate formulations to evaluate the effect of varying the mean diameter for a series of $PGMA_{50}$-$PBzMA_x$ spherical nanoparticles when milling a fixed mass of azoxystrobin. The mass of nanoparticle dispersant was systematically varied to maintain a constant total surface area of 55.6 $m^2$.

| | **$PGMA_{50}$-$PBzMA_{50}$** | **$PGMA_{50}$-$PBzMA_{100}$** | **$PGMA_{50}$-$PBzMA_{150}$** | **$PGMA_{50}$-$PBzMA_{200}$** | **$PGMA_{50}$-$PBzMA_{300}$** |
|---|---|---|---|---|---|
| Nanoparticle diameter | 27 nm | 38 nm | 51 nm | 66 nm | 94 nm |
| Azoxystrobin | 2.00 g | 2.00 g | 2.00 g | 2.00 g | 2.00 g |
| Dispersant | 0.25 g | 0.35 g | 0.47 g | 0.61 g | 0.87 g |
| Antifoam | 0.10 g | 0.10 g | 0.10 g | 0.10 g | 0.10 g |
| Water | 7.65 g | 7.55 g | 7.43 g | 7.29 g | 7.03 g |

Laser diffraction was used to size the azoxystrobin microparticles after milling for 30 min (**Figure 4.6**). A volume-average particle diameter of approximately 2 µm was obtained when milling azoxystrobin in the presence of $PGMA_{50}$-$PBzMA_{50}$, $PGMA_{50}$-$PBzMA_{100}$ or $PGMA_{50}$-$PBzMA_{150}$ nanoparticles (which possessed *z*-average diameters of 27 nm, 38 nm or 51 nm, respectively). In contrast, milling for 30 min in the presence of the two largest nanoparticle dispersants (i.e. $PGMA_{50}$-$PBzMA_{200}$ or $PGMA_{50}$-$PBzMA_{300}$) only produced relatively large azoxystrobin microparticles of approximately 3 µm diameter.

Three centrifugation-redispersion cycles were performed on the resulting SCs to remove any non-adsorbed excess nanoparticles. **Figure 4.6** includes SEM images recorded for such purified azoxystrobin microparticles. In each case, individual microparticles are uniformly coated with a layer of adsorbed $PGMA_{50}$-$PBzMA_x$ nanoparticles. Moreover, using larger nanoparticles appears to result in lower surface coverages. This study suggests that smaller spheres ensure the most efficient milling and perhaps also lead to higher surface coverages, at least when milling azoxystrobin in the presence of this particular class of nanoparticle dispersants. The long-term stability of this series of resulting SCs is also assessed using laser diffraction (**section 4.3.6**).

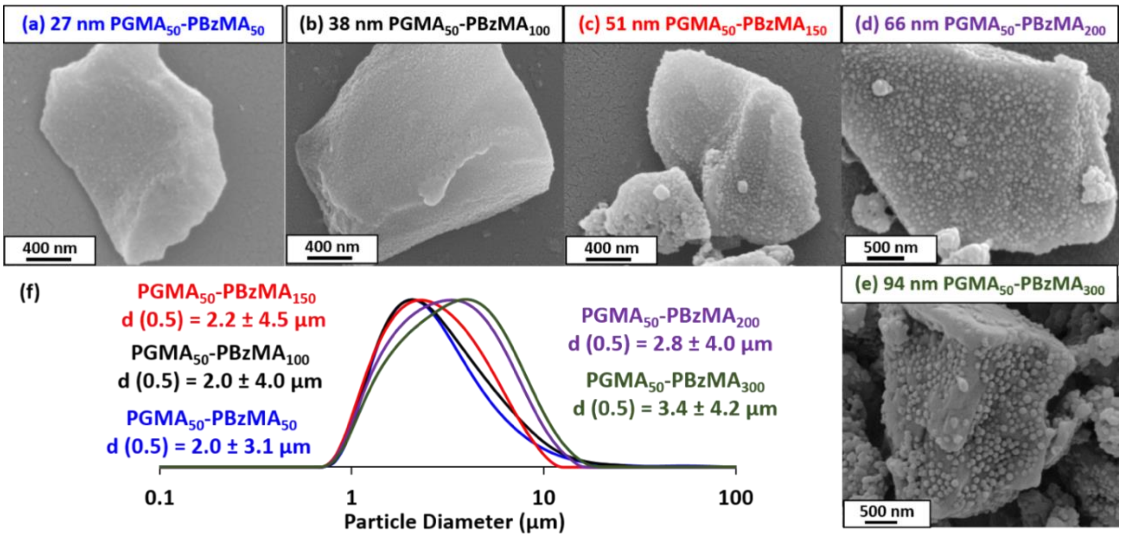

**Figure 4.6.** (a-e) SEM images of individual azoxystrobin microparticles prepared *via* ball milling with five examples of PGMA$_{50}$-PBzMA$_x$ nanoparticles of varying size (after removing excess non-adsorbed nanoparticles by centrifugation). (f) Corresponding laser diffraction particle size distribution curves recorded for azoxystrobin microparticles obtained after a milling time of 30 min when using the same five examples of PGMA$_{50}$-PBzMA$_x$ nanoparticles.

### 4.3.3 Effect of Crosslinking the Nanoparticle Cores

In 2012 Chambon *et al*. reported that linear diblock copolymer nano-objects prepared *via* aqueous PISA could be covalently stabilized simply by chain extension using a divinyl monomer to generate a third block.[35] Accordingly, core-crosslinked PGMA$_{50}$-PMMA$_{80}$-PEGDMA$_{10}$ nanoparticles were readily prepared by adding 12.5 mol% EGDMA (based on MMA monomer) after the MMA was fully consumed (**Scheme 4.3**).

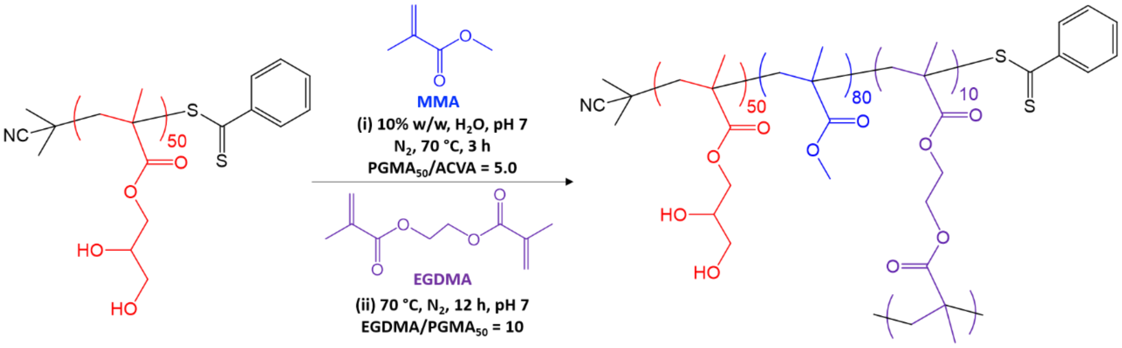

**Scheme 4.3.** Synthesis of core-crosslinked PGMA$_{50}$-PMMA$_{80}$-PEGDMA$_{10}$ triblock copolymer nanoparticles *via* RAFT aqueous emulsion polymerization of (i) BzMA and (ii) EGDMA at 70 °C.

Representative TEM images obtained for the linear $PGMA_{50}$-$PMMA_{80}$ precursor nanoparticles dried from water and the final core-crosslinked $PGMA_{50}$-$PMMA_{80}$-$PEGDMA_{10}$ nanoparticles dried from DMF are shown in **Figure 4.7**. The former nanoparticles exhibit a well-defined spherical morphology as expected. DMF is a good solvent for both the $PGMA_{50}$ stabilizer block and the $PMMA_{80}$ core-forming block, thus molecular dissolution of the linear nanoparticles occurs in this solvent (indeed, DMF is the eluent of choice for GPC analysis of such diblock copolymer chains).[33] However, TEM indicates a similar spherical morphology for the $PGMA_{50}$-$PMMA_{80}$-$PEGDMA_{10}$ nanoparticles dried from DMF, which confirms successful core-crosslinking in this case.

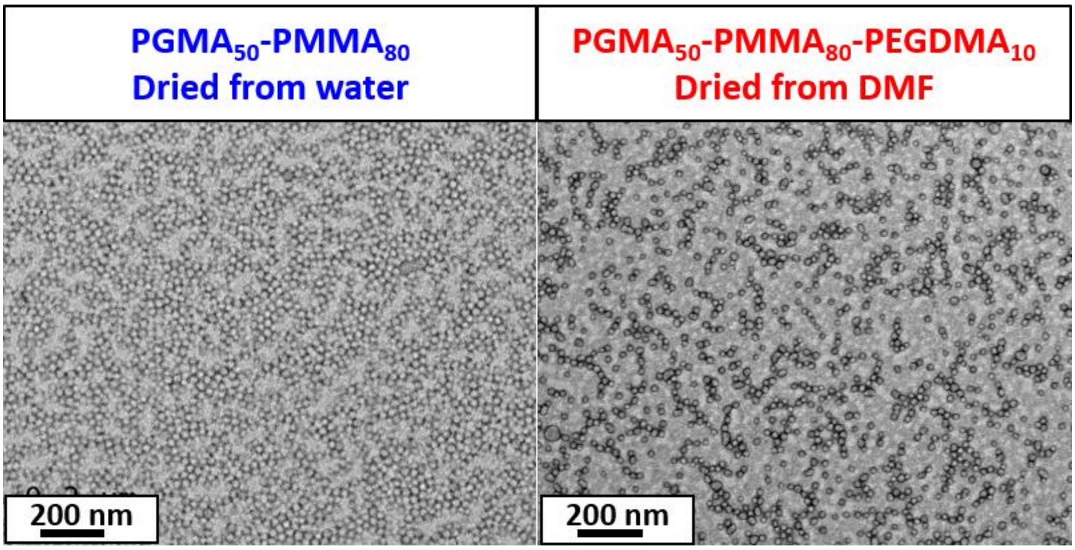

**Figure 4.7.** TEM images obtained for linear $PGMA_{50}$-$PMMA_{80}$ nanoparticles dried from water and core-crosslinked $PGMA_{50}$-$PMMA_{80}$-$PEGDMA_{10}$ nanoparticles dried from DMF.

Moreover, DLS studies of the same $PGMA_{50}$-$PMMA_{80}$-$PEGDMA_{10}$ nanoparticles dispersed in DMF (**Figure 4.8**) indicated the presence of slightly swollen spheres with a *z*-average diameter of 34 nm, rather than molecularly-dissolved copolymer chains. Given that the linear precursor $PGMA_{50}$-$PMMA_{80}$ nanoparticles had a *z*-average diameter of 29 nm, this suggests relatively high degree of core-crosslinking. Furthermore, DLS experiments conducted on a dilute *aqueous* dispersion of the $PGMA_{50}$-$PMMA_{80}$-$PEGDMA_{10}$ core-crosslinked nanoparticles indicated a *z*-average particle diameter of 31 nm (**Figure 4.8**), which suggests that core cross-linking has a minimal effect on the nanoparticle dimensions.

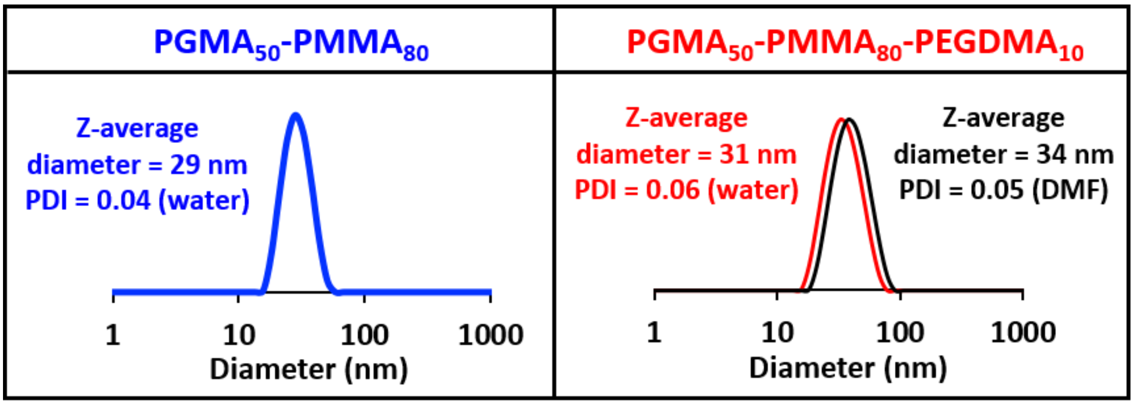

**Figure 4.8.** DLS intensity-average particle size distributions recorded for 0.1% w/w dispersions of linear PGMA$_{50}$-PMMA$_{80}$ nanoparticles (in water) and core-crosslinked PGMA$_{50}$-PMMA$_{80}$-PEGDMA$_{10}$ nanoparticles (in water and DMF).

Subsequently, the nanoparticle dispersant performance of the core-crosslinked nanoparticles was directly compared to that of the linear nanoparticles for the same SC formulation under identical milling conditions. The SCs produced in each case were then sized by laser diffraction (**Figure 4.9a**). Clearly, covalent stabilization of the nanoparticle cores has essentially no effect on the size of the final azoxystrobin microparticles. This is an important observation because it eliminates the possibility that individual amphiphilic diblock copolymer chains are in equilibrium with the linear diblock copolymer nanoparticles, with the former species potentially playing an important role in either initial surface wetting or subsequent steric stabilization of the azoxystrobin microparticles.

Moreover, three centrifugation-redispersion cycles were performed to remove any excess non-adsorbed nanoparticles from these two SCs. TEM images of the resulting purified azoxystrobin microparticles are shown in **Figure 4.9b**. A relatively high surface coverage is obtained when using either the linear PGMA$_{50}$-PMMA$_{80}$ nanoparticles or the core-crosslinked PGMA$_{50}$-PMMA$_{80}$-PEGDMA$_{10}$ nanoparticles. Such images provide compelling evidence that crosslinking the nanoparticle cores has no discernible effect on either the milling efficiency or their ability to adsorb at the surface of the azoxystrobin microparticles.

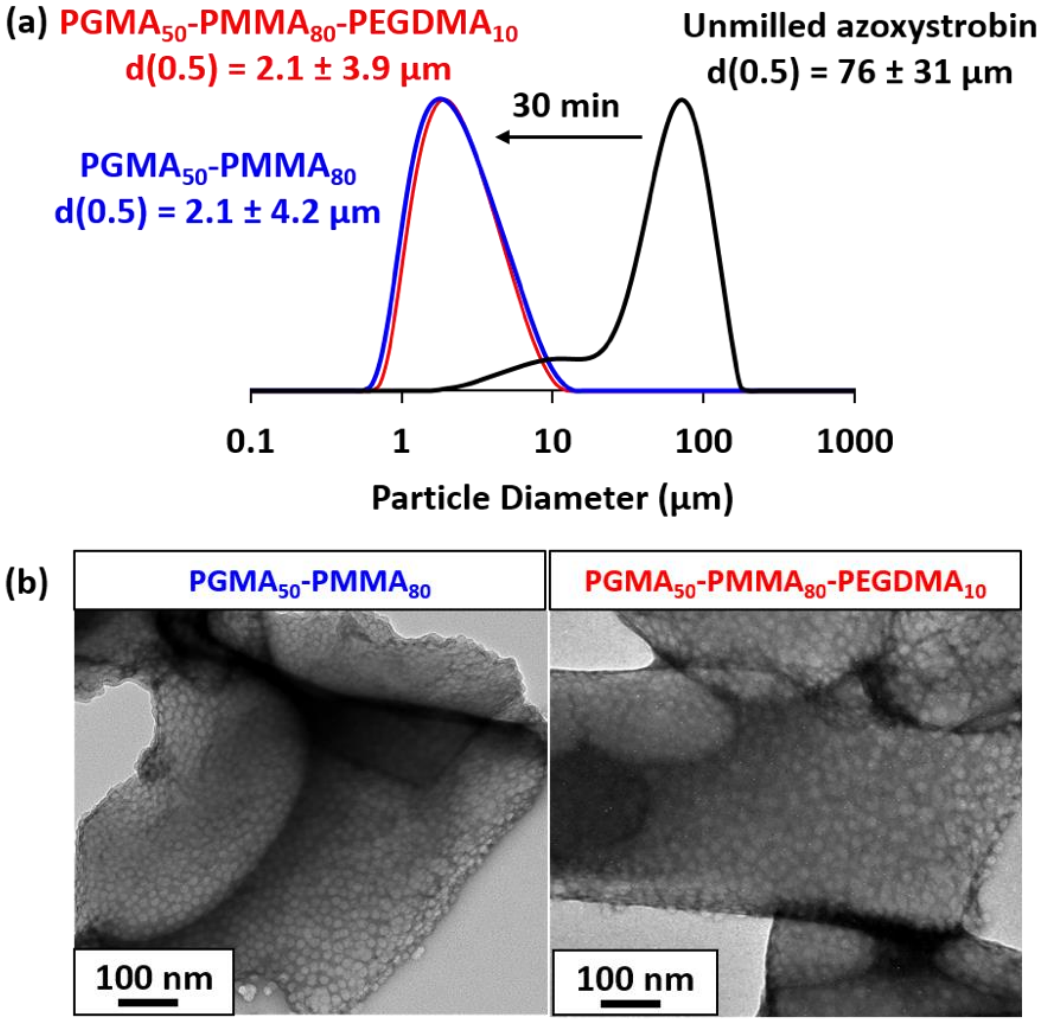

**Figure 4.9.** (a) Laser diffraction particle size distribution curves (and corresponding volume-average diameters) recorded for the unmilled azoxystrobin (black) and milled azoxystrobin coated with either linear $PGMA_{50}$-$PMMA_{80}$ nanoparticles (blue) or cross-linked $PGMA_{50}$-$PMMA_{80}$-$PEGDMA_{10}$ nanoparticles (red); (b) TEM images recorded for azoxystrobin microparticles prepared by milling in the presence of either linear or cross-linked nanoparticle dispersions after removal of excess nanoparticles by centrifugation.

### 4.3.4 Effect of Varying the Glass Transition Temperature ($T_g$) of the Core-forming Block

High $T_g$ $PNAEP_{67}$-$PS_{100}$ nanoparticles were prepared by RAFT aqueous emulsion polymerization of styrene. In addition, analogous diblock copolymer nanoparticles comprising a core-forming statistical block exhibiting a much lower $T_g$ were prepared by statistical copolymerization of styrene (45 wt %) with *n*-butyl acrylate (55 wt %) using the same $PNAEP_{67}$ precursor. Differential scanning calorimetry (DSC) curves recorded for the $PNAEP_{67}$ precursor, $PNAEP_{67}$-$PS_{100}$ nanoparticles and $PNAEP_{67}$-P(S-*stat*-nBA)$_{100}$ nanoparticles are shown in **Figure 4.10**. The $PNAEP_{67}$-$PS_{100}$ diblock copolymer exhibits two $T_g$ values at -1.8 and 83.4 °C respectively, which is the result of microphase separation between the two mutually incompatible blocks. In contrast, only a single $T_g$ of 8.6 °C was observed for the PNAEP$_{67}$-P(S-*stat*-nBA)$_{100}$ diblock copolymer. The theoretical $T_g$ of a statistical copolymer can be calculated using the Fox equation (**Equation 4.1**).

$$\frac{1}{T_g} = \frac{w_1}{T_{g1}} + \frac{w_2}{T_{g2}} \tag{4.1}$$

Here $w_1$ and $w_2$ are the weight fractions of each component, and $T_{g1}$ and $T_{g2}$ are the $T_g$ values of the respective homopolymers. Using known experimental $T_g$ values for the PS$_{100}$ and PnBA$_{100}$ blocks,[23] a theoretical $T_g$ of 9°C was calculated for the PNAEP$_{67}$-P(S-*stat*-nBA)$_{100}$ diblock copolymer. This value compares well to the experimental value measured by DSC in **Figure 4.10**. Furthermore, two overlapping thermal transitions are observed for the blue curve: this is attributed to the PNAEP$_{67}$ block and the statistical copolymer block possessing similar $T_g$ values.

DLS studies indicated that these PNAEP$_{67}$-PS$_{100}$ and PNAEP$_{67}$-(PS-PnBA)$_{100}$ nanoparticles had comparable *z*-average particle diameters of 35 nm and 39 nm, respectively (**Figure 4.11**).

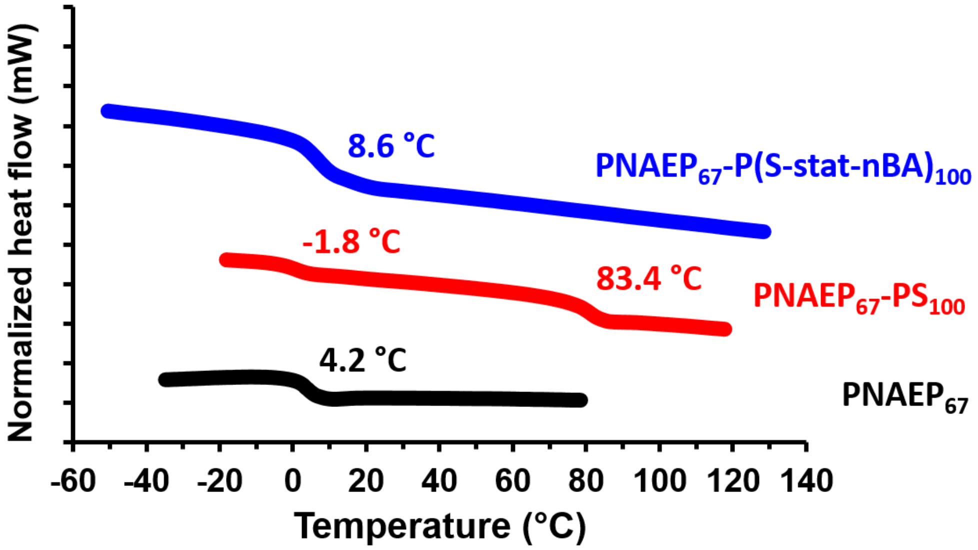

**Figure 4.10.** Differential scanning calorimetry (DSC) curves recorded for PNAEP$_{67}$-PS$_{100}$ spheres PNAEP$_{67}$-P(S-*stat*-nBA)$_{100}$ (nBA = 55% by mass) spheres and the PNAEP$_{67}$ precursor.

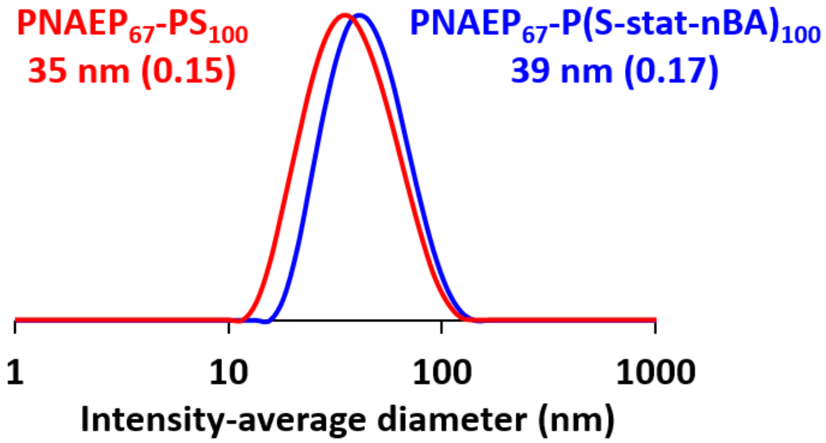

**Figure 4.11.** DLS intensity-average particle size distributions recorded for 0.1% w/w aqueous dispersions of $PNAEP_{67}$-$PS_{100}$ and $PNAEP_{67}$-P(S-*stat*-nBA)$_{100}$ diblock copolymers.

Both types of nanoparticles were evaluated as putative dispersants during the milling of azoxystrobin. Laser diffraction studies confirmed that azoxystrobin microparticles with a volume-average diameter of approximately 2 μm could be obtained after milling for 30 min when using either nanoparticle dispersant (**Figure 4.12**). SEM images of the azoxystrobin microparticles after the removal of excess nanoparticles are shown in **Figure 4.13.** SEM studies provide evidence for the adsorption of $PNAEP_{67}$-$PS_{100}$ nanoparticles onto azoxystrobin, but comparable images could not be obtained for the low-$T_g$ $PNAEP_{67}$-P(S-*stat*-nBA)$_{100}$ nanoparticles, which is consistent with *in situ* film formation in this case. These experiments suggest that retention of the original copolymer morphology is not required for sterically-stabilized nanoparticles to act as a dispersant for azoxystrobin.

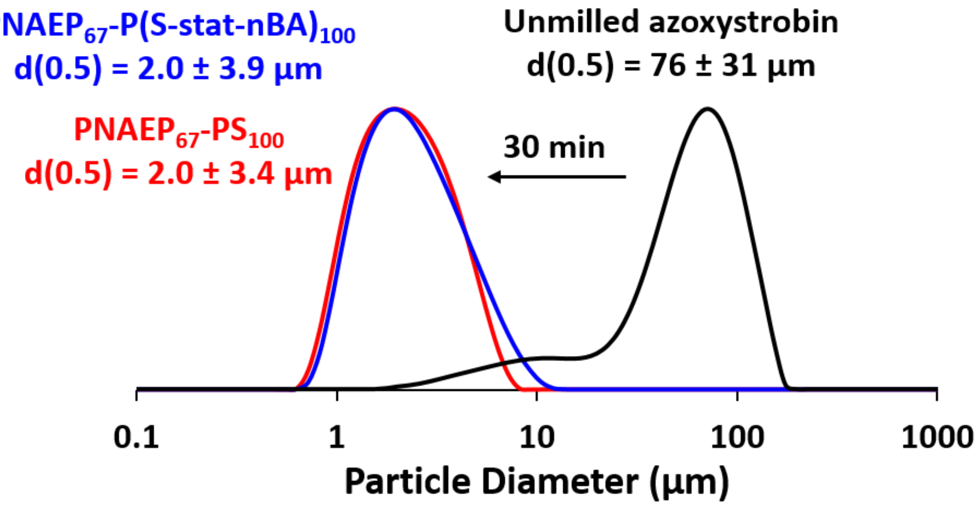

**Figure 4.12.** Laser diffraction particle size distribution curves (and corresponding volume-average diameters) recorded after milling azoxystrobin with either PNAEP$_{67}$-PS$_{100}$ nanoparticles (red curve) or PNAEP$_{67}$-P(S-*stat*-nBA)$_{100}$ nanoparticles (blue curve) for 30 min.

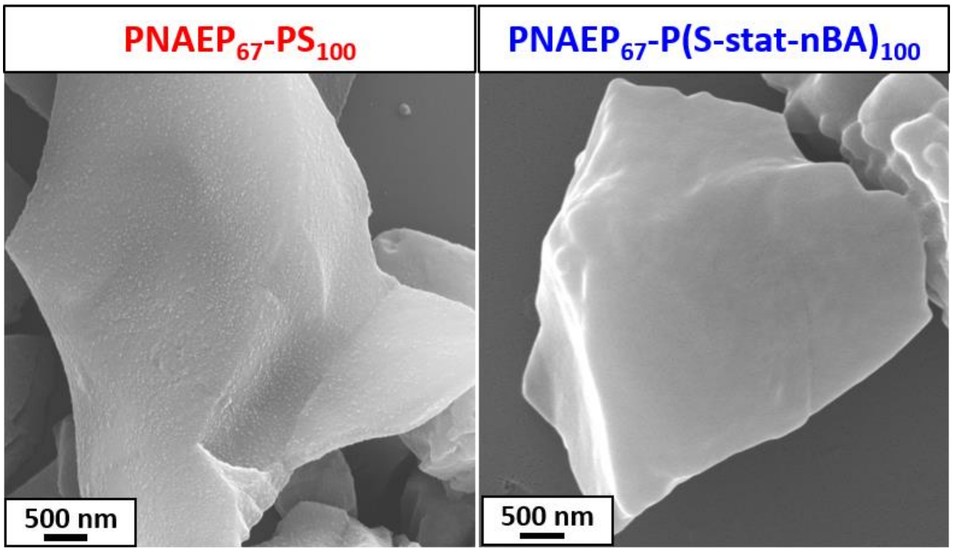

**Figure 4.13.** SEM images recorded for azoxystrobin microparticles prepared by milling in the presence of either PNAEP$_{67}$-PS$_{100}$ or PNAEP$_{67}$-P(S-*stat*-nBA)$_{100}$ diblock copolymers after removal of excess nanoparticles by centrifugation.

### 4.3.5 Effect of Varying the Chemical Nature of the Agrochemical Active

Finally, we wished to examine whether this nanoparticle dispersant approach could also work for alternative hydrophobic organic crystalline compounds exhibiting minimal aqueous solubility. Accordingly, the following five agrochemical actives were evaluated for the preparation of nanoparticle-stabilized aqueous SCs: cyproconazole (CCZ), difenoconazole (DFZ), isopyrazam (IZM), tebuconazole (TEB) and pinoxaden (PXD). The first four compounds are alternative fungicides to azoxystrobin with varying modes of action, whereas the latter is a highly selective systemic herbicide that is used to control monocotyledonous grass weeds in crops such as wild oats, wheat and barley.[36–39]

PGMA$_{50}$-PMMA$_{80}$ nanoparticles were used as the dispersant when attempting to mill each of these alternatives to azoxystrobin. SC formulations comprising just the agrochemical active, the nanoparticle dispersant, an antifoam agent and water were used in this set of experiments. **Figure 4.14** summarizes the laser diffraction curves recorded before and after milling: organic microparticles with a volume-average particle diameter of approximately 2 µm could be obtained in each case after milling for 25-40 min using the IKA tube drive. Optical microscopy images recorded for the various coarse crystals prior to milling and the much finer corresponding microparticles obtained after milling are shown in **Figure 4.15**. These observations clearly demonstrate that PGMA$_{50}$-PMMA$_{80}$ nanoparticles can act as an effective wetting agent and dispersant for a range of agrochemical actives, not just azoxystrobin.

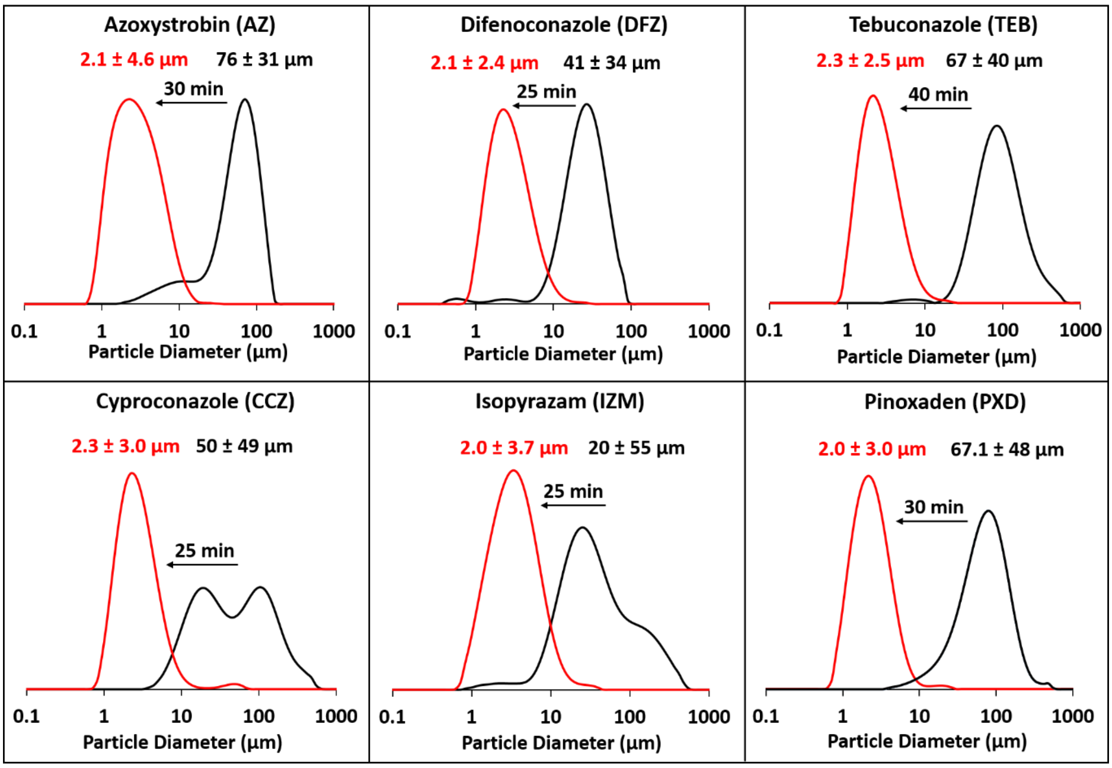

**Figure 4.14.** Laser diffraction particle size distribution curves (and corresponding volume-average diameters) recorded for (i) six unmilled (black curves) agrochemical active ingredients (azoxystrobin, difenoconazole, tebuconazole, cyproconazole, isopyrazam and pinoxaden) and (ii) after milling each of these active ingredients in the presence of PGMA$_{50}$-PMMA$_{80}$ nanoparticles (red curves).

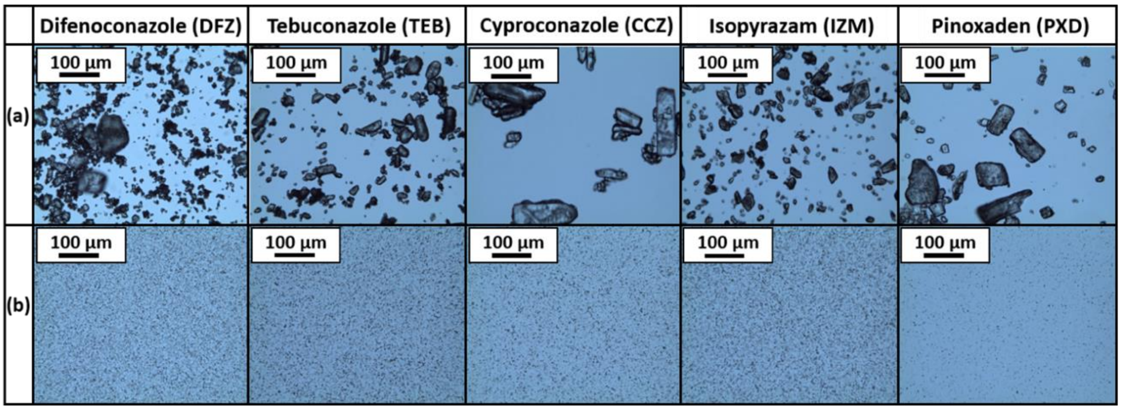

**Figure 4.15.** Optical microscopy images recorded for the following five active ingredients (a) before ball milling and (b) after ball milling using the tube drive: difenoconazole, tebuconazole, cyproconazole, isopyrazam and pinoxaden. In these experiments, ball milling of each active ingredient was performed in the presence of $PGMA_{50}$-$PMMA_{80}$ nanoparticles (*z*-average diameter = 29 nm).

These five new SCs were each subjected to three centrifugation-redispersion cycles to remove any non-adsorbed $PGMA_{50}$-$PMMA_{80}$ nanoparticles. **Figure 4.16** shows representative TEM images of individual CCZ, DFZ, IZM, TEB and PXD microparticles, which are each clearly coated with a uniform layer of $PGMA_{50}$-$PMMA_{80}$ nanoparticles. In the case of IZM, analysis using ImageJ software indicates a surface coverage of approximately 40-45%. This is somewhat higher than that estimated for azoxystrobin microparticles coated with the same nanoparticles (32-35 %). However, the grayscale adjustment within ImageJ software is rather subjective, so these apparently higher fractional surface coverages ideally require corroboration by conducting further XPS studies, similar to the approach discussed in Chapter 3. In that case, a surface coverage of 24% was determined by XPS for azoxystrobin microparticles coated with $PGMA_{50}$-$PMMA_{80}$ nanoparticles.

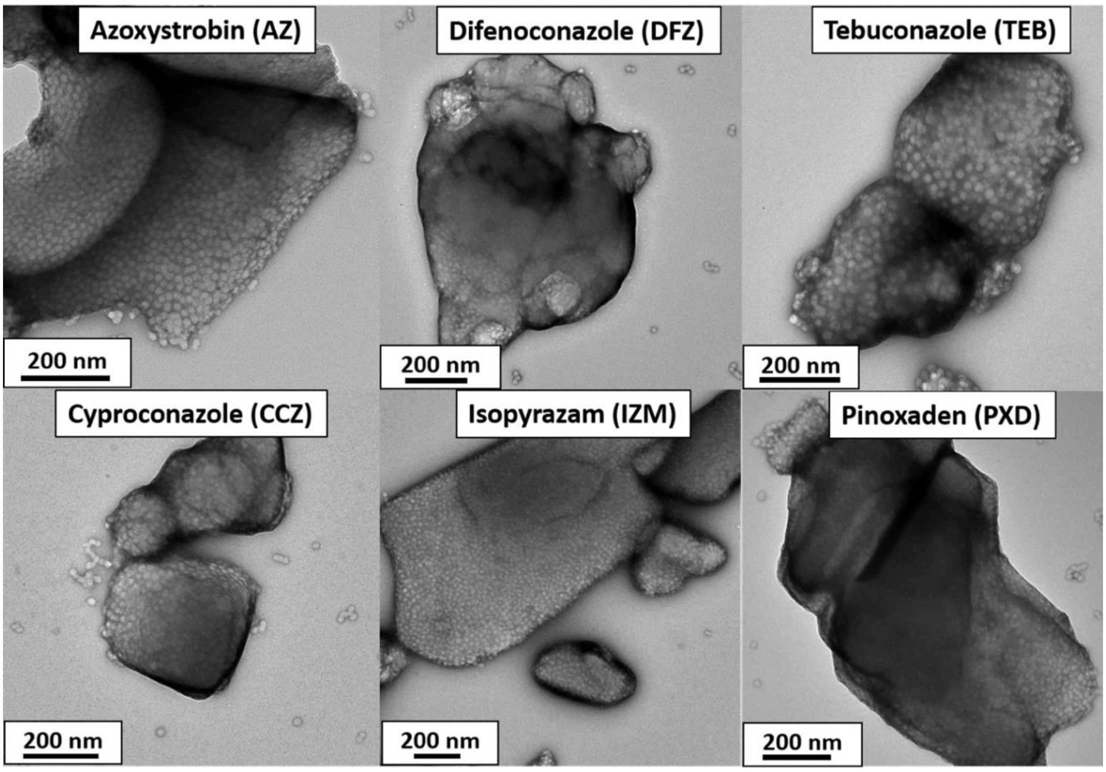

**Figure 4.16.** TEM images recorded for microparticles prepared by milling six different agrochemical active ingredients in the presence of PGMA$_{50}$-PMMA$_{80}$ nanoparticles (after removal of excess nanoparticles by centrifugation-redispersion cycles). In each case, the nanoparticles are clearly adsorbed at the surface of the organic crystalline microparticles at relatively high surface coverage.

### 4.3.6 Long-term Stability of Azoxystrobin-based Suspension Concentrates

The long-term stability of azoxystrobin-based SCs was assessed using laser diffraction. Given the mean size and density of the azoxystrobin microparticles, such formulations tended to sediment over time in the absence of any structuring agents. However, in each case redispersion was readily achieved upon hand-shaking. This enabled repeated particle size analyses to be conducted on each suspension after one, six and twelve months, as well as on the fresh (i.e. day-old) suspension (**Figure 4.17**).

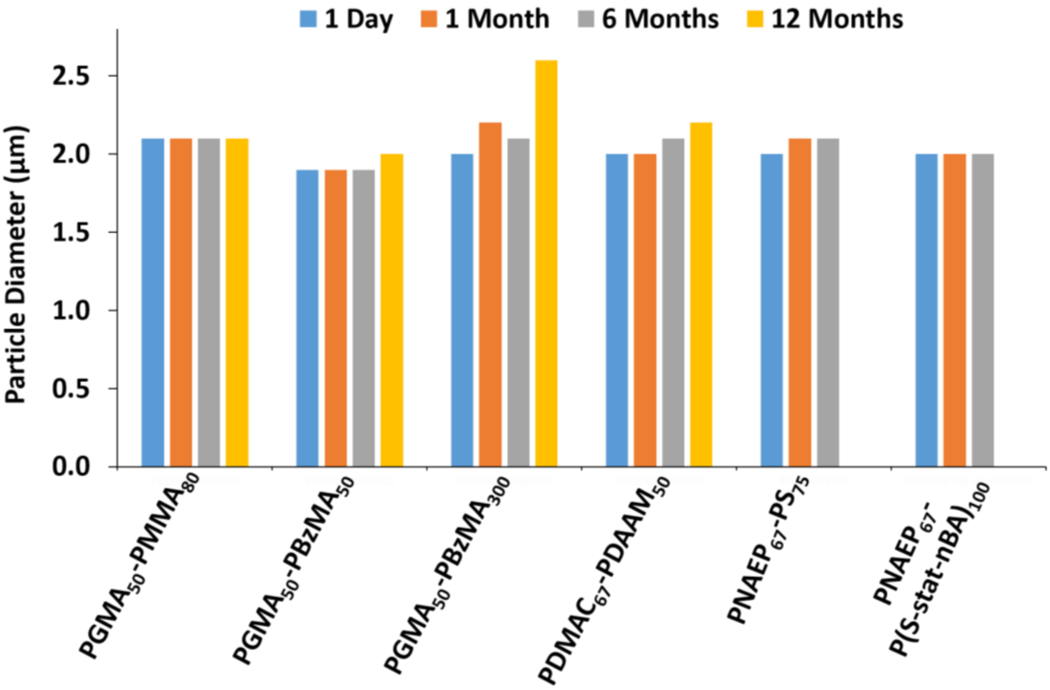

**Figure 4.17.** Volume-average particle diameter data obtained *via* laser diffraction for various azoxystrobin-based suspension concentrates using the stated diblock copolymer nanoparticles as dispersants and subsequently aged at 20 °C for 1 day, 1 month, 6 months or 12 months. In such experiments, an approximately constant mean particle diameter indicates a stable suspension.

In each case, the original SC exhibited an initial volume-average particle diameter of approximately 2 µm after ball milling. For the formulation prepared using the largest $PGMA_{50}$-$PBzMA_{300}$ nanoparticles, the milling time was extended to 45 min to achieve the desired 2 µm diameter for the azoxystrobin microparticles. Over time, these SCs exhibited minimal change in particle size after six months and in most cases remained stable after one year of storage at ambient temperature. The outlier was the SC prepared using the largest $PGMA_{50}$-$PBzMA_{300}$ nanoparticles but even for this least stable formulation the mean particle diameter only increased from 2.0 µm to 2.5 µm after twelve months. Interestingly, there was no discernible difference in long-term stability when varying the chemical nature of the steric stabilizer block, the core-forming block, or when employing soft, film-forming diblock copolymer nanoparticles as the dispersant.

## 4.4 Conclusions

Various sterically-stabilized diblock copolymer nanoparticles prepared *via* RAFT polymerization using various aqueous PISA formulations have proven to be effective dispersants for the preparation of SCs comprising six different agrochemical actives *via* ball milling. Changing the chemical nature of the non-ionic core-forming block had essentially no effect on dispersant performance. However, nanoparticles comprising either cationic or anionic steric stabilizer chains proved to be ineffective. A series of $PGMA_{50}$-$PBzMA_x$ nanoparticles with varying mean diameters were also evaluated as dispersants. In this case, nanoparticles of up to 51 nm diameter were effective but larger nanoparticles led to less efficient ball milling and the formation of marginally less stable microparticles. The effect of crosslinking the nanoparticle cores and adjusting the $T_g$ of the core-forming block was also examined. In the former case, the covalently-stabilized nanoparticles performed as well as the corresponding linear nanoparticles, which suggests that individual amphiphilic diblock copolymer chains do not play a significant role in the production of SCs. In the latter case, stable SCs could be obtained when using film-forming nanoparticles, so perseveration of the original copolymer morphology after adsorption at the surface of the azoxystrobin crystals is not a prerequisite for successful processing. Moreover, this nanoparticle dispersant approach developed for azoxystrobin was extended to include five other common agrochemical actives, which suggests that is likely to be generic in scope. Finally, laser diffraction studies of the long-term stability of azoxystrobin-based SCs suggests that most of these formulations remained stable for at least one year.

## 4.5 References

(1) Zhang, Y.; Lorsbach, B. A.; Castetter, S.; Lambert, W. T.; Kister, J.; Wang, N. X.; Klittich, C. J. R.; Roth, J.; Sparks, T. C.; Loso, M. R. Physicochemical Property Guidelines for Modern Agrochemicals. *Pest Manag. Sci.* **2018**, *74*, 1979–1991.

(2) Tadros, T. F. Colloids in Agrochemicals. In *Colloids and Interface Science Series*; Wiley: Weinheim, 2011.

(3) Haas, S.; Hässlin, H. W.; Schlatter, C. Influence of Polymeric Surfactants on Pesticidal Suspension Concentrates: Dispersing Ability, Milling Efficiency and Stabilization Power.

*Colloids Surfaces A Physicochem. Eng. Asp.* **2001**, *183*, 785–793.

(4) Tadros, T. F. Physical Stability of Suspension Concentrates. *Adv. Colloid Interface Sci.* **1980**, *12*, 141–261.

(5) Ferguson, C. J.; Hughes, R. J.; Pham, B. T. T.; Hawkett, B. S.; Gilbert, R. G.; Serelis, A. K.; Such, C. H. Effective Ab Initio Emulsion Polymerization under RAFT Control. *Macromolecules* **2002**, *35*, 9243–9245.

(6) Zetterlund, P. B.; Thickett, S. C.; Perrier, S.; Bourgeat-Lami, E.; Lansalot, M. Controlled/Living Radical Polymerization in Dispersed Systems: An Update. *Chem. Rev.* **2015**, *115*, 9745–9800.

(7) Charleux, B.; Delaittre, G.; Rieger, J.; D'Agosto, F. Polymerization-Induced Self-Assembly: From Soluble Macromolecules to Block Copolymer Nano-Objects in One Step. *Macromolecules* **2012**, *45*, 6753–6765.

(8) Canning, S. L.; Smith, G. N.; Armes, S. P. A Critical Appraisal of RAFT-Mediated Polymerization-Induced Self-Assembly. *Macromolecules* **2016**, *49*, 1985–2001.

(9) Derry, M. J.; Fielding, L. A.; Armes, S. P. Polymerization-Induced Self-Assembly of Block Copolymer Nanoparticles via RAFT Non-Aqueous Dispersion Polymerization. *Prog. Polym. Sci.* **2016**, *52*, 1–18.

(10) Semsarilar, M.; Jones, E. R.; Blanazs, A.; Armes, S. P. Efficient Synthesis of Sterically-Stabilized Nano-Objects via RAFT Dispersion Polymerization of Benzyl Methacrylate in Alcoholic Media. *Adv. Mater.* **2012**, *24*, 3378–3382.

(11) Fielding, L. A.; Derry, M. J.; Ladmiral, V.; Rosselgong, J.; Rodrigues, A. M.; Ratcliffe, L. P. D.; Sugihara, S.; Armes, S. P. RAFT Dispersion Polymerization in Non-Polar Solvents: Facile Production of Block Copolymer Spheres, Worms and Vesicles in n-Alkanes. *Chem. Sci.* **2013**, *4*, 2081–2087.

(12) Tan, J.; Liu, D.; Huang, C.; Li, X.; He, J.; Xu, Q.; Zhang, L. Photoinitiated Polymerization-Induced Self-Assembly of Glycidyl Methacrylate for the Synthesis of Epoxy-Functionalized Block Copolymer Nano-Objects. *Macromol. Rapid Commun.* **2017**, *38*, 1–7.

(13) Tan, J.; He, J.; Li, X.; Xu, Q.; Huang, C.; Liu, D.; Zhang, L. Rapid Synthesis of Well-Defined All-Acrylic Diblock Copolymer Nano-Objects: Via Alcoholic Photoinitiated Polymerization-Induced Self-Assembly (Photo-PISA). *Polym. Chem.* **2017**, *8*, 6853–6864.

(14) Figg, C. A.; Simula, A.; Gebre, K. A.; Tucker, B. S.; Haddleton, D. M.; Sumerlin, B. S. Polymerization-Induced Thermal Self-Assembly (PITSA). *Chem. Sci.* **2015**, *6*, 1230–1236.

(15) Tan, J.; Sun, H.; Yu, M.; Sumerlin, B. S.; Zhang, L. Photo-PISA: Shedding Light on Polymerization-Induced Self-Assembly. *ACS Macro Lett.* **2015**, *4*, 1249–1253.

(16) Liu, G.; Qiu, Q.; An, Z. Development of Thermosensitive Copolymers of Poly(2-Methoxyethyl Acrylate-Co-Poly(Ethylene Glycol) Methyl Ether Acrylate) and Their Nanogels Synthesized by RAFT Dispersion Polymerization in Water. *Polym. Chem.* **2012**, *3*, 504–513.

(17) Shen, W.; Chang, Y.; Liu, G.; Wang, H.; Cao, A.; An, Z. Biocompatible, Antifouling, and Thermosensitive Core-Shell Nanogels Synthesized by RAFT Aqueous Dispersion Polymerization. *Macromolecules* **2011**, *44*, 2524–2530.

(18) Khor, S. Y.; Truong, N. P.; Quinn, J. F.; Whittaker, M. R.; Davis, T. P. Polymerization-Induced Self-Assembly: The Effect of End Group and Initiator Concentration on Morphology of Nanoparticles Prepared via RAFT Aqueous Emulsion Polymerization. *ACS Macro Lett.* **2017**, *6*, 1013–1019.

(19) Truong, N. P.; Dussert, M. V; Whittaker, M. R.; Quinn, J. F.; Davis, T. P. Rapid Synthesis of Ultrahigh Molecular Weight and Low Polydispersity Polystyrene Diblock Copolymers by RAFT-Mediated Emulsion Polymerization. *Polym. Chem.* **2015**, *6*, 3865–3874.

(20) Rieger, J.; Zhang, W.; Stoffelbach, F.; Charleux, B. Surfactant-Free RAFT Emulsion Polymerization Using Poly(N,N -Dimethylacrylamide) Trithiocarbonate Macromolecular Chain Transfer Agents. *Macromolecules* **2010**, *43*, 6302–6310.

(21) Boissé, S.; Rieger, J.; Belal, K.; Di-Cicco, A.; Beaunier, P.; Li, M. H.; Charleux, B. Amphiphilic Block Copolymer Nano-Fibers via RAFT-Mediated Polymerization in Aqueous Dispersed System. *Chem. Commun.* **2010**, *46*, 1950–1952.

(22) Chaduc, I.; Girod, M.; Antoine, R.; Charleux, B.; D'Agosto, F.; Lansalot, M. Batch Emulsion Polymerization Mediated by Poly(Methacrylic Acid) MacroRAFT Agents: One-Pot Synthesis of Self-Stabilized Particles. *Macromolecules* **2012**, *45*, 5881–5893.

(23) Deane, O. J.; Musa, O. M.; Fernyhough, A.; Armes, S. P. Synthesis and Characterization of Waterborne Pyrrolidone- Functional Diblock Copolymer Nanoparticles Prepared via Surfactant-Free RAFT Emulsion Polymerization. *Macromolecules* **2020**, *53*, 1422–1434.

(24) Binauld, S.; Delafresnaye, L.; Charleux, B.; Dagosto, F.; Lansalot, M. Emulsion Polymerization of Vinyl Acetate in the Presence of Different Hydrophilic Polymers Obtained by RAFT/MADIX. *Macromolecules* **2014**, *47*, 3461–3472.

(25) Zhang, W.; D'Agosto, F.; Dugas, P. Y.; Rieger, J.; Charleux, B. RAFT-Mediated One-Pot Aqueous Emulsion Polymerization of Methyl Methacrylate in Presence of Poly(Methacrylic Acid-Co-Poly(Ethylene Oxide) Methacrylate) Trithiocarbonate Macromolecular Chain Transfer Agent. *Polymer* **2013**, *54*, 2011–2019.

(26) D'Agosto, F.; Rieger, J.; Lansalot, M. RAFT-Mediated Polymerization-Induced Self-Assembly. *Angew. Chemie - Int. Ed.* **2020**, *59*, 8368–8392.

(27) Guimarães, T. R.; Khan, M.; Kuchel, R. P.; Morrow, I. C.; Minami, H.; Moad, G.; Perrier, S.; Zetterlund, P. B. Nano-Engineered Multiblock Copolymer Nanoparticles via

Reversible Addition-Fragmentation Chain Transfer Emulsion Polymerization. *Macromolecules* **2019**, *52*, 2965–2974.

(28) Clothier, G. K. K.; Guimarães, T. R.; Khan, M.; Moad, G.; Perrier, S.; Zetterlund, P. B. Exploitation of the Nanoreactor Concept for Efficient Synthesis of Multiblock Copolymers via Macroraft-Mediated Emulsion Polymerization. *ACS Macro Lett.* **2019**, *8*, 989–995.

(29) Cunningham, V. J.; Alswieleh, A. M.; Thompson, K. L.; Williams, M.; Leggett, G. J.; Armes, S. P.; Musa, O. M. Poly(Glycerol Monomethacrylate)-Poly(Benzyl Methacrylate) Diblock Copolymer Nanoparticles via RAFT Emulsion Polymerization: Synthesis, Characterization, and Interfacial Activity. *Macromolecules* **2014**, *47*, 5613–5623.

(30) Akpinar, B.; Fielding, L. A.; Cunningham, V. J.; Ning, Y.; Mykhaylyk, O. O.; Fowler, P. W.; Armes, S. P. Determining the Effective Density and Stabilizer Layer Thickness of Sterically Stabilized Nanoparticles. *Macromolecules* **2016**, *49*, 5160–5171.

(31) Chan, D. H. H.; Kynaston, E. L.; Lindsay, C.; Taylor, P.; Armes, S. P. Block Copolymer Nanoparticles Are Effective Dispersants for Micrometer-Sized Organic Crystalline Particles. *ACS Appl. Mater. Interfaces* **2021**, *13*, 30235–30243.

(32) Byard, S. J.; Blanazs, A.; Miller, J. F.; Armes, S. P. Cationic Sterically Stabilized Diblock Copolymer Nanoparticles Exhibit Exceptional Tolerance toward Added Salt. *Langmuir* **2019**, *35*, 14348–14357.

(33) Chan, D. H. H.; Cockram, A. A.; Gibson, R. R.; Kynaston, E. L.; Lindsay, C.; Taylor, P.; Armes, S. P. RAFT Aqueous Emulsion Polymerization of Methyl Methacrylate: Observation of Unexpected Constraints When Employing a Non-Ionic Steric Stabilizer Block. *Polym. Chem.* **2021**, *12*, 5760–5769.

(34) Fleer, G. J.; Cohen Stuart, M. A.; Scheutjens, J. M. H. M.; Cosgrove, T.; Vincent, B.; *Polymers at Interfaces*; Chapman & Hall: Cambridge, 1993.

(35) Chambon, P.; Blanazs, A.; Battaglia, G.; Armes, S. P. Facile Synthesis of Methacrylic ABC Triblock Copolymer Vesicles by RAFT Aqueous Dispersion Polymerization. *Macromolecules* **2012**, *45*, 5081–5090.

(36) Walter, H.; Tobler, H.; Gribkov, D.; Corsi, C. Sedaxane, Isopyrazam and Solatenol$^{TM}$: Novel Broad-Spectrum Fungicides Inhibiting Succinate Dehydrogenase (SDH) - Synthesis Challenges and Biological Aspects. *Chimia* **2015**, *69*, 425–434.

(37) Russell, P. E. A Century of Fungicide Evolution. *J. Agric. Sci.* **2005**, *143*, 11–25.

(38) Munkvold, G. P. Seed Pathology Progress in Academia and Industry. *Annu. Rev. Phytopathol.* **2009**, *47*, 285–311.

(39) Hofer, U.; Muehlebach, M.; Hole, S.; Zoschke, A. Pinoxaden - For Broad Spectrum Grass Weed Management in Cereal Crops. *J. Plant Dis. Prot.* **2006**, *113*, 989–995.

# Chapter 5

# Synthesis and Characterization of Polypyrrole-Coated Anthracene Microparticles

Reproduced in full with permission from [Chan, D. H. H.; Millet, A.; Fisher, C. R.; Price, M. C.; Burchell, M. J.; Armes, S. P. Synthesis and Characterization of Polypyrrole-Coated Anthracene Microparticles: A New Synthetic Mimic for Polyaromatic Hydrocarbon-Based Cosmic Dust. *ACS Appl. Mater. Interfaces* **2021**, *13*, 3175–3185.]

## 5.1 Introduction

Polyaromatic hydrocarbons (PAHs) such as anthracene, phenanthrene, perylene, and pyrene are naturally occurring molecules found in coal and petroleum deposits, oil shale, hydrothermal vents, and volcanic ash.[1] They are also present in cigarette smoke and automotive exhaust gas and can be generated during wood burning. As such, PAHs are considered to be long-lived organic pollutants whose persistence in the environment is linked to their strong resistance to oxidative and photochemical degradation. However, it is this chemical stability that has attracted growing interest from the space science community, not least because infrared emission spectroscopy studies have confirmed the ubiquitous presence of PAHs throughout the universe.[2–5]

Indeed, Greenberg *et al*. have postulated that photoprocessing of organic dust mantles within the interstellar medium during solar irradiation may be a possible mechanism for generating PAHs.[6] More recently, PAHs have been detected in Martian meteorites,[7] interplanetary dust,[2,8] in the upper atmosphere of Titan,[9,10] and within comets.[11,12] They have even been implicated as an important component in the emergence of early life on Earth – the so-called ‘Aromatic World’ hypothesis.[13,14] Moreover, one of the objectives of the ExoMars rover mission is to search for such molecules up to 2 m below the surface of the Martian soil.[15]

In principle, laboratory-based high energy impact experiments can shed considerable light on the behavior of various types of micrometeorites, which typically travel at hypervelocities (> 1 km $s^{-1}$) in outer space.[16] This is because when such fast-moving micrometeorites strike a metal target, they are almost instantaneously converted into molecular and/or atomic fragments by the high-energy impact.[17] This enables their chemical composition to be inferred by time-of-flight mass spectrometric analysis of the ionic plasma.[18–21] Indeed, this was the fundamental detection mechanism for the Cosmic Dust Analyzer (CDA) instrument deployed by the CASSINI spacecraft when orbiting Saturn and its moons.[22] For example, this CDA detector has detected both low- and high-mass aromatic compounds within the plumes of water ejected from the interior of the Saturnian satellite Enceladus.[23,24]

In practice, it is not trivial to design appropriate synthetic mimics that can be accelerated up to the hypervelocity regime that typically characterizes the behavior of such ‘cosmic dust’. Nevertheless, Armes and co-workers have prepared a series of (sub)micrometer-sized particles that have proven to be useful mimics for either carbonaceous or silicate-rich micro-meteorites.[16] This has been achieved by coating either polystyrene or silica particles with an ultrathin overlayer of polypyrrole (PPy).[25,26] This relatively air-stable organic conducting polymer ensures that such synthetic particles can acquire sufficient surface charge to enable their electrostatic acceleration up to the hypervelocity regime using a high-field van de Graaff accelerator.[27] In addition, certain naturally-occurring mineral grains such as olivine, pyroxene and pyrrhotite have been coated with PPy and successfully accelerated for hypervelocity impact experiments.[28–30] Moreover, by coating appropriate particles with PPy,[31] it has been possible to demonstrate *via* laboratory experiments that impact ionization time-of-flight spectra can be used to distinguish between at least some types of aromatic and aliphatic organic microparticles.[20,32] However, it has not yet been possible to examine PAH-based particles in this context.

One of the simplest members of the PAH family is anthracene (see **Figure 5.1**). This planar fused molecule forms large organic crystals with very limited solubility in common organic solvents and is essentially insoluble in water. In Chapters 3 and 4, it was demonstrated that suspension concentrates comprising hydrophobic micrometer-sized particles could be readily prepared *via* ball milling. Chapter 5 utilizes a similar protocol to prepare micrometer-sized anthracene particles in the presence of a commercial dispersant (Morwet D-425). Originally, we envisaged that anthracene might be a useful benign surrogate for various agrochemical actives. However, this requirement was eventually deemed unnecessary. Subsequently, it was found that PPy could be deposited onto such anthracene microparticles to produce an electrically conductive overlayer. These new microparticles are expected to become useful synthetic PAH mimics for laboratory-based hypervelocity experiments using either a light gas gun[27,33,34] or a van der Graaf accelerator.[17,35]

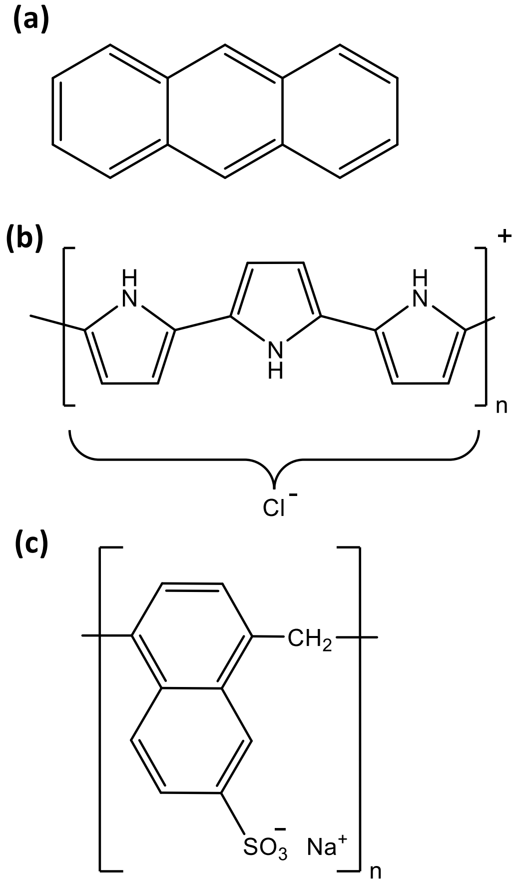

**Figure 5.1.** Chemical structures for (a) anthracene, (b) polypyrrole (PPy), and (c) Morwet D-425 dispersant. [N.B. The chemical structure shown for PPy is the typical idealized structure reported in the literature; in reality, the conjugated backbone also contains unpaired electrons (radicals) as well as delocalized cationic charge].

## 5.2 Experimental

### 5.2.1 Materials

Iron(III) chloride hexahydrate (97%) was purchased from Alfa Aesar (UK). $(NH_4)_2S_2O_8$ (APS), anthracene (97%), and pyrrole were each purchased from Sigma-Aldrich (UK). Pyrrole was purified by alumina chromatography (basic alumina, Sigma-Aldrich UK) prior to use. Silicone SAG1572 (Momentive, Germany) was used as an antifoaming agent, while Morwet D-425 (Nouryon, Sweden; molecular weight range = 1 000 to 5 000 g $mol^{-1}$) was used as a dispersant. Deionized water was obtained from an Elga Medica DV25 water purification unit. Finally, 1.0 mm ceramic beads (zirconium aluminum oxide) were obtained from Sigmund-Lindner (Germany).

### 5.2.2 Synthesis of PPy Bulk Powder

$FeCl_3.6H_2O$ (9.10 g) was dissolved in deionized water (100 mL) in a 125 mL glass bottle, and this orange-brown aqueous solution was stirred using a magnetic stirrer bar. The pyrrole monomer (1.0 mL) was added to this reaction solution and allowed to polymerize for 12 h at 20 °C. The resulting black precipitate was vacuum-filtered using a Buchner funnel and washed first with deionized water and then methanol. The purified moist black powder was placed on a petri dish and dried in a 50 °C oven overnight. The approximate isolated yield of PPy was 0.87 g (73% based on the pyrrole monomer).

### 5.2.3 Preparation of Anthracene Microparticles

#### (a) By IKA Ultra-Turrax Tube Drive

Anthracene (2.28 g, 20% w/w), Morwet D-425 dispersant (0.2850 g, 2.5% w/w), silicone antifoam (0.114 g, 1.0% w/w), and deionized water (8.72 g, 76.5% w/w) were mixed in a 30 mL tube with approximately 15 g of 1 mm ceramic beads. The tube was then attached to the IKA Ultra-Turrax tube drive and milled at 6 000 rpm for 90 to 120 min until the target particle size was achieved. The ceramic beads were then removed by filtration to obtain a white free-flowing aqueous dispersion.

#### (b) By Retsch Planetary Ball Mill

Anthracene (5.00 g, 20% w/w), Morwet D-425 dispersant (0.6250 g, 2.5% w/w), silicon antifoam (0.250 g, 1.0% w/w), and deionized water (19.125 g, 76.5% w/w) were added to a 50 mL ball milling jar together with 10 g of 2 mm beads. This mixture was milled at 250 rpm using a Retsch Planetary Ball Mill PM 100 for a rotation time of 15 min and a break time of 10 min at 250 rpm. Once the target particle size was achieved, the ceramic beads were removed by filtration to obtain a white free-flowing dispersion.

### 5.2.4 Purification of Aqueous Anthracene Dispersions to Remove Excess Dispersant

Aqueous anthracene dispersions were subjected to three centrifugation–redispersion cycles (6 000 rpm, 10 min per cycle). Each cycle required careful decantation of the aqueous supernatant and redispersion of the sediment using fresh deionized water. The purified aqueous dispersions were either then freeze-dried to recover anthracene microparticles in the form of a fine white powder or coated with an ultrathin overlayer of PPy prior to further characterization studies.

### 5.2.5 Synthesis of PPy-Coated Anthracene Crystals

The following protocol was used to coat 0.50 g of 4 μm anthracene microparticles with a target PPy overlayer of 20 nm and is representative. A 20% w/w aqueous dispersion of anthracene microparticles (2.50 g), pyrrole (37.0 μL; equivalent to a mass loading of 3.5%), and deionized water (25.0 mL) were added to a 120 mL glass bottle to give a low-viscosity dispersion. $FeCl_3.6H_2O$ (0.34 g) was dissolved in deionized water (5.0 mL), and the final aqueous dispersion was stirred for 24 h at 20 °C. The resulting black dispersion was purified by three centrifugation–dispersion cycles (6 000 rpm, 10 min) to remove excess inorganic salts and any unreacted pyrrole and then freeze-dried overnight to recover a fine black powder. To target other PPy overlayer thicknesses, the masses of anthracene and water were kept constant and the amounts of the pyrrole monomer and $FeCl_3$ oxidant were varied accordingly (always employing a fixed oxidant/monomer molar ratio of 2.33).

**Table 5.1** summarizes the various target and actual PPy mass loadings required to achieve a desired nominal overlayer thickness. Such mass loadings depend on the mean diameter of the anthracene microparticles and the solid-state densities of the anthracene (1.25 g $cm^{-3}$) and PPy (1.46 g $cm^{-3}$), which were determined by helium pycnometry. Similar calculations have been previously reported by Lascelles and Armes, who assumed a core–shell morphology to derive a simple equation for coating experiments involving well-defined spherical polystyrene latex particles.[25]

In the present case, the core comprises anthracene, while the shell is composed of PPy. The targeted polypyrrole overlayer thickness, x (in nm), was calculated using **Equation 5.1**:

$$x = R\left[\left(\frac{M_2\rho_1}{M_1\rho_2}+1\right)^{1/3}-1\right] \qquad \textbf{(5.1)}$$

where $R$ is the mean radius of the anthracene microparticles in nm, $M_1$ and $\rho_1$ are the mass fraction and density of the anthracene component and $M_2$ and $\rho_2$ are the mass fraction and density of the polypyrrole component.

In practice, the anthracene microparticles do not have a well-defined spherical morphology (see later). Thus, the target PPy overlayer thicknesses are calculated for “sphere-equivalent” anthracene microparticles. It is implicitly assumed that (i) all of the pyrrole is converted into PPy and (ii) all of the PPy is deposited onto the surface of the anthracene microparticles. In principle, the actual PPy mass loading can be calculated by nitrogen microanalysis by comparing the nitrogen content of the PPy-coated anthracene microparticles to that of PPy bulk powder prepared in the absence of any anthracene microparticles.[25]

**Table 5.1.** Summary of the target PPy overlayer thicknesses, target PPy mass loadings, nitrogen microanalyses, and actual PPy mass loadings (calculated by nitrogen microanalyses) for the two types of anthracene microparticles prepared in this study.

| **Sample description** | **Anthracene microparticle diameter[a] (μm)** | **Target PPy overlayer thickness (nm)** | **Target PPy mass loading (%)** | **Nitrogen microanalysis[b] (%)** | **Calculated PPy mass loading from microanalysis (%)** |
|---|---|---|---|---|---|
| PPy bulk powder | N/A | N/A | 100 | 15.90 | 100 ± 2.7 |
| Uncoated anthracene | 4 | N/A | N/A | 0.0 | N/A |
| PPy-coated anthracene | 4 | 10 | 1.8 | 0.0 | 0.0 |
| PPy-coated anthracene | 4 | 20 | 3.5 | 0.43 | 2.7 ± 1.9 |
| PPy-coated anthracene | 4 | 30 | 5.0 | 0.96 | 6.0 ± 1.9 |
| PPy-coated anthracene | 2 | 20 | 6.7 | 1.36 | 8.6 ± 1.9 |

a. As determined by laser diffraction studies  b. Microanalysis has an error of 0.3%

### 5.2.6 Characterization Techniques

**Helium Pycnometry**

The solid-state densities of anthracene and PPy bulk powder were determined to be 1.25 and 1.46 g cm$^{-3}$, respectively, using a Micromeritics AccuPyc 1330 instrument operating at 20 °C.

**Optical Microscopy**

Optical images were recorded using a Cole–Palmer compound optical microscope equipped with a LCD tablet display and a Moticam BTW digital camera. This technique was used to estimate the mean number–average diameter of the anthracene microparticles (approximately 100 particles counted per sample).

**Particle Size Analysis by Laser Diffraction**

Uncoated and PPy-coated anthracene microparticles were analyzed using a Malvern Mastersizer 3000 laser diffraction instrument equipped with a Hydro EV sample dispersion unit, a He–Ne laser ($\lambda$ = 633 nm), and a solid-state blue laser ($\lambda$ = 466 nm). The stirring rate was set at 2 000 rpm, and data from five measurements were averaged. The standard operating procedure parameters were assumed non-spherical particles with an absorption index of 0.01. The refractive index for anthracene was taken to be 1.5948.

**Solution Densitometry**

The solution densities of a series of aqueous solutions of Morwet D-425 (ranging from 0.05 to 3.00% w/w) were determined using an Anton Paar DMA 4500 M density meter at 20 °C. Subsequently, ball milled anthracene dispersions with mean diameters of either 2 or 4 μm were centrifuged at 10 000 rpm for 10 min and the solution densities of their respective supernatants were measured. This information was used to calculate the amount of Morwet D-425 that was adsorbed onto the surface of the anthracene microparticles.

### Scanning Electron Microscopy

Images were obtained using an Inspect-F instrument operating at an accelerating voltage of 5 kV. Each powder was dispersed and dried onto a thin glass layer before being sputter-coated with a 5 nm overlayer of gold to prevent sample charging.

### FT-IR Spectroscopy

FT-IR spectra were recorded for the uncoated anthracene microparticles, PPy bulk powder, and PPy-coated anthracene microparticles using a Thermo Scientific Nicolet iS10 spectrometer equipped with a Diamond ATR Golden Gate accessory. The spectral resolution was 4 $cm^{-1}$ and 32 scans were averaged per spectrum.

### Raman Microscopy

Raman spectra were recorded using a HORIBA LabRam-HR spectrometer equipped with an infrared laser ($\lambda$ = 785 nm, 3 mW). This wavelength was selected to minimize the well-known problem of fluorescence associated with the Raman spectra of polymers.[36] Given the well-known strongly absorbing nature of highly conjugated polymers such as PPy,[37] either 1 or 10% filters were employed to attenuate the laser power in order to avoid sample degradation. The spectrometer utilized a 600 $mm^{-1}$ grating with a spectral resolution of approximately 2 $cm^{-1}$ and an Olympus BX41 microscope equipped with a ×100 objective lens, which provided a spatial resolution of 1–2 µm. The spectra were obtained from individual anthracene microparticles, with typically five spectra being averaged per sample.

### Aqueous Electrophoresis

Zeta potential versus pH curves were constructed using a Malvern Zetasizer NanoZS instrument operating at 20 °C. Measurements were conducted on dilute (0.5% w/w) aqueous dispersions in the presence of 1 mM KCl as the background electrolyte, with the pH being adjusted using either NaOH or HCl. Zeta potentials were calculated from an average of three measurements *via* the Henry equation using the Smoluchkowski approximation.

### X-ray Photoelectron Spectroscopy

Uncoated and PPy-coated anthracene microparticles and PPy bulk powder were analyzed in turn by X-ray photoelectron spectroscopy (XPS) using a Kratos Axis Supra X-ray photoelectron spectrometer. Step sizes of 0.5 and 0.05 eV were used to record the survey spectra and high resolution coreline spectra, respectively. In each case, powders were placed on an indium foil and spectra were recorded from at least two separate areas.

### Light Gas Gun Experiments and Impact Crater Analysis

A two-stage light gas gun[27] was used to fire PPy-coated anthracene microparticles (4 µm diameter; coated with a nominal PPy overlayer thickness of 30 nm) at an aluminum foil target with a mean thickness of 110 µm. The target chamber was evacuated to less than 0.5 mbar while firing the gun, and the shot speed was determined to be 1.87 km $s^{-1}$ (±0.5%). After this shot, the aluminum foil target was examined using a Hitachi S4700-N FEG-SEM instrument equipped with a Bruker Xflash EDX detector to identify impact craters caused by the impinging microparticles.

## 5.3 Results and Discussion

### 5.3.1 Preparation of Anthracene Microparticles *via* Ball milling

As demonstrated in Chapters 3 and 4, ball milling can be used to prepare micron-sized particles of molecular organic crystals. It is thought that the same approach could be applicable to PAHs such as anthracene, which form relatively large crystals. Accordingly, ball milling was used to prepare aqueous dispersions of anthracene microparticles using a commercially available anionic polymeric dispersant (Morwet D-425) to prevent aggregation of the microparticles *via* a steric stabilization mechanism.[38,39]

Two commercial ball milling devices were examined: an IKA Ultra-Turrax tube drive was used to mill relatively small quantities of material, while a planetary ball mill enabled larger (multigram) quantities to be processed. A substantial reduction in the mean size of the anthracene microparticles was achieved in both cases. **Figure 5.2a** shows the laser diffraction size distributions obtained for the initial anthracene crystals and the anthracene microparticles obtained after grinding an aqueous suspension of anthracene for 30–90 min in the presence of Morwet D-425 dispersant using the tube drive. This particle sizing technique reports a "sphere-equivalent" volume–average diameter, *d*(0.5), which is defined such that 50% of the particles fall below this size. The as-supplied anthracene crystals have an initial volume–average diameter of 302 ± 65 μm, but this was reduced to 7 ± 2 μm within a milling time of 30 min. Longer milling times (60–90 min) produced reasonably uniform microparticles with a volume–average diameter of 4 ± 2 μm, but thereafter, there was little or no further reduction in mean particle size.

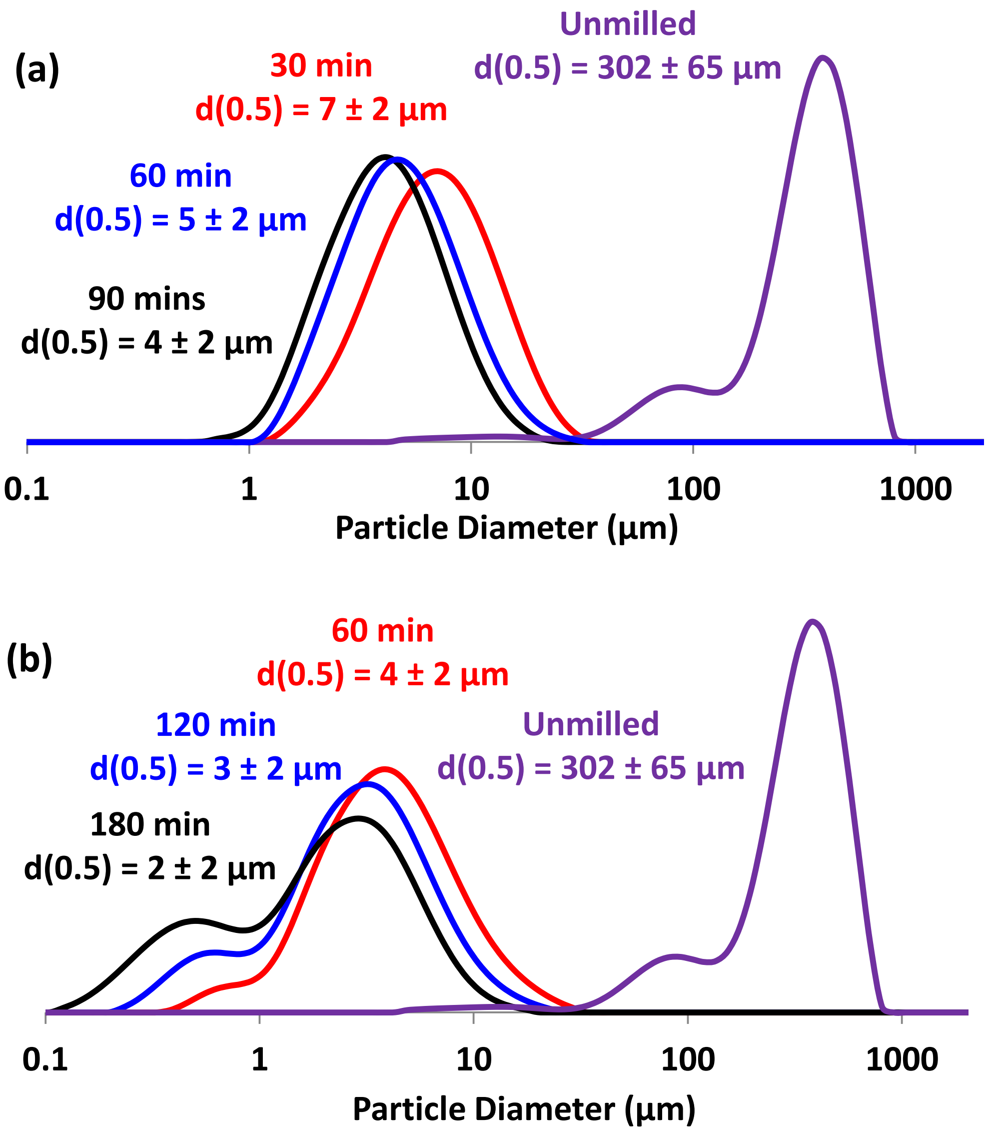

**Figure 5.2.** Laser diffraction particle size distribution curves obtained for the reduction in anthracene particle size *via* ball milling in the presence of Morwet D-425 dispersant using (a) the IKA Ultra-Turrax tube drive and (b) Retsch planetary ball mill.

Even smaller microparticles could be achieved using the planetary ball mill (**Figures 5.2b**). However, the latter technique usually gave broader size distributions owing to the formation of a population of relatively fine particles. It is noteworthy that mean anthracene microparticle diameters of 2–4 µm are comparable with that expected for PAH-based microparticles in space. For example, the NASA *Stardust* mission collected similar-sized cometary dust within its aerogel targets during a cometary fly-by at 6.1 km $s^{-1}$.[40,41] Moreover, the plumes of water erupting from the interior of the Jovian satellite Europa and the Saturnian satellite Enceladus are also believed to contain microparticles within this size range.[42,43]

The aqueous dispersion of 4 µm anthracene microparticles was purified to remove excess non-adsorbed dispersant. This was achieved by three centrifugation–redispersion cycles, with careful decantation of each supernatant prior to redispersion of the sedimented microparticles. Laser diffraction studies indicated no change in the mean anthracene particle size after washing, suggesting a colloidally stable dispersion (**Figure 5.3**).

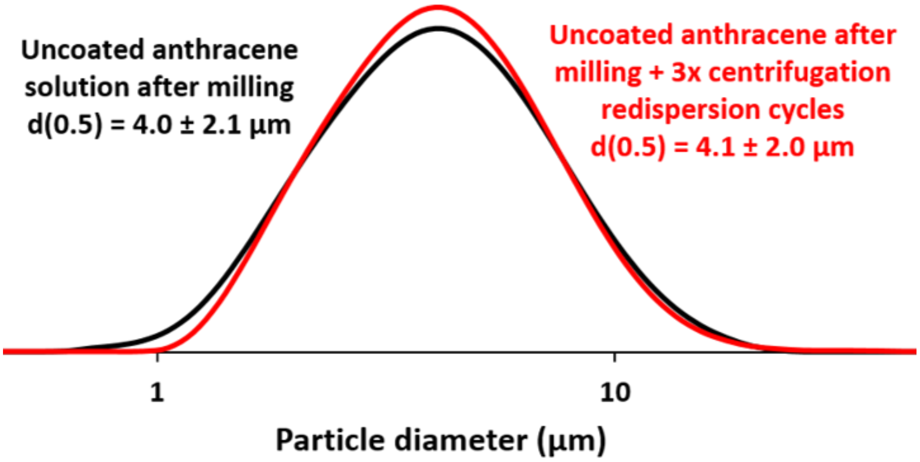

**Figure 5.3.** Laser diffraction particle size distribution curves recorded for uncoated anthracene microparticles obtained immediately after ball milling (black curve) and after centrifugal purification to remove the excess Morwet D-425 dispersant (red curve).

Solution densitometry was used to monitor the concentration of the Morwet D-425 dispersant in the aqueous phase before and after ball milling (**Figure 5.4**). A linear calibration plot was obtained for solution density vs. Morwet D-425 concentration. This relationship was used to calculate the Morwet D-425 concentration remaining in the aqueous supernatant after ball milling to produce: (a) 2 µm anthracene microparticles and (b) 4 µm anthracene microparticles. In each case, an initial concentration of 2.50% was used to prepare the anthracene dispersion. The solution densities determined for the aqueous supernatants in (a) and (b) indicated Morwet D-425 concentrations of 2.19% and 2.40%, respectively (**Figure 5.4**). Based on the initial mass of anthracene, the latter measurement indicated that the 4 µm anthracene microparticles contained approximately 0.50% Morwet D-425 by mass. As expected, the 2 µm anthracene microparticles contained a higher Morwet D-425 content (1.50% by mass).

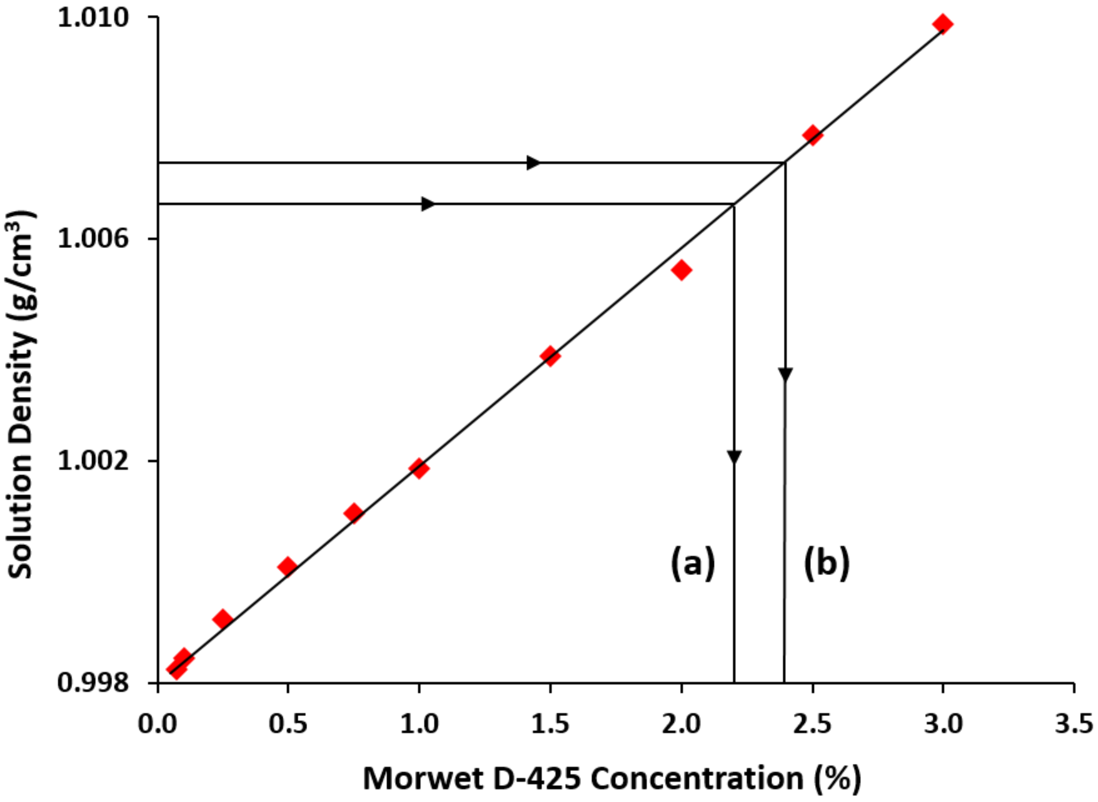

**Figure 5.4.** Linear calibration plot obtained for solution density vs. Morwet D-425 concentration. This relationship was used to calculate the Morwet D-425 concentration remaining in the aqueous supernatant after ball milling to produce: (a) 2 µm anthracene microparticles and (b) 4 µm anthracene microparticles.

### 5.3.2 Coating Anthracene Microparticles with Polypyrrole

PPy is readily prepared in aqueous solution using mild chemical oxidants such as $FeCl_3$. It is usually obtained in the form of an insoluble macroscopic precipitate that has a distinctive globular morphology, but it is well known that PPy can be deposited onto various types of colloidal particles with good control over its coating thickness.[25,37,44] This aqueous deposition process works rather well for hydrophobic substrates such as polystyrene latex but is less suitable for hydrophilic substrates such as silica, for which chemical modification of the surface is usually required.[25,45–47] However, for the highly hydrophobic anthracene microparticles reported herein, the aqueous deposition of PPy was expected to be straightforward.

Accordingly, the pyrrole monomer and $FeCl_3.6H_2O$ oxidant were added to an aqueous dispersion of anthracene microparticles, and the pyrrole polymerization was allowed to proceed for 24 h at 20 °C. The PPy-coated anthracene microparticles were then subjected to three centrifugation–redispersion cycles to remove the spent oxidant and any unreacted pyrrole prior to freeze-drying overnight (**Figure 5.5**). Some of this purified aqueous dispersion was retained for particle size analysis.

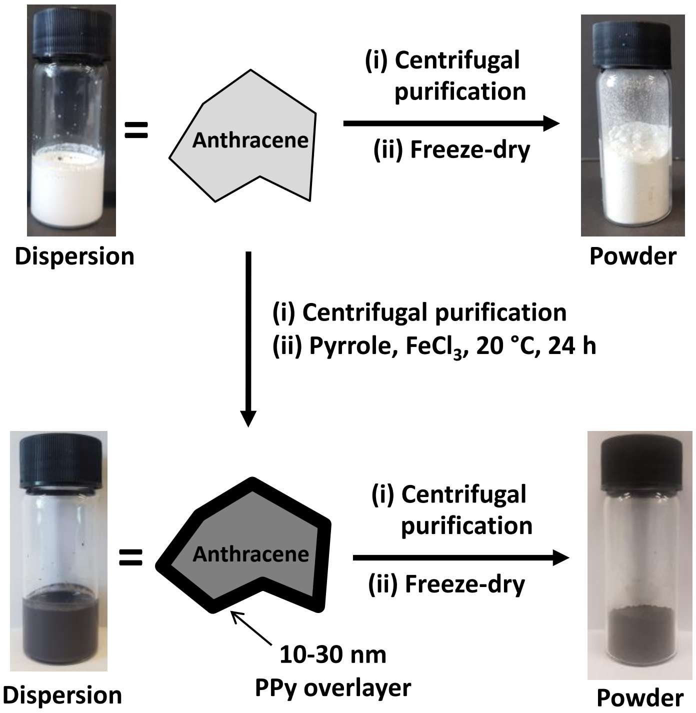

**Figure 5.5**. Schematic representation of the aqueous deposition of an ultrathin PPy overlayer onto the surface of ball milled Morwet-stabilized anthracene microparticles.

### 5.3.3 Characterization of Polypyrrole-coated Anthracene Microparticles

The mean particle size of the purified PPy-coated anthracene microparticles was assessed using laser diffraction (**Figure 5.6**). The dried black powder proved to be relatively hydrophobic, so a wetting agent, Aerosol OT-B (0.01% w/w based on PPy-coated anthracene microparticles), was required to disperse it. A volume–average diameter of approximately 6 ± 3 μm was determined, which was significantly larger than what was expected, given that a PPy overlayer of just 20 nm was targeted. This indicates incipient flocculation of the PPy-coated anthracene microparticles during drying, which is not unexpected in view of the relatively high Hamaker constant for this conducting polymer.[48] However, ultrasonication for 3 min just prior to laser diffraction analysis enables the microparticle floccs to be broken up. This protocol produces a volume–average diameter of 4.3 ± 2.1 μm, which is comparable to that of the original uncoated Morwet-stabilized anthracene microparticles (**Figure 5.6**).

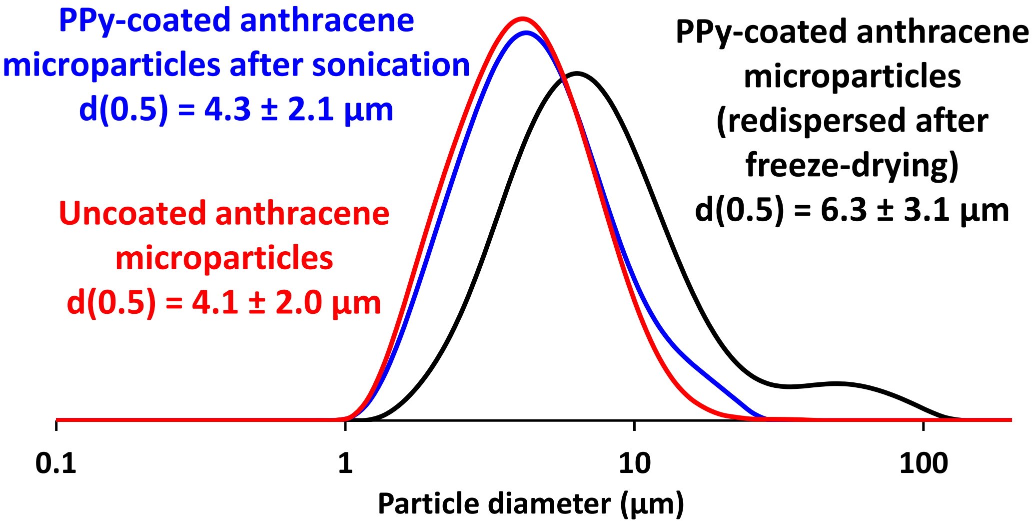

**Figure 5.6.** Laser diffraction particle size distribution curves recorded for an aqueous suspension of uncoated anthracene microparticles (red) and PPy-coated anthracene microparticles before (black) and after (blue) ultrasonication.

Optical microscopy images of the milled anthracene microparticles obtained using Morwet D-425 were in good agreement with the laser diffraction measurements (**Figure 5.7a,c**). The visual appearance of the PPy-coated anthracene microparticles did not differ significantly from that of the uncoated anthracene microparticles (**Figure 5.7b,d**). This is attributed to the rather low conducting polymer mass loadings and hence relatively thin overlayers (see **Table 5.1**). It is perhaps worth emphasizing that the PPy grain size is around 5–10 nm,[49] so a PPy thickness of 10 nm is essentially the thinnest coating that can be targeted to achieve a contiguous overlayer, which is required for the efficient accumulation of surface charge in van de Graaff accelerator experiments.[16–21]

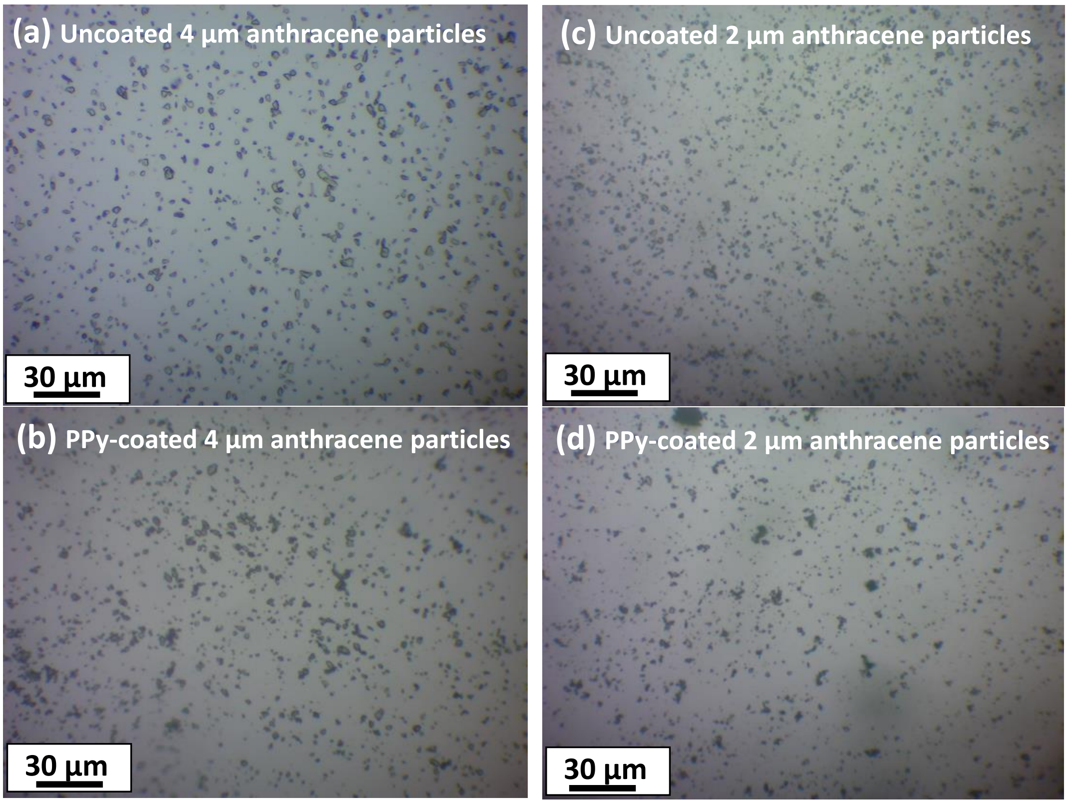

**Figure 5.7**. Optical microscopy images recorded for (a) uncoated and (b) PPy-coated 4 μm anthracene microparticles (PPy overlayer thickness = 20 nm) and (c) uncoated and (d) PPy-coated 2 μm anthracene microparticles (PPy overlayer thickness = 20 nm).

Scanning electron microscopy (SEM) images obtained for PPy bulk powder are shown in **Figure 5.8** and indicate a distinctive globular morphology similar to that reported in the literature.[45] Further SEM studies confirmed that the milled anthracene microparticles were somewhat ill-defined in terms of their size and morphology (**Figure 5.9a,b**). Nevertheless, the mean microparticle dimensions are consistent with those indicated by optical microscopy and laser diffraction studies. There is also some evidence for an unusual perforated, porous surface morphology. Targeting a PPy loading of 3.5% by mass (mean coating thickness = 20 nm) produced a relatively uniform overlayer (**Figure 5.9c,d**). The deposited PPy overlayer has a distinct globular morphology that resembles that of PPy bulk powder, albeit with finer features.

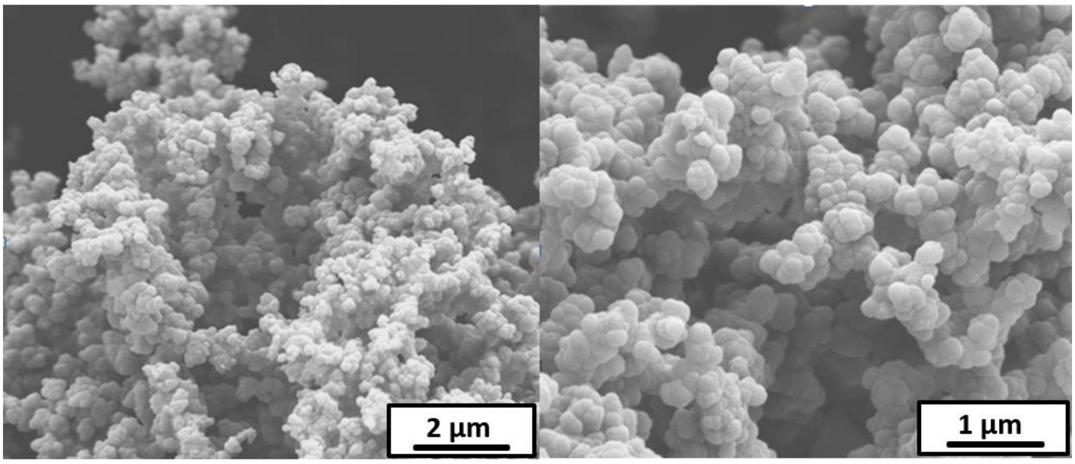

**Figure 5.8.** Scanning electron microscopy images recorded for polypyrrole bulk powder, which has a distinctive globular morphology.

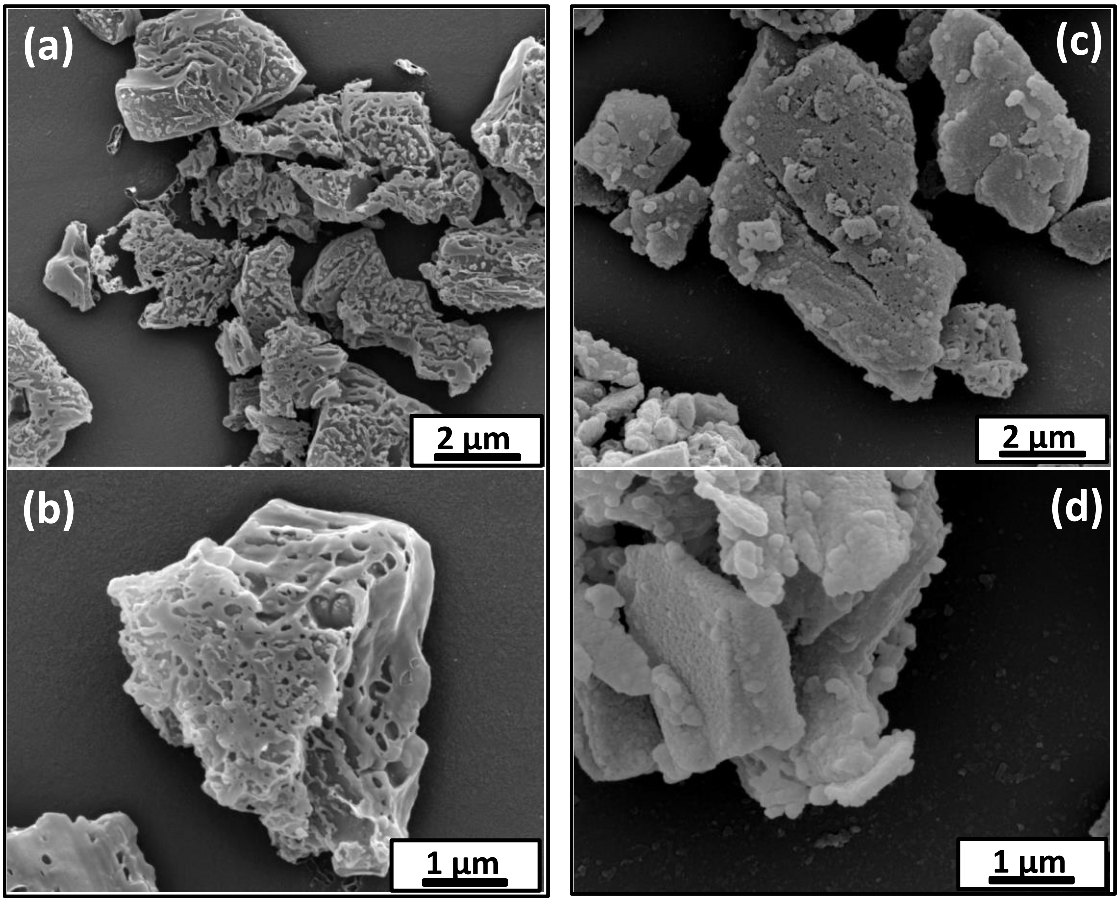

**Figure 5.9.** SEM images recorded for (a,b) uncoated 4 µm anthracene microparticles and (c,d) PPy-coated 4 µm anthracene microparticles (PPy mass loading = 3.5%, corresponding to a mean coating thickness of 20 nm).

The same PPy morphology was observed on smaller 2 μm anthracene microparticles, which were coated with a target overlayer of 20 nm (**Figure 5.10**). A similar surface morphology has been observed for other PPy-coated particles.[37] Moreover, the surface voids observed for the uncoated anthracene microparticles were no longer visible for the PPy-coated anthracene microparticles (**Figure 5.9d and 5.10b**).

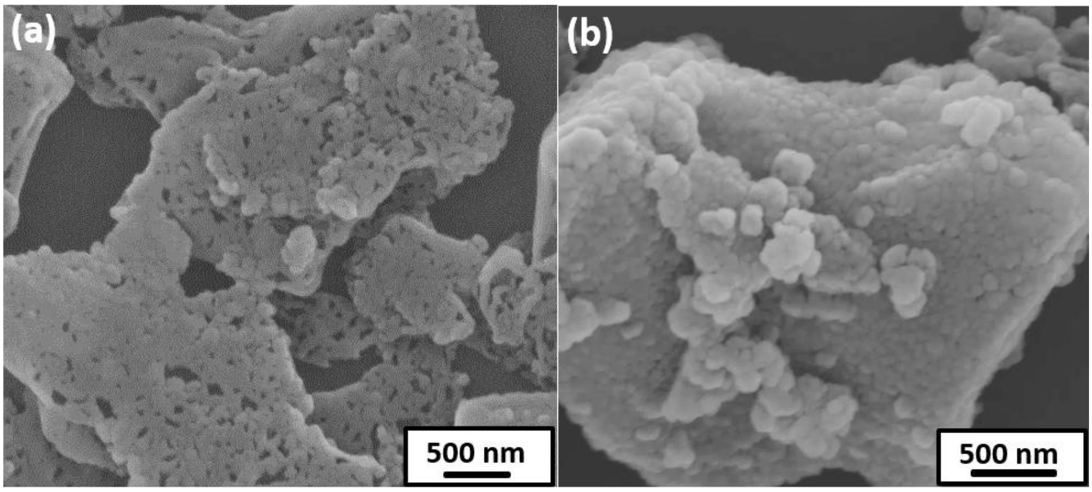

**Figure 5.10.** SEM images recorded for (a) uncoated 2 μm anthracene microparticles and (b) PPy-coated 2 μm anthracene microparticles (target PPy mass loading = 6.7 %, corresponding to a mean target coating thickness of 20 nm).

The nitrogen content of PPy bulk powder is 15.9% by mass (see **Table 5.1**). However, the highest target PPy mass loading for the anthracene microparticles (which have zero nitrogen content) was 6.7%, which means that their nitrogen contents should be of the order of 1.0% by mass. Given that the generally accepted accuracy for nitrogen microanalysis is typically ±0.30%, this technique is clearly not very reliable for compositional analysis of this particular system. Nevertheless, we conducted nitrogen microanalyses of PPy bulk powder and the four examples of PPy-coated anthracene microparticles (see **Table 5.1**). Within the admittedly large experimental uncertainty, the PPy mass loadings calculated from the nitrogen microanalyses are consistent with those targeted, with higher PPy loadings being obtained when coating finer anthracene microparticles (2 vs 4 μm diameter).

Transmission mode FT-IR spectra recorded for PPy bulk powder, milled anthracene microparticles prepared using the Morwet D-425 dispersant, and a series of PPy-coated anthracene microparticles are shown in **Figure 5.11**. The latter three samples exhibit strong bands at 1550, 1180, and 1030 cm$^{-1}$, corresponding to the PPy overlayer, which became more intense as thicker PPy overlayers are targeted.

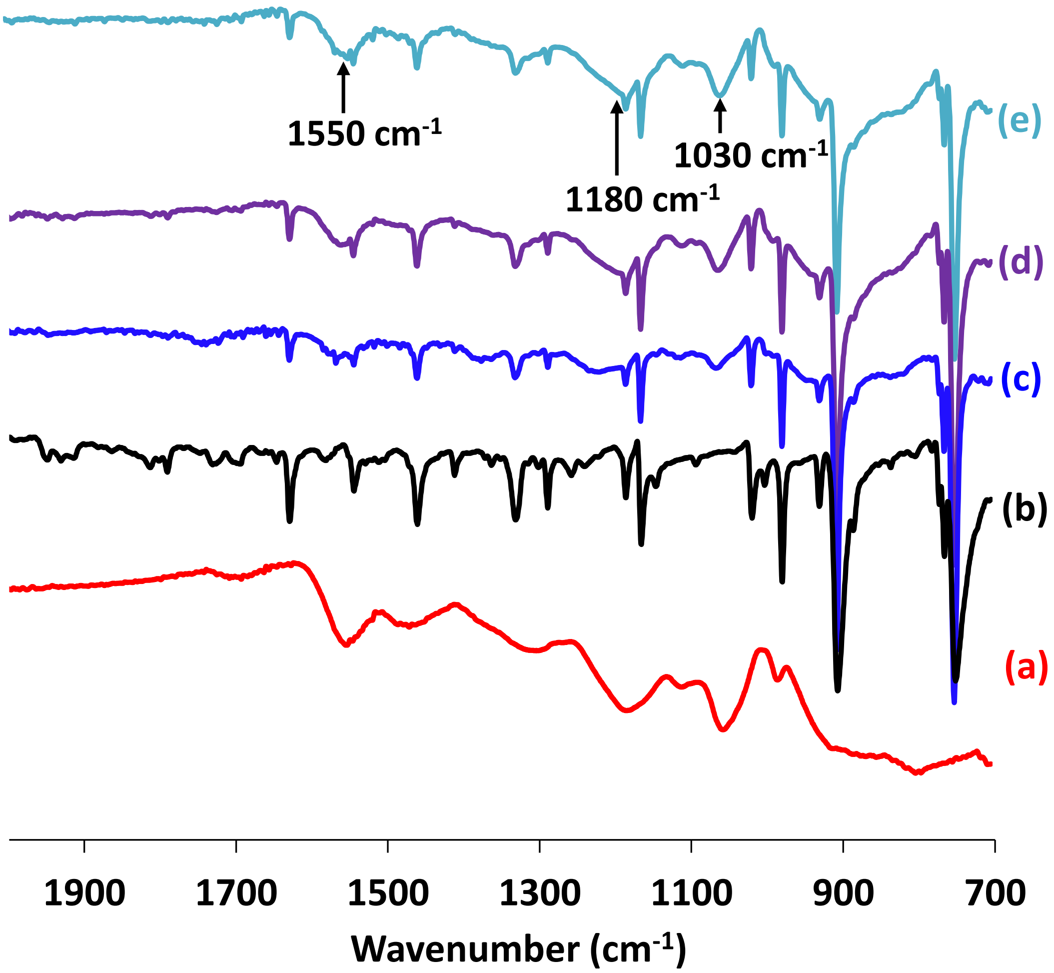

**Figure 5.11**. FT-IR spectra recorded for (a) PPy bulk powder; (b) uncoated milled 4 µm anthracene microparticles prepared using the Morwet D-425 dispersant; (c) 4 µm anthracene microparticles coated with a nominal 10 nm PPy overlayer; (d) 4 µm anthracene microparticles coated with a nominal 20 nm PPy overlayer; and (e) 4 µm anthracene microparticles coated with a nominal 30 nm PPy overlayer.

Raman spectra recorded for PPy bulk powder, pure anthracene, and PPy-coated anthracene microparticles are shown in **Figure 5.12**. The Raman spectrum for pure anthracene exhibited strong sharp bands at 121, 395, 752, 1401, and 1556 cm$^{-1}$, which correspond well to those reported in the literature.[50] The PPy bulk powder reference spectrum exhibited strong broad bands at 925, 1066, 1237, 1370, and 1592 cm$^{-1}$, which are in good agreement with our previously reported observations.[45–49]

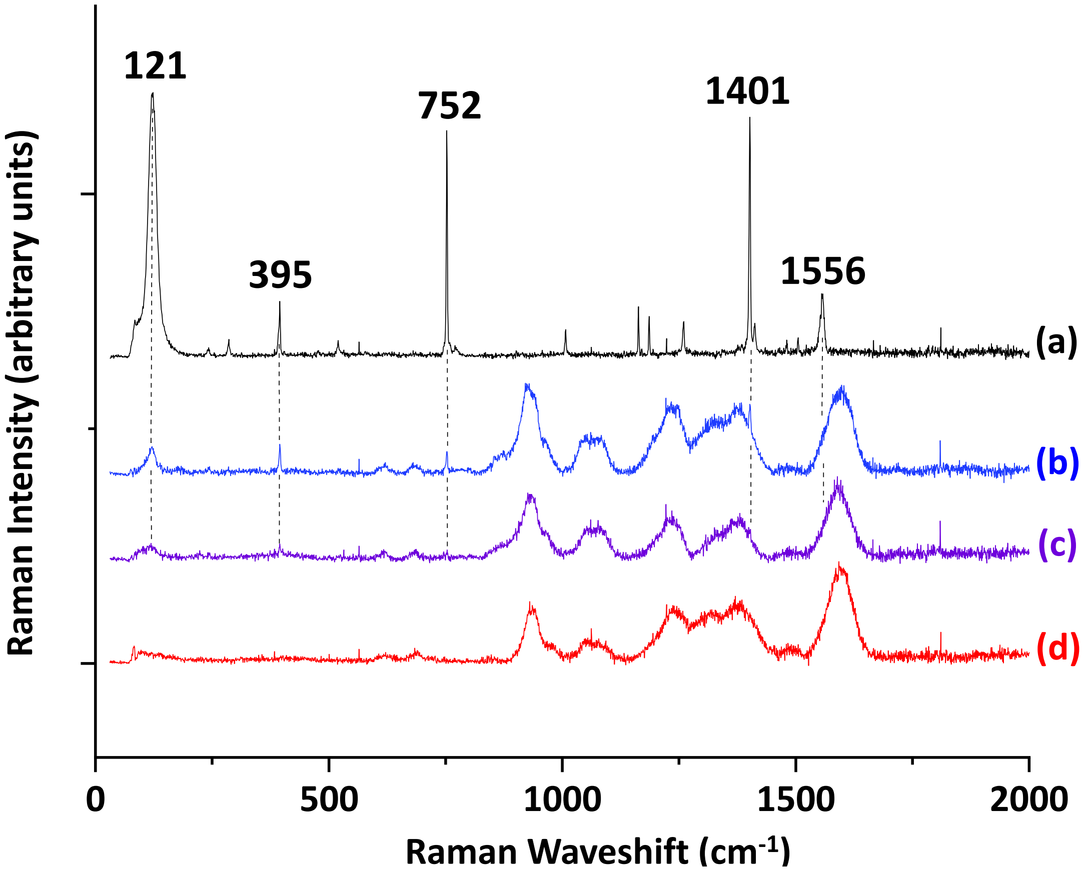

**Figure 5.12.** Raman spectra recorded for (a) pure anthracene crystals, (b) PPy-coated 4 μm anthracene microparticles (target PPy overlayer thickness = 10 nm), (c) PPy-coated 4 μm anthracene microparticles (target PPy overlayer thickness = 20 nm), and (d) PPy bulk powder. The five most intense Raman lines in the pure anthracene crystals are at 121, 395, 752, 1401, and 1556 cm$^{-1}$ (see vertical dashed lines), which is in good agreement with the literature.[50] The two spectra obtained for the PPy-coated anthracene microparticles are both dominated by signals from the conducting polymer component owing to a resonance Raman effect.

The Raman spectrum recorded for the anthracene microparticles coated with a nominal 10 nm PPy overlayer is strikingly similar to that recorded for the PPy bulk powder, with relatively weak bands attributable to the underlying anthracene being observed at 121, 395, 752, and 1401 cm$^{-1}$.[51-55] There is also some evidence for the 1556 cm$^{-1}$ band as a rather weak shoulder on a strong

PPy band. The first four bands are also present for the anthracene microparticles coated with a nominal 20 nm PPy overlayer, although they are all somewhat attenuated (compare **Figure 5.12b** and **Figure 5.12c**). These observations are rather remarkable, given that the 10 nm PPy-coated anthracene microparticles contain more than 98% anthracene by mass (see **Table 5.1**). Similar observations have been previously reported for PPy-coated latex particles and have been explained in terms of a resonance Raman effect. This leads to efficient absorption of the incident laser light by the conducting polymer overlayer, which causes obscuration of the underlying substrate.[30,41,51]

It is perhaps worth emphasizing that such attenuation is much weaker for infrared radiation (see **Figure 5.11**). In summary, these observations provide good evidence for a relatively uniform, rather than patchy, PPy overlayer at the surface of the anthracene microparticles. Such a core–shell morphology is highly desirable if such synthetic mimics are to be useful in the context of space science applications. For light gas gun experiments, it means that the PPy overlayer can serve as a sacrificial layer with a strong spectroscopic signature, which makes such microparticles potentially useful when assessing the likely extent of thermal ablation suffered by PAH dust grains during their capture within aerogel targets at hypervelocities of 1–6 km $s^{-1}$.[33] Similarly, a contiguous PPy overlayer should enable the efficient accumulation of surface charge, which is a prerequisite for acceleration up to the hypervelocity regime when using a van de Graaff instrument.[17,27]

Zeta potential versus pH curves were determined for both the milled anthracene microparticles and the PPy-coated anthracene microparticles *via* aqueous electrophoresis (see **Figure 5.13**). The former microparticles exhibited negative zeta potentials (approximately −40 to −50 mV) regardless of the solution pH, which is consistent with the surface presence of the anionic Morwet D-425 dispersant. In contrast, the PPy-coated anthracene microparticles exhibited an isoelectric point at around pH 7.7 and acquired cationic character at low pH (e.g., +30 mV at pH 3). These observations are consistent with the deposition of an electrically conductive PPy overlayer at the surface of the anthracene microparticles.

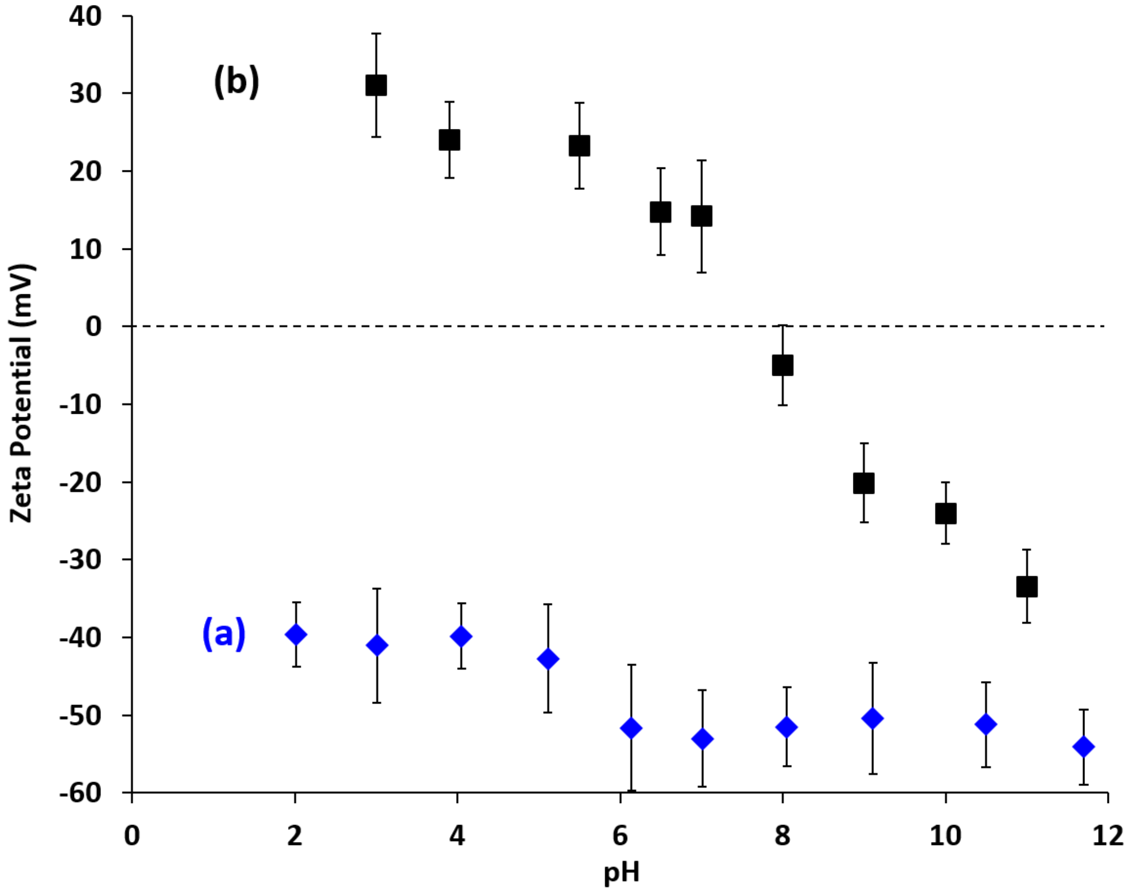

**Figure 5.13**. Zeta potential versus pH curves recorded for (a) 4 μm anthracene microparticles prepared using the anionic Morwet D-425 dispersant and (b) PPy-coated 4 μm anthracene microparticles (nominal overlayer thickness = 20 nm).

The milled 4 μm anthracene microparticles prepared using the Morwet D-425 dispersant, PPy bulk powder, and a series of PPy-coated anthracene microparticles were studied using XPS. In addition to the expected strong C1s signal, the survey spectrum recorded for the milled anthracene microparticles also contained Si2s and Si2p signals (**Figure 5.14**). These features are attributed to the silicone-based antifoam agent, which is not fully removed after the centrifugation–redispersion wash cycles. A weak S2p signal was also discernible, which is assigned to the anionic sulfonate groups of the Morwet D-425 dispersant.

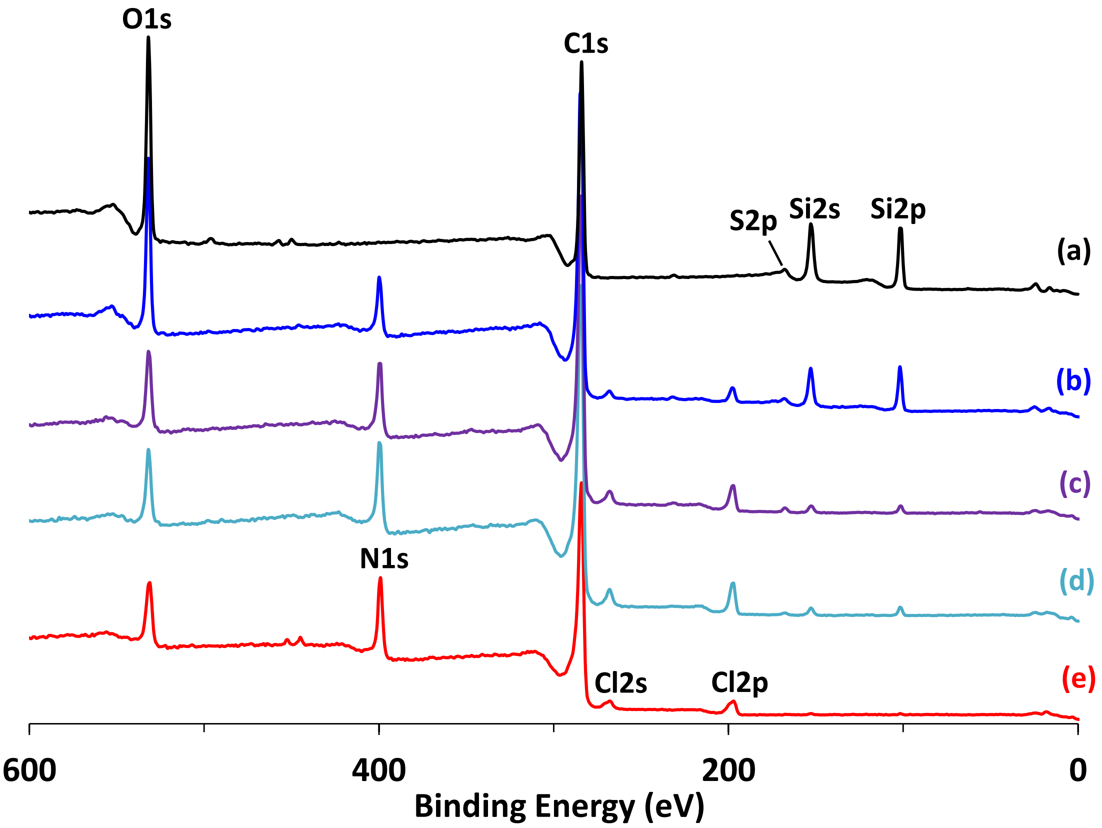

**Figure 5.14.** X-ray photoelectron survey spectra recorded for (a) uncoated milled 4 µm anthracene microparticles prepared using the Morwet D-425 dispersant; (b) PPy-coated 4 µm anthracene microparticles (nominal overlayer thickness = 10 nm); (c) PPy-coated 4 µm anthracene microparticles (nominal overlayer thickness = 20 nm); (d) PPy-coated 4 µm anthracene microparticles (nominal PPy overlayer thickness = 30 nm); and (e) PPy bulk powder.

As expected, the survey spectrum obtained for PPy bulk powder contains both N1s and Cl2p signals.[56] These signals are also detected in the spectra recorded for the series of three PPy-coated anthracene microparticles (nominal PPy overlayer thicknesses = 10, 20 and 30 nm). Comparing the relative intensities of the O1s and N1s signals for each of these three spectra, it is clear that the latter signal becomes progressively stronger as thicker PPy overlayers are targeted. The Cl/N atomic ratio calculated for the PPy bulk powder spectrum is 0.23, which is consistent with the chloride-doped, electrically conductive form of this organic polymer.[56,57] Similar Cl/N atomic ratios (0.22–0.30) were determined for the PPy overlayers deposited at the surface of the anthracene microparticles. Moreover, the S2p and Si2s/Si2p signals assigned to the Morwet D-425 dispersant and the silicone defoamer, respectively, gradually become attenuated as higher mass PPy loadings are targeted. It is also noteworthy that the survey spectra recorded for the PPy bulk powder and the PPy-coated anthracene microparticles (nominal PPy overlayer thickness =

30 nm) are strikingly similar. Such observations are understandable given the highly surface-specific nature of XPS analysis, which has a typical sampling depth of not more than 10 nm.[58]

Finally, C1s core-line spectra for selected samples are shown in **Figure 5.15**. Interestingly, the C1s core-line spectrum recorded for the uncoated anthracene microparticles (**Figure 5.15a**) is significantly shifted in its binding energy compared to those recorded for PPy alone (**Figure 5.15e**) and the three examples of PPy-coated anthracene microparticles (**Figure 5.15b-d**). This provides good evidence that the former sample is electrically insulating, whereas the latter four samples are electrically conductive, as expected.[58]

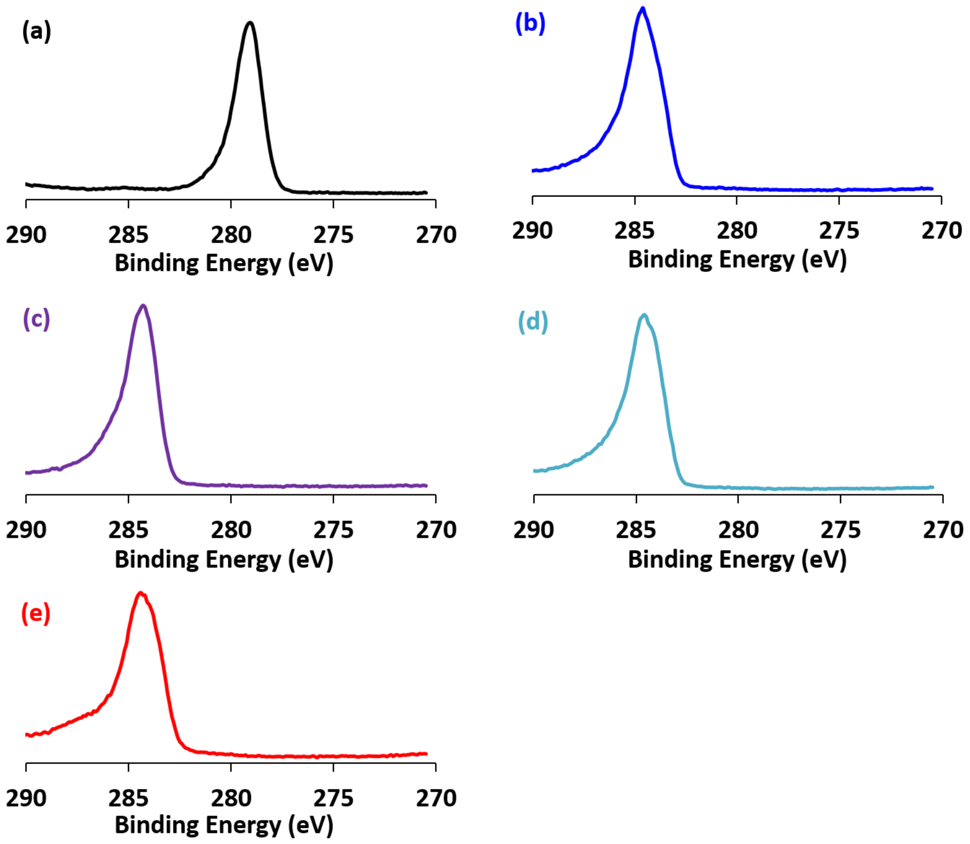

**Figure 5.15.** X-ray photoelectron C1s core-line spectra recorded for: (a) uncoated 4 µm anthracene microparticles prepared using the Morwet D-425 dispersant; (b) PPy-coated 4 µm anthracene microparticles (nominal overlayer thickness = 10 nm); (c) PPy-coated 4 µm anthracene microparticles (nominal overlayer thickness = 20 nm); (d) PPy-coated 4 µm anthracene microparticles (nominal PPy overlayer thickness = 30 nm); (e) polypyrrole bulk powder.

### 5.3.4 Light Gas Gun Experiments and Impact Crater Analysis

A preliminary hypervelocity experiment was conducted using a two-stage light gas gun[27] to fire PPy-coated 4 μm anthracene microparticles (nominal PPy overlayer thickness = 30 nm) at 1.87 km $s^{-1}$ into an aluminum foil target (mean foil thickness = 110 μm). Subsequent SEM studies of this target revealed impact craters created by the impinging microparticles (see **Figure 5.16a**). These craters are relatively shallow, with barely raised lips at their edges. There is no visible sign of significant projectile fragments or residue lining the craters. Nevertheless, a faint ring of carbonaceous debris is discernible when the same crater is subjected to X-ray elemental mapping analysis (see **Figure 5.16b**). Some larger carbon-rich fragments are also visible that may also originate from the impinging projectile. However, we cannot be certain that the latter debris does not originate from contamination by the sabot employed in this light gas gun experiment.

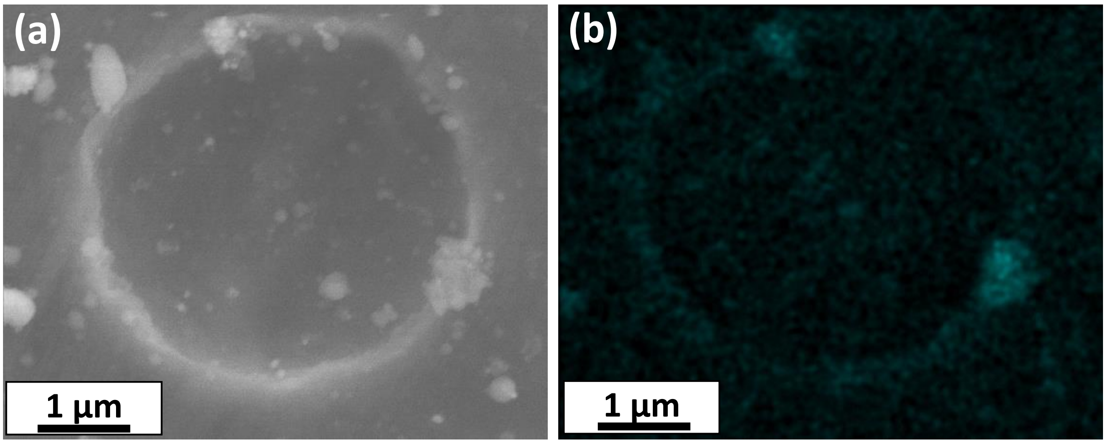

**Figure 5.16**. (a) SEM image of an impact crater formed by firing PPy-coated anthracene microparticles (4 μm diameter; coated with a nominal PPy overlayer thickness of 30 nm) at an aluminum foil target (mean thickness = 110 μm) at 1.87 km $s^{-1}$ using a two-stage light gas gun. (b) Corresponding elemental carbon image obtained when using X-ray elemental mapping to examine the same impact crater. Carbonaceous debris is discernible as a faint crater ring, with some larger fragments also being visible (see main text for further details).

These observations can be compared to earlier attempts to simulate what would happen if organic microparticles entrained in the water plumes emitted from icy satellites of Jupiter and Saturn (i.e., Europa and Enceladus, respectively) were to be intercepted by a passing spacecraft. For example, New *et al.*[59] fired poly(methyl methacrylate) microparticles of 4, 6, and 10 μm diameter at five different metal targets (including aluminum) at hypervelocities ranging from 0.5 to 3 km $s^{-1}$.

Below the hypervelocity regime (<1 km $s^{-1}$), the impinging microparticles either adhered or rebounded. At hypervelocities of around 1 km $s^{-1}$, imprints were left in the surface of the metal target, with carbon residues being detected by X-ray elemental mapping analysis. At 2–3 km $s^{-1}$, craters lined with partially melted residues were obtained. Up to and including impacts at 2 km $s^{-1}$, Raman microscopy studies confirmed the presence of PMMA fragments, but at higher speeds, no such debris was found. This is consistent with the prior work by Burchell and co-workers,[33] who found that PPy-coated polystyrene microparticles of 20 μm diameter survived intact when fired at aerogel targets at up to 2 km $s^{-1}$ but underwent extensive thermal ablation when impinging at higher hypervelocities.

Separately, Burchell and Harriss[60] recently reported that firing polystyrene and PMMA microparticles at aluminum targets at 5 km $s^{-1}$ produced impact craters that were solely lined with carbonaceous residues–there were no identifiable polystyrene or PMMA residues. The preliminary data reported herein extend the growing number of hypervelocity impact studies involving organic microparticles to include PAH-rich projectiles. Moreover, they suggest that the chemical nature of the projectile is an important factor, so the earlier observations made for PMMA microparticles cannot be assumed to be valid for all types of organic microparticles. Thus, given the ubiquity of PAH throughout the universe, it is clearly important to develop suitable synthetic mimics to understand the behavior of this type of organic cosmic dust.

## 5.4 Conclusions

The simplest member of the PAH family, anthracene, can be conveniently prepared in the form of microparticles by ball milling macroscopic organic crystals using a commercial polymeric dispersant (Morwet D-425). These precursor microparticles were then coated with PPy, an air-stable electrically conductive polymer. Both the original uncoated microparticles and the PPy-coated microparticles were characterized by optical microscopy, laser diffraction, aqueous electrophoresis, SEM, vibrational spectroscopy, and XPS. These techniques are consistent with the presence of an ultrathin contiguous overlayer of PPy on the surface of the anthracene microparticles. Such microparticles are expected to be useful synthetic mimics for PAH-rich cosmic dust, which is found throughout the universe. Finally, we demonstrate that a light gas gun[27,33,34] can be used to accelerate such microparticles up to the hypervelocity regime. Moreover, we note that the electrically conductive nature of the PPy overlayer should enable the efficient accumulation of surface charge[17,27,35] and hence provide access to higher hypervelocities using a van de Graaff accelerator. In such experiments, this overlayer is also likely to be a useful sacrificial layer for assessing the extent of thermal ablation of such microparticles during their capture within aerogel targets.[33]

## 5.5 References

(1) Abdel-Shafy, H. I.; Mansour, M. S. M. A Review on Polycyclic Aromatic Hydrocarbons: Source, Environmental Impact, Effect on Human Health and Remediation. *Egypt. J. Pet.* **2016**, *25*, 107–123.

(2) Allamandola, L. J.; Sandford, S. A.; Wopenka, B. Interstellar Polycyclic Aromatic Hydrocarbons and Carbon in Interplantary Dust Particles and Meteorites. *Science* **1987**, *237*, 55–59.

(3) Allamandola, L. J.; Tielens, A. G. G. M.; Barker, J. R. Interstellar Polycyclic Aromatic Hydrocarbons: The Infrared Emission Bands, The Excitation/Emission Mechanism, and the Astrophysical Implications. *Astrophys. J. Suppl. Ser.* **1989**, *71*, 733–775.

(4) Tielens, A. G. G. M. Interstellar Polycyclic Aromatic Hydrocarbon Molecules. *Annu. Rev. Astron. Astrophys.* **2008**, *46*, 289–337.

(5) Roser, J. E.; Ricca, A. Polycyclic Aromatic Hydrocarbon Clusters as Sources of Interstellar Infrared Emission. *Astrophys. J.* **2015**, *801*, 1-8.

(6) Greenberg, J. M.; Gillette, J. S.; Muñoz Caro, G. M.; Mahajan, T. B.; Zare, R. N.; Li, A.; Schutte, W. A.; de Groot, M.; Mendoza-Gómez, C. Ultraviolet Photoprocessing of Interstellar Dust Mantles as a Source of Polycyclic Aromatic Hydrocarbons and Other Conjugated Molecules. *Astrophys. J.* **2000**, *531*, L71–L73.

(7) Steele, A. A.; Mccubbin, F. M.; Fries, M.; Kater, L.; Boctor, N. Z.; Fogel, M. L.; Glamoclija, M.; Spencer, M.; Morrow, A. L.; Hammond, M. R.; Zare, R. N.; Siljeström, S.; Bowden, R.; Herd, C. D. K.; Mysen, B. O.; Shirey, S. B.; Treiman, A. H.; Bullock, E. S.; Jull, A. J. T. A Reduced Organic Carbon Component in Martian Basalts. *Science* **2012**, *337*, 212–215.

(8) Derenne, S.; Robert, F. Model of Molecular Structure of the Insoluble Organic Matter Isolated from Murchison Meteorite. *Meteorit. Planet. Sci.* **2010**, *45*, 1461–1475.

(9) Dinelli, B. M.; Adriani, A.; Funke, B.; Moriconi, M. L.; Boersma, C.; Allamandola, L. J. Large Abundances Of Polycyclic Aromatic Hydrocarbons in Titan's Upper Atmosphere. *Astrophys. J.* **2013**, *770*, 1–8.

(10) Zhao, L.; Kaiser, R. I.; Xu, B.; Ablikim, U.; Ahmed, M.; Evseev, M. M.; Bashkirov, E. K.; Azyazov, V. N.; Mebel, A. M. Low-Temperature Formation of Polycyclic Aromatic Hydrocarbons in Titan's Atmosphere. *Nat. Astron.* **2018**, *2*, 973–979.

(11) Moreels, G.; Clairemidi, J.; Hermine, P.; Brechignac, P.; Rousselot, P. Detection of a Polycyclic Aromatic Molecule in Comet P/Halley. *Astron. Astrophys.* **1994**, *282*, 643–656.

(12) Clairemidia, J.; Brechignac, P.; Moreelsa, G.; Pautetc, D. Tentative Identification of Pyrene as a Polycyclic Aromatic Molecule in UV Spectra of Comet P/Halley: An Emission from 368 to 384 nm. *Planet. Space Sci.* **2004**, *52*, 761–772.

(13) Clemett, S. J.; Maechling, C. R.; Zare, R. N.; Swan, P. D.; Walker, R. M. Identification of Complex Aromatic Molecules in Individual Interplanetary Dust Particles. *Science* **1993**, *262*, 721–725.

(14) Liebert, M. A.; Ehrenfreund, P.; Rasmussen, S.; Cleaves, J.; Chen, L. Experimentally Tracing the Key Steps in the Origin of Life: The Aromatic World. *Astrobiology* **2006**, *6*, 490–521.

(15) Stockton, A. M.; Chiesl, T. N.; Scherer, J. R.; Mathies, R. A. Polycyclic Aromatic Hydrocarbon Analysis with the Mars Organic Analyzer Microchip Capillary Electrophoresis System. *Anal. Chem.* **2009**, *81*, 790–796.

(16) Fielding, L. A.; Hillier, J. K.; Burchell, M. J.; Armes, S. P. Space Science Applications for Conducting Polymer Particles: Synthetic Mimics for Cosmic Dust and Micrometeorites. *Chem. Commun.* **2015**, *51*, 16886–16899.

(17) Burchell, M. J.; Cole, M. J.; Lascelles, S. F.; Khan, M. A.; Barthet, C.; Wilson, S. A.; Cairns, D. B.; Armes, S. P. Acceleration of Conducting Polymer-Coated Latex Particles as Projectiles in Hypervelocity Impact Experiments. *J. Phys. D. Appl. Phys.* **1999**, *32*, 1719–1728.

(18) Srama, R., Woiwode, W., Postberg, F. ; Armes, S. P., Fujii, S., Dupin, D., Ormond-Prout, J., Sternovsky, Z., Kempf, S., Moragas-Klostermeyer, G., Mocker, A., Grün, E. Mass Spectrometry of Hyper-Velocity Impacts of Organic Micrograins. *Rapid Commun. Mass Spectrom.* **2009**, *23*, 3895–3906.

(19) Mellado, E. M.; Hornung, K.; Srama, R.; Kissel, J.; Armes, S. P.; Fujii, S. Mass Spectrometry of Impact Fragmented Polymers: The Role of Target Properties. *Int. J. Impact Eng.* **2011**, *38*, 486–494.

(20) Goldsworthy, B. J.; Burchell, M. J.; Cole, M. J.; Armes, S. P.; Khan, M. A.; Lascelles, S. F.; Green, S. F.; McDonnell, J. A. M.; Srama, R.; Bigger, S. W. Time of Flight Mass

Spectra of Ions in Plasmas Produced by Hypervelocity Impacts of Organic and Mineralogical Microparticles on a Cosmic Dust Analyser. *Astron. Astrophys.* **2003**, *409*, 1151–1167.

(21) Goldsworthy, B. J.; Burchell, M. J.; Cole, M. J.; Green, S. F.; Leese, M. R.; McBride, N.; McDonnell, J. A. M.; Müller, M.; Grün, E.; Srama, R.; Armes, S. P.; Khan, M. A. Laboratory Calibration of the Cassini Cosmic Dust Analyser (CDA) Using New, Low Density Projectiles. *Adv. Sp. Res.* **2002**, *29*, 1139–1144.

(22) Srama, R.; Ahrens, T. J.; Altobelli, N.; Auer, S.; Bradley, J. G. The Cassini Cosmic Dust Analyzer. *Space Sci. Rev.* **2004**, *114*, 465–518.

(23) Postberg, F.; Khawaja, N.; Abel, B.; Choblet, G.; Glein, C. R.; Gudipati, M. S.; Henderson, B. L.; Hsu, H. W.; Kempf, S.; Klenner, F.; Moragas-Klostermeyer, G.; Magee, B.; Nölle, L.; Perry, M.; Reviol, R.; Schmidt, J.; Srama, R.; Stolz, F.; Tobie, G.; Trieloff, M.; Waite, J. H. Macromolecular Organic Compounds from the Depths of Enceladus. *Nature* **2018**, *558*, 564–568.

(24) Khawaja, N.; Postberg, F.; Hillier, J.; Klenner, F.; Kempf, S.; Nölle, L.; Reviol, R.; Zou, Z.; Srama, R. Low-Mass Nitrogen-, Oxygen-Bearing, and Aromatic Compounds in Enceladean Ice Grains. *Mon. Not. R. Astron. Soc.* **2019**, *489*, 5231–5243.

(25) Lascelles, S. F.; Armes, S. P. Synthesis and Characterization of Micrometre-Sized, Polypyrrole-Coated Polystyrene Latexes. *J. Mater. Chem.* **1997**, *7*, 1339–1347.

(26) Lovett, J. R.; Fielding, L. A.; Armes, S. P.; Buxton, R. One-Pot Preparation of Conducting Polymer-Coated Silica Particles: Model Highly Absorbing Aerosols. *Adv. Funct. Mater.* **2014**, *24*, 1290–1299.

(27) Burchell, M. J.; Cole, M. J.; McDonnell, J. A. M.; Zarnecki, J. C. Hypervelocity Impact Studies Using the 2 MV Van de Graaff Accelerator and Two-Stage Light Gas Gun of the University of Kent at Canterbury. *Meas. Sci. Technol.* **1999**, *10*, 41–50.

(28) Li, Y. W.; Bugiel, S.; Trieloff, M.; Hillier, J. K.; Postberg, F.; Price, M. C.; Shu, A.; Fiege, K.; Fielding, L. A.; Armes, S. P.; Wu, Y. Y.; Grün, E.; Srama, R. Morphology of Craters Generated by Hypervelocity Impacts of Micron-Sized Polypyrrole-Coated Olivine Particles. *Meteorit. Planet. Sci.* **2014**, *49*, 1375–1387.

(29) Hillier, J. K.; Sternovsky, Z.; Armes, S. P.; Fielding, L. A.; Postberg, F.; Bugiel, S.; Drake, K.; Srama, R.; Kearsley, A. T.; Trieloff, M. Impact Ionisation Mass Spectrometry of Polypyrrole-Coated Pyrrhotite Microparticles. *Planet. Space Sci.* **2014**, *97*, 9–22.

(30) Li, Y. W.; Dupin, D.; Fielding, L. A.; Fujii, S.; Gainsforth, Z.; Un, E. G. R. Stardust Interstellar Preliminary Examination IX : High-Speed Interstellar Dust Analog Capture in Stardust Flight-Spare Aerogel. *Meteorit. Planet. Sci.* **2014**, *49*, 1666–1679.

(31) Hillier, J. K.; Sestak, S.; Green, S. F.; Postberg, F.; Srama, R.; Trieloff, M. The Production of Platinum-Coated Silicate Nanoparticle Aggregates for Use in Hypervelocity Impact

Experiments. *Planet. Space Sci.* **2009**, *57*, 2081–2086.

(32) Burchell, M. J.; Armes, S. P. Impact Ionisation Spectra from Hypervelocity Impacts Using Aliphatic Poly(Methyl Methacrylate) Microparticle Projectiles. *Rapid Commun. Mass Spectrom.* **2011**, *25*, 543–550.

(33) Burchell, M. J.; Foster, N. J.; Ormond-Prout, J.; Dupin, D.; Armes, S. P. Extent of Thermal Ablation Suffered by Model Organic Microparticles during Aerogel Capture at Hypervelocities. *Meteorit. Planet. Sci.* **2009**, *44*, 1407–1419.

(34) Wozniakiewicz, P. J.; Price, M. C.; Armes, S. P.; Burchell, M. J.; Cole, M. J.; Fielding, L. A.; Hillier, J. K.; Lovett, J. R. Micron-Scale Hypervelocity Impact Craters: Dependence of Crater Ellipticity and Rim Morphology on Impact Trajectory, Projectile Size, Velocity, and Shape. *Meteorit. Planet. Sci.* **2014**, *49*, 1929–1947.

(35) Burchell, M. J.; Willis, M. J.; Armes, S. P.; Khan, M. A.; Percy, M. J.; Perruchot, C. Impact Ionization Experiments with Low Density Conducting Polymer-Based Micro-Projectiles as Analogues of Solar System Dusts. *Planet. Space Sci.* **2002**, *50*, 1025–1035.

(36) Cloutis, E.; Szymanski, P.; Applin, D.; Goltz, D. Identification and Discrimination of Polycyclic Aromatic Hydrocarbons Using Raman Spectroscopy. *Icarus* **2016**, *274*, 211–230.

(37) Ormond-Prout, J.; Dupin, D.; Armes, S. P.; Foster, N. J.; Burchell, M. J. Synthesis and Characterization of Polypyrrole-Coated Poly(Methyl Methacrylate) Latex Particles. *J. Mater. Chem.* **2009**, *19*, 1433–1442.

(38) Narayanan, K. S.; Jon, D. I.; Patel, J. New Value-Added Polymeric Dispersants and Uses Thereof in Agricultural Formulations. *J. ASTM Int.* **2005**, *2*, 299–312.

(39) Knowles, D. A. *Chemistry and Technology of Agrochemical Formulations*; Springer: Boston, 1998.

(40) Hörz, F. et al. Impact Features on Stardust : Implications for Comet 81P/Wild 2 Dust. *Science* **2006**, *314*, 1716–1720.

(41) Burchell, M. J.; Fairey, S. A. J.; Wozniakiewicz, P.; Brownlee, D. E.; Hörz, F.; Kearsley, A. T.; See, T. H.; Tsou, P.; Westphal, A.; Green, S. F.; Trigo-Rodríguez, J. M.; Domingúez, G. Characteristics of Cometary Dust Tracks in Stardust Aerogel and Laboratory Calibrations. *Meteorit. Planet. Sci.* **2008**, *43*, 23–40.

(42) Lorenz, R. D. Europa Ocean Sampling by Plume Flythrough: Astrobiological Expectations. *Icarus* **2016**, *267*, 217–219.

(43) Guzman, M.; Lorenz, R.; Hurley, D.; Farrell, W.; Spencer, J.; Hansen, C.; Hurford, T.; Ibea, J.; Carlson, P.; McKay, C. P. Collecting Amino Acids in the Enceladus Plume. *Int. J. Astrobiol.* **2019**, *18*, 47–59.

(44) Fujii, S.; Armes, S. P.; Jeans, R.; Devonshire, R.; Warren, S.; McArthur, S. L.; Burchell, M. J.; Postberg, F.; Srama, R. Synthesis and Characterization of Polypyrrole-Coated

Sulfur-Rich Latex Particles: New Synthetic Mimics for Sulfur-Based Micrometeorites. *Chem. Mater.* **2006**, *18*, 2758–2765.

(45) Maeda, S.; Armes, S. P. Preparation and Characterisation of Novel Polypyrrole-Silica Colloidal Nanocomposites. *J. Mater. Chem.* **1994**, *4*, 935–942.

(46) Han, M. G.; Armes, S. P. Preparation and Characterization of Polypyrrole-Silica Colloidal Nanocomposites in Water-Methanol Mixtures. *J. Colloid Interface Sci.* **2003**, *262*, 418–427.

(47) Lo, M.; Pires, R.; Diaw, K.; Gningue-Sall, D.; Oturan, M. A.; Aaron, J.-J.; Chehimi, M. M. Diazonium Salts: Versatile Molecular Glues for Sticking Conductive Polymers to Flexible Electrodes. *Surfaces* **2018**, *1*, 43–58.

(48) Cawdery, N.; Obey, T. M.; Vincent, B. Colloidal Dispersions of Electrically Conducting Polypyrrole Particles in Various Media. *J. Chem. Soc. Chem. Commun.* **1988**, 1189–1190.

(49) Armes, S. P.; Aldissi, M.; Hawley, M.; Beery, J. G.; Gottesfeld, S. Morphology and Structure of Conducting Polymers. *Langmuir* **1991**, *7*, 1447–1452.

(50) Rasanen, J.; Stenman, F.; Penttinen, E. Raman Scattering from Molecular Crystals--II . Anthracene. *Spectrochim. Acta Part A Mol. Biomol. Spectrosc.* **1973**, *29A*, 395–403.

(51) Cheung, K. M.; Smith, B. J. E.; Batchelder, D. N.; Bloor, D. Raman Spectroscopy of Conductive Polypyrroles. *Synth. Met.* **1987**, *21*, 249–253.

(52) Furukawa, Y.; Tazawa, S.; Fujii, Y.; Harada, I. Raman Spectra of Polypyrrole and Its 2,5-13C-Substituted and C-Deuterated Analogues in Doped and Undoped States. *Synth. Met.* **1988**, *24*, 329–341.

(53) Liu, Y. C. Characteristics of Vibration Modes of Polypyrrole on Surface-Enhanced Raman Scattering Spectra. *J. Electroanal. Chem.* **2004**, *571*, 255–264.

(54) T. Inoue T., I. H. and T. Y. Change of Raman Scattering Intensity of a Polypyrrole Film during Reversible Doping and Emitting Processes of $ClO^{4-}$. *Chem. Lett.* **1987**, *16*, 563–566.

(55) Lascelles, S. F.; Armes, S. P.; Zhdan, P. A.; Greaves, S. J.; Brown, A. M.; Watts, J. F.; Leadley, S. R.; Luk, S. Y. Surface Characterization of Micrometre-Sized, Polypyrrole-Coated Polystyrene Latexes: Verification of a “core-Shell” Morphology. *J. Mater. Chem.* **1997**, *7*, 1349–1355.

(56) Perruchot, C.; Chehimi, M. M.; Delamar, M.; Lascelles, S. F.; Armes, S. P. Surface Characterization of Polypyrrole-Coated Polystyrene Latex by X-Ray Photoelectron Spectroscopy. *Langmuir* **1996**, *12*, 3245–3251.

(57) Armes, S. P. Optimum Reaction Conditions for the Polymerization of Pyrrole by Iron(III) Chloride in Aqueous Solution. *Synth. Met.* **1987**, *20*, 365–371.

(58) Watts, J. F., Wolstenholme, J. *An Introduction to Surface Analysis by XPS and AES*; Wiley, Chichester, 2003.

(59) New, J. S.; Mathies, R. A.; Price, M. C.; Cole, M. J.; Golozar, M.; Spathis, V.; Burchell, M. J.; Butterworth, A. L. Characterizing Organic Particle Impacts on Inert Metal Surfaces: Foundations for Capturing Organic Molecules during Hypervelocity Transits of Enceladus Plumes. *Meteorit. Planet. Sci.* **2020**, *55*, 465–479.

(60) Burchell, M.; Harriss, K. Organic Molecules: Is It Possible to Distinguish Aromatics from Aliphatics Collected by Space Missions in High Speed Impacts? *Sci* **2020**, *2*, 56.

# Chapter 6

# Conclusions and Future Work

Over the last twenty years or so, pseudo-living radical polymerization techniques have underpinned substantial developments in synthetic polymer chemistry. In particular, RAFT polymerization has become a widely used method for the efficient synthesis of amphiphilic diblock copolymers, which can undergo polymerization-induced self-assembly (PISA) to form nano-objects in the form of concentrated colloidal dispersions.[1,2]

Diblock copolymers have been utilized as dispersants for carbon black, silica, titanium oxide or iron oxide particles.[3–6] Interestingly, the use of diblock copolymer micelles for certain agrochemical applications has already been patented by Syngenta.[7] However, the aim of such prior studies was to moderate active ingredient (AI) release by creating a copolymer layer on the surface of the AI particles, rather than using diblock copolymer nanoparticles as a dispersant. Thus, the primary objective of the current PhD project was to examine whether diblock copolymer nanoparticles could be used to prepare a range of agrochemical AIs in the form of suspension concentrates.

Accordingly, the RAFT aqueous emulsion polymerization of MMA using a non-ionic PGMA stabilizer is explored in Chapter 2. Colloidally stable PGMA-PMMA diblock copolymer nanoparticles could be prepared at 10% w/w solids but only flocculated nanoparticles were produced when targeting DPs above 100 for the PMMA core-forming block.[8] This was wholly unexpected given that similar PGMA precursors have been used to target much higher DPs of alternative hydrophobic core-forming blocks to produce relatively large spheres.[9,10] György *et al.* recently reported similar colloidal instability problems: flocculated spheres were invariably produced when targeting PMMA DPs at or above 108 for the PISA synthesis of $PLMA_{22}$-$PMMA_x$ nano-objects in mineral oil.[11] For this non-polar formulation, nanoparticle aggregation appears to be related to the relatively high $T_g$ of the core-forming PMMA block. Interestingly, replacing the non-ionic PGMA stabilizer with an anionic PMAA stabilizer enables colloidally stable nanoparticles to be prepared when targeting PMMA DPs of up to 2000. Similar observations were made when using a cationic PMETAC precursor to target PMMA DPs of up to 500. Clearly, the additional electrostatic repulsion between neighbouring polyelectrolytic chains provides sufficient electrosteric stabilization to allow access to relatively large spherical nanoparticles.

Organosulfur-based RAFT chain end-groups confer a distinct malodor and intrinsic color, which is undesirable for industrial applications.[2] In this Thesis, chain-end removal *via* visible light irradiation has been briefly explored to address these problems, which are likely to prevent commercialization of diblock copolymer nanoparticles for applications in agrochemical formulations. Accordingly, blue LED light irradiation ($\lambda$ = 405 nm) was used in Chapter 2 to cleave dithiobenzoate end-groups from a 10% w/w aqueous dispersion of $PGMA_{50}$-$PMMA_{80}$ nanoparticles. UV GPC studies indicated 87% end-group removal within 12 h at 80 °C. Furthermore, the same visible light irradiation protocol was used to remove trithiocarbonate end-groups from HOO-$PGMA_{54}$-$PMMA_{80}$ nanoparticles. This method does not require any chemical reagents and would likely only require dialysis to remove the small molecules. In principle, a more intense visible light source might mean that the reaction temperature and/or reaction time could be significantly reduced. Using UV irradiation is likely to offer similar benefits but such shorter wavelengths may lead to copolymer degradation. Future work could also include investigating how end-group removal *via* light irradiation is affected by varying the copolymer composition, copolymer morphology (e.g. worms or vesicles), or the nature of the RAFT end-group (e.g. xanthates or dithiocarbamates).

As reported in Chapter 2, PGMA-PMMA nanoparticles with appreciable anionic character could be prepared using a carboxylic acid-functionalized RAFT agent. In as-yet-unpublished work conducted during this PhD project (but not included in this Thesis), a morpholine-functionalized trithiocarbonate-based $PGMA_{48}$ precursor was chain-extended *via* RAFT aqueous emulsion polymerization of MMA to afford colloidally stable cationic PGMA-PMMA spherical nanoparticles when targeting a PMMA DP of 80. Thus, PGMA-PMMA nanoparticles can be prepared with comparable mean particle diameters with the steric stabilizer chain-ends bearing neutral, anionic or cationic charge. An on-going collaboration with a senior Syngenta scientist (Dr. P. Taylor) is focused on determining the effect of such terminal charge on the extent of nanoparticle adsorption at the oil-water interface. More specifically, physical adsorption of each of the three types of nanoparticles from aqueous solution onto giant (mm-sized) oil droplets is monitored by studying their interfacial rheology at various pH values. Furthermore, the effect of varying the chemical nature of the hydrophobic nanoparticle cores on the extent of interfacial adsorption is currently being investigated by using the PGMA-PMMA, PGMA-BzMA and PGMA-PTFEMA nanoparticles described within this Thesis.

Various diblock copolymer nanoparticles were evaluated as putative dispersants for six agrochemical AIs in Chapters 3 and 4. Initial attention focused on wet ball milling techniques to reduce the particle size of macroscopic hydrophobic organic crystals of azoxystrobin, a widely-used fungicide originally developed by Syngenta. Despite unexpected constraints being observed for the PGMA-PMMA formulation (e.g. nanoparticle aggregation when targeting a PMMA DP above 100), a colloidally stable dispersion of $PGMA_{50}$-$PMMA_{80}$ nanoparticles was prepared and utilized to prepare azoxystrobin microparticles.[12] Subsequently, the same nanoparticles proved to be an effective generic dispersant for five further AIs, which suggests that this new approach is likely to be rather generic. Nanoparticle adsorption at the surface of each type of AI microparticle was confirmed by electron microscopy, with the azoxystrobin microparticles also being characterized by XPS and aqueous electrophoresis. Furthermore, these nanoparticle dispersants proved to be as effective as a commercial water-soluble polymer dispersant (Morwet D-425). One interesting finding was that the chemical nature of the hydrophobic core-forming block (e.g. PMMA vs. PBzMA vs. PTFEMA) did not have a discernible effect on the milling efficiency of the nanoparticles. Further changes to the nanoparticle composition were investigated in Chapter 4, including variation of the nature of the stabilizer block, the mean nanoparticle diameter, and the glass transition temperature ($T_g$) of the core-forming block. Diblock copolymer nanoparticles prepared using a non-ionic steric stabilizer proved to be more effective dispersants than nanoparticles comprising either cationic or anionic steric stabilizer chains. Moreover, nanoparticles with mean particle diameters of up to 51 nm were found to be optimum for efficient milling and lowering the $T_g$ of the core-forming block to produce relatively soft nanoparticles had little, if any, effect on milling performance.

The majority of the diblock copolymer nanoparticles discussed in this Thesis have been prepared *via* RAFT aqueous *emulsion* polymerization. However, PDMAC-PDAAM nanoparticles synthesized *via* RAFT aqueous *dispersion* polymerization also proved to be an effective dispersant for azoxystrobin. Moreover, only a relatively short milling time of 15 min was required when using such PDMAC-PDAAM nanoparticles, compared to approximately 30 min when using PGMA-PMMA nanoparticles. Thus the former system may offer a significant processing advantage. In summary, this project has confirmed that a wide range of diblock copolymer nanoparticles can act as effective dispersants for azoxystrobin and, most likely, many other agrochemical AIs.

Laser diffraction studies of selected agrochemical SCs indicated little or no change in their apparent size on storage at 20 °C for up to 12 months, suggesting good stability over this timescale. According to Syngenta scientists, commercial SC formulations require a shelf-life of at least two years,[13] therefore further long-term stability testing is desirable. This may involve using standard industrial test methods. For example, SC stability could be monitored when subjected to a temperature cycle to ensure that the AI properties are not affected by elevated temperature. In principle, such experiments might also give some indication of the likely long-term storage stability of such SCs within a shorter time frame.

This Thesis has focused solely on the preparation and use of spherical nanoparticles as dispersants. However, alternative copolymer morphologies such as worms or vesicles can also be accessed *via* PISA and have offered various potential applications ranging from stem cell storage to next-generation lubricants for automotive engine oils to nanoparticle encapsulation and controlled release.[14–16] Although beyond the scope of this project, such nano-objects might be suitable for other agrochemical purposes. For example, vesicles could be used to encapsulate AIs, which may enable their transportation to the appropriate site. Alternatively, highly anisotropic worms could be effective rheological modifiers for SCs and therefore prevent sedimentation of the AI microparticles during their long-term storage.

Finally, Chapter 5 described the preparation of 2-4 µm sized anthracene microparticles through similar ball milling techniques reported in Chapters 3 and 4. Ultimately, this crystalline polyaromatic hydrocarbon (PAH) was not required as a model agrochemical AI system in this PhD project. However, such anthracene microparticles could be coated with an ultrathin overlayer of polypyrrole (PPy), which is an electrically conductive polymer. SEM, elemental microanalysis, FT-IR spectroscopy, Raman spectroscopy and XPS studies were used to characterize the resulting PPy-coated anthracene microparticles.[17] Moreover, these PPy-coated anthracene microparticles could be accelerated up to the hypervelocity regime using a light gas gun. Importantly, the electrically conductive PPy overlayer should enable the efficient accumulation of surface charge and hence provide access to higher hypervelocities when using a van de Graaff accelerator.[18] Indeed, acceleration of these PPy-coated anthracene microparticles up to 20 km $s^{-1}$ has been recently achieved by Dr. Z. Sternovsky and his team at U. Boulder, with subsequent impact ionization producing intriguing preliminary mass spectra.

This work could be further extended by investigating alternative PAHs such as phenanthrene, which consists of three benzene rings fused to give a non-linear structure. Although a structural isomer of anthracene, phenanthrene has been reported to exhibit significantly greater chemical stability.[19] Moreover, phenanthrene has a melting point of 100 °C, whereas anthracene has a much higher melting point of 216 °C.[20] Thus, it may be feasible to drip-feed molten phenanthrene into an aqueous solution containing a suitable water-soluble polymeric dispersant to produce more well-defined, spherical microparticles. If such microparticles can be coated with a thin overlayer of PPy, then comparing their performance in various hypervelocity experiments could be of considerable interest.

## 6.1 References

(1) Canning, S. L.; Smith, G. N.; Armes, S. P. A Critical Appraisal of RAFT-Mediated Polymerization-Induced Self-Assembly. *Macromolecules* **2016**, *49*, 1985–2001.

(2) Perrier, S. 50th Anniversary Perspective: RAFT Polymerization - A User Guide. *Macromolecules* **2017**, *50*, 7433–7447.

(3) Growney, D. J.; Mykhaylyk, O. O.; Derouineau, T.; Fielding, L. A.; Smith, A. J.; Aragrag, N.; Lamb, G. D.; Armes, S. P. Star Diblock Copolymer Concentration Dictates the Degree of Dispersion of Carbon Black Particles in Nonpolar Media: Bridging Flocculation versus Steric Stabilization. *Macromolecules* **2015**, *48*, 3691–3704.

(4) North, S. M.; Jones, E. R.; Smith, G. N.; Mykhaylyk, O. O.; Annable, T.; Armes, S. P. Adsorption of Small Cationic Nanoparticles onto Large Anionic Particles from Aqueous Solution: A Model System for Understanding Pigment Dispersion and the Problem of Effective Particle Density. *Langmuir* **2017**, *33*, 1275–1284.

(5) Creutz, S.; Jérôme, R.; Kaptijn, G. M. P.; Van Der Werf, A. W.; Akkerman, J. M. Design of Polymeric Dispersants for Waterborne Coatings. *J. Coatings Technol.* **1998**, *70*, 41–46.

(6) North, S. M.; Armes, S. P. Aqueous One-Pot Synthesis of Well-Defined Zwitterionic Diblock Copolymers by RAFT Polymerization: An Efficient and Environmentally-Friendly Route to a Useful Dispersant for Aqueous Pigments. *Green Chem.* **2021**, *23*, 1248–1258.

(7) Mulqueen, P. J.; Thomson, N. R.; Biggs, S. R.; Chagneux, N.; Dubois, M. E. R.; Sarker, P.; Scanlon, S. Micelle-Coated Crystalline Particles. WO 2013/004705 A1, 2013.

(8) Chan, D. H. H.; Cockram, A. A.; Gibson, R. R.; Kynaston, E. L.; Lindsay, C.; Taylor, P.; Armes, S. P. RAFT Aqueous Emulsion Polymerization of Methyl Methacrylate: Observation of Unexpected Constraints When Employing a Non-Ionic Steric Stabilizer Block. *Polym. Chem.* **2021**, *12*, 5760–5769.

(9) Cunningham, V. J.; Alswieleh, A. M.; Thompson, K. L.; Williams, M.; Leggett, G. J.; Armes, S. P.; Musa, O. M. Poly(Glycerol Monomethacrylate)-Poly(Benzyl Methacrylate) Diblock Copolymer Nanoparticles via RAFT Emulsion Polymerization: Synthesis, Characterization, and Interfacial Activity. *Macromolecules* **2014**, *47*, 5613–5623.

(10) Akpinar, B.; Fielding, L. A.; Cunningham, V. J.; Ning, Y.; Mykhaylyk, O. O.; Fowler, P. W.; Armes, S. P. Determining the Effective Density and Stabilizer Layer Thickness of Sterically Stabilized Nanoparticles. *Macromolecules* **2016**, *49*, 5160–5171.

(11) György, C.; Verity, C.; Neal, T. J.; Rymaruk, M. J.; Cornel, E. J.; Smith, T.; Growney, D. J.; Armes, S. P. RAFT Dispersion Polymerization of Methyl Methacrylate in Mineral Oil: High Glass Transition Temperature of the Core-Forming Block Constrains the Evolution of Copolymer Morphology. *Macromolecules* **2021**, *54*, 9496–9509.

(12) Chan, D. H. H.; Kynaston, E. L.; Lindsay, C.; Taylor, P.; Armes, S. P. Block Copolymer Nanoparticles Are Effective Dispersants for Micrometer-Sized Organic Crystalline Particles. *ACS Appl. Mater. Interfaces* **2021**, *13*, 30235–30243.

(13) Urkude, R. Shelf Life Studies on Bifenthrin 10 EC Using GC-FID. *Int. Res. J. Sci. Eng.* **2019**, *7*, 101–104.

(14) Canton, I.; Warren, N. J.; Chahal, A.; Amps, K.; Wood, A.; Weightman, R.; Wang, E.; Moore, H.; Armes, S. P. Mucin-Inspired Thermoresponsive Synthetic Hydrogels Induce Stasis in Human Pluripotent Stem Cells and Human Embryos. *ACS Cent. Sci.* **2016**, *2*, 65–74.

(15) Derry, M. J.; Smith, T.; O'Hora, P. S.; Armes, S. P. Block Copolymer Nanoparticles Prepared via Polymerization-Induced Self-Assembly Provide Excellent Boundary Lubrication Performance for Next-Generation Ultralow-Viscosity Automotive Engine Oils. *ACS Appl. Mater. Interfaces* **2019**, *11*, 33364–33369.

(16) Mable, C. J.; Gibson, R. R.; Prevost, S.; McKenzie, B. E.; Mykhaylyk, O. O.; Armes, S. P. Loading of Silica Nanoparticles in Block Copolymer Vesicles during Polymerization-Induced Self-Assembly: Encapsulation Efficiency and Thermally Triggered Release. *J. Am. Chem. Soc.* **2015**, *137*, 16098–16108.

(17) Chan, D. H.; Millet, A.; Fisher, C. R.; Price, M. C.; Burchell, M. J.; Armes, S. P. Synthesis and Characterization of Polypyrrole-Coated Anthracene Microparticles: A New Synthetic Mimic for Polyaromatic Hydrocarbon-Based Cosmic Dust. *ACS Appl. Mater. Interfaces* **2021**, *13*, 3175–3185.

(18) Burchell, M. J.; Cole, M. J.; McDonnell, J. A. M.; Zarnecki, J. C. Hypervelocity Impact Studies Using the 2 MV Van de Graaff Accelerator and Two-Stage Light Gas Gun of the University of Kent at Canterbury. *Meas. Sci. Technol.* **1999**, *10*, 41–50.

(19) Dominikowska, J.; Palusiak, M. Does the Concept of Clar's Aromatic Sextet Work for Dicationic Forms of Polycyclic Aromatic Hydrocarbons? - Testing the Model against Charged Systems in Singlet and Triplet States. *Phys. Chem. Chem. Phys.* **2011**, *13*, 11976–11984.

(20) Goldfarb, J. L.; Külaots, I. Melting Points and Enthalpies of Fusion of Anthracene and Its Heteroatomic Counterparts. *J. Therm. Anal. Calorim.* **2010**, *102*, 1063–1070.